Transport électronique et Verres de Spins

Guillaume Paulin

N° d'ordre : 569
N° attribué par la bibliothèque : _ENSL569

THÈSE

en vue d'obtenir le grade de

Docteur de l'Université de Lyon - École Normale Supérieure de Lyon

spécialité : Physique

LABORATOIRE DE PHYSIQUE

Ecole doctorale de Physique et Astrophysique De Lyon

présentée et soutenue publiquement le 22/06/2010 par

Guillaume Paulin

Transport Electronique et Verres de Spins

Directeur de thèse : *David Carpentier*

Après avis de : Madame Leticia CUGLIANDOLO
Monsieur Gilles MONTAMBAUX

Devant la commission d'examen formée de :

Monsieur David CARPENTIER	*Membre*
Madame Leticia CUGLIANDOLO	*Membre/Rapporteur*
Monsieur Peter C.W. HOLDSWORTH	*Membre*
Monsieur Gilles MONTAMBAUX	*Membre/Rapporteur*
Monsieur Laurent SAMINADAYAR	*Membre*

Résumé

Les travaux décrits dans cette thèse apportent une contribution à la physique de la matière condensée des systèmes désordonnés, à la physique mésoscopique d'une part et à la physique des verres de spins d'autre part.
La première partie de cette thèse étudie de manière numérique le transport électronique cohérent dans un metal non magnétique dopé par des impuretés magnétiques gelées (un verre de spins à basse température). À l'aide d'un code récursif de calcul de la conductance à deux terminaux du système, nous étudions en détail le régime métallique de conduction (conductance élevée) ainsi que le régime isolant (faible conductance). Dans ces deux régimes, des comportements universels du système sont mis en évidence. En outre, une étude des corrélations de conductance pour deux configurations différentes des spins des impuretés permet de relier ces corrélations aux corrélations entre configurations de spins (appelées recouvrement). Cette étude ouvre la voie à la première détermination expérimentale du recouvrement par des mesures de transport.
Une deuxième partie de cette thèse consiste à étudier le modèle de champ moyen de Sherrington-Kirkpatrick, qui décrit la phase à basse température d'un verre de spins d'Ising. Nous nous intéressons ici à la généralisation au cas de spins d'Ising quantiques (*i.e* en champ magnétique transverse) de ce modèle classique très étudié ces trente dernières années. Nous déduisons analytiquement des équations du mouvement dans le cas semi-classique où l'influence des fluctuations quantiques est faible, que nous comparons au cas classique. Ces équations sont résolues numériquement par une méthode pseudo-spectrale.
Mots-Clefs : Physique Mésoscopique, Transport Électronique Cohérent, Localisation Faible, Fluctuations Universelles de Conductance, Systèmes Désordonnés, Verres de Spins, Recouvrement de configurations de Spins, modèle de Sherrington-Kirkpatrick, Fluctuations Quantiques, Théorie des Répliques.

Abstract

The results reported in this thesis contribute to the understanding of disordered systems, to mesoscopic physics on the one hand, and to the physics of spin glasses on the other hand.
The first part of this thesis studies numerically coherent electronic transport in a non magnetic metal accurately doped with frozen magnetic impurities (a low temperature spin glass). Thanks to a recursive code that calculates the two terminal conductance of the system, we study in detail the metallic regime of conduction (large conductance) as well as the insulating regime (small conductance). In both regimes, we highlight a universal behavior of the system. Moreover, a study of correlations between the conductance of different spin configurations of impurities allows us to link these correlations with correlations between spin configurations. This study opens the route for the first experimental determination of the overlap via transport measurements.
A second part of this thesis deals with the study of the mean field Sherrington-Kirkpatrick model, which describes the low temperature phase of an Ising spin glass. We are interested here in the generalization of this model to quantum spins (*i.e* including the possibility to flip by quantum tunneling) of this classical model that was well studied during the past thirty years. We deduce analytically motion equations at the semi-classical level, for which the influence of quantum tunneling is weak, and we compare them with the classical case. We finally solve numerically these equations using a pseudo-spectral method.
Keywords: Mesoscopic Physics, Coherent Electronic Transport, Weak Localization, Universal Conductance Fluctuations, Disordered Systems, Spin Glasses, Spin Overlap, Sherrington-Kirkpatrick model, Quantum Fluctuations, Replica Theory.

Remerciements

Tutant que je me souvienne, j'ai toujours été, comme beaucoup, intéressé par le fonctionnement du monde. Cela dit, je ne considère pas que c'est cet intérêt qui m'a fait suivre la voie de la recherche en physique. Après avoir obtenu la baccalauréat scientifique au Lycée de LA MURE, je n'étais pas trop sûr de savoir ce que j'allais faire. En tant que bon élève, il m'a été fortement conseillé de rentrer dans une CPGE. J'optai pour la plus proche : la PCSI du Lycée Champollion de GRENOBLE. C'est en deuxième année que le déclic s'est produit pour moi : mon professeur de physique était, à cette époque, Monsieur Philippe Odermatt, et c'est lui qui m'a donné le goût pour la physique, avec ses raisonnements qualitatifs, sa rigueur et ses exercices tous plus originaux les uns que les autres. C'est pourquoi je voulais le remercier tout particulièrement car sans son intervention je n'aurais probablement pas poursuivi dans cette voie.

Cela dit, je voulais remercier chaleureusement David Carpentier, mon directeur de thèse, pour sa disponibilité et son encadrement. Il a fair preuve tout au long de mon travail de thèse d'une présence irréprochable et d'une aide très précieuse. Plus généralement, je remercie les membres du groupe de travail de Matière Condensée, le GdT MaCon, qui ont supporté en silence quelques unes de mes présentations orales. Dans le désordre, merci à Tommaso, Peter, Pascal, Edmond, Eric, Andrey, Charles, ...

Je remercie aussi Jean-François Pinton pour m'avoir accueilli cordialement au sein du laboratoire de Physique de l'ENS, et Jean-Michel Maillet, responsable de l'équipe 4 de m'avoir accueilli dans celle-ci. Nos trois secrétaires Laurence, Nadine et Laure méritent toute mon estime pour leur dévouement et leur gentillesse au quotidien.

En ce qui concerne le manuscrit de thèse, je suis extrêmement reconnaissant et honoré que Leticia Cugliandolo et Gilles Montambaux aient accepté d'être rapporteurs. Je remercie de même Peter et Laurent d'avoir bien voulu faire partie de mon jury de soutenance.

À titre plus personnel, je voudrais remercier tout particulièrement Joubs, Gaut (et Solène!!) et JC pour toutes les discussions (scientifiques ou non) qui ont été un véritable exutoire aux problèmes du quotidien. De la même façon j'ai une pensée particulière pour les deux autres membres du fameux groupe de musique "Las Meulas" : dan et thieu, ainsi que tous les joueurs des équipes première et réserve du Rhône Sportif Rugby. J'ai également énormémement apprécié les discussions et les moments de détente avec mes co-bureaux successifs Karol, Seb, Ludo et Pierre.

Je voulais remercier tout particulièrement ma nièce Noélie, qui, du haut de ses (presque!) trois ans est venue assister à ma soutenance, qui été très attentive, et je lui souhaite bon vent, à elle qui va commencer l'école, lorsque moi j'en ai terminé! Je remercie également mon frère Christophe et Sandrine, Alain et Sylvie, Jacques et Annie et Vilma pour tout ce qu'il m'ont

apporté, ainsi que pour leur présence à ma soutenance. Je pense également à Jérôme et Sylvie, à Sabine et Jeroen et à Bénédicte, et bien sûr à Sissi.

Enfin, *last but not least* comme disent les anglo-saxons, je voudrais remercier mes parents Monique et Guy sans qui cette thèse (ainsi que beaucoup d'autres choses) n'aurait pas été possible. Pour moi il n'y a pas de mot assez fort pour leur exprimer ce que je pense, je leur dédie donc cette thèse. Merci encore pour tout.

Contents

Introduction

As pointed out very recently by David Sherrington [1], it has been recognized that, for almost fifty years[1] that: *the cooperative physics of interacting systems can exhibit fundamental new behavior that is not apparent in the properties of the individual "elementary units" that make up a many-body system of a very large number of these units.* One famous example of complex systems are spin glasses, where the "elementary unit" is a spin.

As we will see in the following of this manuscript, a "cartoon" to illustrate the character of a complex system is a rugged energy landscape with many hills and valleys. The complexity arising in the case of spin glasses can be illustrated by the so-called Dean's problem[2]. A College Dean is faced with the task of placing students into two dormitories in such a way to ensure that the students are as happy as possible, given that any individual pair might want to be in the same dormitory or in different (we assume for simplicity that feelings between pairs of students are mutual). If, for any three students the number of pairing preferences for being apart is odd, then not all these preferences can be satisfied simultaneously. In chapter I, we present the general feature of frustration in the case of Ising spins (spins pointing "up" or "down"), but if the reader is not accustomed to spins, he can remind this analogy with spin "up" represented by a positive feeling (the corresponding students are willing to be in the same dormitory) and with a spin "down" represented by a negative feeling. This impossibility to satisfy all the students is precisely at the origin of the rich and interesting physics of spin glasses.

On the other hand in the past thirty years, the development of nano technologies made it possible to build very tiny metallic wires and electric devices and allowed to study electronic transport in such circuits. The classical representation of electric transport described at the beginning of last century (Kirchoff, Drude, ...) no longer hold at low temperatures and the requirement of quantum mechanics became compulsory to explain the behavior of electrons in these nanometric samples. In figure 1 is presented one of the numerous devices used to measure the so-called Integer Quantum Hall Effect (IQHE). The classical Hall effect is known for more than 100 years, but IQHE has been observed experimentally only very recently (Nobel Prize for Klaus von Klintzing in 1985 for the first observation of IQHE in 1980).

Most of the time, the nano-devices are built with metals or semiconductors, but hardly any studies are performed with spin glass nanowires inside to measure their resistance. The main goal of this thesis is to perform a quantitative theoretical analysis of transport in nano wires built of spin glasses. One major reason to do this lies in the fact that the resistance, in the quantum (or coherent as we will see later) regime is characteristic of the internal disorder that is encountered by the electrons (*i.e* impurities, ...).

In the first part of this thesis, we introduce in detail the spin glass physics (chapter 1), in particular, we show the occurrence of a phase transition between a paramagnetic and a magnetically frozen state (the spin glass phase). At the end of this chapter, we present different theoretical proposals aiming to describe the spin glass phase. We show that it is a very poorly understood state. This lack of information lead us to propose a new technique to get information on the complexity of spin glasses, which is coherent transport. Chapter 2 and 3 introduce the coherent transport in metallic devices at the theoretical and experimental level in detail. Moreover, e present in chapter 3, the few experimental studies of coherent transport in spin glasses. In part II, we describe the numerical method we use for that purpose (chapter 4), and in chapter 5 and 6 we present our results. In chapter 6 we address in particular the issue of the experimental measurement of our proposal.

[1] since the theoretical explanation of superconductivity by Bardeen, Cooper and Schrieffer.

[2] this example is a first approach to **frustration** arising in spin glasses, due to random interactions between spins

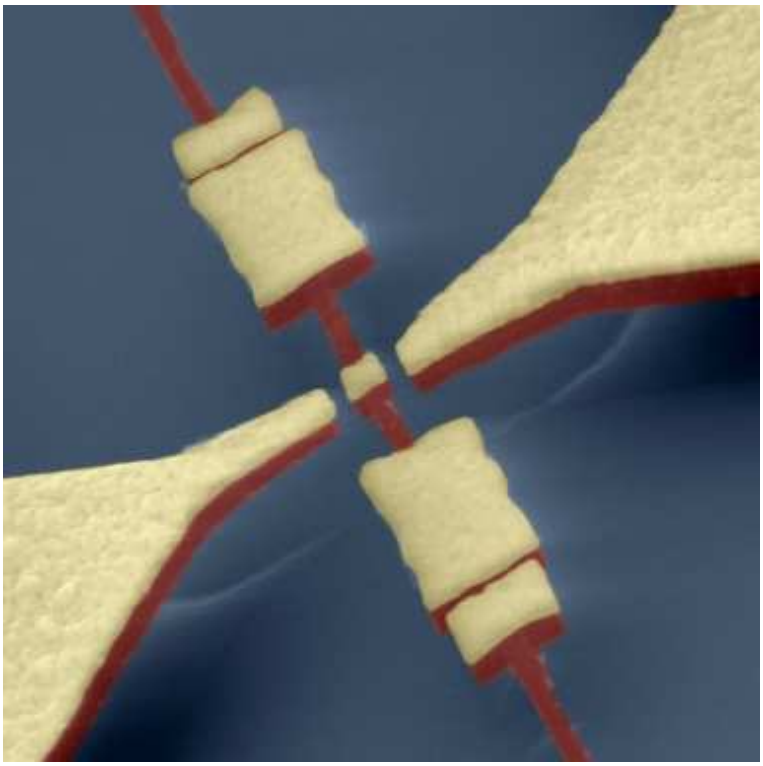

Figure 1: *Illustration of a nano circuit with metallic wires of width of a few tens of nanometers. This particular shape is used to measure the Hall effect in the quantum regime (Integer Quantum Hall Effect).*

The last part of this thesis deals with a model of spin glasses which is a generalization of the Sherrington-Kirkpatrick model, and that accounts for the description of an Ising spin glass in a transverse magnetic field[3] at the mean field level. We present our motivations in chapter 7 and chapter 8 is devoted to the analytical derivation of the equations of motion, and preliminary numerical solutions of these equations are presented.

[3]here transverse means that the magnetic field is perpendicular to the direction of the Ising spins.

Part I

Introduction

Le commencement est comme un dieu qui, aussi longtemps qu'il séjourne parmi les hommes, sauve toutes choses.

Platon

L'avantage du désordre c'est qu'il se transforme en ordre, tôt ou tard.

Jean Basile

Chapter 1
The Spin Glass physics

1.1 Spin Glasses: the physics of complexity

1.1.1 A new state of matter

One of the effort of physics during the last two centuries has been to understand condensed states of matter. These efforts began with Van der Waals and the study of the liquid-gas transition, continued with the study of perfectly condensed matter, such as the paramagnetic-ferromagnetic transition, or the superconducting state of matter, characterized by a non resistive current conduction, which has been studied in great details and rewarded by Nobel prizes. All these states are characterized by long range order and pure materials. But in the nature, there exists no crystal perfectly grown on a scale greater than the centimeter. For instance inclusions in diamonds or precious stones are defects, and the definition of the "carat" concerning gold is representative of the degree of purity of the metal, see table 1.1. On this table we see that even a 24 carat gold piece has impurities (0.01% of the atoms are impurities). We then conclude that in the nature, matter is *ill-condensed*[1].

Table 1.1: *Definition of the carat as a function of the atomic percentage of gold.*

carats	24	20	18	16	14	12	10	8	6	4
% of gold	99.99	83.34	75.01	66.68	58.35	50.02	41.69	33.36	25.03	16.7

Spin glasses are one famous example of disordered materials. The simplest definition of a spin glass is the following: it is a collection of magnetic moments, frozen at low temperature, with no simple long range order. This disordered phase is unconventional as we are more accustomed to the perfect order of usual magnets (*i.e* ferromagnets). A first type of spin glasses consists in doping a non magnetic noble metal matrix (Au, Ag or Cu) with transition metal impurities (for instance Mn or Fe). But later in this manuscript we will also study insulating spin glasses, that are alloys of the type: $LiHo_xY_{1-x}F_4$, with dipolar interactions between impurities. A third type of spin glasses are semi-conducting. There exists then a wide range of types of spin glasses. In part II, we study metallic spin glasses, and in part III, we will mostly focus on insulating spin glasses. In all these compounds, the disordered phase that characterizes the spin glass implies the occurrence of a competition between the moments, so that no single configuration is uniquely favored. In the next section, a brief presentation of the interaction between the spins is presented.

1.1.2 Interaction between spins

At high enough concentration of impurities, the interactions between spins of impurities cannot be neglected. The type of interactions depends on the nature of the spin glass. For canonical spin glasses the interactions are indirect and due to the polarization of the electronic cloud as we will see in the following, and for insulating spin glasses the interactions appears to be of dipolar kind. In this section, we focus on the origin of the interactions for canonical spin glasses, since they are the most widespread category of spin glasses.

As shown by Ruderman and Kittel in 1954 [3], Kasuya in 1956 [4] and Yosida in 1957 [5], the RKKY interaction between two magnetic impurities is an indirect polarization interaction. A first impurity polarizes the surrounding cloud of electrons of conduction: the spins of these electrons

[1] this expression is taken from the title of a school at Les Houches [2].

will tend to align or anti-align with the spin of the impurity. The corresponding susceptibility of the cloud is of the form:

$$\chi(r) \propto \frac{\cos(k_F r)}{(k_F r)^3}, \qquad \text{for} \qquad r \to \infty \tag{1.1}$$

k_F is the Fermi wave vector of the electrons in the sample. The spatial oscillations of the

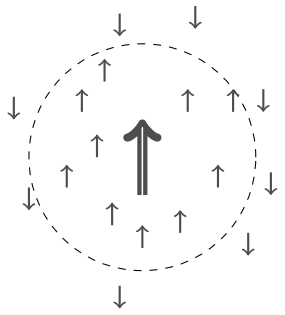

Figure 1.1: *Schematic representation of the electronic cloud surrounding an impurity. Spins of electrons are polarized because of Friedel oscillation of the susceptibility of the cloud. These oscillations tend to favor ferromagnetic interactions up to distance d_1. Then antiferromagnetic couplings tend to anti align the spins of electrons.*

susceptibility are known as the Friedel oscillations and the consequence on electrons is illustrated in figure 1.1. The polarized cloud will then act on the spin of another impurity in the same way. The consequence of RKKY interaction and of random distances between impurities leads to a random sign in the interaction (*i.e* the interaction between the magnetic impurities is either ferromagnetic or antiferromagnetic, depending on the distance between them). Concerning insulating spin glasses, the interaction is different quantitatively but it also leads to a random ferromagnetic or antiferromagnetic interaction between spins (or pseudo spins, see chapter 7, section 7.3).

1.1.3 The physics of frustration

Interactions between impurities whose main characteristic is to be either ferromagnetic or anti ferromagnetic, leads to frustration. Two main types of frustration exist: the geometrical frustration, due to the topology of the lattice (it is for instance the case in spin ice as described below). The second type of frustration, which occurs in spin glasses is due to disorder. It is the goal of this section to present these two types of frustration.

Geometrical frustration

Consider a triangular lattice with antiferromagnetic bounds as illustrated on figure 1.2. We show that, if the product of the couplings J in the loop is negative, the system is frustrated: no single configuration of the spins satisfies all the constraints in the lattice. This geometrical frustration is crucial in compounds as $Dy_2Ti_2O_7$ or $Ho_2Ti_2O_7$ [6, 7] called spin ice, by analogy with real water ice. In these compounds, the frustration is related to the tetragonal topology of the pyrochlore lattice.

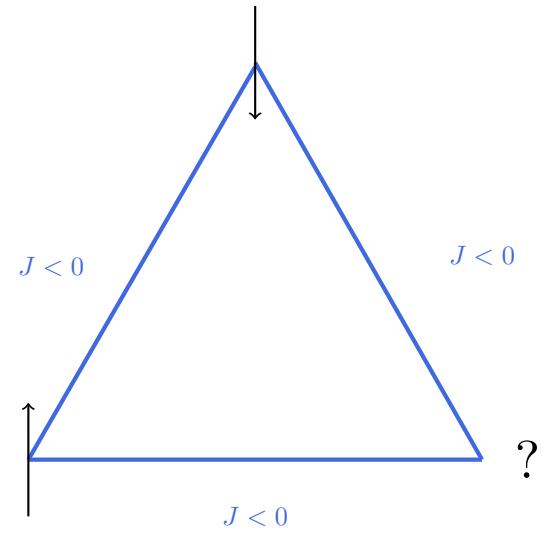

Figure 1.2: *Triangular lattice with antiferromagnetic bounds between the Ising spins. No configuration (up or down) for the third spin satisfies all the constraints in the system.*

Frustration due to disorder

Another type of frustration is the frustration due to disorder: in the previous section, it has been shown that in canonical spin glasses, interactions between impurities have an oscillatory behavior with the distance between impurities. Consider three impurities labeled by (A), (B) and (C). We suppose impurity (A) to be at the origin as illustrated in figure 1.3. The impurity (B) is at

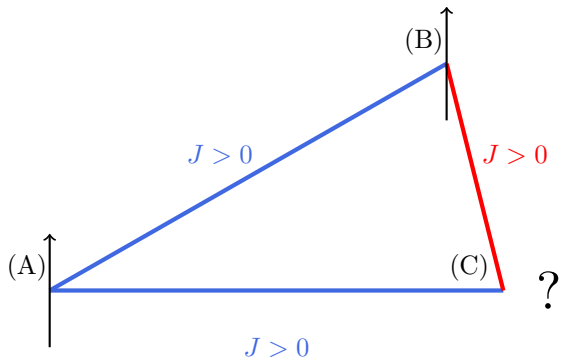

Figure 1.3: *Random positions of impurities (A), (B) and (C) lead to couplings with random signs following equation (1.1), and therefore to frustration. $J > 0$ leads to ferromagnetic couplings and $J < 0$ to antiferromagnetic couplings.*

a distance $r_{(\mathrm{B})}$, which corresponds to an antiferromagnetic coupling thanks to equation (1.1). In the same way, impurity (C) is at a distance $r_{(\mathrm{C})}$ of (A) which also leads to an antiferromagnetic coupling between impurities. Between (B) and (C), the distance is such that the coupling is ferromagnetic. Here again if the spin of (A) is up and the one of (B) is down, no configuration

for the spin of (C) satisfies all the constraints in the system. This kind of frustration is intrinsically due to the random positions of impurities and to the Friedel oscillations of the couplings between them.

At low temperature, when interactions between spins are dominant with respect to the thermal fluctuations, the system freezes into a magnetic state with no long range order: spins are frozen in a configuration where all constraints cannot be simultaneously be satisfied, the system is called *frustrated*. This phase is characterized by a vanishing spontaneous global magnetization but a non vanishing spontaneous local magnetization[2] at each site. Consequently, the description of the freezing in terms of a standard magnetic order parameter, such as the averaged magnetization for the paramagnetic-ferromagnetic transition will fail.

1.2 The Spin Glass state

This section is not a exhaustive description of all properties of Spin Glasses, it is a brief introduction to some relevant characteristics of the Spin Glass phase due to frustration. For a more detailed analysis see [8, 9, 10].

1.2.1 From a paramagnet to a Spin Glass: a conventional phase transition?

The existence or not of a real phase transition from a high temperature paramagnetic state, where the spin of each impurity flips almost freely to a low temperature spin glass where the spins appear frozen with no long range order, has been a debating issue for years. The temperature of freezing of the spins is deduced experimentally from susceptibility measurements. In figure 1.4 Mulder et al. [11] show the "hallmark" of spin glass behavior. The susceptibility is measured by applying an oscillating magnetic field and measuring the magnetic response of the material (a Cu:Mn spin glass in that case). At high temperatures the susceptibility follows a usual Curie law, similarly to what is found for an ideal paramagnet. At low temperature, the spins can no longer follow the oscillating magnetic field, and hence the real part of the susceptibility $\chi'(\omega)$ shows a sharp drop. The spin glass temperature is defined as the temperature of the maximum in χ' as shown by the arrow on this figure. In inset, a zoom on the peak shows that it is rounded and that it depends weakly on the frequency of the magnetic field. The exact value of the spin glass temperature is the extrapolation in the true static limit ($\omega \to 0$).

Usually, to prove the existence of a conventional phase transition thermodynamically, and to deduce the order of the transition, we use the discontinuity or the cusp of the specific heat of the system [12]. In figure 1.5, Wenger and Keesom [13] show that there is no detectable cusp or discontinuity in the specific heat at the spin glass transition indicating no standard phase transition.

Another proof of the existence of a phase transition lies in the divergence of the non linear part of the magnetization M in a magnetic field H. Writing the expansion for M in a weak magnetic field:

$$\frac{M}{H} = \chi_0^{\text{n.i}} \left[a_1 - \frac{1}{3} a_3 \left(\frac{\mu H}{k_B T} \right)^2 + \frac{2}{15} a_5 \left(\frac{\mu H}{k_B T} \right)^4 + \dots \right], \tag{1.2}$$

where μ is the magnetic moment per spin and $\chi_0^{\text{n.i}}$ is the linear susceptibility for a non interacting paramagnet, one can find an expression for the non linear susceptibility $1 - M/(\chi_0 H)$, where χ_0 is

[2] this local magnetization indicates a freezing of the spins and it vanishes in the high temperature phase.

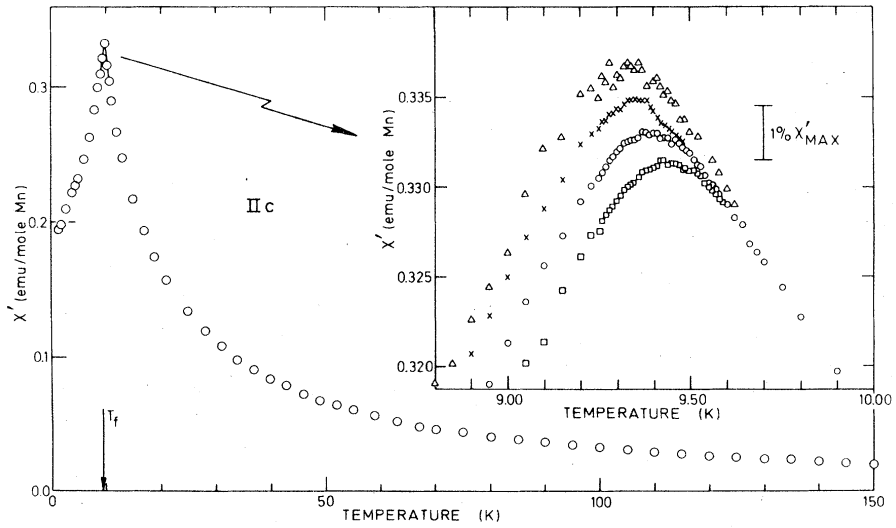

Figure 1.4: *Real part χ' of the complex susceptibility $\chi(\omega)$ as a function of temperature for a Cu:Mn sample (). The inset shows the frequency dependence and rounding of the cusp by use of strongly expanded coordinate scales. Measuring frequencies:* 1.33 *kHz (squares),* 234 *Hz (circles),* 104 *Hz (crosses) and* 2.6 *Hz (triangles). Extracted from Mulder et al. [11].*

the susceptibility of the paramagnet. Omari et al. [14] have studied this quantity experimentally. They have shown that it diverges at the spin glass temperature as predicted by [15]

$$1 - \frac{M}{\chi_0 H} = (1 - T/T_g)^{\beta} \tilde{M} \left[\left(\frac{H}{T} \right)^2 (1 - T/T_g)^{-(\gamma+\beta)} \right]. \tag{1.3}$$

Figure 1.6 presents corresponding data for the Cu:Mn spin glass in a scaling form. See also [16].

To end up with the study of the transition, it is also possible to characterize the freezing temperature T_g from measurement of the out of phase susceptibility χ''. In figure 1.7 are plotted the real and imaginary parts of the susceptibility as functions of temperature. The imaginary part presents a sudden evolution near the spin glass temperature T_g, with a maximum at the transition. This temperature corresponds also to the maximum of the variation of χ'', $\mathrm{d}\chi''/\mathrm{d}T$. Dissipation[3] in the system strongly indicates the appearance of relaxation phenomena. We will come back to this point in the next two sections.

It is worth noticing that the study of linear or non-linear susceptibilities gives hardly any information on the spin configuration of the spin glass and its modification with time or successive quenching of the system as they measure correlations between spins in the same configuration and at different positions. One aim of this thesis is to find another quantity that is able to describe such modifications.

1.2.2 Field cooled (FC) and zero-field cooled (ZFC) susceptibilities

Another characteristic of spin glasses is their sensitivity to small perturbations, such as a weak magnetic field upon cooling. More accurately, for temperatures below the spin glass temperature

[3] *i.e* a non vanishing imaginary part for the susceptibility.

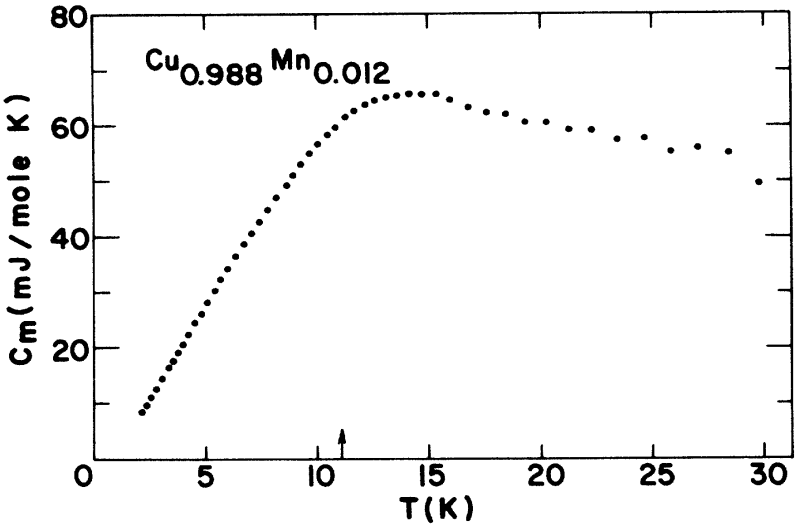

Figure 1.5: *The specific heat of a Cu:Mn alloy plotted versus temperature. The arrow shows where the susceptibility has its cusp. Extracted from Wenger and Keesom [13].*

T_g, the value of the susceptibility depends on how the system was cooled down at T_g. Two possibilities are considered:

(i) **Zero field cooled:** the system is cooled down from a temperature above T_g to a temperature below T_g without applying any magnetic field. In the low temperature phase, a small magnetic field is applied to measure the susceptibility.

(ii) **Field cooled:** the system is cooled down under a given weak magnetic field H. The curve of susceptibility obtained is almost constant and different from the one obtained via a ZFC process.

The results are presented in figure 1.8 and are extracted from [18]. Again, the study is done with a Cu:Mn spin glass. Only a weak magnetic field is sufficient to modify completely the spin glass response, resulting in very different values of susceptibility. Experimentally, concerning ZFC, each measure of susceptibility implies the use of a magnetic field and takes a few minutes. The transition temperature T_g is defined as the temperature of appearance of the irreversibility ZFC-FC, it will then depend weakly on time as seen previously in figure 1.4, where the real part of the susceptibility depends on the frequency of the magnetic field.

This curve shows also that the behavior of a spin glass depends on its *history*: the value at low temperature of the susceptibility depends on the way the system has been cooled down previously (with or without a magnetic field). All these results suggest that a spin glass is not at equilibrium: the frustrated spins may relax. Measures of the dynamic susceptibility [19] in figure 1.9 allows the determination (at least qualitatively) of the distribution of relaxation times.

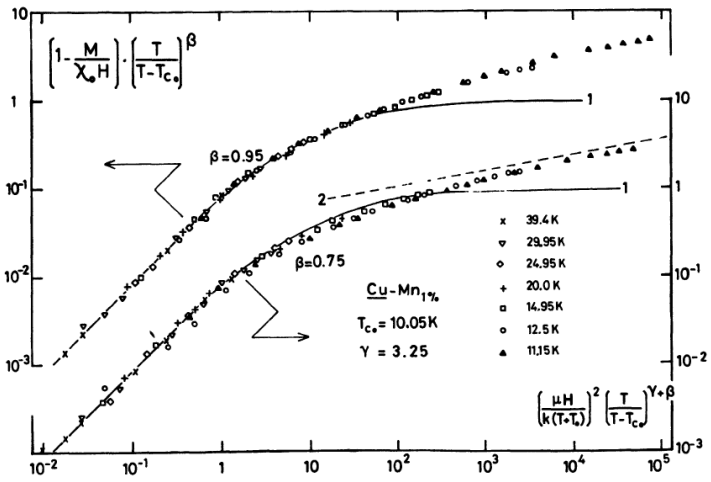

Figure 1.6: *Universal plot of equation (1.3) showing the success of the scaling argument for all the data points (H up to 70 kOe, T up to 4 TJ with $\gamma = 3.25$ and $\beta = 0.75$ as deduced from the temperature dependence of a_3 and a_5. The continuous curve 1 and the dashed curve 2 give the asymptotic behaviours. Extracted from Omari et al. [14]. The spin glass considered is Cu:Mn for 1 at %.*

Following [19], it is possible to write for the real and imaginary parts of the susceptibility:

$$\chi'(\omega) = \chi_s + (\chi_T - \chi_s) \int_{\tau_{min}}^{\tau_{max}} g(\tau) \frac{\mathrm{d}(\log \tau)}{1 + \omega^2 \tau^2}, \tag{1.4}$$

$$\chi''(\omega) = (\chi_T - \chi_s) \int_{\tau_{min}}^{\tau_{max}} \omega \tau g(\tau) \frac{\mathrm{d}(\log \tau)}{1 + \omega^2 \tau^2}, \tag{1.5}$$

where χ_T and χ_s are respectively the isothermal and the adiabatic susceptibilities. This defines an effective distribution of relaxation times $g(\tau)$. The existence of a lower (τ_{min}) and an upper (τ_{max}) bound for the relaxation times is assumed. Experimentally, it is possible to estimate these bounds as well as the average relaxation time τ_{av}, as shown in figure 1.9. This curve indicates the existence of a great range of relaxation times, and consequently a complex landscape for the phase space of a spin glass. In the next section we will present more quantitative examples of dynamic effects in spin glasses and come back to this notion of complexity.

1.3 Aging and rejuvenation in a spin glass

Spin glasses are *aging* due to frustration: after a quench of the system, spins will relax to satisfy more and more constraints. The more constraints satisfied, the slower the relaxation as the number of frustrated spins diminishes. As a consequence, the only characteristic time of the dynamics is its age, as we will see below.

1.3.1 Thermo-remanent magnetization

To measure the thermo-remanent magnetization (TRM) of a system, the system is cooled down from a temperature above the spin glass temperature T_g to a temperature $T_0 < T_g$, in a small magnetic field. It then "waits" during time t_w at T_0 in the same field. At $t = 0$, the field is shut

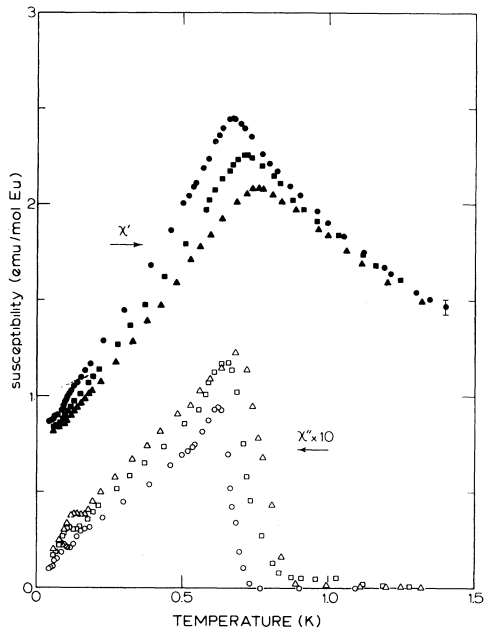

Figure 1.7: . *Temperature dependence of the dispersion χ' (solid symbols) and absorption χ'' (open symbols) for $Eu_{0.2}Sr_{0.8}S$, for $\omega = 10.9$ Hz (circles), 261 Hz (squares) and 1969 Hz (triangles) (applied ac field $h \approx 0.1$ Oe). Extracted from [17].*

down and the magnetization is measured. Results are presented by Vincent et al. [20] in figure 1.10, plot 1.a. Different curves correspond to different waiting times t_w.

This plot shows that the relaxation curves of the magnetization $M(t)$ depend on the age t_w of the system. Qualitatively, the more one waits, the slower the relaxation of the magnetization. Aging phenomenon is highlighted: TRM is a **non-stationary** quantity. In this semi-log plot, each curve presents an inflection point around $\log t \approx \log t_w$. As the relaxations are slower than exponential, the assumption of one single relaxation time is wrong as seen in the previous section, and the magnetization is written in terms of the distribution of relaxation times $g(\tau)$ [20]:

$$m_{t_w}(t) \equiv \frac{M(t+t_w, t_w)}{M_{fc}} = \int_{\tau_0}^{\infty} g_{t_w}(\tau) e^{-t/\tau} \mathrm{d}\tau, \tag{1.6}$$

where τ_0 is a microscopic attempt time. M_{fc} is the field cooled magnetization[4]. The distribution depends also on the waiting time t_w. The derivative with respect to $\log t$ of this equation gives access to the distribution of relaxation times:

$$\frac{\mathrm{d}m_{t_w}(t)}{\mathrm{d}\log t} \approx g_{t_w}(t). \tag{1.7}$$

Figure 1.11 from reference [21] shows a plot of the spectrum of relaxation times. As previously said, the maximum of the distribution verifies $\log t \approx \log t_w$. Therefore, in first approximation, aging can be seen as a "*logarithmic shift towards longer times* of a wide spectrum of response times" [20]. This suggests a t/t_w scaling in the TRM. This is the plot 1.b of figure 1.10.

[4]for $T < T_g$, the field cooled magnetization is almost constant, according to figure 1.8.

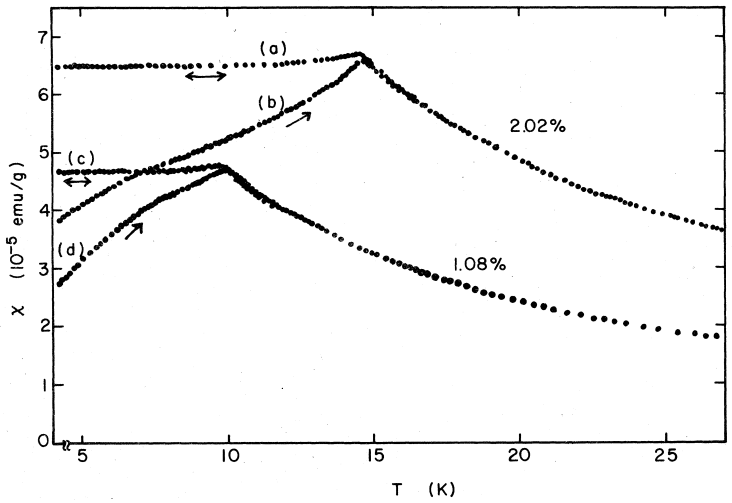

Figure 1.8: *Static susceptibilities of Cu:Mn vs temperature for 1.08- and 2.02-at.% Mn. After zero-field cooling ($H < 0.05G$), initial susceptibilities (b) and (d) were taken for increasing temperature in a field of $H = 5.90G$. The susceptibilities (a) and (c) were obtained in the field $H = 5.90G$ applied before cooling the samples. Extracted from [18].*

1.3.2 Temperature cycles

Up to now, we have considered dynamics of the spin glass at a single temperature below the transition. In this part we discuss what happens when the temperature is varied in the spin glass phase, giving rise to spectacular effects of frustration as the one presented in figure 1.12. On the left curve, the authors [20] quenched a system below the spin glass temperature (at $T_1 = 12K$). The results on the out of phase susceptibility is the sharp decrease we have already discussed. After aging during a time t_1 at temperature T_1, the system is cooled down to $T_2 = 10K$. The imaginary part of the susceptibility starts again to age, as if the system just came from the paramagnetic state (sharp decrease of χ''). This effect is called **rejuvenation**: the system acts as if it did not remember it was in the spin glass phase during time t_1. At this temperature, the system starts to age during time t_2. At that time, the temperature is increased to $T_1 = 12K$ again. The aging starts again as if the system had not been cooled down to T_2 (see the inset of that figure). This is one spectacular signature of **memory effect** as seen previously. The right curve of figure 1.12 shows the same effects for two steps in temperature, and for a canonical spin glass in inset.

In this section both static and dynamic characteristic behaviors of spin glasses were illustrated, but no experiments showed the measurement of a true order parameter for the spin glass transition, as the magnetization in the case of the paramagnetic/ferromagnetic phase transition[5]. The next section deals with the theory of spin glasses and the question of the order parameter will be addressed.

[5] we remind the reader that here the magnetization is not a good order parameter as it is vanishing in both phases when no magnetic field is applied.

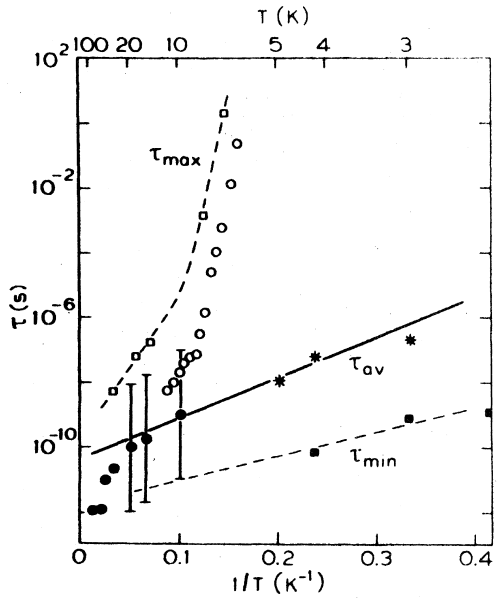

Figure 1.9: *Relation times as obtained from χ'' measurements for the $(CoO)_{0.4}(Al_2O_3)_{0.1}(SiO_2)_{0.5}$ spin glass, plotted versus inverse temperature: maximum and minimum relaxation times (respectively open and solid squares), average relaxation time (stars). Open circles are deduced from the frequency dependance of $T_g(\omega)$ (peak of $\chi'(\omega)$) and solid circles are μSR measurements. Extracted from [19].*

1.4 Theoretical proposals for Ising spins

In this section we focus for simplicity on Ising spins since most of the theoretical studies are done for Ising spins. See [24, 25] for very recent studies on Heisenberg spin glasses.

Two main theories are available to describe the Ising spin glass phase: a model first developed by Edwards and Anderson (EA) [26, 27] followed by its solution at the mean field level: the Sherrington-Kirkpatrick (SK) model. A second theory was developed in the early eighties by Fisher and Huse [28], which gives different results. The goal of this section is to introduce both models and to give the main differences between them.

1.4.1 Mean field theory: the Sherrington-Kirkpatrick model

Preamble: the EA model

In 1975, Edwards and Anderson [26] proposed a model to describe the nature of the low temperature spin glass phase, given by the following Hamiltonian:

$$\mathcal{H} = -\sum_{<i,j>} J_{ij}\vec{S}_i \cdot \vec{S}_j + h\sum_i S_i^z, \tag{1.8}$$

where $\vec{S}_i$ is the spin at site i and h a magnetic field along the z-axis. J_{ij} represents the coupling between spin i and j. These spins are situated on a regular lattice and J_{ij} is random in sign, with equal probability to have positive or negative couplings. See [8] and [10] for a review. The

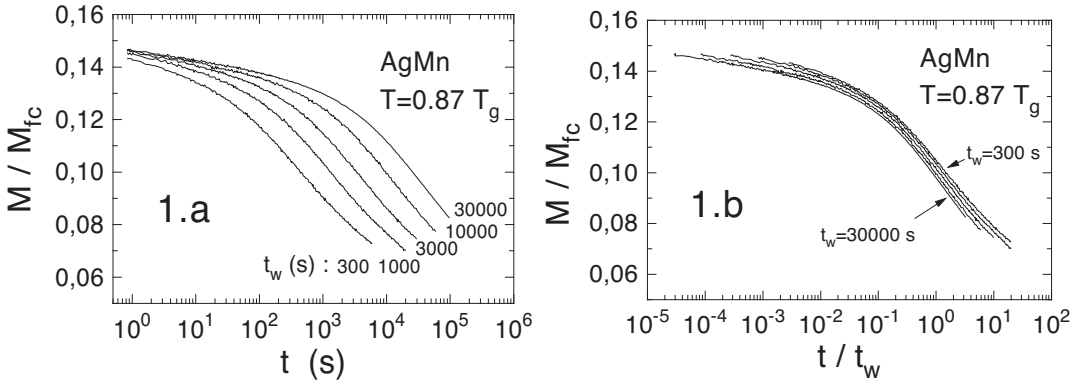

Figure 1.10: *1.a: Thermo-remanent magnetization M, normalized by the field cooled value M_{fc}, versus time (in seconds) (log scale) for the Ag:$Mn_{2.6\%}$ sample, at $T = 0.87T_g$. The sample has been cooled in a $0.1Oe$ field from above T_g to $0.87T_g$; after waiting t_w, the field has been cut at $t = 0$, and the decaying magnetization recording. 1.b: Same data as 1.a presented as a function of t/t_w. Extracted from [20].*

distribution of couplings $P[J_{ij}]$ is often considered gaussian

$$P[J_{ij}] = \prod_{i<j} \sqrt{\frac{N}{2\pi J}} \exp\left(-\frac{NJ_{ij}^2}{2J^2}\right) \tag{1.9}$$

or bi-modal:

$$P[J_{ij}] = \frac{1}{2}\delta(J_{ij} - J) + \frac{1}{2}\delta(J_{ij} + J). \tag{1.10}$$

This last model is also often called the "$\pm J$ model".

Suggesting that the spin glass phase is characterized by a freezing of spins in random orientations, Edwards and Anderson proposed the following order parameter, known as the Edwards-Anderson (EA) order parameter:

$$q_{EA} = \frac{1}{N}\sum_{\alpha} P_\alpha \sum_{i=1}^{N} (\langle \vec{S}_i^\alpha \rangle)^2, \tag{1.11}$$

where $\langle\cdot\rangle$ represents the ensemble average and N is the number of magnetic impurities. P_α is defined by:

$$P_\alpha = \frac{e^{-\beta F_\alpha}}{\sum_\alpha e^{-\beta F_\alpha}} \tag{1.12}$$

F_α is the free energy of the system in the energy valley α ($\beta = 1/(k_B T)$). At high temperature, when spins flip freely, this quantity is equal to zero, whereas it is non zero when is system is trapped in one domain of phase space[6] following the illustration of figure 1.14. This definition of the EA order holds in the static limit (the system cannot escape from its energy valley), which is the limit we will consider in all the following. For the original dynamical definition of the EA order parameter, see below.

[6] called an ergodic component.

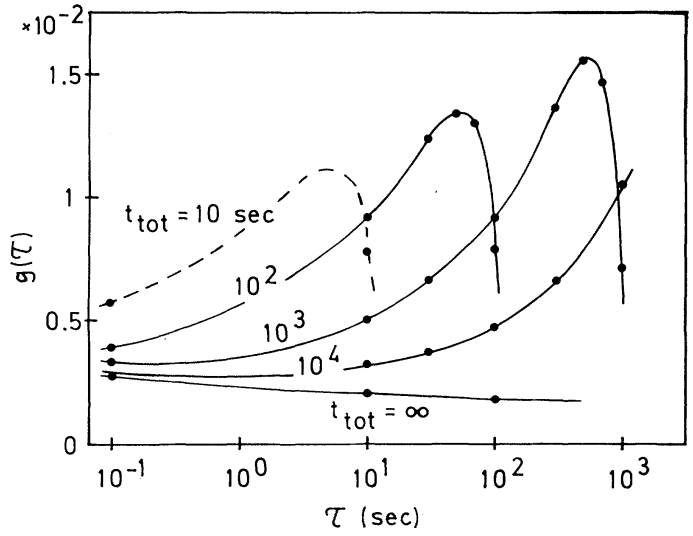

Figure 1.11: *Evolution of the relaxation time spectrum ($g(\tau)$ vs τ) for different total time $t_{tot} = t + t_w$ the system is kept at fixed temperature ($T = 23K$) for a Cu:Mn spin glass (4 at % Mn). The relaxation time spectrum is normalized according to $\int g(\tau) \mathrm{d} \log \tau = 1$. Extracted from [21].*

The EA order parameter and dynamics.
As we have seen in the previous section, spin glasses are slowly relaxing materials. To take the time dependance (aging) into account, the Edwards-Anderson order parameter is defined as:

$$q_{EA} = \lim_{t \to \infty} \lim_{N \to \infty} \langle \vec{S}_i(t_0) \vec{S}_i(t_0 + t) \rangle \tag{1.13}$$

This order parameter measures the memory of spin $\vec{S}_i$ from time t_0 to time $t_0 + t$. In the paramagnetic phase, it tends to 0, whereas it can take finite values in the spin glass phase (even if the limit $t \to \infty$ is taken).

The SK model

A mean field version of the EA model is provided through the Sherrington-Kirkpatrick (SK) model developed in 1975 in [29]. It is an infinite range (mean field) generalization of the EA model in the simpler case of *Ising* spins ($S_i^z = \pm 1$). All spins interact with each other (not only the nearest neighbors as in the EA model) and the Hamiltonian is given by:

$$\mathcal{H}_{SK} = -\frac{1}{2} \sum_{i,j} J_{ij} S_i^z S_j^z + h \sum_i S_i^z. \tag{1.14}$$

The couplings J_{ij} are taken according to the gaussian distribution of equation (1.9), and h is a longitudinal (along the axis of the Ising spins) magnetic field. We will not describe here the calculations within the SK model as chapter 8 is devoted to the solution of this model with an additional transverse magnetic field term: $\Gamma \sum_i S_i^x$. The solution of this model is performed

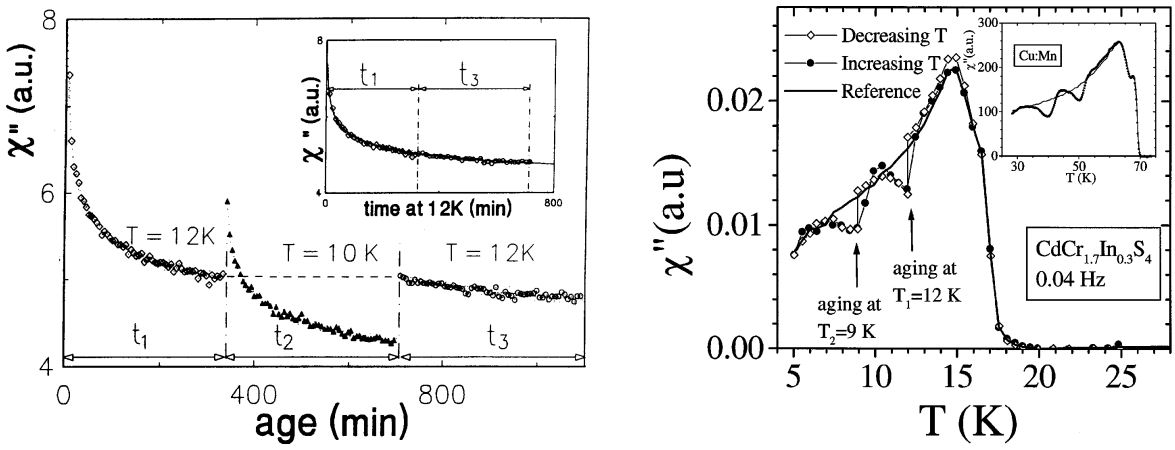

Figure 1.12: *Left curve: out of phase susceptibility χ'' of the $CdCr_{1.7}In_{0.3}S_4$ sample ($T_g = 16.7K$) during a temperature cycle. The frequency ω is equal to $0.01Hz$. The inset shows that, despite the strong relaxation at $10K$, both parts at $12K$ are in continuation of each other. Extracted from [20]. Right curve: same sample as the left curve, but with two stops during cooling, which allow the spin glass to $7h$ at $12K$ and then $40h$ at $9K$. Both aging memories are retrieved independently when heating back (solid circles). The inset shows a similar "double memory" experiment performed on the Cu:Mn metallic spin glass [22]. Extracted from [23].*

using the so called **replica theory** (see [30, 31] for a recent review and chapter 8). This method is useful to calculate disorder averaged free energies in disordered systems, as the averaged free energy is defined by:

$$\overline{F} = -k_B T \overline{\log Z}, \tag{1.15}$$

where Z is the partition function of the system and the overline operator represents disorder averaging. It consists in considering the following "replica trick"

$$\overline{\log Z} = \lim_{n \to 0} \frac{\overline{Z^n} - 1}{n}. \tag{1.16}$$

Assuming n is integer, the quantity $\overline{Z^n}$ is interpreted as the product of the partition functions of n replicas of the same system. When all replicas are assumed equivalent, the paramagnetic phase can be accurately described, but it is not the case of the spin glass phase: in 1978, de Almeida and Thouless (AT) showed [32] that the replica symmetric solution of the SK model is unstable at low temperature: the resulting entropy is found negative.

Instability of the SK solution: the de Almeida and Thouless (AT) line

The accurate description of the spin glass phase is achieved [33] by breaking the symmetry of permutation of replicas, as explained in [32]. From this point, it is possible to define the spin overlap $Q^{\alpha\gamma}$, which accounts for the similarity between replica α and γ.

$$Q^{\alpha\gamma} = \frac{1}{N} \sum_{i=1}^{N} S_i^{z,\alpha} S_i^{z,\gamma}. \tag{1.17}$$

In the symmetric case, this overlap becomes equal to the EA order parameter. In the non symmetric case, it defines a non trivial distance between two replicas in ultrametric trees:

$$d^{\alpha\gamma} = \frac{1}{2}(1 - Q^{\alpha\gamma}). \tag{1.18}$$

The distribution of overlaps $Q^{\alpha\gamma}$ for all pairs of replicas (α, γ) is defined as the order parameter of the spin glass transition [34, 33, 35].

In this article, the influence of the magnetic field h is also studied and the following phase diagram (figure 1.13) shows the AT line[7] in the (h, T) plane. See also [36].

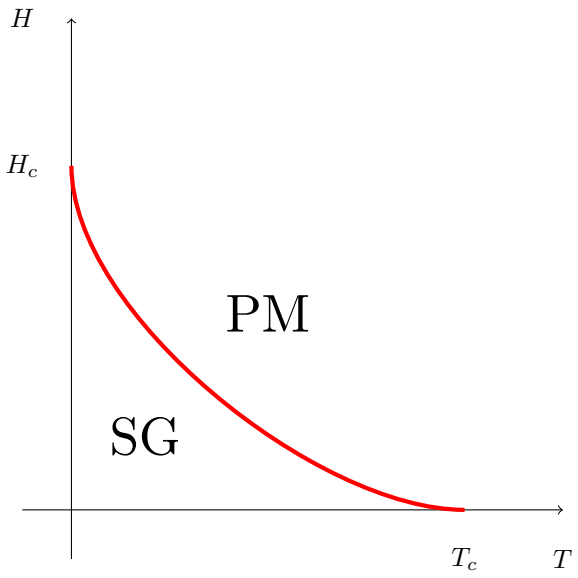

Figure 1.13: *The magnetic field-temperature phase diagram in the Parisi and replica symmetry breaking (RSB) picture.*

Interpretation in terms of a hierarchical structure of the free energy

To explain qualitatively the previous results, a hierarchical view of the free energy of the system has been proposed, as illustrated in figure 1.14. Consider a system quenched at temperature T. It is then trapped in valley α, β or γ (at a given level of the hierarchical tree). The system must search for equilibrium in a new landscape, aging starts. If the temperature is decreased to $T - \Delta T$, new free energy barriers appear and the system, again, must search for the equilibrium, it restarts aging (as seen on figure 1.12). If the temperature is increased back to T, the new metastable states disappear and the system is quenched in its energy valley α, β or γ, and previous aging at temperature $T - \Delta T$ does not play any role. This hierarchical structure for the metastable states explains both rejuvenation and memory effects. Moreover, the appearance in the free energy landscape, of energy barriers with very different heights, is strongly in favor of a wide distribution of relaxation times (*i.e* times to go from one energy valley to another at fixed temperature).

[7] this line represents the frontier between a region where replica symmetry holds and a region where replica symmetry breaking (RSB) appears.

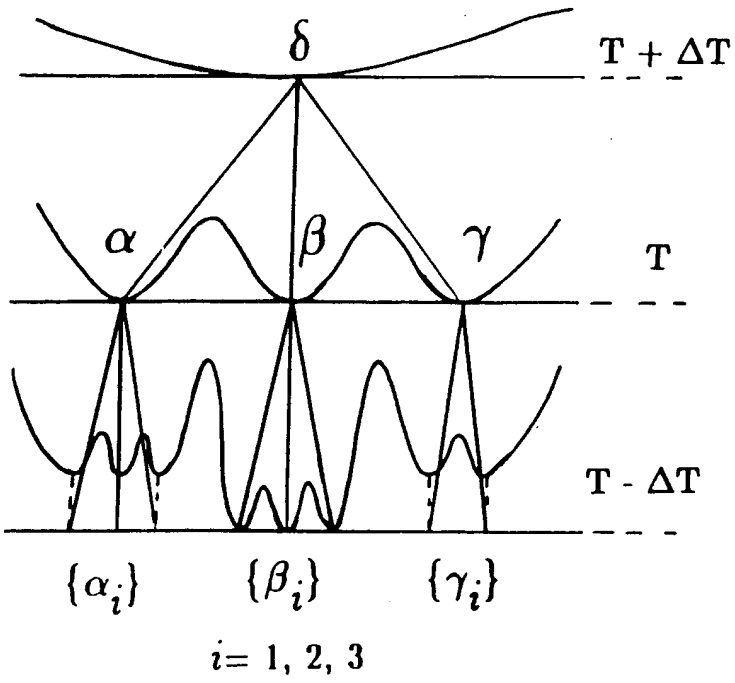

Figure 1.14: *Schematic picture of the hierarchical structure of the metastable states as a function of temperature. Extracted from [20].*

1.4.2 Scaling theory: the droplets model

This phenomenological model, proposed by Fisher and Huse in 1986 [28] and reviewed in [8], accounts for the short-range Ising spin glass. This is a scaling theory based on a simple *ansatz*, motivated by works of Bray and Moore [37] and MacMillan [38]: at zero or very low temperature, the spin glass phase is constituted of one unique fundamental state (up to the reversal of all spins). Flipping all the spins in one compact region of the sample (one "droplet") of size L will cost a free energy[8] that grows with the size of the droplet with a power law: $F_L \sim L^\theta$. θ is called the stiffness exponent [38]. It is crucial to deduce the sign of this exponent as, if $\theta < 0$, the energy of the phase with droplets decreases with L and thermal fluctuations can break this phase, or if $\theta > 0$ the energy of droplets grows with their size and the phase is not destroyed by thermal fluctuations.

The case of ferromagnets

Let consider first the simpler case of ferromagnets before studying the Ising spin glass. In Ising ferromagnets, the low temperature phase sees all its spins pointing in the same direction. Reversing a droplet will then cost an energy proportional to the size of the domain boundary:

$$\Delta E \sim J L^{d-1}, \tag{1.19}$$

[8] this droplet contains L^d spins, where d is the dimension of the sample.

where J is the coupling between spins. In that case, if $d > 1$ the ferromagnetic phase is stable. $d_l = 1$ is called the lower critical dimension.

The case of spin glasses

In the case of Ising spin glasses [39], the random coupling lowers the free energy of the domain, and:

$$\Delta F_L \sim \Upsilon L^\theta, \tag{1.20}$$

with $\theta \leq 1/2(d-1)$ and Υ is a generalization of the interfacial tension. The distribution of the excitation free energies F_L of droplets has the scaling form:

$$P_L(F_L) \approx \frac{1}{\Upsilon L^\theta} \rho(F_L/\Upsilon L^\theta) \tag{1.21}$$

for large L, with $\rho(0) > 0$.

Spin glasses in a magnetic field: the argument of Imry-Ma [40] states that a droplet has a magnetization of order $L^{d/2}$ so that any field aligns the large droplets since $\theta < d/2$. As a consequence, no spin glass phase survives in a magnetic field. Figure 1.15 shows the phase diagram in the (h, T) plane, where h is the magnetic field.

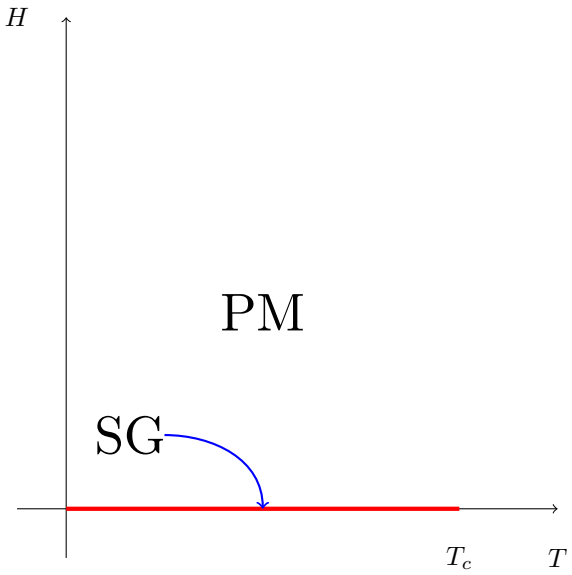

Figure 1.15: *The magnetic field-temperature phase diagram in the droplet picture.*

1.4.3 Slow dynamics and aging

Before concluding, we propose, in this section an overview of theories describing slow dynamics in spin glasses. For a recent review of these results see [41].

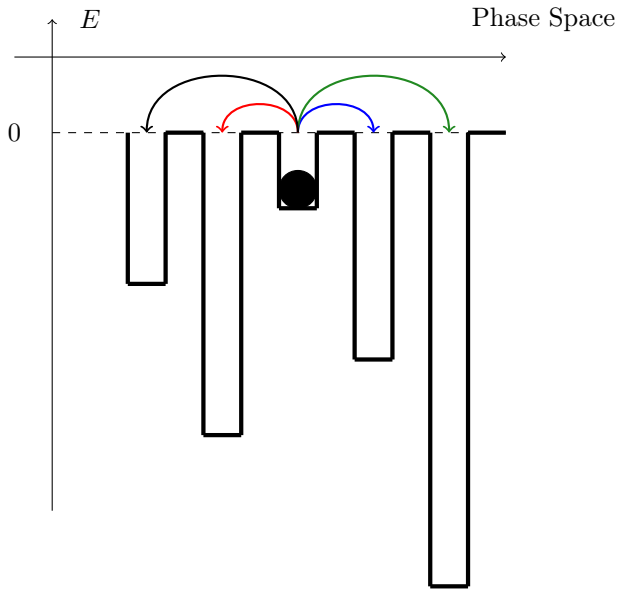

Figure 1.16: *Illustration of the trap model.*

The trap model

This is a mean field model that accounts well for the description of aging phenomena, and it has been developed by Bouchaud in the 90's [42]. In the SK model, it is possible to show that the free energy of states, in the limit of small energies ($E \to -\infty$) is distributed following:

$$\rho(E) = \rho_0 e^{x\beta E}, \qquad \text{with} \qquad x = \frac{T}{T_g}. \tag{1.22}$$

This exponential distribution can also be found when we consider the Random Energy Model of Derrida [43], not described here. The trap model links this distribution with the statistics of energy barriers between states. As illustrated in figure 1.16, the energy needed to go from one state to another is constant and taken to zero. States are distributed as equation (1.22). If the system evolves by thermal activation, the characteristic time of stay in a well of depth E is given by an Arrhenius law: $\tau(E) \propto \exp(\beta E)$.

As soon as the system has left a well, all the other wells in the phase space are accessible with the same probability. In this approach, the dynamics inside a well is neglected since it is assumed to be faster than the dynamics to exit a well. The crucial tool is the exit time $\tau(E)$. We can calculate the average time of presence in a well, and we find it diverging in the spin glass phase. Consequently, the system is incapable to sample correctly the whole phase space. It is called a **weak ergodicity breaking**. This ergodicity breaking is only statistical, it does not correspond to a reduction of the phase space of the *static* states. This model allows to study the consequences of this weak ergodicity breaking on the aging properties of the system.

We also mention the existence of an extended version of the trap model developed by Bouchaud and Dean [44]: the ultrametric trap model.

Brief introduction to the mean field approach to glassy dynamics

The Langevin dynamics of the SK and other mean field disordered models have been studied [41] in the thermodynamic limit ($N \to \infty$), where exact integro-differntial equations on the correlation and linear response are derived, and have been solved both numerically and analytically in the asymptotic limit. Below the critical temperature, the dynamics is studied by considering the autocorrelation function $C(t + t_w, t_w)$ defined as:

$$C(t + t_w, t_w) = \frac{1}{N} \sum_i \overline{\langle S_i(t_w + t) S_i(t_w) \rangle}. \tag{1.23}$$

We write C as the sum of a stationary and an aging contribution [45]: $C(t + t_w, t_w) = C_{st}(t) + C_{ag}(t + t_w, t_w)$. Similarly, we decompose the response function to a variation of magnetic field h as $R(t + t_w, t_w) = R_{st}(t) + R_{ag}(t + t_w, t_w))$. R is defined by:

$$R(t + t_w, t_w) = \frac{1}{N} \sum_i \overline{\frac{\partial \langle S_i(t + t_w) \rangle}{\partial h_i(t_w)}\Big|_{h=0}}. \tag{1.24}$$

It is possible to prove formally that the Fluctuation Dissipation Theorem (FDT) holds for short time differences [46]:

$$R_{st}(t) = \frac{1}{T} \frac{\partial C_{st}(t)}{\partial t}. \tag{1.25}$$

From this FDT, it is possible to define the Fluctuation Dissipation Ratio (FDR) as the ratio of the autocorrelation and response [47]. When the FDT holds (1.25), the FDR is proportional to the temperature of the system.

The aging components of R and C do not verify FDT. It has been proposed a generalization which states that the FDR is proportional to an **effective temperature** T_{eff}, different from the temperature measured by a thermometer [48]. Hérisson and Ocio have tried to measure this effective temperature experimentally in [49], whose results are shown in figure 1.17. The experimental occurrence of several effective temperatures each of which related to one of the numerous time scales seems to work here.

1.4.4 Conclusion

It is important to study spin glasses as they are model systems to study disordered phases in general (structural glasses, for instance [50, 51]) as their source of disorder is very well controlled experimentally (doping with magnetic impurities) and is well-known. The complexity of these materials originates from frustration. It leads to exotic behavior as aging or rejuvenation phenomena, as we have shown in this chapter.

These compounds have been well studied during the last 30 years but the spin glass phase is still a very poorly understood state of matter: the validity of both competing theories for the description of Ising spin glasses as shown above is discussed in [52], and the conclusions of these proposals are contradictory, as concerns first the nature of the low temperature phase and second the effect of a magnetic field on a spin glass.

(i) The mean field approach predicts that the phase space has a huge number of energy valleys with diverging barriers between them. This phase space has an ultrametric structure as shown in figure 1.14, with hierarchy, which is consistent with the replica approach as we will see in chapter 8. The consequence of this complexity is that the distribution of overlaps $P(Q)$ (equation (1.17)) has a non trivial structure.

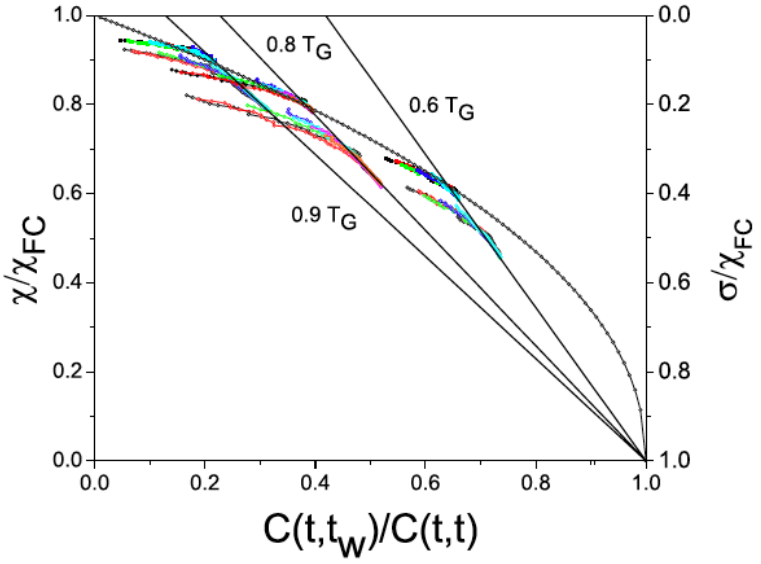

Figure 1.17: *Experimental Fluctuation Dissipation diagram in a spin glass, for different temperatures. Violation of FDT is clear, as well as the apparent disagreement with one effective temperature scenarii. Extracted from [49].*

On the contrary, in the droplet picture the ground state of a short range Ising spin glass is trivially degenerate (Z_2 symmetry of the ground state), which leads to a trivial distribution of overlaps $P(Q)$. The low-lying excitations of the spin glass are droplets (clusters of connected spins with similar orientations) and are responsible for the slow dynamics of spin glasses.

(ii) As shown on figure 1.13, at the mean field level spin glasses exist in a longitudinal magnetic field. The spin glass phase is separated from the paramagnetic phase with the AT line. On the contrary, no spin glass phase survives the application of a magnetic field in the droplet theory as shown on figure 1.15.

Moreover, the spin overlap, which is known to be the order parameter of the transition has still not been measured experimentally and should be of great interest to discriminate between both theories.

The main part (part II) of this manuscript deals with an original theoretical proposal to deduce experimentally the order parameter from electronic transport measurements. Part III deals with the more fundamental issue of the ground state of the infinite range Ising spin glass in a transverse magnetic field. The next two chapters present electronic transport in metals and in spin glasses.

Si l'électron nous a servi à comprendre beaucoup de choses, nous n'avons jamais bien compris l'électron lui-même

Louis de Broglie

Chapter 2
Coherent transport: first approach

2.1 What is coherent transport?

2.1.1 Introduction

Classical transport and Ohm's law

ELECTRONIC transport deals with the issue of how electrons move in a conductor. In a classical point of view, it has well been studied and, in particular, Ohm found a linear law that links the current I of electrons to the potential difference U applied to the conductor. The coefficient of proportionality is called the resistance R if we note $U = RI$. The greater the resistance, the harder for an electron to travel across the conductor. We furthermore define the conductance G of that device as the inverse of the resistance: $G = 1/R$.

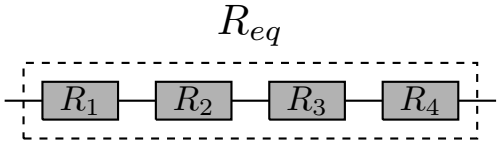

Figure 2.1: *Schematic representation of the series association of M conductors pictured as rectangular boxes. Each conductor is defined by its resistance R_i. The equivalent conductor (dashed lines) has a resistance given by equation* (2.1).

Moreover the resulting resistance R_{eq} of the association in series of M conductors of respective resistance R_i as shown in figure 2.1 is given by the formula:

$$R_{eq} = \sum_{i=1}^{M} R_i, \tag{2.1}$$

deduced from Kirchhoff's circuit laws [53]. In 1900, Drude proposed an explanation for the appearance of a resistance in metals [54, 55], which is based on the presence of impurities. In Appendix A (section A.1) the Drude model is briefly described. For that purpose, we define the *electronic elastic mean free path* l_e, which represents the average distance between two scattering events. It is related to the time of flight τ_e of an electron between two scattering events by the relation[1]: $l_e = v\tau_e$, where v is the velocity of the electron. l_e is characteristic of the disorder inside the conductor. The Drude model relates this time τ_e to the conductivity[2] of the conductor. The conductivity of a material is defined as the conductance per meter of this material. Electrons are assumed classical and their behavior in the conductor is very much similar to the behavior of a ball in a pinball machine.

But we know that electrons are quantum particles and not classical. The purpose of this chapter and the next one is to study both qualitatively and quantitatively this supplementary contribution, which is called the *coherent electronic transport*.

Coherent electronic transport

The supplementary contribution to electronic transport has a quantum origin, as it is now well-known that electron's behavior is described by quantum mechanics. For that purpose, we take

[1] the electron has a ballistic behavior between two successive collisions.

[2] we use the conductivity more than the conductance here because the conductivity is geometry independent.

the wave nature of electrons into account, and we show that it will lead to a breakdown of classical Kirchhoff's law (2.1) at least at very short length scales. The combination of multiple scattering on impurities and on the wave nature of electrons will lead to the appearance of the phenomenon of interference. In this chapter, we will try to answer the following question:

Given a conductor, when shall we take the quantum nature of electrons into account?. Or, equivalently: *When is it sufficient to describe the conductor with purely classical electrons?* and therefore *When is it sufficient to use the Drude model for electronic transport?*

2.1.2 The speckle in optics

Caution: This section presents an analogy to coherent transport in optics, in a very *qualitative* way: the physical origin of the phenomenon described below is completely different in optics and in electronics.

Before trying to answer the previous question in details, we will, in this section present a useful analogy to coherent transport to make things clearer. Consider the following experiment in optics: enlighten a sample containing random scatterers with a Helium-Neon laser whose beam was previously spread. The resulting intensity pattern looks as shown in figure 2.2. To

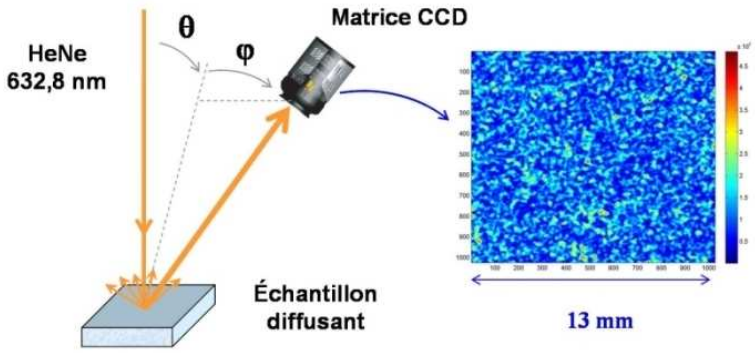

Figure 2.2: *Representation of a speckle pattern in optics. The experimental setup is explained. Credits: Institut Fresnel, UMR 6133, Marseille, FRANCE.*

understand such a pattern, one has to consider interferences between the incoming photons [56], as diffraction of photons on impurities is responsible for that pattern. Its main property is obviously randomness, but it is characteristic of the disorder inside the sample. The speckle figure is denominated as a "fingerprint" of the disorder configuration. It is a quantum phenomenon as it deals with interferences of photons. The interference pattern is governed by the dephasing of photons the ones with the others, which is proportional to the so called optical path difference. If the thickness of the disordered sample grows, all optical path differences grow, and the interference pattern disappears. In the same way, in this manuscript, we consider the injection of electrons in a random medium. The optical intensity is, in that case replaced by the conductance G, which is then a fingerprint of the disorder in the sample (see chapter 3 for more details). If the size of the sample increases, interferences are lost. It is then possible to define a length beyond which all quantum phenomena disappear. This length is called the **coherence length** L_ϕ, and discriminates between phase coherent and phase incoherent phenomena. In electronics, the phenomena at the origin of loss of coherence is inelastic scattering, which leads to an irreversible phase change. In optics the phase change is reversible, as only elastic scattering on photons

occur; the increasing width of the sample leads to an increasing of optical path difference and interferences are lost.

2.2 The coherence length

2.2.1 The significance of the coherence length

Coherent vs incoherent wires

Consider a metallic wire of length L. If it is longer than the coherence length L_ϕ, the phases of the different electrons are random with respect to each others and are time varying, therefore no interference phenomenon takes place. Electrons are not coherent the ones with the others. On the contrary, for wires of length smaller than L_ϕ, despite their randomness, the phases of electrons are precisely determined (no time variation). Then the electrons interfere: this is the regime of *coherent transport*. We recover the classical structure of the previous section for large samples by assuming that the conductance of a conductor of length $L \gg L_\phi$ is given by the formula (2.1), if we divide the sample into a set of smaller samples (*i.e* of respective size L_ϕ) in series. The conductance of the smaller samples is determined using the quantum nature of electrons. The regime for which $L < L_\phi$ is called a *mesoscopic regime*, by opposition to the macroscopic regime for which no coherent behavior has to be taken into account. It is not a "microscopic" regime either as we consider a great number of electrons.

By now, we have a clear definition of the domain of application of the Drude model, we have clearly extracted the coherent regime, with the help of a length, the coherence length L_ϕ. The question that arises now is: *What are the mechanisms responsible for a non-vanishing coherence length?*, and in relation to this: *What is the order of magnitude of this length?* We try to answer these questions in the next section.

The sources of decoherence

Generally speaking, the mechanisms that limit the coherence length are all the inelastic processes that occur in a diffusive conductor, as the phase is not conserved in such processes. Following [57], the effect of the environment on the interference is to multiply the interference term by the average value of $e^{\imath\phi}$, where ϕ is the accumulated phase. An optical analogy of this is the experiment due to Aharonov and Bohm, who introduced a supplementary uniform magnetic field in a Young's holes experimental setup. The influence of the magnetic field is felt by the system as a supplementary phase in the interference term (which is a function of the vector potential). We define

$$\langle e^{\imath\phi}\rangle = \int P(\phi) e^{\imath\phi} \mathrm{d}\phi, \tag{2.2}$$

where P is the statistical distribution of the phase. For a normal distribution, we get:

$$\langle e^{\imath\phi}\rangle = e^{\imath\langle\phi\rangle - \langle\delta\phi^2\rangle/2}, \tag{2.3}$$

where $\langle\delta\phi^2\rangle$ is the phase uncertainty due to the coupling with the environment. (This expression is exact if the environment is composed of harmonic oscillators, with a linear coupling to the interfering waves). The loss of interferences is due to the **random nature** of that supplementary term.

In metals, the main inelastic processes are:

(i) **Electron-phonon** interaction:

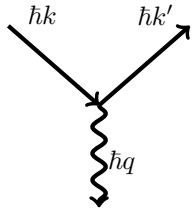

Figure 2.3: *Diagrammatic representation of the electron-phonon interaction. The straight line represents the electron and the curly line represents the phonon. A momentum q is transfered in this process.*

it gives, via the Debye model [58] to a temperature dependence for the corresponding inelastic scattering time τ_{e-ph} in a clean bulk material. It is proportional to T^{-3} [59, 60, 61] if $k_B T \ll \hbar\omega_D$, where ω_D is the Debye frequency and represents the theoretical maximum frequency of vibration for the oscillating atoms of the crystal. At high temperature, $\tau_{e-ph} \propto T^{-4}$ ($k_B T \gg \hbar\omega_D$) [59].

(ii) **Electron-electron** interaction:

Following [62, 63, 64], it is possible to find a temperature dependence for the inelastic scattering time of electron-electron interaction (known as the AAK theory). In metals electrons interact via the Coulombic interaction. Every electron, "dressed" by the cloud formed by all the others, is called a *quasi-particle*. The Landau theory of fermi liquids [65] states that these quasi-particles are essentially non interacting electrons with a modified mass. The inelastic scattering time is given exactly by the lifetime of these quasi particles, and the temperature dependence is given by: $\tau_{e-e} \propto T^{-2/3}$ [66, 67, 63] for quasi-one dimensional systems[3]. On figure 2.4 is represented diagrammatically the electron-electron interaction. Straight lines represent electronic paths, and the curved line represent the interaction between them.

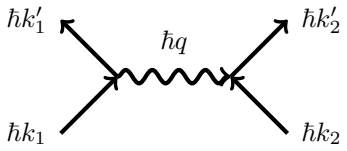

Figure 2.4: *Diagrammatic representation of the electron-phonon interaction. The straight lines represent the electrons and the curly line represents the interaction between them. A momentum q is transfered in this process.*

(iii) **Free** magnetic impurities: Scattering on magnetic impurities leads to a saturation of the phase coherence length at low temperatures. At lower temperatures, the Kondo effect is responsible for the increase of L_ϕ, as impurities are screened by conduction electrons.

[3]for two dimensional systems, $\tau_{e-e} \propto T^{-1}$ and for three dimensional systems, $\tau_{e-e} \propto T^{-3/2}$.

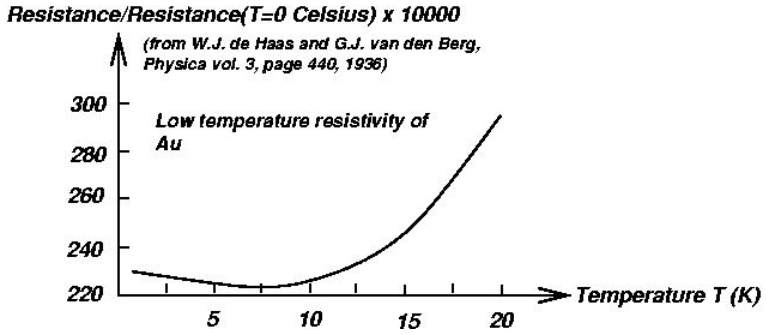

Figure 2.5: *Evolution of the resistance of a Au sample with temperature, showing an increase of the resistance at very low temperature: this is the Kondo effect. Extracted from [68].*

The Kondo effect.
The Kondo effect [68, 69, 70] is the increase of the resistivity when the temperature decreases in metals doped by magnetic impurities at low concentration (see figure 2.5): the RKKY interaction between the spins can be neglected, as they are far away from each other. At very low temperatures, the conduction electrons screen the spin of the impurity by creating a singlet state, which causes an increase of the resistivity (the conduction electrons are localized near the impurity).
At higher temperatures, thermal fluctuations break this singlet state, and it is possible to define a temperature, called the Kondo temperature T_K which is given by:

$$T_K = \varepsilon_F e^{-1/2|J|\rho_0}, \tag{2.4}$$

where ε_F is the Fermi energy, J is the coupling between the impurity and the electrons and ρ_0 is the density of states at the Fermi level. This temperature represents the temperature of the minimum of resistivity with temperature, if the Kondo effect dominates: one defines the Kondo temperature as the energy scale limiting the validity of the perturbative calculations. See [71] for a review.

Conclusion

As expected, all these inelastic processes tend to vanish at low temperature and the coherence length increases. At low temperatures, it is then possible to obtain experimentally coherence lengths of order $1\mu m$, which allows to have samples of comparable size. In the next chapters, we will theoretically only consider the experimental relevant case of perfectly coherent wires (*i.e* the regime of small length $L < L_\phi$ and low temperature, to increase the coherence length). The electron-electron interaction dominates the electron-phonon interaction at low temperature: the cross-over occurs typically at $1K$.

The transport for wires larger than the coherence length is classical. As said before, we sum incoherently the quantum conductances of portions of wires of length L_ϕ. The resistance of such a wire is the sum of the resistances (following equation (2.1) and Kirchhoff's circuit laws) of portions of length L_ϕ.

2.2.2 Experimental study of the coherence length

How is τ_ϕ or L_ϕ measured experimentally?

As we will see in details in the next chapter, the quantum corrections to conductivity are those arising from the interference between the diffusing electrons wave packets. These corrections for a quasi 1D wire can be written in the form [72, 73]:

$$\frac{\Delta R(T,H)}{R_0} \propto \tilde{L}(T,H), \tag{2.5}$$

where T is the temperature, H the magnetic field applied and

$$\tilde{L}(T,H) = \frac{1}{\sqrt{L_\phi(T)^{-2} + L_H^{-2}}}, \tag{2.6}$$

with $L_H = (\sqrt{3}/\pi)\phi_0/HW$. $\phi_0 = h/e$ is the magnetic flux quantum, W is the width of the two-dimensional sample. Recording the resistance (or the conductance) with increasing magnetic field of the sample for a given temperature and fitting it with the previous formula gives access to $L_\phi(T)$. The phase coherence time τ_ϕ is related to L_ϕ via the relation: $L_\phi = \sqrt{D\tau_\phi}$, where D is the diffusion coefficient.

In the following we call this measure a **magnetoresistance** measurement, and the resulting trace of resistance is called a *magnetofingerprint*.

Low temperature behavior

In [74] Echternach et al study the magnetoresistance of Au wires. From these measurements, the authors are able to compute the inelastic time τ_ϕ as a function of temperature. The power law behavior ($T^{-2/3}$) agrees with the theory AAK [63, 64]: figure 2.6.

In [75], it is also possible to study the cross-over from electron-electron scattering to electron-phonon scattering, at higher temperature. The results are presented in figure 2.7. Good agreement with a power law of the type:

$$\tau_\phi^{-1}(T) = AT^{2/3} + BT^3 \tag{2.7}$$

is found for pure samples, which implies that down to $1K$, the electron-phonon interaction is the major inelastic scattering mechanism. At lower temperatures, the electron-electron mechanism dominates. The saturation at very low temperature ($T < 0.1K$) is attributed to other mechanisms, as we will see in the next section.

Very low temperature behavior

As seen above, the discrepancy between theory and experiments at very low temperatures is due to a supplementary source of decoherence that leads to a saturation of $\tau_\phi(T)$ at very low temperature. One candidate is the presence of a small amount of magnetic impurities inside the sample giving rise to the so-called Kondo effect (see above). In [76], the authors show very good agreement between theory and experiments if it is assumed that the samples possess impurities with a Kondo temperature smaller than 1mK and concentration smaller than 0.08 ppm (parts per million).

Mohanty and Webb [77, 78] in the experimental side and Golubev and Zaikin [79] on the theoretical side proposed another explanation for the very low temperature behavior of the phase coherence time τ_ϕ. They suggest that the zero point fluctuations of the electromagnetic

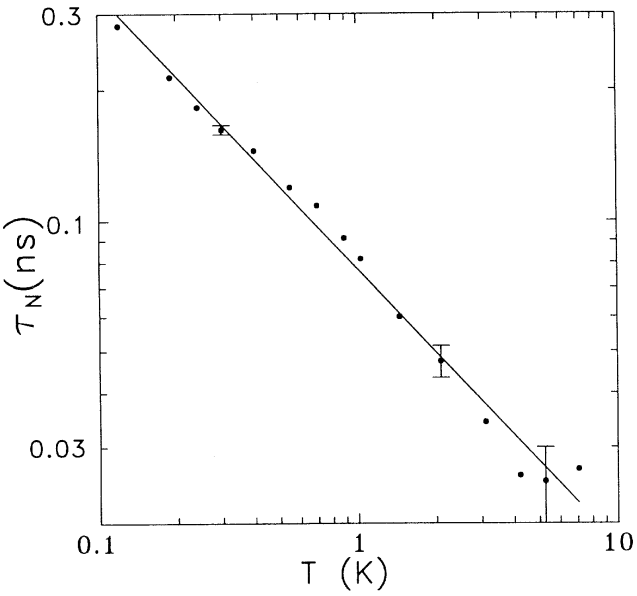

Figure 2.6: *Phase coherence time τ_ϕ as a function of temperature in a Au wire. Straight line corresponds to $\tau_\phi \propto T^{-0.64}$ (fit of experimental data). Extracted from [74].*

field are responsible for the observed saturation of τ_ϕ. In figure 3 and 4 of [78] the authors present results from a series of pure gold wires $18nm$ thick and $30nm$ wide, under high magnetic fields (up to $15T$) to polarize all magnetic impurities. The saturation of the phase coherence time is nevertheless present, which is explained in terms of zero point fluctuations [79]. For a review on this still debating issue, see [80].

Very recently, new results [81] seem to show that this is the Kondo effect that is responsible for the increase of the phase coherence time at very low temperatures.

2.2.3 Coherence length and spin glasses

In [82], an anomaly at low temperature in the phase coherence time τ_ϕ is attributed to the appearance of a spin glass phase. This anomaly is a saturation of the phase coherence rate, as shown in figure 2.9. The phase coherence rate is defined as: $\gamma_\phi = \hbar/(2\tau_\phi)$. This result suggest that a constant spin scattering rate, associated with the appearance of a spin glass, is the cause of the observed saturation in the total scattering rate. Moreover, in [83], magnetoresistance measurements in a spin glass allowed the authors to deduce the phase coherence length of a 0.35μm segment at 22mK. They found $L_\phi = 0.3\mu m$ to $1\mu m$, for magnetic fields applied from 10 kG to 60kG, by two different methods.

2.2.4 Conclusion

To answer the question raised in section 2.1, the experimental coherent regime is found at low temperature, where the influence on electrons of all inelastic processes is reduced. it is also the regime of short wires, in the sense that the length of coherent wires must be smaller than the coherence length L_ϕ. If the length of the wire is larger than L_ϕ, the coherent phenomena that

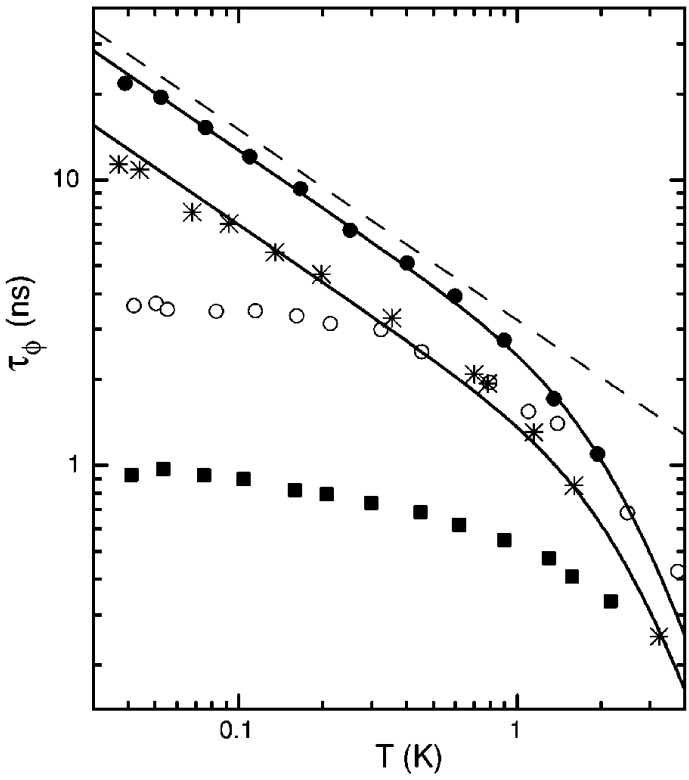

Figure 2.7: *Behavior of the phase coherence time τ_ϕ for different metallic wires (silver for dots, gold for stars and copper for squares)via magnetoresistance measurements. In the purest samples (solid circles and stars) we observe a dependence $\tau_\phi^{-1}(T) = AT^{2/3} + BT^3$ (plain lines). Dashed line represents the contribution with power 2/3 for silver. We attribute down to $0.1K$ the decoherence to electron-phonon and electron-electron interactions. For samples with more impurities deviations with the power law is observed. Saturation at very low temperature has been attributed to other dephasing mechanisms. Extracted from [75].*

occur are averaged over the coherence length as shown on the illustration of figure 2.10. The resulting resistance of the wire is: $R_{\text{wire}} = R_q^1 + R_q^2 + \dots$.

We have seen in this chapter that inelastic processes are of high importance when dealing with coherent transport. The evolution of the phase coherence time or length is well described at low and very low temperatures by usual theories (AAK, ...): the appearance of decoherence is mainly due to interactions (with phonons or the other electrons). In the next chapters, we assume that the experimental conditions are set in order that the phase coherence length is greater than the dimensions of the sample under consideration, so that we mimic the experimental relevant case of perfectly coherent wires. In this chapter, we have also shown that the presence of free magnetic impurities modifies the coherence length [82] through the Kondo effect. On the other hand, the presence of frozen magnetic impurities also contributes to the elastic diffusion: this has clear signatures on transport properties at low temperatures ($T \ll T_g$), as we will see in the next chapters.

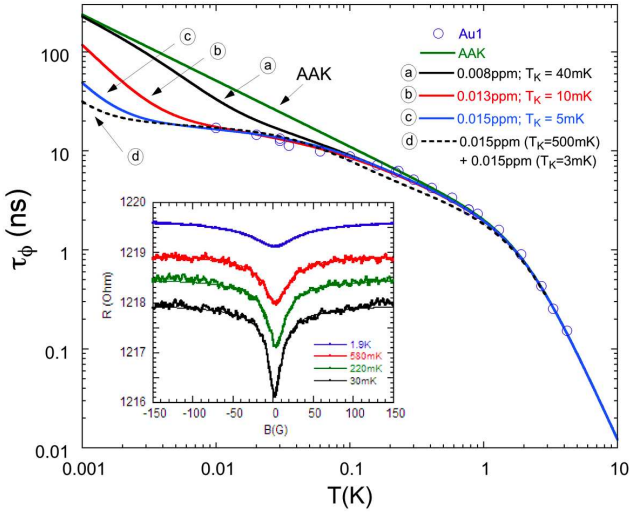

Figure 2.8: *Phase coherence time as a function of temperature for a sample of a* 120 *nm width,* 50 *nm thick and* 450 *nm long Au wire doped with magnetic impurities at various concentration (open circles). Extracted from [76].*

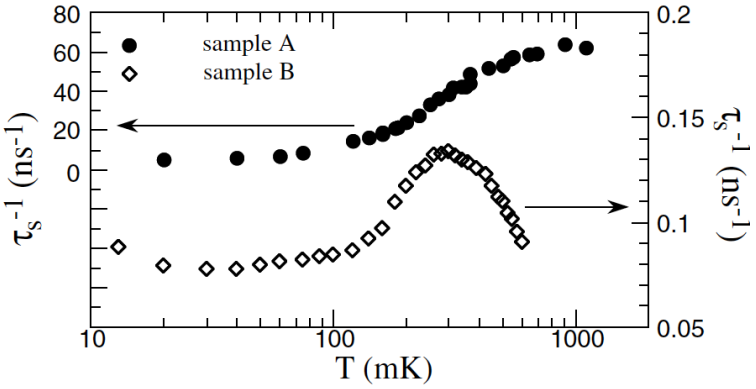

Figure 2.9: *Magnetic scattering rate for different samples obtained by subtraction of the standard dephasing rate (term proportional to* $T^{2/3} + aT^3$*). Extracted from [82].*

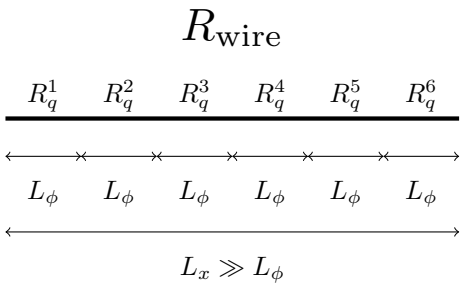

Figure 2.10: *Resistance of a wire of length L_x larger than the coherence length L_ϕ. Each resistance R_q^i is calculated in the coherent regime. The total resistance is calculated using equation* (2.1).

- Qu'est-ce que vous regardez ? C'est la carte routière? - Non! C'est la carte des vins. C'est pour éviter les bouchons!

Raymond Devos

Chapter 3
Coherent transport: a more quantitative approach

3.1 Diffusion on scalar impurities

3.1.1 Disorder and coherent transport

The importance of disorder

STATIC impurities present in a metal are of high importance to explain classical or quantum conduction of electrons phenomena: electrons must pave their way inside the metal, with diffusions on impurities. This leads to the appearance of a resistance in the material, which would not be the case if the conductor was perfect. The goal of this section is to get an analytical expression for the averaged conductance over the scalar disorder by considering only scalar impurities, that is to say on impurities without any spin. Different contributions from the more obvious to the more complicated one will be described. The formalism used to study phase coherence in metals is semi-classical in the sense that electrons are considered as localized wave packets and they diffuse elastically, recalling that all inelastic collisions are taken into account in the phase coherence length L_ϕ described in section 2.2. Applying this formalism is valid provided that the disorder is "weak": the Fermi wavelength λ_F of the electron must be much smaller than the mean free path l_e to consider the electron as a localized particle. Moreover interactions between electrons will be considered as weak, *i.e* much weaker than the kinetic energy of electrons, which is true in "good" conductors. Using this formalism, we are able to determine with high accuracy the behavior of an electron in a disordered conductor.

The models of disorder

An electron in a given crystalline structure, which is modeled by a perfect periodic potential, with disorder is described by the following Hamiltonian:

$$\mathcal{H} = \frac{\vec{p}^2}{2m^*} + V_{\text{scal}}(\vec{r}). \tag{3.1}$$

m^* is the effective mass of the electron in the periodic potential [84] and V_{scal} represents the scalar disorder potential. It is random and encodes the position of the scalar impurities. Static disorder corresponds to a situation where electrons diffuse elastically. There are different models to describe the random positions of impurities:

- A first model of interest is the gaussian model. In this model of disorder, the potential V_{scal} is supposed to be a continuous function of space. The probability for the potential to have a value $V(\vec{r})$ at position $\vec{r}$ is given by:

$$P[V(\vec{r})]\mathcal{D}V(\vec{r}) = \frac{1}{\mathcal{Z}} \exp\left[-\frac{1}{2}\int \mathrm{d}\vec{r}\mathrm{d}\vec{r}_1 V(\vec{r})\Delta(\vec{r}-\vec{r}_1)V(\vec{r}_1)\right]\mathcal{D}V(\vec{r}) \tag{3.2}$$

  This general model is used in analytical studies as we will see in part III.

- Another model for the scalar disorder is the Anderson model, which is particularly useful and efficient for numerical studies. It is a tight binding lattice model, so the precedent Hamiltonian (3.1) is replaced by:

$$\mathcal{H}_{\text{t.b.}} = \sum_{i,j} t_{ij} c_i^\dagger c_j + \sum_i v_i c_i^\dagger c_i, \tag{3.3}$$

  where the first term represents the hopping from site j to i and the second term is an on-site random potential, v_i. It has a flat distribution in the interval $[-W/2; W/2]$, where W

measures the strength of the disorder potential. These random energies are supposed to be decorrelated from one site to the other.

In our numerical study of transport in a mesoscopic spin glass wire, we will consider the latter Anderson model. In the following one given set of of these random energies for each site i will be called a *realization of disorder* and denoted by $V = \{v_i\}_i$: one sample corresponds to one given position of all impurities, this is a realization of disorder. In practice, to modify this potential, one has to change the sample, with a fixed density of impurities: same number of impurities but at a different position, by *e.g* annealing it.

Probability of diffusion

In the following, we will neglect the influence of spin-orbit coupling on the electrons. It is described in [85] and see [86] for a review.

Let us start by considering the probability for an electron to evolve from a position $\vec{r}_1$ to a position $\vec{r}_2$ during a time t: $P(\vec{r}_1, \vec{r}_2, t)$ or its temporal Fourier transform $\tilde{P}(\vec{r}_1, \vec{r}_2, \omega)$. The larger this probability, the easier the electron moves inside the sample, the greater the conductance[1]. We will first describe incoherent transport (or classical transport), for which electrons are considered classical (without a phase). To go beyond this hypothesis we will take the phase of electrons into account and describe the effect of interferences between electrons, in the coherent regime (to mimic the experimental relevant case of coherent wires) studied in the previous chapter. In the following, we will focus on the weak disorder limit: $k_F l_e \gg 1$, which is the relevant experimental limit for good metals as Cu or Ag[2]. This limit corresponds to a semi-classical theory for electrons: the trajectory of the center of mass of the wave packet of each electron is restrained inside a "tube" of diameter λ_F^{d-1}, where d is the dimension, and of length the length of the electronic diffusion path $\mathcal{L}$.

It is highly important to notice that the probabilities of diffusion $P(\vec{r}_1, \vec{r}_2, t)$ and $\tilde{P}(\vec{r}_1, \vec{r}_2, \omega)$ are quantities that are averaged over disorder[3].

3.1.2 Incoherent transport: Drude-Boltzmann approximation

In the classical case, the use of the Drude model allows one to compute the *classical* part of the conductivity (see Appendix A (section A.1) for the details):

$$\sigma_0 = \frac{ne^2\tau_e}{m_e}, \tag{3.4}$$

where m_e is the mass of the electron, and τ_e is the elastic time of flight[4]. The corresponding probability is:

$$P_0(\vec{r}_1, \vec{r}_2, t) = \frac{\delta(R - vt)e^{-t/\tau_e}}{4\pi R^2}, \tag{3.5}$$

where $R = |\vec{r}_1 - \vec{r}_2|$. In that case, P_0 represents the probability to evolve from $\vec{r}_1$ to $\vec{r}_2$ without having encountered an impurity.

Other mechanisms are to be taken into account to describe properly the scattering of electrons on impurities in a metal. The simplest assumption to make concerning these mechanisms is that multiple diffusion happens as the electron goes from $\vec{r}_1$ to $\vec{r}_2$, as shown on figure 3.1.

[1] the conductance transports momentum that is orthogonal to the entrance and exit interfaces of the sample.
[2] In these metals, $k_F l_e \approx 1000 \gg 1$.
[3] *i.e* over different configurations of the positions of impuritites
[4] we recall here that $l_e = v_F \tau_e$, where l_e is the elastic mean free path and v_F the Fermi velocity.

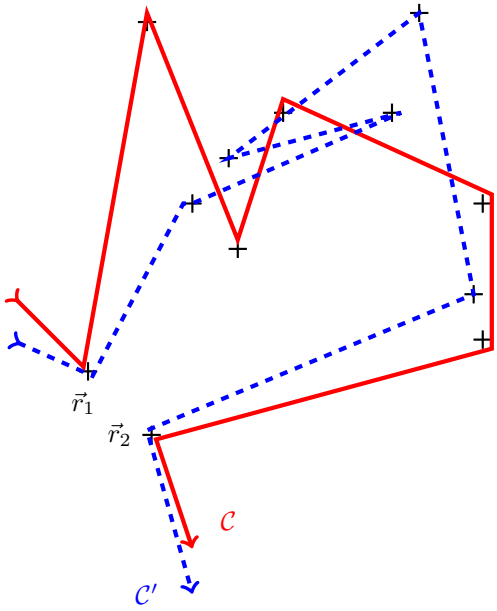

Figure 3.1: *Possible routes taken by an electron to diffuse from $\vec{r}_1$ to $\vec{r}_2$, with different collision sequences $\mathcal{C}$ and $\mathcal{C}'$.*

3.1.3 Mutliple diffusion: the Diffuson and the Cooperon

Introduction

The probability for an electron to go from $\vec{r}_1$ to $\vec{r}_2$ during time t can be expressed under the following form using Green's functions (see [87] and Appendix A.). For a complete review of quantum transport see [86]. One shows that the probability takes the following form:

$$P(\vec{r}_1, \vec{r}_2, t) = \sum_{\mathcal{C},\mathcal{C}'} \mathcal{A}_{\mathcal{C}} \mathcal{A}^*_{\mathcal{C}'}. \tag{3.6}$$

In this equation, $\mathcal{C}$ and $\mathcal{C}'$ are two different diffusive paths (*i.e* scattering sequences), and $\mathcal{A}_{\mathcal{C}}$ and $\mathcal{A}_{\mathcal{C}'}$ are diffusion electronic amplitudes[5] along the respective paths. The star symbol in this equation is the complex conjugation operation. This equality can be understood in the following way: it is the product of two electronic propagator amplitudes, one for the particle and the second one (the conjugate amplitude) for the hole as electronic transport carries in reality a particle-hole pair excitation, as schematically shown in figure 3.2.

Which type of paths for $\mathcal{C}$ and $\mathcal{C}'$?

The constraint on these paths is that they must start at $\vec{r}_1$ and end at $\vec{r}_2$. $\vec{r}_1$ and $\vec{r}_2$ are not necessarily the coordinates of an impurity. $\mathcal{C}_N$ is a path of N impurities in the sequence $(\vec{r}_1, \vec{r}_a, \vec{r}_b, ..., \vec{r}_N, \vec{r}_2)$ and $\mathcal{C}'$ is a path of N' impurities in the sequence $(\vec{r}_1, \vec{r}_\alpha, \vec{r}_\beta, ..., \vec{r}_{N'}, \vec{r}_2)$. For each path, the accumulated phase is proportional to its own algebraic length $\mathcal{L}_N$ or $\mathcal{L}_{N'}$. The phase $\delta\phi_{\mathcal{C},\mathcal{C}'}$ of the product in the sum of equation (3.6) is given by:

$$\delta\phi_{\mathcal{C},\mathcal{C}'} \approx k_F(\mathcal{L}_N - \mathcal{L}_{N'}). \tag{3.7}$$

[5] more precisely the Green's functions are written in terms of $\mathcal{A}e^{\imath\phi}$.

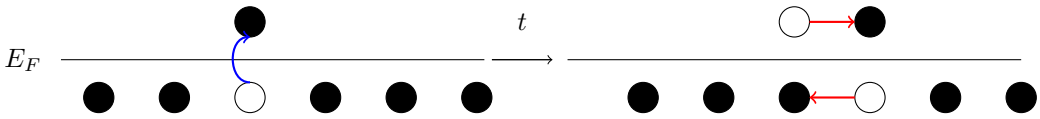

Figure 3.2: *Schematic view of the creation and propagation of a particle-hole excitation of the Fermi sea. On the left, the pair particle-hole is created and then the occupied state (particle) and the unoccupied state (hole) propagate independently. The propagation of a hole is similar to the propagation of a particle with reversed time evolution. Electrons are represented by black circles and holes by white circles.*

If paths are different[6] as shown in figure 3.1, the difference $\mathcal{L}_N - \mathcal{L}_{N'}$ will be at least of order l_e. Due to disorder averaging or sum over the different paths (as it is the case in optics), the corresponding term will vanish, as $k_F l_e \gg 1$ (weak disorder limit). Therefore, the only terms that remain in equation (3.6) are the terms for which both paths $\mathcal{C}$ and $\mathcal{C}'$ have the same number of diffusors and the same sequence, which means that scatterers are encountered in the same order. The remaining degree of freedom is the direction of propagation of these paths: $(\vec{r}_1, \vec{r}_a, \vec{r}_b, ..., \vec{r}_N, \vec{r}_2)$ or $(\vec{r}_1, \vec{r}_N, ..., \vec{r}_b, \vec{r}_a, \vec{r}_2)$. In that case, $\mathcal{L}_N = \mathcal{L}_{N'}$ or $\mathcal{L}_N = -\mathcal{L}_{N'}$. The equation for the probability (3.6) can then be separated into two parts:

$$P(\vec{r}_1, \vec{r}_2, t) = P_d + P_c, \tag{3.8}$$

where

$$P_d = \sum_{\mathcal{C}_N} |\mathcal{A}_N|^2, \tag{3.9}$$

$$P_c = \sum_{\mathcal{C}_N, \mathcal{C'}_N} \mathcal{A}_N \times (\mathcal{A}'_N)^*. \tag{3.10}$$

In this equation $\mathcal{C}_N$ is a path with N diffusion centers $(\vec{r}_1, \vec{r}_a, \vec{r}_b, ..., \vec{r}_N, \vec{r}_2)$ and $\mathcal{C'}_N$ the reversed $(\vec{r}_2, \vec{r}_N, ..., \vec{r}_b, \vec{r}_a, \vec{r}_1)$.

For a quantitative analysis of this probability in terms of Green's functions, as well as the link between this probability P and the conductivity of the metal, refer to Appendix A. the goal of this section is to introduce two useful tools concerning electronic transport: the Diffuson and the Cooperon.

The Diffuson

The term of equation (3.9) is called a Diffuson. This term is characterized by identical paths $\mathcal{C}$ and $\mathcal{C}'$, the phase of the product $\mathcal{A}_\mathcal{C}\mathcal{A}^*_{\mathcal{C}'}$ vanishes: the Diffuson is an incoherent contribution to transport. Using this term and the Drude-Boltzmann one for the probability for electron to go from $\vec{r}_1$ to $\vec{r}_2$ in time t gives a well normalized probability (see [86] for the details of the calculation of this probability and its normalization). A schematic view of the Diffuson is given in figure 3.3; the Diffuson term is interpreted as the combination of an electron propagating in one direction (plain line) and of a hole propagating in the same direction (dashed line). It is the usual particle-hole propagation in a solid as seen in figures 3.3 and 3.2. This term has a non vanishing contribution to the probability for all $\vec{r}_1$ and $\vec{r}_2$.

In Appendix A, section A.2.3, we show quantitatively that the Diffuson term, in the isotropic case, gives no contribution to the conductivity. It is nonetheless of high importance as it has a non vanishing contribution to the probability P defined above. This term, in addition to the

[6] $N \neq N'$ or a different sequence

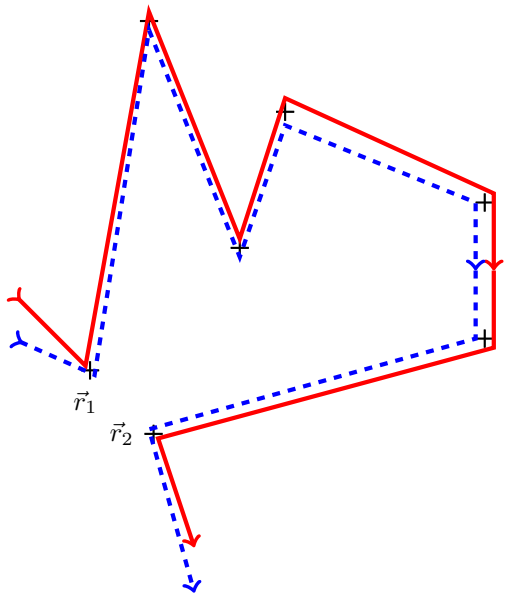

Figure 3.3: *The Diffuson. Loops are similar. Its phase vanishes for all values of $\vec{r}_1$ and $\vec{r}_2$. There is a direct correspondence between this curve and the diagram of figure A.1.*

classical one (*i.e* P_0 of equation (3.5)), must be taken into account to have a normalized total probability.

The Cooperon

Consider now that the electronic diffusion path makes a loop as shown in figure 3.4. In the parts outside the loop, the only term that contributes to the probability P is the Diffuson as schematically drawn in figure 3.1. We now focus on the loop of the electronic path. As a particular case of multiple scattering, a Diffuson term is associated with any loop. But an other term appears: the Cooperon, which is schematically drawn in figure 3.5. The fact that the path is closed allows to reverse one diffusion path with respect to the other: the reversal does not

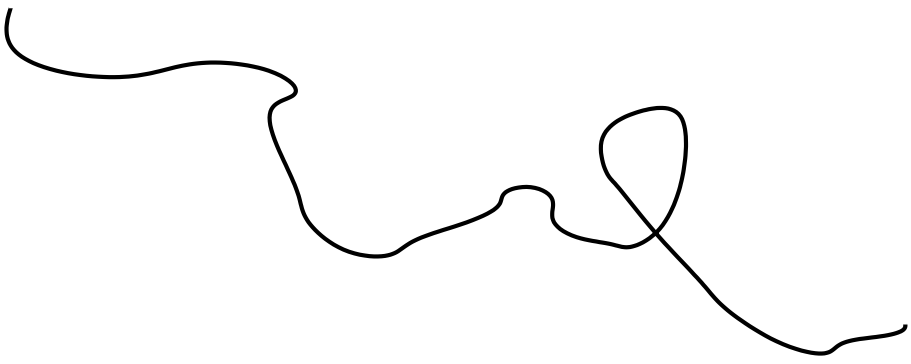

Figure 3.4: *Schematic plot of multiple scattering of an electron on impurities. Along the path, a loop occurs.*

introduce any further dephasing, which is the case if one reverse for instance the dashed curve between $\vec{r}_1$ and $\vec{r}_2$ in figure 3.3. This supplementary term gives exactly the same contribution as the Diffuson, the probability to go from $\vec{r}_0$ to $\vec{r}_0$ is doubled (a Diffuson plus a Cooperon term) by comparison to the case with no loop. Under these conditions, the probability reads:

$$P_c = \sum_{\mathcal{C}_N} |\mathcal{A}_N|^2, \tag{3.11}$$

which is exactly identical to the Diffuson term (see equation (3.9)). The probability is then doubled compared to the case without quantum corrections. This is the so-called **coherent backscattering**, which leads to the *weak localization* phenomena that will be described in the next section.

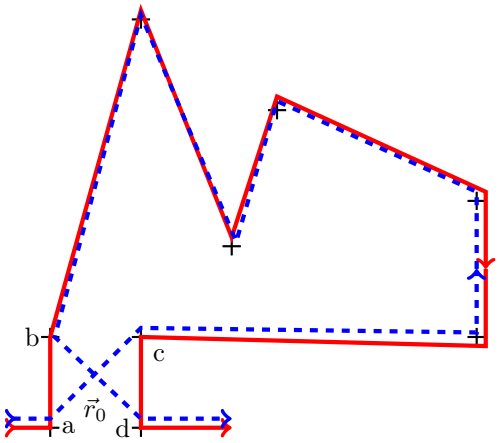

Figure 3.5: *The Cooperon: a quantum crossing between paths occurs at point $\vec{r}_0$. Contribution to the quantum correction to the probability of return to $\vec{r}_0$. There is a direct correspondence between this curve and the diagram of figure A.3. To produce a loop with no supplementary phase, 4 impurities (a, b, c and d) are needed.*

We stress that every external parameter (see section A.3) like a magnetic field, that breaks time reversal symmetry will kill the Cooperon term [88, 89] and the associated quantum corrections to the conductance vanish.

The resulting probability of diffusion is qualitatively drawn in figure 3.6. On this plot the sum of the Diffuson and the Cooperon terms are represented schematically to show the enhancement of the probability of return to the origin (in $r = 0$).

The Cooperon term can be described as an electron propagating in one direction (plain line of figure 3.5) and a hole propagating in the opposite direction or equivalently another electron propagating in the same direction (dashed line). The name "Cooperon" has been given in reference to the so-called *Cooper pairs* appearing in the Bardeen-Cooper-Shrieffer (BCS) theory of superconductivity.

Contrary to what happens for the Diffuson term, the Cooperon gives a non vanishing contribution to the conductivity and hence to the conductance (section A.4). In the following, we study the influence of this term on transport properties.

The conductance

The resulting conductance G for one given realization of disorder is unique. The conductance is a fingerprint of the disorder configuration as the phase in the Cooperon encodes loops that

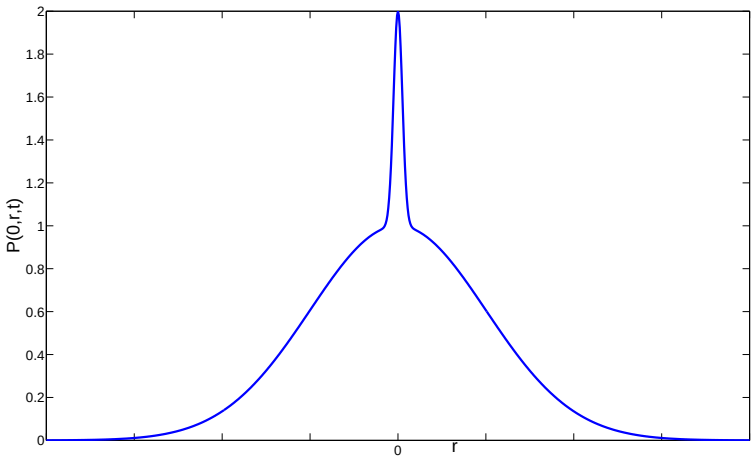

Figure 3.6: *Schematic plot of the full probability of diffusion $P(0, \vec{r}, t)$ of an electron as a function of the distance $\vec{r}$ from the origin during time t. Doubling of the probability of due to the quantum corrections (the Cooperon).*

are created by the position of each impurity the electron encounters. Changing the scalar configuration of disorder will cause the conductance to fluctuate. In other words, the conductance is not a self-averaging quantity, with respect to scalar disorder[7]. Therefore the conductance for one particular realization of the scalar disorder potential is not a physical quantity: it is not reproducible from one sample to another. The statistical distribution of conductance is of greater interest. All the theoretical and experimental efforts on coherent transport consist in sampling correctly this statistical distribution.

3.2 Weak localization and conductance fluctuations

Weak localization has two main signatures on mesoscopic transport: conductance magneto-fingerprints and Universal Conductance Fluctuations (UCF). In the following, we will consider for the theoretical parts a quasi one dimensional system, *i.e* a thick wire of length L_x, width L_y and thickness L_z connected electrically with two metallic leads. The transverse dimensions L_y and L_z are smaller than the elastic mean free path so that diffusion occurs dominantly in the longitudinal direction (the x-direction).

3.2.1 Conductance magneto-fingerprints

See Appendix A (section A.3) for the calculations of weak localization corrections under an external parameter as the magnetic field [72]. The effect of the magnetic field is to dephase the electronic paths. The Diffuson term, as a classical contribution, is not affected by a magnetic field. On the contrary, the Cooperon term is affected by a magnetic field: the phase of this contribution is modified by the magnetic field, so is the interference pattern and then the resulting conductance.

[7] Define $\mathcal{O}_N$ a statistical observable. N is the number of degrees of freedom of the corresponding system. $\mathcal{O}_N$ is self averaging if and only if it takes the value $\mathcal{O}_\infty$ at the thermodynamic limit ($N \to \infty$) with probability 1 (it does not fluctuate any more).

The ergodic hypothesis

In the previous theoretical analysis of coherent transport, all quantities of interest such as the conductance or the probability of return of an electron to point $\vec{r}$ in time t are averaged over the scalar disorder. In practice, one given sample represents one realization of the position of impurities. Therefore to modify the scalar disorder configuration experimentally, one has to change the sample or anneal it, to get a new positions of impurities with the same concentration. For instance, in [90], the authors used a GaAs sample doped by Si and measured the magneto conductance after 46 annealing processes. In figure 3.7 are presented all these 46 random fingerprints. We see clearly that, for magnetic fields greater than 4.10^{-2}T, all these curves fluctuate around

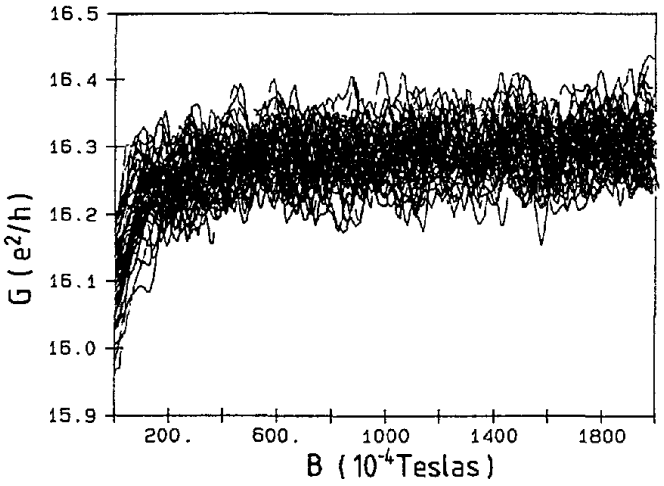

Figure 3.7: *46 reproducible magneto conductance curves at $T = 45mK$ in the same GaAs wire doped with Si. Extracted from [90].*

an horizontal line and the averaged value over disorder (also shown in figure 3.8) is the same as the average over the magnetic field applied (for fields greater than 4.10^{-2}T). These results show that the conductance is a fluctuating quantity with respect to the magnetic field or the scalar disorder. From these results, we present the *ergodic hypothesis*, which states that the statistical ensemble of the conductance is similar if one changes the sample or the magnetic field[8] [91], see figure 3.9. Changing the magnetic field causes indeed a modification of phases of the amplitudes (3.6) $\mathcal{A}_\mathcal{C}$ along the paths. This is similar to changing directly the length of the paths (*i.e* the realization of disorder). This hypothesis gives a correspondence between theoretical works that calculate averages over scalar disorder and experiments that perform averages over the magnetic field: it is experimentally much easier to measure the conductance for several values of magnetic field than for several samples. In the next chapters, we will present original results on transport with averages performed over scalar disorder. We use this hypothesis to link our theoretical results to experiments.

[8]This is true provided that the modification of the magnetic field is greater than the decorrelation field B_c defined as $B_c = \phi_0/\Sigma$, where $\phi_0 = h/e$ is the flux quantum and $\Sigma = L_x \times L_y$ is the surface of the sample.

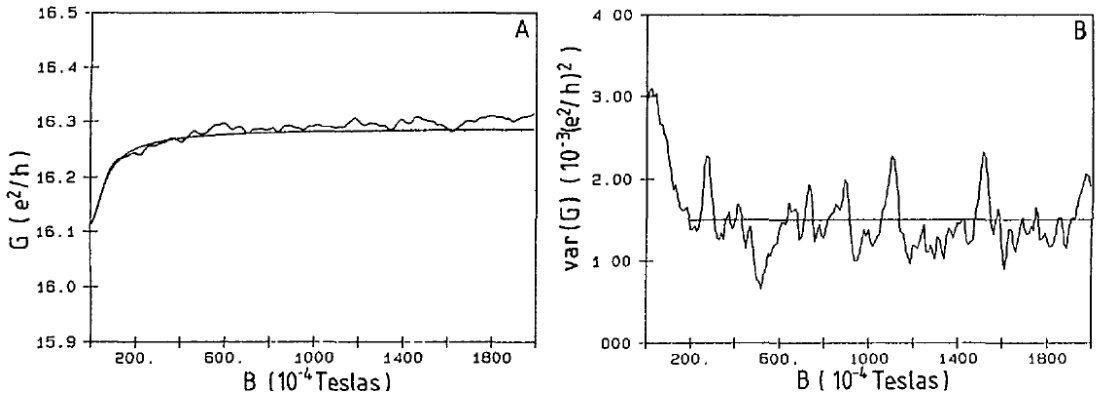

Figure 3.8: *A: mean conductance obtained from figure 3.7 and the weak localization fit [72]. B: the variance over the 46 disorder configurations (at fixed magnetic field) as a function of the magnetic field. Extracted from [90].*

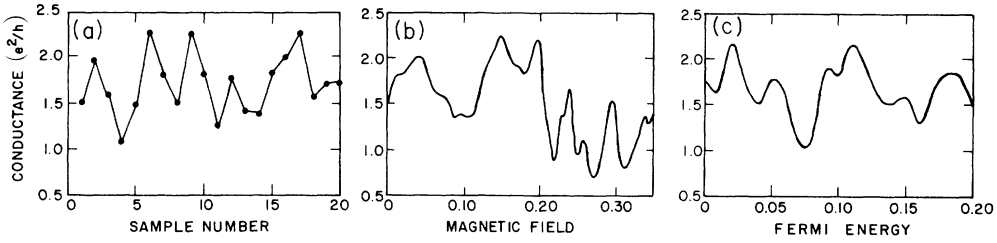

Figure 3.9: *Illustration of the ergodic hypothesis that states that the statistical ensembles of the conductance with respect to disorder or magnetic field (or the Fermi energy) are similar. Numerical data extracted from [89].*

The negative magnetoresistance

A first result is given in figure 3.8A, where averages are directly performed over disorder. It shows clearly that the magnetoconductance increases with the magnetic field, for small magnetic fields. The plain line represents the theory [72], and see also Appendix A, section A.3 for the details. Another example is given in experiments [73] using Lithium films of variable width and applying a magnetic field perpendicular to the plane of the sample which give the results shown in figure 3.10. In this curve, points are experimental data and plain lines are analytical fits as previously. In these experiments, the authors use only one sample with non annealing. The plot shows all the same an average resistance as they use long wires: they are longer than the phase coherence length L_ϕ of the system, so that it is possible to divide the sample in a number k of coherent wires of length L_ϕ. According to section 2.1, these k coherent contributions are summed as resistances in series. This is equivalent to average over different samples.

In both cases, the averaged magnetoresistance decreases with an increasing magnetic field perpendicular to the plane defined by the two-dimensional sample. An increasing magnetic field breaks progressively the quantum corrections. As seen on figure 3.3, both trajectories are in the plane of the sample and propagate in the same direction for the Diffuson. A magnetic field perpendicular to that plane will then have no influence in terms of dephasing one trajectory with

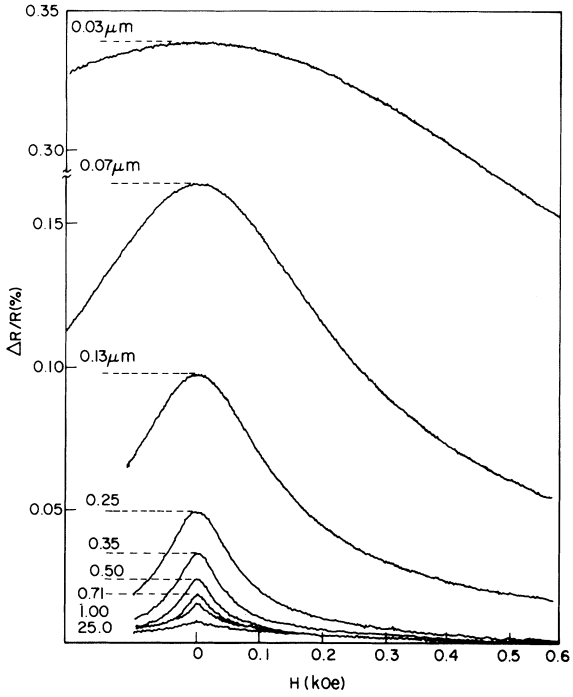

Figure 3.10: *Experimental averaged magnetoresistance of Li films, H is the magnetic field applied. The different curves correspond to different widths of the system and show a negative magnetoresistance. Extracted from [73].*

respect to the other. This is not the case for the Cooperon since trajectories are propagating in opposite directions. The magnetic field's influence on the system is to add a phase difference between both trajectories. The intensity of the field is weak enough to prevent the system from being in the Quantum Hall regime (no edge states). Consequently the Cooperon contribution vanishes progressively for increasing magnetic fields.

3.2.2 UCF

Theory

As already said in the previous section, the conductance is a fingerprint of the disorder configuration encountered, and from one configuration to another the conductance will fluctuate. This section studies the amplitude of the fluctuations of conductance in the so-called mesoscopic regime where the length L_x of the sample is smaller than the phase coherence length L_ϕ, but much greater than the mean free path l_e (diffusive regime). This regime is of great interest as it is the only one that is easily accessible experimentally. For a quasi one dimensional system, diffusion of electrons takes place only in the longitudinal direction (x direction), whereas the finite transverse direction acts as a confinement potential for the electrons. In the following we denote by $\vec{q}$ the diffusion modes of the electrons. The principle of the calculation uses, as in section A.3 (Appendix A), the Green's functions of the system. Al'tshuler [91] and Lee et al. [93, 89] showed that the sum of diagrams like those of figure 3.11 must be calculated. In this figure, only the diagram contributing to the fluctuations of the diffusion coefficient is shown.

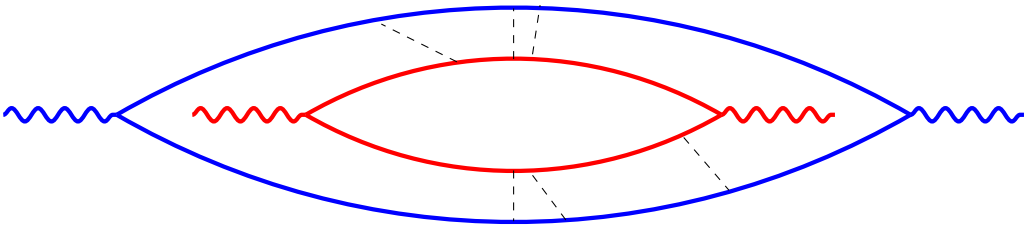

Figure 3.11: *Feynman diagrams entering in the calculation of the fluctuations of conductance. Dashed lines are interaction with impurities. Contribution to the Diffusion coefficient only. See [92] for the diagram contributing to the density of states.*

Another diagram contributes to the density of states. See [92], and [86] for a review.

The fluctuations of conductance are calculated by substituting the realization of disorder V_1 in one electron loop and a realization V_2 in the other, and one then finds for the disorder averaged fluctuations of conductance[9]:

$$\langle G^2\rangle_c \equiv \langle G^2\rangle - \langle G\rangle^2 \propto \frac{s^2}{\beta}\left(\frac{e^2}{h}\right)^2 \sum_{\vec{q}} \left(\frac{1}{Dq^2}\right)^2, \tag{3.12}$$

where s is the spin degeneracy of the electron, β is a symmetry factor (see section 3.2.5 below), e the charge of the electron and h the Planck constant. This expression is found with the use of the Fourier transform of the Diffuson and Cooperon terms in space and time. With no additional dephasing terms than the scalar impurities, this Fourier transform takes the following form, as explained in section A.2.4:

$$\tilde{P}(q,\omega) = \frac{1}{Dq^2}, \tag{3.13}$$

since this term is solution of a diffusion equation. For a box of size $L_x \times L_y \times L_z$, with $L_x = L_y = L_z = L$, the components of the wave vector q are quantized, and we find in general that:

$$\langle G^2\rangle_c \propto \frac{s^2}{\beta}\left(\frac{e^2}{h}\right)^2 \sum_{n_x\neq 0, n_y, n_z} \frac{1}{n_x^2+n_y^2+n_z^2}. \tag{3.14}$$

In this equation, we assume that $q_\alpha = n_\alpha \pi/L$. The mode $n_x = 0$ is forbidden if we assume that the electrodes are situated in the x direction (in $x = 0$ and $x = L$). In the case of a quasi-one dimensional system with $L_x \gg L_y, L_z$ and with $L_z = 1$ in units of lattice spacing (see introduction of section 3.2), we find:

$$\langle G^2\rangle_c = \frac{2}{15\beta} G_0^2, \tag{3.15}$$

where $G_0 = se^2/h$ is the quantum of conductance. These fluctuations are constant and do not depend on disorder.They are called universal (UCF stands for Universal Conductance Fluctuations) as they only depend on the symmetries characterized by s and β.

Definition: we define the dimensionless conductance g as $g = G/G_0$.

[9] we recall that the Diffuson and Cooperon terms are solution of a diffusion equation (see section A.2.4) in the reciprocal space, in the diffusive regime ($L_x \gg l_e$, where L_x is the length of the wire).

Experiment

Thanks to the previous equation (3.15), one predicts that the fluctuations of conductance of a metallic diffusive sample are of order 1, in units of G_0^2. In figure 3.12 is plotted the conductance as a function of the magnetic field of two different devices. This plot is extracted from [89]. The

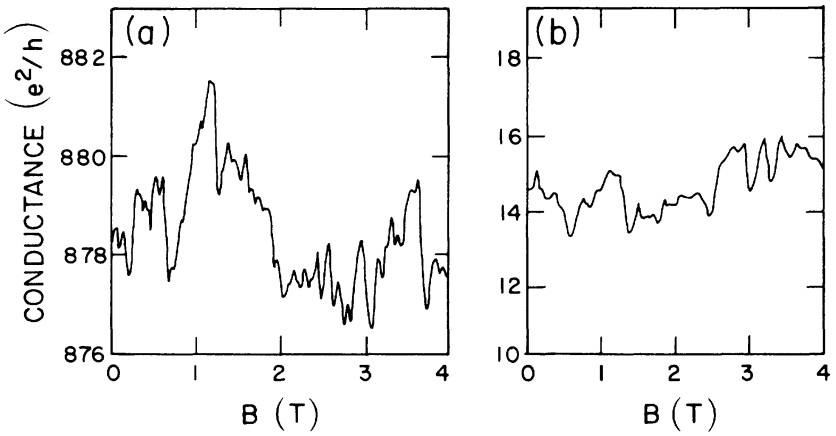

Figure 3.12: *Evolution of the conductance with increasing magnetic field. The left curve (a) corresponds to a* 0.8μ *m-diam gold ring, and the right one (b) corresponds to a quasi-1D silicon MOSFET. These experimental data are extracted from [89].*

conductance fluctuates and the order of magnitude of the fluctuations in both cases is $(e^2/h)^2$. Another example of UCF is given in figure 3.8B. In this plot, it is also shown that the magnetic field changes the value of the fluctuations: the value of UCF is twice in the presence of magnetic field compared to the value without a magnetic field, as expected in [89, 91]. The effect of a external parameter (as magnetic impurities or magnetic field) is described in Appendix A, section A.3.

3.3 Coherent transport in a spin glass

3.3.1 Effect on electrons

A pioneering theoretical study of coherent transport in disordered wires was performed in 1985 by Alt'shuler and Spivak [88]. They studied the effect of external perturbations on conductance fluctuations including spin glass effects. Following them, we model the spin glass as a set of frozen magnetic impurities with no simple long range order due to frustration. This description in terms of frozen spins is valid at low temperature ($T \ll T_g$) as the dynamics of the spins in a spin glass is slowed down (see chapter 1). Moreover, the action of the eventual remaining free spins on the conduction electrons is inelastic scattering which is taken into account in the phase coherence length L_ϕ. The interaction between the spin of impurities and the conduction electrons is of the RKKY (see chapter 1) type, which is an exchange interaction. The spin of the conduction electrons will be scattered by the orientation of the spin of the impurities as the momentum of these electrons is scattered by the position of the impurities (which happens for both magnetic and non magnetic impurities). Similarly to all diffusion processes, we define a

diffusion length of the spin that we denote L_m (see the next section for more details on this length), the magnetic length, and a corresponding diffusion time τ_m. This quantity is related to the intensity of magnetic disorder J by the relation:

$$\tau_m = \frac{1}{2\pi\rho_0 n_i J^2 \langle S^2 \rangle_{\vec{S}}}, \tag{3.16}$$

where ρ_0 is the density of states at the Fermi level, n_i the density of impurities and $\langle S^2 \rangle_{\vec{S}}$ is the average over the orientations of the spin of the impurities $\vec{S}$. L_m and τ_m are linked by: $L_m = \sqrt{D\tau_m}$, where D is the diffusion coefficient. In the following, we study the influence of the presence of frozen magnetic impurities on transport properties; in particular, we derive the Cooperon contribution to the probability of return, and we show that the length L_m plays a crucial role.

3.3.2 The magnetic length and universality classes

The magnetic length

L_m has been defined above as the typical length of spin diffusion: this is the magnetic elastic mean free path. It can be interpreted as the length beyond which the electron has lost the memory of its spin. Indeed, suppose that the electronic path has a length L. If $L_x < L_m$, the spin of the electron does not diffuse efficiently, it remains almost as it was at the entrance of the diffusive sample. On the contrary, if $L_x > L_m$, the spin of the electron diffuses, and then there is no correlation between the spin at the entrance of the sample and the spin at the end of the path. L_m discriminates then systems in which electrons feel the diffusion due to magnetic impurities (case $L_x \gg L_m$) from systems where the influence of the spin of the impurities is negligible (if $L_x \ll L_m$). In this last case, the spin glass is similar to a metal, *i.e* with non magnetic impurities. To study the transport in a spin glass, the relevant case is then when the length of the system is larger than L_m.

Link with universality classes

Consider a diffusive system of length L_x and width L_y connected to two leads as shown on figure 3.13. This system can be equivalently described in terms of a scattering matrix S or a transfer matrix M [94, 95, 96]. As we will see in more details in the next chapter, the scattering matrix links outgoing waves functions to incoming wave functions, whereas the transfer matrix relates states in the left lead to states in the right lead. The advantage of the transfer matrix is that it can be obtained simply by successive multiplication of statistically independent transfer matrices of thin slices of the sample [97, 98], as it links left amplitudes and right amplitudes. The Random Matrix Theory (RMT) is applied to the transfer matrix as a product of random matrices. This theory, developed by Wigner and Dyson consists in the study of an ensemble of Hermitian matrices $\mathcal{H}$, with a statistical distribution given by [99, 100]:

$$P(\mathcal{H}) \propto \exp\left[-\beta Tr(\mathcal{H}^2)\right]. \tag{3.17}$$

The coefficient β depends on the symmetries of the problem. Here the random matrices are the transfer matrices of the thin slices of the sample, and are distributed following equation (3.17).

In the case of a metallic system with no magnetic field applied, time reversal symmetry as well as Kramers degeneracy (spin rotation symmetry) are preserved. In the classification of universality classes of RMT this class is called the Gaussian Orthogonal Ensemble (GOE) and is characterized by a value of the spin degeneracy s equal to 2 (see equation (3.15)) and the β

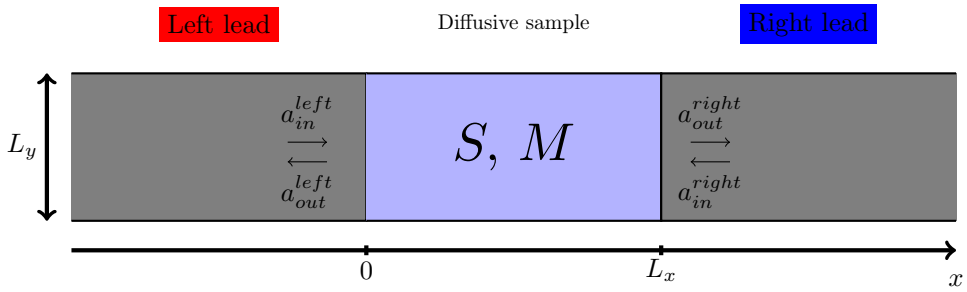

Figure 3.13: *Diffusive sample connected to two leads. S is the scattering matrix of the system and M its transfer matrix. The a's are electronic wave functions.*

parameter equal to 1. This case corresponds to the situation $J = 0$ or $L_x \ll L_m$, where J is the intensity of the magnetic disorder (see equation (3.16)). For a strong magnetic disorder (J large or $L_x \gg L_m$), time reversal symmetry is broken as the spin of impurities play the same role as a local magnetic field felt by the electrons, and the spin rotation degeneracy is also removed. In RMT it corresponds to the Gaussian Unitary Ensemble (GUE) where $s = 1$ and $\beta = 2$. In other words, the spin rotation matrix R_t that is written in equation (3.19) is a product of rotation matrices that do not commute, hence the breaking of time reversal symmetry. For a review on RMT and quantum transport see [101].

3.3.3 The Cooperon and magnetic impurities

Having spins on impurities will change the phase in the Cooperon term as follows [102, 89]:

$$P_c^m = P_c \times \frac{1}{2}\left(3e^{-2t/3\tau_m} - e^{-2t/\tau_m}\right). \tag{3.18}$$

P_c^m represents the Cooperon term with magnetic impurities and P_c is the Cooperon term without magnetic impurities, as already studied in section 3.1, an in Appendix A.2.

Following [60] and [86], we consider R_t the spin rotation operator. From $t = 0$ to $t > 0$, each electron has encountered a certain number of impurities, so its spin state is:

$$|s_t\rangle = R_t|s_0\rangle. \tag{3.19}$$

R_t is a product of rotation matrices corresponding to rotations that the spin of the electron undergoes during the diffusion process.

To describe the effect of coupling to magnetic impurities on the Cooperon, we consider two sequences of collisions conjugated by time reversing, as explained in the precedent section. The time evolution in one direction is given by the factor $\langle s_f|R_t|s_0\rangle$ and the evolution in the other direction is given by $\langle s_f|R_{-t}|s_0\rangle^*$. Both trajectories have the same configuration of spins. The spin part of the Cooperon term (without disorder averaging) is then given by the product of these two contributions for all final spin states $|s_f\rangle$:

$$Q_m(t) = \sum_{s_f=\pm} \langle s_f|R_{-t}|s_0\rangle^* \langle s_f|R_t|s_0\rangle = \sum_{s_f=\pm} \langle s_0|R_{-t}^\dagger|s_f\rangle\langle s_f|R_t|s_0\rangle. \tag{3.20}$$

Mixing these two trajectories is similar to the mixing of two spin-1/2 states, therefore any

tensorial product state can be written in terms of a singlet $|S\rangle$ and triplet $|T_\alpha\rangle$ states. . As

$$|S\rangle\langle S| + \sum_\alpha |T_\alpha\rangle\langle T_\alpha| = 1, \tag{3.21}$$

we show following [89] that the averaged rotation operator can be written as $\langle R_t\rangle = \exp\left(-1/2(t/3\tau_m)(\sigma^a)^2\right)$, and we find

$$\langle Q_m(t)\rangle = \frac{1}{2}(\underbrace{3e^{-2t/3\tau_m}}_{\text{Triplet}} - \underbrace{e^{-2t/\tau_m}}_{\text{Singlet}}). \tag{3.22}$$

From this result, we deduce the modified Cooperon term which is given by:

$$P_c^m(\vec{r},t) = P_c(\vec{r},t) \times \langle Q_m(t)\rangle. \tag{3.23}$$

Similarly to what has been done in the non magnetic case, one is able to have access to the fluctuations of dimensionless conductance [103] as a function of the length of the wire:

$$\langle g^2\rangle = \underbrace{\frac{1}{4}F_2(0) + \frac{3}{4}F_2\left(\sqrt{\frac{4}{3}}\frac{L_x}{L_m}\right)}_{\text{Diffuson term}} + \underbrace{\frac{1}{4}F_2\left(\sqrt{2}\frac{L_x}{L_m}\right) + \frac{3}{4}F_2\left(\sqrt{\frac{2}{3}}\frac{L_x}{L_m}\right)}_{\text{Cooperon term}}, \tag{3.24}$$

where the F_2 function has the form [104]:

$$F_2(x) = \frac{6 + 6x^2 - 6\cosh(2x) + 3x\sinh(x)}{x^4\sinh^2(x)}. \tag{3.25}$$

The limits of that function are: if $x \gg 1$, $F_2(x) \to 0$, and $F_2(0) = 4/15$. See figure 3.14 for the plot of the function F_2. We notice that for conductance fluctuations, both the Diffuson and the Cooperon terms have a non vanishing contribution. To calculate in details the Feynman diagrams corresponding to the conductance fluctuations and that lead to this expression, see [91, 89, 103].

The corrections due to weak localization to the average conductance are also derived (see Appendix A):

$$\delta g_{WL} = \underbrace{\langle g\rangle - \langle g_{class}\rangle = \frac{1}{2}F_1\left(\sqrt{2}\frac{L_x}{L_m}\right) + \frac{3}{2}F_1\left(\sqrt{\frac{2}{3}}\frac{L_x}{L_m}\right)}_{\text{Cooperon term}}, \tag{3.26}$$

where F_1 has the form:

$$F_1(x) = -\frac{\coth(x)}{x} + \frac{1}{x^2}. \tag{3.27}$$

We remark that this contribution is negative, proving that the suppression of the quantum corrections leads to an increase of the average conductance, see figure 3.14. Moreover the Diffuson term does not contribute to the correction of weak localization to the average conductance but contribute to the fluctuations of conductance. We will come back to this point in chapter 6. In figure 3.14 are represented both functions F_1 and F_2.

In the next section we present experimental studies of transport in spin glasses, and in particular we describe a work performed in the early nineties showing that conductance fluctuations measurements allow the possibility to access the spin configurations of the magnetic impurities, which is at the origin of the numerical work of this thesis (see chapters 5 and 6).

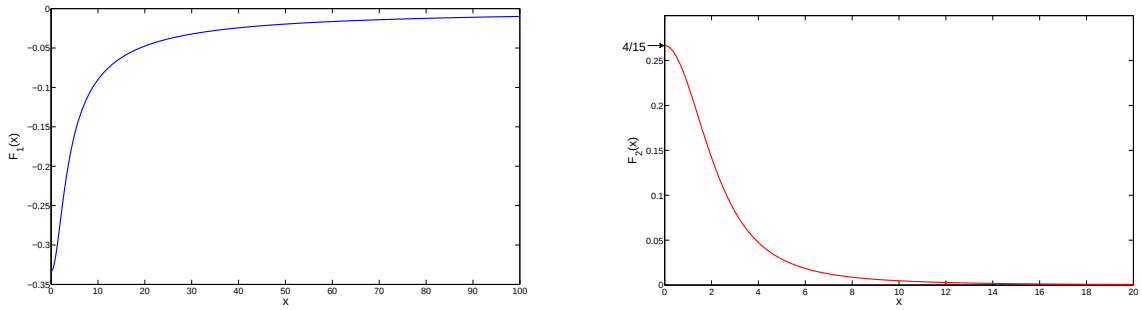

Figure 3.14: *Plot of the functions F_1 and F_2 that correspond to the evolution with the longitudinal length of respectively the average conductance and the variance. We notice that F_1 is always negative, which is related to the negative magnetoresistance effect (see text).*

3.3.4 Experimental transport in a mesoscopic spin glass wire

Pioneering experiment

As seen in chapter 1, despite a lot of experimental efforts, a good understanding of the spin glass phase was still lacking in the late eighties. In this section we present the pioneering experiment that studied coherent transport in a spin glass nanowire. This experimental study has been performed by de Vegvar et al. and their results are summarized in [83]. In this article they study the coherent electronic transport in a Cu matrix doped with Mn impurities at a concentration equal to 1000 ppm (0.1% of impurities). One of their key results is presented in figure 3.15, and measurements are performed in that case on a 0.65μ m long segment of spin glass. The spin glass temperature has been evaluated to be approximately equal to $1.6K$, and the phase coherence length has been evaluated to be of order of 1μm.

One first obvious result lies in the amplitude of the conductance fluctuations: as soon as the system enters the spin glass phase ($T < T_g \approx 1.6K$), the amplitude of the fluctuations grows (appearance of the UCF), indicating the entrance in the coherent regime. Next, curves corresponding to two low temperatures ($0.9K$ and $23mK$) are correlated showing the rigidity of the underlying spin configuration of the spin glass. Next, the authors measured a magnetofingerprint at low temperature ($T_{exp} < T_g$), then they heated up the system above the spin glass temperature, and they cooled it down again to the same temperature T_{exp}, and they measured a second magnetofingerprint. From the correlation between both traces, they managed to prove reorientations of spins occured.

The conclusion of this study is that coherent transport is indeed experimentally observable in a spin glass. From the small correlation between different magneto-fingerprints across the anneal of figure 3.15, the authors managed to show the occurrence of spin reorganizations inside the spin glass phase, which demonstrates the possibility to get information on the spin configuration via conductance measurements. **This experimental result is the starting point of our own study of coherent transport in a spin glass**, as no theoretical support were available at that time to interpret the experimental results more quantitatively.

Other transport studies in spin glasses: noise measurements

Israeloff et al [105] considered the noise spectrum of electrical resistance in a mesoscopic spin glass. In a spin glass phase, the noise spectrum is expected to follow a $1/f$ behavior [106], where f is the frequency. In figure 3.16 is plotted the dimensionless noise parameter $\alpha(f,T) \equiv fS_R(f)N_A/R^2$,

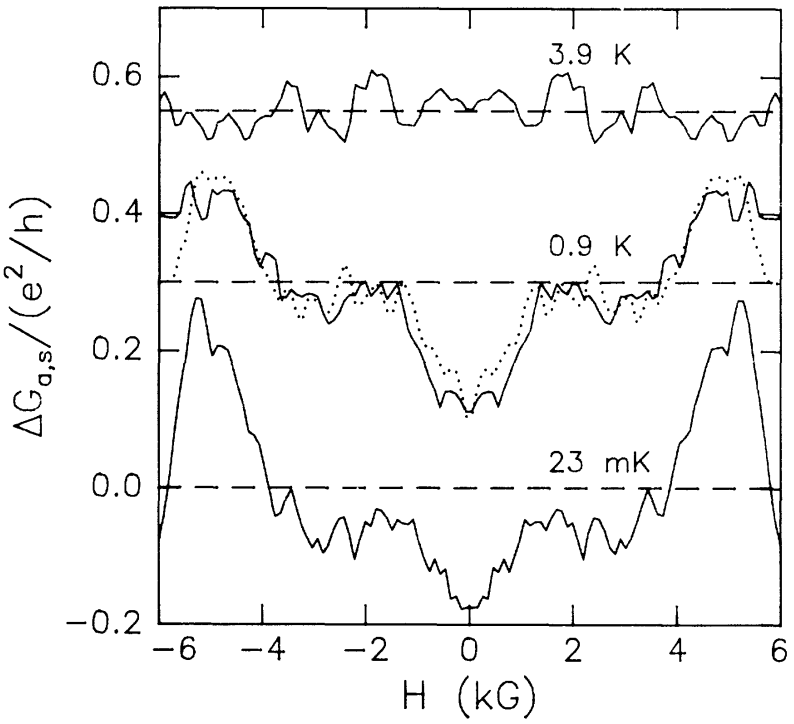

Figure 3.15: *Plot of the magnetic contribution of the conductance, antisymmetric in the magnetic field, as a function of the magnetic field applied in Cu:Mn spin glass ($T_g \approx 1.6K$). The sample was cooled from 4K to 12mK in 7kG and subsequently warmed to the indicated temperatures. The curve are offset vertically for clarity. The two traces at 0.9K indicate the experimental reproducibility and have correlation $C = 0.9$. Extracted from [83].*

where $S_R(f)$ is the spectral density of the fluctuations in resistance R (*i.e* the Fourier transform of the time fluctuations in resistance R of the spin glass), and N_A is the number of atoms in the sample, for a $Cu_{1-x}Mn_x$ spin glass film of thickness $50 - 70nm$, at temperatures above $5K$. It is plotted versus temperature T. It shows approximately two plateaus for which α seems to be constant, and a step. From the position of the step, they deduce the spin glass temperature which is compared to the temperature transition extracted from susceptibility measurements (see the inset of figure 3.16). The effect on noise of field cooling with $H = 2.1T$ is shown in figure 3.17. The noise onset temperature is weakly reduced, while the spectral exponent near T_g is strongly affected. The effects of magnetic fields, which change not only the temperature dependence and the magnitude of the spectrum but also its shape, and the dependence of the noise on the field history confirm that below T_g, they are measuring slow spin dynamics in the resistivity noise, since fields should not be affecting the dynamics of anything else. Therefore, electrical noise is measurable in spin glass phases and it is affected by the presence of frozen magnetic moments.

In 1998, another work on resistance noise is performed by Jaroszyǹski et al [107] in diluted magnetic semiconductors (DMS) [108]. They used sub-micron wires of $Cd_{1-x}Mn_xTe : I$ with electron densities greater than that corresponding to the metal-insulator transition. In the range of temperatures they used, it is highly probable they performed conductance measurements in the coherent regime. They found that if the system enters the spin glass phase, the fluctuations

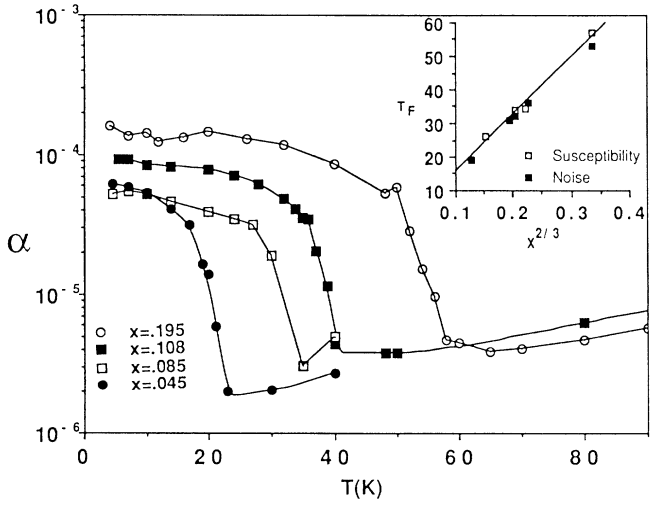

Figure 3.16: *The normalized electrical resistance noise ($0.08 - 17Hz$) plotted versus temperature for $Cu_{1-x}Mn_x$ films with a range of x. The films were $50 - 70nm$ thick. Inset: the SG freezing temperature T_g, determined from magnetic susceptibility measurements and by noise measurements [$max(\partial\alpha/\partial T)$], plotted vs $x^{2/3}$. The line is a fit to the susceptibility points. Extracted from [105].*

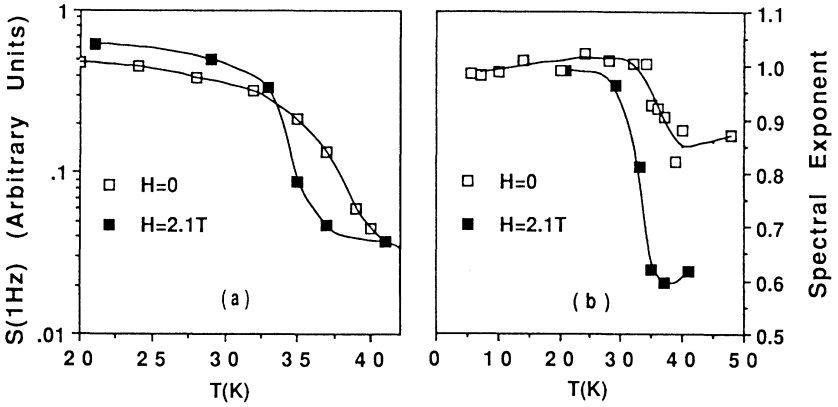

Figure 3.17: *(a) The noise onset (measured near $1Hz$) with zero field and with $2.1T$ for a film with $x = 0.108$. (b) The spectral exponent, $-\partial \log S_R/\partial \log T$, vs T for the same sample with and without field. Extracted from [105].*

of conductance agree, at least qualitatively with theory [89, 109]. Other signatures, particularly strong and complex of the spin glass freezing are found in these DMS: see figure 3.18. In curve (a) are depicted relevant examples of history dependent effects. It shows a series of magneto fingerprints, measured successively as a function of the magnetic field (and time) after a heat pulse and subsequent cooling from $T > T_g$ to $T \approx 0.02T_g$. In this plot, the gradual decrease in both the amplitude of the fluctuations and the differences between subsequent traces is a clear effect of aging. The effect of aging, that is, a gradual decrease in both the fluctuation amplitude

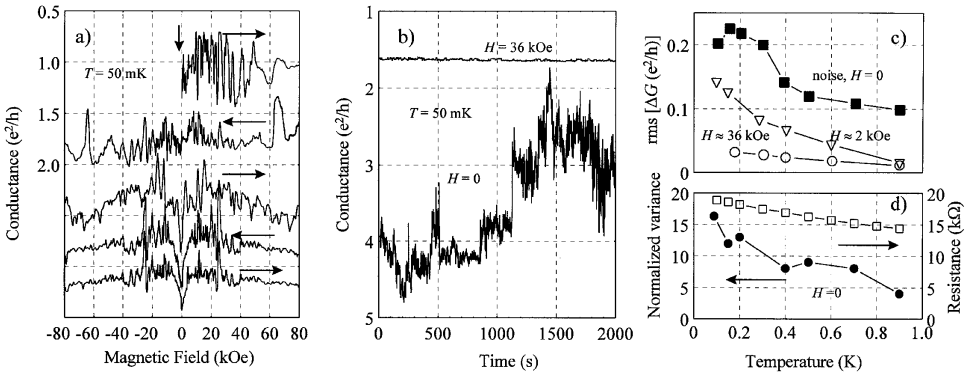

Figure 3.18: *Conductance G as a function of the magnetic field (a) and time (b) in the wire n^+-$Cd_{0.8}Mn_{0.2}Te$ at $50mK$. The traces in (a) were taken in succession starting from the top, and are shifted by e^2/h for clarity. The arrows indicate directions of the sweep. Note that G decreases in the upward direction. Temperature dependencies of the root mean square conductance fluctuations are shown in (c), while time-averaged resistance (open symbols) and normalized variance of the noise spectrum in (d); the solid lines are guides for the eye. Extracted from [107].*

and the difference between subsequent traces, is clearly visible. Magnetic irreversibilities persist even after a long waiting time. This article proves also the existence of a clear signature of the spin glass phase on transport.

In the same way, Neuttiens et al [110] identified an intrinsic $1/f$ noise in narrow AuFe spin glass wires. As in [105], $1/f$ noise is characteristic of spin glass freezing process as it is related with the presence of a huge number of relaxation time scales in the material [106]. All these examples reveal the interplay between spin freezing and electron dephasing in mesoscopic spin glasses. However, none of these experiments were able to extract quantitative information on the local spin configuration of the spin glass, as de Vegvar et al did.

3.3.5 Conclusion

As a conclusion for this chapter, we have shown, both qualitatively and quantitatively that it is possible to have access to the frozen spin configuration of a spin glass via conductance fluctuations measurements. This result is at the origin of our work. Similarly, original works on coherent transport [88] derive the conductance fluctuations in the presence of frozen impurities. All these studies show that frozen magnetic impurities have an influence on transport. To quantify more precisely this influence, we propose to study not the fluctuations $\langle g^2 \rangle$, but conductance correlations $\langle g \times g' \rangle$, where the conductance g corresponds to one frozen spin configuration, and g' to another different frozen spin configuration, both taken in the same scalar disorder configuration. We assume that the comparison of these conductances gives access to the comparison of the different spin configurations.

In the next chapter, we describe the method we use to study coherent transport in a nanowire. In chapter 5, we study in detail the universal properties of transport in different conduction regimes and we manage to calibrate with high accuracy the Universal metallic regime (characterized by the so-called UCF). In chapter 6, we study the conductance correlations and we show that they are directly related to a crucial intrinsic spin property of the spin glass.

Part II

Numerical study of coherent transport in metallic spin glasses

- Est-ce que les histoires que vous racontez ne vous empêchent pas de dormir ? - Si, mais comme ce sont des histoires à dormir debout, je récupère !

Raymond Devos

Chapter 4
The numerical method

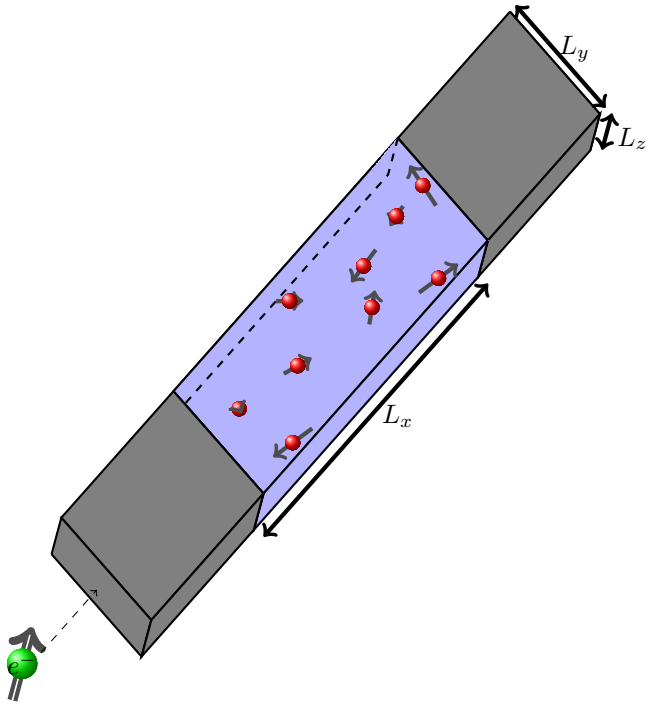

Figure 4.1: *Schematic picture of the system with an incoming electron. The spin glass is a quasi one dimensional wire of length L_x, width L_y and thickness L_z.*

4.1 Introduction

4.1.1 The system

We consider a system modeling a canonical Spin Glass (*i.e* Au doped with Fe or Ag doped with Mn) connected to two electrodes modeled in the following as two semi-infinite metallic wires. The goal of the study is to calculate numerically the conductance of such a device, using the retarded Green's functions formalism. The system we consider in the numerical method has length L_x, width L_y and thickness L_z as shown in figure 4.1. The thickness of the system is set to 1 in units of lattice spacing[1] for efficiency in numerical calculations. We can restrict ourselves to $L_z = 1$ as we are dealing with the regime of one dimensional diffusion in the x direction: the universal properties of diffusive transport do not depend on the transverse dimensions. The Spin Glass nature of this sample is described by a set of classical spins $\{\vec{S}_i\}_i$. These spins are chosen frozen (see section 3.2.3) to mimic a low temperature Spin Glass phase. This basic description is sufficient for the purpose of the calculation of the conductance.

The Hamiltonian of the system is a tight binding Anderson [111] Hamiltonian as described in the previous chapter in equation (3.3) with an added magnetic disorder that couples the SU(2) spin of the electron (described by the Pauli matrices $\vec{\sigma}$) and the Heisenberg classical spin of the

[1] in the following, this length is not varied, we will not talk about it any more.

impurity. In second quantization formalism, the Hamiltonian takes the form:

$$\mathcal{H} = \sum_{<i,j>,s} t_{ij} c^\dagger_{j,s} c_{i,s} + \underbrace{\sum_{i,s} v_i c^\dagger_{i,s} c_{i,s}}_{\text{Scalar disorder}} + \underbrace{J \sum_{i,s,s'} \vec{S}_i \cdot \vec{\sigma}_{s,s'} c^\dagger_{i,s} c_{i,s'}}_{\text{Magnetic disorder}} . \tag{4.1}$$

i represents the position of the electron in the lattice and s its spin state. The magnetic disorder is described as an onsite potential to model the randomly oriented classical spin of the magnetic impurities. We remind the reader that v_i is a random quantity, whose statistical distribution is chosen flat in the interval $[-W/2; W/2]$. The orientation of each impurity spin is random on the sphere of radius $S = 1/2$.

4.1.2 The parameters of the study

The lattice is a grid with longitudinal and transverse hopping amplitudes between sites, t_{ij}, chosen constant in the x ($t_{//}$) and the y ($t_\perp$) directions. In the following, we impose $t_{//} = 1$. Concerning the scalar disorder, we call a *realization of disorder* the set of $\{v_i\}_i$'s, and we note $V \equiv \{v_i\}_i$. The intensity W of the scalar disorder is taken equal to 0.6 in the whole study. In most cases, the number of realizations of disorder used in this study is $N_{\text{dis}} = 5\,000$, the main goal of the study being the study of the statistical distribution of the conductance with respect to scalar disorder. To sample the distribution of conductance with high accuracy we generated up to 50 000 disorder configurations in a particular case (see next chapter).

To mimic a low temperature spin glass, the spin configuration $\{\vec{S}_i\}_i$ is built by generating a random Heisenberg vector at each site i. In this model, $\vec{\sigma}$ is the coherent spin of the electron. J is the amplitude of magnetic disorder and different values of J are taken between 0.025 ("weak" magnetic disorder) and 0.4 ("strong" magnetic disorder).

The width of the system L_y is varied from 5 to 80 (in units of lattice spacing a), and the length L_x from 5 to 60 000. Both the longitudinal and the transverse lengths are supposed to be smaller than the coherence length L_ϕ, defined in chapter 2. It is introduced phenomenalogically via a very small imaginary part given to the energy (in practice, $E = E_0 + \imath\eta_\phi$ with $\eta_\phi = 10^{-7}$.).

Magnetic fluxes, if applied, are chosen from 1 flux quantum to 1 500 flux quanta through the sample. We recall that fluxes are calculated through the whole sample:

$$\phi = BL_x \times L_y. \tag{4.2}$$

In this model, the magnetic field is taken into account through the Peierls substitution[2]:

$$t_{//} \to t_{//} e^{\imath \frac{|e|}{\hbar} \int \vec{A} \cdot \mathrm{d}\vec{r}}, \tag{4.3}$$

where $\vec{A}$ is the vector potential created by the magnetic field.

4.2 The Landauer-Büttiker formula of coherent transport

4.2.1 The scattering matrix

Definition of the scattering matrix

The goal of this part is to present the main properties of the scattering matrix of a diffusive sample, in relation with the current amplitudes coming in and going out of the sample. Considering

[2]we suppose that the magnetic field is weak, so that it only modifies the phase of the Green's functions calculated in Appendix A, section A.2.

a diffusive sample as shown in figure 3.13 (chapter 3), we define incoming **current** amplitudes at the left or right part ($a_{\text{in}}^{\text{left,right}}$) of the sample or outgoing **current** amplitudes $a_{\text{out}}^{\text{left,right}}$ using standard Quantum Mechanics, as:

$$a_{\text{in,out}}^{\text{right,left}} = \sqrt{v_g}\psi_{\text{in,out}}^{\text{right,left}}, \tag{4.4}$$

where ψ is the wave function of an electron and v_g the group velocity of the corresponding mode ψ. By definition, the scattering matrix S of the system links these amplitudes as follows:

$$\begin{pmatrix} a_{\text{out}}^{\text{left}} \\ \\ a_{\text{out}}^{\text{right}} \end{pmatrix} = S \begin{pmatrix} a_{\text{in}}^{\text{left}} \\ \\ a_{\text{in}}^{\text{right}} \end{pmatrix} \tag{4.5}$$

The sample with its leads is described in figure 3.13. In this figure, the sample is taken between $x = 0$ and $x = L_x$. The wave function propagating in the direction of the x-axis (towards positive x) have the form $\psi_+(x) \propto e^{\imath k_x x}$, where k_x is the x component of the wave vector of the electron. Wave functions propagating towards the negative x have the form: $\psi_-(x) \propto e^{-\imath k_x x}$. The wave functions ψ introduced in equation (4.4), can then be calculated, following figure 3.13:

$$\begin{aligned} \psi_{\text{in}}^{left} &= \psi_+(x = 0), \\ \psi_{\text{out}}^{left} &= \psi_-(x = 0), \\ \psi_{\text{in}}^{right} &= \psi_-(x = L_x), \\ \psi_{\text{out}}^{right} &= \psi_+(x = L_x). \end{aligned} \tag{4.6}$$

For a system with a number of N_y transverse modes, the scattering matrix is $2N_y \times 2N_y$ [96]. In the following, the quantity of interest is the transmission probabiltiy $T_{m\leftarrow n}$ from a channel n in the lead[3] p to a channel m in the lead q. It reads:

$$T_{m\leftarrow n} = |s_{mn}|^2, \tag{4.7}$$

where s_{mn} are the coefficients of S.

Interpretation of S

The conservation of current:

$$\underbrace{|a_{\text{in}}^{\text{right}}|^2 + |a_{\text{in}}^{\text{left}}|^2}_{\text{Incoming current}} = \underbrace{|a_{\text{out}}^{\text{right}}|^2 + |a_{\text{out}}^{\text{left}}|^2}_{\text{Outgoing current}} \tag{4.8}$$

imposes that the scattering matrix S must be unitary [97, 112], *i.e* $S^\dagger S = 1$. It is possible to define the scattering matrix from **wave** amplitudes (denoted S'). The coefficients of this matrix are related to the coefficients of the S matrix by (consider equation (4.4)):

$$s'_{mn} = \sqrt{\frac{v_m}{v_n}} s_{mn}, \tag{4.9}$$

where $v_{m,n}$ are the group velocities of respectively channel m and n. Notice that the matrix S' is not unitary.

If one applies a magnetic field B perpendicular to the plane sample, the scattering matrix statisfies a reciprocity relation:

$$S(B) = S^t(-B). \tag{4.10}$$

S^t is the transpose matrix of S.

[3] in this two-terminal geometry, p and q denote either the left or the right lead.

4.2.2 The Landauer-Büttiker formula

In figure 3.13 the left and right reservoirs are particle reservoirs at respective temperature T_L and T_R. Their chemical potential is $\mu_{L,R}$. Both are supposed to be at thermodynamical equilibrium. When an outgoing particle reaches a reservoir, it is absorbed with probability 1. For simplicity in this section, we consider a purely one dimensional system. The probability for an incoming electron with energy E to be transmitted from left to right part of the diffusive sample is given by the transmission amplitude $t(E)$. In other words, the scattering matrix S reads [113]:

$$S = \begin{pmatrix} r(E) & t(E) \\ t(E) & r'(E) \end{pmatrix} \tag{4.11}$$

$r(E)$ and $r'(E)$ are reflexion amplitudes, and $t(E)$ is a transmission amplitudes. The quantity of interest is the net electric current I that flows from left to right as a function of applied voltage V_{elec}.

The form of the wave function of an incoming particle from the left reservoir to the diffusive sample is, following equation (4.6):

$$\psi_L(x) \propto e^{\imath k_x x}, \tag{4.12}$$

for a perfect one dimensional system. Then the wave function of the outgoing particle, in the right electrode, is $\psi_R(x) = t(E)\psi_L(x)$. The corresponding one particle current from the left to the right (far from each particle reservoir) $\mathcal{I}_{L\to R}$, can be derived using standard Quantum Mechanics calculations [114]:

$$\mathcal{I}_{L\to R} \propto e k_x t(E) t^*(E). \tag{4.13}$$

For many particles with energies between E and $E + \mathrm{d}E$, this current is modified as:

$$\mathrm{d}I_{L\to R} = \frac{\mathrm{d}\rho(E)}{\mathrm{d}E} e v(E) f_L(E) |t(E)|^2 \mathrm{d}E, \tag{4.14}$$

where $\frac{\mathrm{d}\rho(E)}{\mathrm{d}E}$ is the density of state at energy E, $v(E)$ is the group velocity of electrons at this energy and f_L is the Fermi-Dirac distribution:

$$f_{L,R}(E) = \frac{1}{\exp\left(\frac{E-\mu_{L,R}}{k_B T_{L,R}}\right) + 1}, \tag{4.15}$$

where $\mu_{L,R}$ is the chemical potential of the left (resp. right) reservoir.

In the case of a one dimensional system, $\rho(E) = N(E)/L_x$ with $N(E)$ the number of particles at energy E, we find that $\rho(E) = k(E)/2\pi$ ($k(E)$ is the wave vector at energy E). As $v(E) = \frac{\mathrm{d}E}{\hbar \mathrm{d}k}$, the net current in one dimension reads:

$$\mathrm{d}I_{L\to R} = \frac{e}{h} f_L(E) T(E) \mathrm{d}E, \tag{4.16}$$

with $T(E) = |t(E)|^2$ the transmission probability. We define the total current I as

$$I = \int (\mathrm{d}I_{L\to R} - \mathrm{d}I_{R\to L}) \tag{4.17}$$

as the difference between the current flowing from left to right and the current flowing from right to left. If $I > 0$, the current flows effectively from left to right, whereas it flows from right to left if $I < 0$. Moreover no reflected current from left to left or from right to right have to be taken into account since we count the number of electrons flowing through a section in the middle of

the conductor. If we assume that the transmission probabilities from right to left and from left to right are equal, we end up with:

$$I = \frac{e}{h} \int \mathrm{d}E \, (f_L(E) - f_R(E)) \, T(E). \tag{4.18}$$

The origin of the movement of the electrons in the wire is the non vanishing applied voltage V_{elec}. The chemical potential reads then: $\mu_{L,R} = \mu \pm \frac{eV_{\mathrm{elec}}}{2}$, and $T_L = T_R$. Therefore

$$I = \frac{e}{h} \int \mathrm{d}E \left(f(E - \frac{eV_{\mathrm{elec}}}{2}) - f(E + \frac{eV_{\mathrm{elec}}}{2}) \right) T(E). \tag{4.19}$$

For sufficiently low potential difference V_{elec} this equation can be simplified by assuming that the difference of the two Fermi-Dirac distributions is approximately equal to $eV_{\mathrm{elec}} \times \left(-\frac{\mathrm{d}f}{\mathrm{d}E} \right)$. This derivative is exactly a Dirac delta-function at zero temperature. We can then conclude that, at that temperature:

$$I = \frac{e^2}{h} V_{\mathrm{elec}} T(E_F), \tag{4.20}$$

where E_F is the Fermi energy. The conductance G is then equal to $\frac{e^2}{h} T(E_F)$. This equation is valid for a one dimensional system. If the sample and electrodes have a transverse extension L_y, and if the spin of the electron is taken into account, the conductance takes the following form (**Landauer-Büttiker** formula [115]):

$$G = \frac{se^2}{h} \sum_{m,n} T_{m \leftarrow n}(E_F), \tag{4.21}$$

where m and n are transverse modes. s is the spin degeneracy, and depends on the universality class (see chapter 3).

For a wire of width L_y, the total wave function has the form:

$$\Psi(x, y) = e^{\imath k_x x} \chi_n(y). \tag{4.22}$$

In the transverse direction, electrons are confined between $y = 0$ and[4] $y = L_y \equiv aN_y$. Solving the Schrödinger equation in the transverse direction (electrons feel a confining potential that is infinite if $y > L_y$ and $y < 0$, and null either) leads to the appearance of quantized energies E_n and transverse modes $\chi_n(y)$ defined as:

$$\mathscr{H}_y \chi_n(y) = E_n \chi_n(y), \tag{4.23}$$

where $\mathscr{H}_y = -\partial_y^2$ (if we impose $\hbar = 1$ and $m_e = 1$). The eigenfunctions χ_n are then:

$$\chi_n(y) = \sqrt{\frac{2}{N_y + 1}} \sin \left(\frac{n\pi y}{N_y + 1} \right). \tag{4.24}$$

The group velocity of this mode is given by:

$$v_n = 2 \frac{t_{//}}{\hbar} \sin k_x, \tag{4.25}$$

[4] N_y represents the number of normal modes, and is equal to L_y/a, where a is the lattice spacing.

where the wave vector k_x is determined by the dispersion relation:

$$E_n = \epsilon - 2t_\perp \cos\left(\frac{n\pi}{N_y+1}\right) - 2t_{//}\cos k_x, \tag{4.26}$$

where ϵ is the on-site energy. In the following these transverse modes are called propagating modes or channels. We impose the supplementary condition $t_{//} = 2t_\perp$ to stay near the band center (and therefore avoiding the presence of fluctuating states [116].

4.3 The Fisher-Lee relation.

4.3.1 What are Green's functions?

The Green's functions of a physical system provide the response at any point of the system due to an excitation at any other point. Assume that the response $\psi(\vec{r},\vec{r}')$ of a system is related to the external excitation $\mathscr{B}(\vec{r},\vec{r}')$ by a generic linear differential operator $\mathscr{L}$

$$\mathscr{L}[\psi](\vec{r},\vec{r}') = \mathscr{B}(\vec{r},\vec{r}'), \tag{4.27}$$

it is possible to define a Green's function $G(\vec{r},\vec{r}')$ as the response to a Dirac like excitation:

$$\mathscr{L}[G](\vec{r},\vec{r}') = \delta(\vec{r},\vec{r}'), \tag{4.28}$$

with δ the Dirac distribution function.

Example.
Consider a free particle in a magnetic field. The Hamiltonian of this particle is:

$$\mathscr{H} = \frac{(\imath\hbar\nabla + e\mathbf{A})^2}{2m}.$$

The eigenstates Ψ and eigenvalues E are calculated via the equation:

$$\mathscr{H}\Psi(r) = E\Psi(r).$$

This equation can be written in terms of one operator applied to the state Ψ and a source:

$$(\mathscr{H} - E)\,\Psi(r) = 0.$$

The Green's function $\mathscr{G}$ of this system is then the state that verifies

$$(\mathscr{H} - E)\,\mathscr{G}(r,r') = \delta(r,r').$$

This is the response for a pulse excitation at position r'.

The Green's function is formally equal to

$$G \equiv \mathscr{L}^{-1}. \tag{4.29}$$

4.3.2 Link between the Green's function and the scattering matrix

Considering the system described by figure 3.13, one can calculate the Green's function between a point lying on the line $x_p = 0$ in lead p and another point lying on the line $x_q = L_x$ in lead q, denoted by $G^R_{pq}(x_q = L_x, y_q; x_p = 0, y_p) \equiv G^R_{qp}(y_q; y_p)$. The upper script R stands for retarded Green's functions (see [112]). As shown on figure 3.13, there are several transverse channels in each lead (p or q), so the retarded Green's function has the following expression [112]:

$$G^R_{qp}(y_q; y_p) = \sum_{n\in p}\sum_{m\in q} \left(\delta_{nm} A^-_n + s'_{mn} A^+_n\right) \chi_m(y_q). \tag{4.30}$$

χ_m is the eigenstate of the transverse Hamiltonian (4.24) (the potential in the transverse direction is only confining, equal to zero if $0 \leq y \leq L_y$ and infinite either, see section 4.2.2). A^+_m is the wave amplitude of an electron in channel $m \in q$ going in the direction of the diffusive sample, A^-_m is the wave amplitude of an electron in the same channel but in the direction opposite to the diffusive sample. The channel n belongs to lead p. s'_{mn} is the scattering matrix defined in section 4.2.1 in terms of wave amplitudes. Recall that this matrix is not unitary[5]. Considering continuity arguments for the wave function, one finds:

$$A^+_n = A^-_n = -\frac{\imath}{\hbar v_n}\chi_n(y_p). \tag{4.31}$$

Using equation (4.9), the Green's function reads:

$$G^R_{qp}(y_q; y_p) = \sum_{n\in p}\sum_{m\in q} -\frac{\imath}{\hbar\sqrt{v_n v_m}}\chi_n(y_p)\left(\delta_{nm} + s_{mn}\right)\chi_m(y_q). \tag{4.32}$$

In order to obtain the expression of the scattering matrix elements as a function of the Green's functions of the system, we multiply equation (4.32) by $\chi_n(y_p)\chi_m(y_q)$, integrate over y_p and y_q and make use of the orthogonality between the χ functions.

$$s_{mn} = \imath\hbar\sqrt{v_n v_m}\int\int \mathrm{d}y_p \mathrm{d}y_q \chi_n(y_p, x_p = 0) \times G^R(y_p, x_p = 0 | y_q, x_q = L_x)\chi_m(y_q, x_q = L_x), \tag{4.33}$$

This relation is known under the name of *Fisher-Lee relation* [117].

Thanks to this last relation and equation (4.21), one is able to link directly the conductance of any conductor to its retarded Green's functions. The last step needed to obtain the conductance is the calculation of the Green's functions of the system. In this study, we use a numerical method based on a recursive calculation of the Green's functions.

4.4 Computing Green's functions

In this section, we study the influence of perturbations of a free system. In section 4.4.1, we present general results on Green's functions in perturbed systems, and we apply in section 4.4.2 these results to our own Anderson model.

[5] the unitary scattering matrix links current amplitudes

4.4.1 Green's functions and perturbed systems

The perturbed Hamiltonian can be expressed in the form

$$\mathcal{H} = \mathcal{H}_0 + \mathscr{V}, \tag{4.34}$$

where $\mathcal{H}_0$ is the free part of the Hamiltonian and $\mathscr{V}$ is a perturbation potential. We define two types of Green's functions:

$$G_0^R = (E - \mathcal{H}_0)^{-1} \tag{4.35}$$
$$G^R = (E - \mathcal{H})^{-1} \tag{4.36}$$

G_0^R is the Green's function of the free Hamiltonian $\mathcal{H}_0$, and G^R is the Green's function of the complete system. It is generally difficult (if not impossible) to calculate directly the Green's function of such a system, but it appears that

$$G^R = \left((G_0^R)^{-1} - \mathscr{V}\right)^{-1}. \tag{4.37}$$

Provided that the perturbation $\mathscr{V}$ is small compared to the free part of the Hamiltonian ($\mathscr{V} \ll \mathcal{H}_0 \equiv (G_0^R)^{-1}$), one can expand the above equation in powers of $\mathscr{V}$ [118]:

$$\begin{aligned} G^R &= \left((G_0^R)^{-1}(1 - G_0^R\mathscr{V})\right)^{-1} = \left(1 - G_0^R\mathscr{V}\right)^{-1} G_0^R \\ &= G_0^R + G_0^R\mathscr{V}G_0^R + G_0^R\mathscr{V}G_0^R\mathscr{V}G_0^R + \dots \\ &= G_0^R + G_0^R\mathscr{V}\left(\underbrace{G_0^R + G_0^R\mathscr{V}G_0^R + \dots}_{G^R}\right) \\ &= G_0^R + G_0^R\mathscr{V}G^R \end{aligned} \tag{4.38}$$

In the following, we use this so-called **Dyson equation** in the tight binding model presented above to calculate recursively the retarded Green's functions of the whole system.

4.4.2 The recursive numerical method

We calculate the Green's functions recursively by building the wire row by row as shown in figure 4.2. In this case, the perturbation $\mathscr{V}$ is the hopping from a slice at step n and the slice with only one row. Using a Dyson equation (4.38), the recursive method to calculate numerically the propagators is described schematically in figure 4.2. We also refer to [119] for the description of the method in the three dimensional case.

We define $G_{M,M}^M$, the Green's function for a system with M columns (the number of columns in the previous expression is given by the upper script), that links any point at $x = M$ with any point at $x = M$. See figure 4.3 for the definition of all the relevant Green's functions. We explain, in this section how we use the Dyson equation (4.38) to calculate recursively all of them, and we concentrate on $G_{M,M}^M$.

For that purpose, we define the hopping from column $x = n$ to column $x = n + 1$ by the operator $V(n, n+1)$, and we define $V(n+1, n)$ the hopping in the opposite direction (*i.e* from column $n + 1$ to column n). As illustrated in figure 4.2, we suppose that the sample is already built from $x = 0$ to $x = n$ (*i.e* the Green's functions of such a system are supposed known), and we want to add one column to build a sample with $n + 1$ columns. the unperturbed system is constituted by a sample of size n, and one column. These two systems are unconnected and the

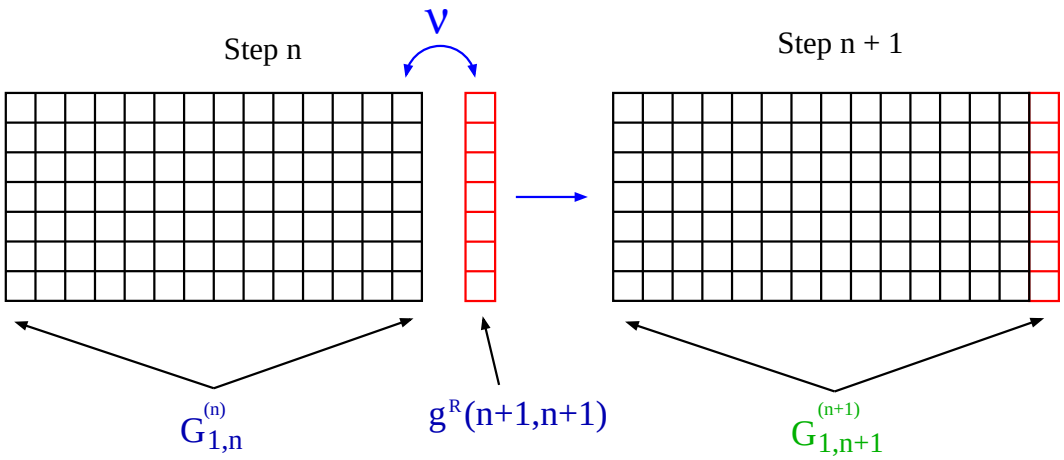

Figure 4.2: *Explanation of the recursive method of calculation of the retarded Green's functions of the system. The potential $\nu = \mathscr{V}$ in the text is the longitudinal hopping term in the Hamiltonian. At step n, all retarded Green's functions are supposed known. One transverse column is then added to the system via a Dyson equation: the Green's function for a single transverse column is calculated numerically. The Green's function of a system of $n+1$ columns is deduced from the knowledge of the Green's function of a system of n columns and the calculation of the Green's function of a system of one column, by inversion of the transverse Hamiltonian at $n+1$ (see equation (4.39)).*

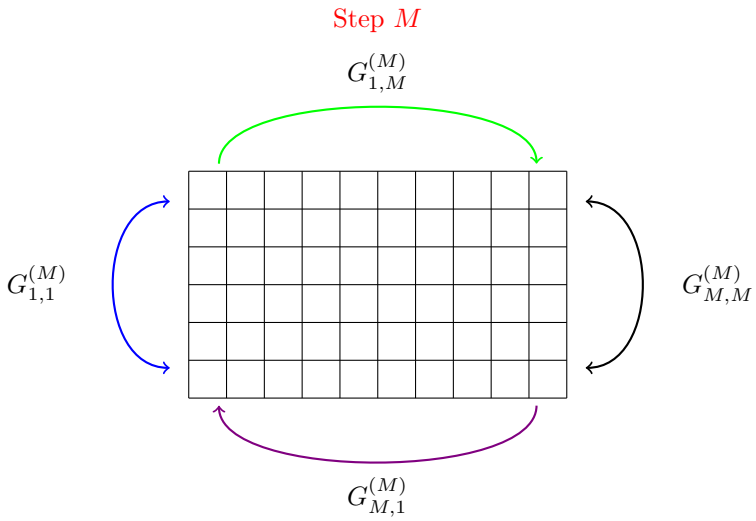

Figure 4.3: *Definition of the different Greens functions at an arbitrary step M. $G^{(M)}_{1,1}$ is the Green's function of an electron going from any point of the first column to any other point of the first column. The electron diffuse nonetheless in the whole sample. In the same way $G^{(M)}_{M,M}$ links any point of column M to any other point of column M, $G^{(M)}_{1,M}$ links any point of the first column to any other point of column M, and $G^{(M)}_{M,1}$ links any point of column M to any other point of the first column.*

Dyson equation is required to connect them. The Green's function of one column of the system

is denoted $g^R(n+1,n+1)$ and is equal to:

$$g^R(n+1,n+1) = (E - \mathcal{H}_{\text{trans}})^{-1}, \tag{4.39}$$

where $\mathcal{H}_{\text{trans}}$ is the Hamiltonian of a slice of one column of the system ("transverse" Hamiltonian), and takes the following form:

$$\begin{pmatrix} w_1 & -t_\perp \mathbb{I}_2 & 0 & ... & 0 \\ -t_\perp \mathbb{I}_2 & w_2 & 0 & ... & 0 \\ & & & & \\ 0 & 0 & ... & -t_\perp \mathbb{I}_2 & w_N \end{pmatrix} \tag{4.40}$$

The w_i's are the onsite potential terms defined as follows (see equation (4.1)):

$$w_i = v_i \mathbb{I}_2 + J\vec{S}_i \cdot \vec{\sigma}, \tag{4.41}$$

where $\mathbb{I}_2$ is the 2 by 2 identity matrix and $\vec{\sigma}$ gathers the three Pauli matrices. This form is justified since the spin of the electron is a quantum number: the transverse Hamiltonian is a $2N_y \times 2N_y$ block matrix, whose blocks are of size 2×2. Each block represents one propagating channel and the 2×2 structure represents the spin of the electron in each channel.

To calculate $G^{(n+1)}_{n+1,n+1}$, we use equation (4.38) in the following way: the perturbed Green's function G^R is equal to the Green's function of the linked system. Before linking, the Green's function that relates any point at $x = n+1$ to any point at $x = n+1$ is $g^R(n+1,n+1)$. We have then $G^R_0 \equiv g^R(n+1,n+1)$. Then V links any point at $x = n+1$ to any point at $x = n$. We end up with the equation:

$$G^{(n+1)}_{n+1,n+1} = g^R(n+1,n+1) + g^R(n+1,n+1)V(n+1,n)G^{(n+1)}_{n,n+1}. \tag{4.42}$$

Similarly, we deduce from equation (4.38), the expression of $G^{(n+1)}_{n,n+1}$, as a function of $g^R(n+1,n+1)$ and Green's functions of the sample of n columns:

$$G^{(n+1)}_{n,n+1} = 0 + G^{(n)}_{n,n}V(n,n+1)G^{(n+1)}_{n+1,n+1}. \tag{4.43}$$

In the unperturbed system, columns n and $n+1$ are not connected, therefore G^R_0 is zero in the previous equation. Combining both equations, we find an expression for $G^{(n+1)}_{n+1,n+1}$ depending only on $g^R(n+1,n+1)$ and on the Green's functions defined in figure 4.3. In equation (4.44) we report the results for the four Green's functions needed:

$$\begin{aligned}
G^{(n+1)}_{n+1,n+1} &= \left(1 - g^R(n+1,n+1)V(n+1,n)G^{(n)}_{n,n}V(n,n+1)\right)^{-1} g^R(n+1,n+1), \\
G^{(n+1)}_{1,n+1} &= G^{(n)}_{1,n}V(n,n+1)G^{(n+1)}_{n+1,n+1}, \\
G^{(n+1)}_{n+1,1} &= \left(1 - G^{(n)}_{n,n}V(n,n+1)g^R(n+1,n+1)V(n+1,n)\right)^{-1} G^{(n)}_{n,1}, \\
G^{(n+1)}_{1,1} &= G^{(n)}_{1,1} + G^{(n)}_{1,n}V(n,n+1)G^{(n+1)}_{n+1,1},
\end{aligned} \tag{4.44}$$

We remark that this set of Green's functions is a closed set of operators, we do not need one more to perform the calculation at each step.

Justification of the recursive method.
This method is efficient as the time of calculation is *linear* with the longitudinal size of the system. The quasi one dimensional geometry allows the building of the sample column by column. The calculation time is not linear in the transverse size, which limits the extension of the sample in that direction.

4.4.3 The boundaries.

One issue that has not been discussed up to now, is the injection and the collection of electrons to measure a current and a potential difference. The leads that connect the diffusive sample are modeled as semi infinite metallic wires without disorder, so that no electron can come back in the diffusive sample: all electrons are perfectly absorbed by the electrodes. The Green's functions of such a system between two points at the interface of the semi infinite wire are known analytically:

$$G_{\text{lead}}(y_1, y_2) = -\frac{1}{t_{//}} \sum_{n=1}^{N_y} \chi_n(y_1) e^{\imath k_x x_0} \chi_n(y_2), \tag{4.45}$$

where x_0 is the position of the interface. According to figure 4.4, the initial step for the recursive method is given by the left electrode Green's function, and the terminal point is given by the right electrode Green's function.

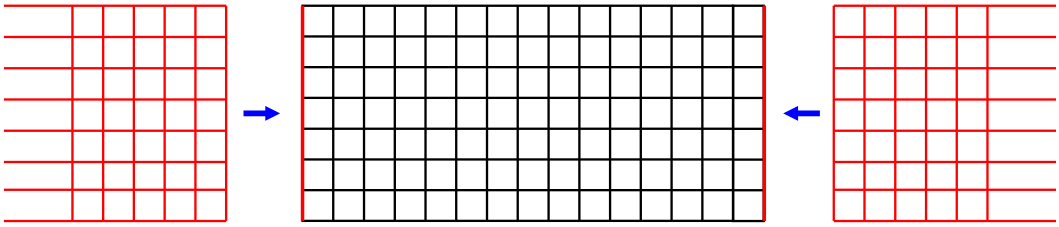

Figure 4.4: *Boundary conditions are given by the Green's functions of the electrode (two semi infinite metallic wires). The left electrode is the first step of the recursive method, and the right one is the terminal point of the method.*

To sum up the results of this chapter, for one given realization of scalar disorder and one given spin configuration for the impurities, we are able to calculate recursively the Green's functions of the spin glass, from the Fisher-Lee relation, equation (4.33), it is possible to deduce the scattering matrix of the system, and from the Landauer-Büttiker formula, equation (4.21), the two terminal conductance is derived.

4.4.4 Numerical tests

Basic tests can be performed to control numerical errors. After having calculated recursively the Green's functions, the scattering matrix can be computed numerically thanks to equation (4.33). The system has a physical meaning provided that this matrix is unitary (recall that this unitarity is a consequence of current conservation). The matrix

$$A = S^\dagger S \tag{4.46}$$

is computed, with the coefficients of the matrix A equal to:

$$a_{ij} = \sum_k s^*_{ki} s_{kj}. \tag{4.47}$$

If the S matrix is unitary, A must be the identity matrix. the first test is to calculate the trace of A and to compare it to the number of channels in the leads:

$$\text{testunit1} = \sum_i a_{ii} - N_y \tag{4.48}$$

The second test checks if there are non zero terms outside the diagonal:

$$\text{testunit2} = \sum_{i,j\neq i} a_{ij}. \tag{4.49}$$

The third test is very similar to the second one, it is:

$$\text{testunit3} = \sum_{i,j} a_{ij} - \text{testunit1}. \tag{4.50}$$

If these three tests are equal to zero, the scattering matrix is unitary, and the system is physical, the conductance is then calculated via equation (4.21). In practice the first test remains lower than 10^{-4} even for the largest sizes we considered.

Chapter 5
Universal properties of conduction in disordered media

In the previous chapter we presented the numerical method that is at the origin of this thesis. The next two chapters deal with the results we obtained in different conduction regimes. The goal of this part is to show that, depending on the length of the wire, there exists an insulating regime (Anderson localization) and a metallic regime for the conduction of electrons. The length that discriminates between both regimes is studied in detail, and universal properties (*i.e* that only depend on the symmetries of the problem) are extracted in both regimes. A particular focus is made on the conditions for obtaining the universal metallic regime, since it is the regime of interest for the next chapter and the only experimentally accessible regime. At the end of the chapter, the issue of the validity of the ergodic hypothesis (see section 3.2.1) is raised.

5.1 The Anderson localization in quasi one dimensional systems

5.1.1 What is Anderson localization?

In 1958 Anderson [111] proved that diffusion in random lattices can disappear due to the quantum interferences. For a three dimensional system, a transition between a metallic and an insulating regime appears when the strength of disorder is increased. For large disorder, electrons cannot escape the system, they are localized in a region of the solid: this is the Anderson localization. In an electronic transport point of view, Anderson localization is characterized by a vanishing conductance, as the electrons have difficulties to escape the solid. On the contrary, the conductance is large in the metallic regime. In the following more quantitative characterizations of the Anderson localized state will be highlighted. In 1979, Abrahams et al. [120] established a scaling theory of localization stating the absence of quantum diffusion in one and two dimensions. Their argument is presented briefly in the following.

They assume the existence of a *single parameter scaling* that describes the behavior of electronic transport when the typical size L of the system is modified. This single parameter is the dimensionless conductance $g(L)$[1]. In other words, they assume:

$$g(bL) = f(b, g(L)), \tag{5.1}$$

where b is a scaling factor. In continuous terms, it is practical to define a scaling function $\beta(g)$ by:

$$\beta(g) = \frac{\mathrm{d}\log g}{\mathrm{d}\log L}. \tag{5.2}$$

At large and small conductance, it is possible to deduce the asymptotics of that function from general arguments.

Large conductance

In that case, macroscopic transport can be used, the quantum effects are negligible (the effects of disorder are small). We use then the relationship between the conductance and the conductivity σ (because the conductivity does not depend on L), and for a sample of size L^d (where d is the dimension of the sample), we get $G(L) = \sigma L^{d-2}$. We deduce then:

$$\lim_{g\to\infty} \beta(g) = d - 2. \tag{5.3}$$

[1] we remind the reader that $g = G/G_0$, where G is the conductance of the system and G_0 the quantum of conductance defined in section 3.2.2.

Small conductance

In the limit of small conductance, all electronic states are predicted to be exponentially localized around the impurities, and therefore g falls off also exponentially (at least at zero temperature):

$$g = g_0 e^{-\alpha L}. \tag{5.4}$$

From this relation, we deduce the behavior of the scaling function in that regime:

$$\beta(g) = \log g - \log g_0 \tag{5.5}$$

at all dimensions.

The scaling function

From these limits, the authors sketched the universal curve $\beta(g)$ reproduced in figure 5.1, using continuity arguments. The flow of renormalization (by increasing at each step the size of the

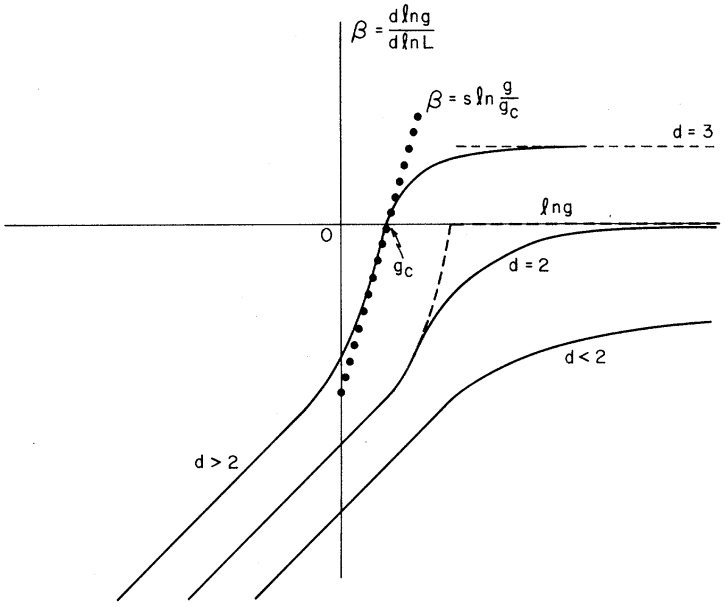

Figure 5.1: *Plot of the scaling function as a function of* $\log g$ *for one, two and three dimensional systems. The absence of fixed points for a finite value of conductance in one and two dimensions leads to the absence of metallic regime in the asymptotic limit. Extracted from [120].*

system) tends to $g(L_x \to \infty) = 0$ in one and two dimensions, as the sign of the β function indicates the increase or decrease of the conductance with the length of the system. The presence of a fixed point in three dimensions ensures the existence of a transition at $g = g_c$. Recently, the possibility to probe directly the properties of this localization with cold atoms [121, 122] has greatly renewed interest for this physics.

In the case of quasi one dimensional wires with a fixed amplitude of disorder, the conductance vanishes with increasing longitudinal length L_x. For short wires, the conductance can reach large

values as shown on figure 5.2. Changing the length of the sample allows the system to reach both metallic and insulating regimes of conduction. The goal of this chapter is to study these regimes and in particular the conditions to enter the diffusive metallic behavior, which is the relevant experimental regime of usual nanowires.

5.1.2 Universal and non universal regimes

As we have seen in chapter 3 (section 3.2.5), systems with longitudinal length L_x much larger than the magnetic length L_m are in GOE and systems of length much smaller than L_m are in GUE. Each of these ensembles defines a different universality class, as both ensembles are characterized by different symmetries. Experimentally speaking, real spin glass nanowires are generally neither in one class nor in the other, but in a non universal regime, which corresponds to the case of moderate values of magnetic disorder J or of a longitudinal length in between the two limits described above. In the following we will study both the universal and the non universal properties of transport in the insulating and metallic regimes of conduction.

5.2 Study of universal properties of the Anderson localized regime

5.2.1 The localization length

In a metallic nanowire with a given value of disorder, there exists a value of the longitudinal length for which the average conductance becomes smaller than one, as explained before. Figure 5.2 shows this behavior for a purely metallic wire and for a spin glass wire with different values of magnetic disorder J. This curve illustrates our point that the conductance of a wire vanishes

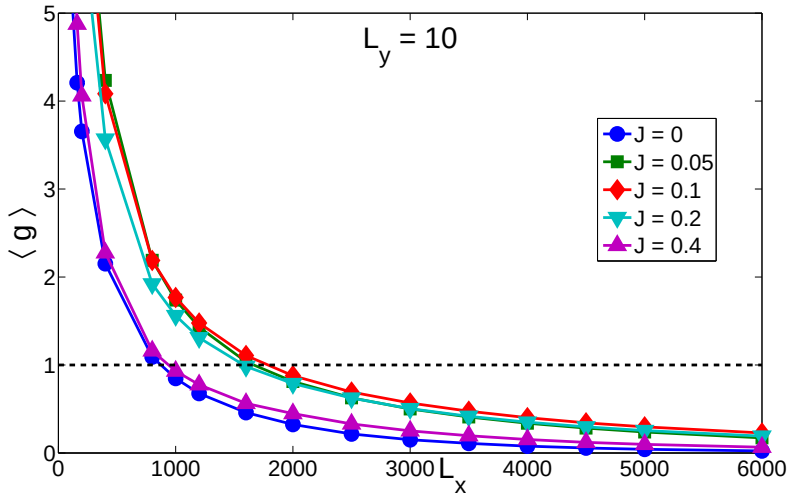

Figure 5.2: *Evolution of average conductance with longitudinal length L_x for different values of magnetic disorder. The line $\langle g \rangle = 1$ is shown, to emphasize that for large systems, the wire acquires vanishingly small values of conductance.*

with increasing length. As shown in section 5.1 in the regime of small conductance, exponential localization occurs which implies that the conductance is exponentially decreasing: equation (5.4). Using dimensional arguments, α^{-1} is the decaying length of the conductance. It is natural

to assume that this length is directly proportional to the so called *localization length* ξ which characterizes the cross-over between the metallic ($L_x < \xi$) and the localized ($L_x > \xi$) regimes. In this section, we present two methods to determine this length via transport properties.

The determination of ξ

First we consider the typical conductance of the system defined as:

$$g_{typ} = e^{\langle \log g \rangle}. \tag{5.6}$$

From the above discussion (see equation (5.4)), we expect the following scaling behavior:

$$g_{typ} \sim e^{-\frac{2L_x}{\xi}} \qquad \text{for} \qquad L_x \gg \xi \tag{5.7}$$

Knowing equation (5.7) we plot the average value of the logarithm of the conductance as a function of the longitudinal length of the sample. This is shown in figures 5.3, 5.4 and 5.5, for different values of magnetic disorder. These curves show that for very small longitudinal lengths

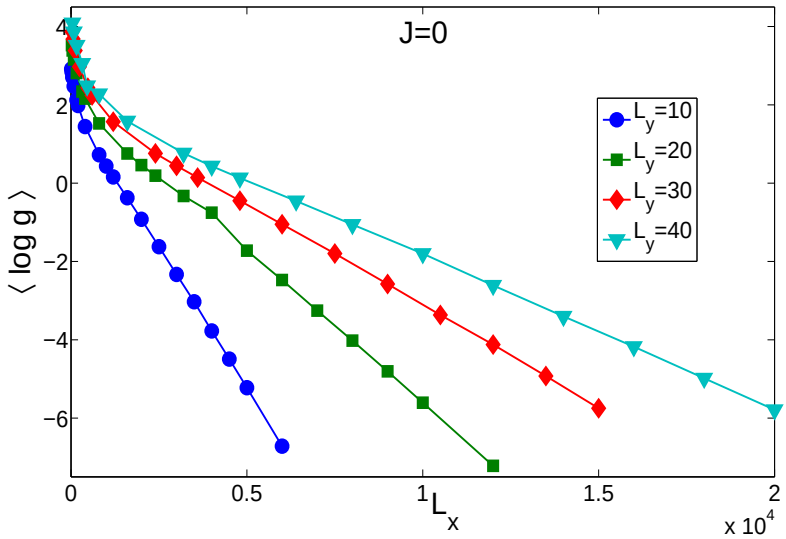

Figure 5.3: *Evolution of* $\langle \log g \rangle = \log g_{typ}$ *as a function of longitudinal size for different transverse lengths. The amplitude of magnetic disorder is* $J = 0$*. The linear part of the curve allows one to get the localization length from the scaling form in the insulating regime* $\langle \log g \rangle = -\frac{2Lx}{\xi}$.

$\langle \log g \rangle$ is not proportional to L_x. For large values of the longitudinal length, $\langle \log g \rangle$ is directly proportional to L_x as expected and a basic fit of this linear part of the curve gives access to the localization length. Notice well that the linear part in all these curves is clearly identified, so the evaluation of ξ is straightforward. This method allows to determine the localization length for each value of L_y and J we consider.

Another way to extract the localization length from the conductance consists in studying the Lyapunov exponent γ of the transfer matrix of the system. In the scaling theory of localization (RMT), a Lyapunov exponent can be defined related to the product of transfer matrices [123, 124, 125, 101] (see section 3.2.5 for the definition of the transfer matrix). Consider the transfer matrix Θ of the entire wire. It is a product of random matrices (each of size $2N \times 2N$) as:

$$\Theta = \prod_{a=1}^{n} T_a. \tag{5.8}$$

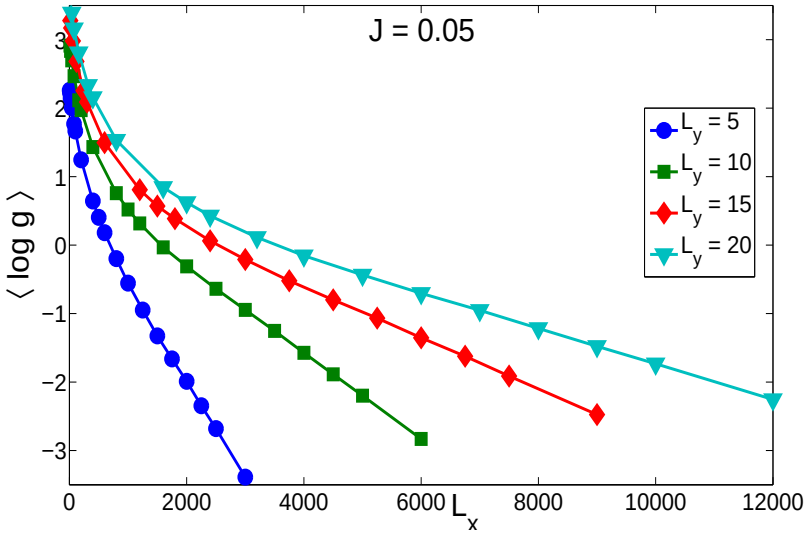

Figure 5.4: *Evolution of* $\langle \log g \rangle$ *as a function of longitudinal size for different transverse lengths and* $J = 0.05$*. The linear part of the curve allows one to get the localization length from the scaling form in the insulating regime* $\langle \log g \rangle = -\frac{2L_x}{\xi}$.

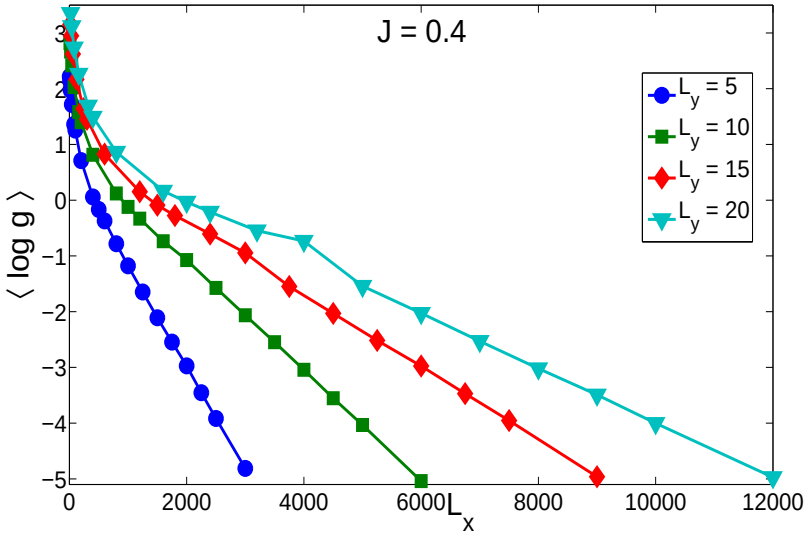

Figure 5.5: *Evolution of* $\langle \log g \rangle$ *as a function of longitudinal size for different transverse lengths and* $J = 0.4$*. The linear part of the curve allows one to get the localization length from the scaling form in the insulating regime* $\langle \log g \rangle = -\frac{2L_x}{\xi}$.

In the limit of large wires ($n \to \infty$), the $2N$ random eigenvalues $e^{\pm 2x_i}$ of $\Theta\Theta^\dagger$ tend to the non-random values $e^{\pm 2\gamma_i L_x}$, with γ_i independent of L_x [101]. The largest Lyapunov exponent is equal to this inverse of the localization length.

Following [126, 116] it is a function of the conductance:

$$\gamma(L_x) = \frac{1}{2L_x} \log\left(1 + \frac{1}{g(L_x)}\right) \underset{L_x \to \infty}{\longrightarrow} \frac{1}{\xi}. \tag{5.9}$$

On figure 5.6 and 5.7 we have plotted the Lyapunov exponent versus the inverse of the longitudinal length for different values of magnetic disorder. Different curves correspond to different widths of the wire. The advantage of this method is that there is no need of any numerical fitting

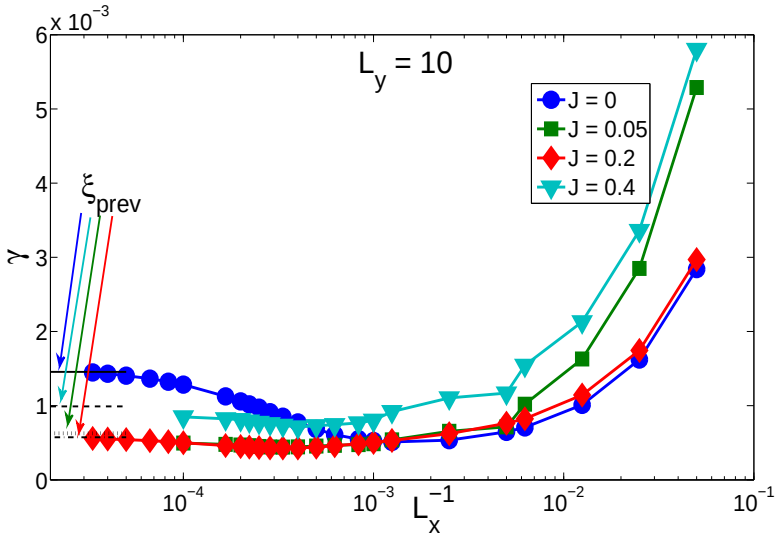

Figure 5.6: *Evolution of Lyapunov exponent with the inverse of longitudinal length in semi-log plot. Circles correspond to $J = 0$, squares to $J = 0.05$, diamonds to $J = 0.2$ and triangles to $J = 0.4$. The value of the transverse length is 10. The localization length can be extrapolated from the value of γ for $L_x \to \infty$. The denomination ξ_{prev} is the value of the localization length determined previously using the typical conductance. The different values correspond to the different values of magnetic disorder in consideration.*

procedure, only an extrapolation is necessary to get the value of the inverse of the localization length for an infinite wire. Nevertheless, this method has less accuracy than the previous one (with the use of the typical conductance) as on many plots of figures 5.6 or 5.7, the Lyapunov exponent is still significantly varying with the longitudinal length. To reduce the error, very long wires are needed[2], which is limited by calculation time. Both methods give finally comparable results but the accuracy on the localization length is better with the first method using the typical conductance, as for all geometries and all values of magnetic disorder a linear behavior of the average of the logarithm of conductance has settled. On all these curves one obviously notice that the localization length depends on both the magnetic disorder J and the width of the sample. The next section deals with the study of the behavior of ξ as a function L_y, plotted for different values of magnetic disorder.

The evolution of ξ with the width of the wire

Qualitatively the localization length is a growing function of the width of the wire as the entrance in the insulating regime corresponds to the progressive closure of all propagating modes whose

[2]compare for instance figure 5.6 and 5.7: in the first one, the maximum aspect ratio is 3 000, whereas it is only 600 in the second one.

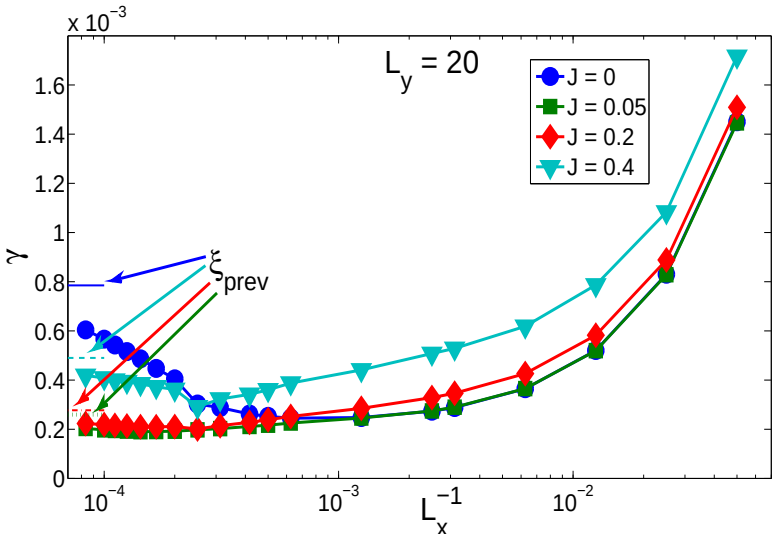

Figure 5.7: *Evolution of Lyapunov exponent with the inverse of longitudinal length in semi-log plot. Circles correspond to $J = 0$, squares to $J = 0.05$, diamonds to $J = 0.2$ and triangles to $J = 0.4$. The value of the transverse length is 20. The localization length can be extrapolated from the value of γ for $L_x \to \infty$. The denomination ξ_{prev} is the value of the localization length determined previously using the typical conductance. The different values correspond to the different values of magnetic disorder in consideration.*

number is directly proportional to the width of the sample. Quantitatively, the evolution of $\xi(L_y)$ is expected to follow [101, 127]:

$$\xi = (\beta L_y + 2 - \beta) l_e. \tag{5.10}$$

l_e is the mean free path and β is the symmetry index. $\beta = 1$ corresponds to the Gaussian Orthogonal Ensemble universality class GOE while $\beta = 2$ for the Gaussian Unitary Ensemble GUE. Note that this change in β is accompanied by an artificial doubling of the number of propagating modes as a consequence of the breaking of Kramers degeneracy [101] and the modification of the definition of the quantum of conductance (equation (3.13)). In GUE, the quantum of conductance is then twice smaller than in GOE. Comparison of numerical localization lengths for different J with (5.10) is shown in fig 5.8. In this curve, the elastic mean free path is determined for $J = 0$ by fitting the numerical data with the previous expression for the localization length. In units of lattice spacing, this length is found equal to 60. For $J \neq 0$, we deduce the value of the elastic mean free path using the ratio: $l_e(J)/l_e(0)$, which is found to be equal to the ratio of $\sigma_0(J)/\sigma_0(0)$ (see section 5.3.2) using the Matthiesen rule. For the largest values ($J = 0.2$ and $J = 0.4$) of magnetic disorder, a comparison between the value found by this method and a fit using equation (5.10) gives very close results.

Excellent agreement is found for $J = 0$ (GOE class, $\beta = 1$). In the case $J \neq 0$ we observe a crossover between GOE and GUE for intermediate values of magnetic disorder, while a good agreement with the GUE class is reached for $J \geq 0.2$. The intermediate values of J are not compatible with the linear behavior (5.10) (see in particular the curve for J = 0.05). This signals a non-universal behavior of localization properties for intermediate magnetic disorder.

From these results, we already notice that the localization regime is reached for much longer wires in the GUE case than for GOE. As shown below, this allows for an easier numerical

investigation of the universal metallic regime in the GUE case: magnetic impurities help in finding the universal conductance fluctuations!

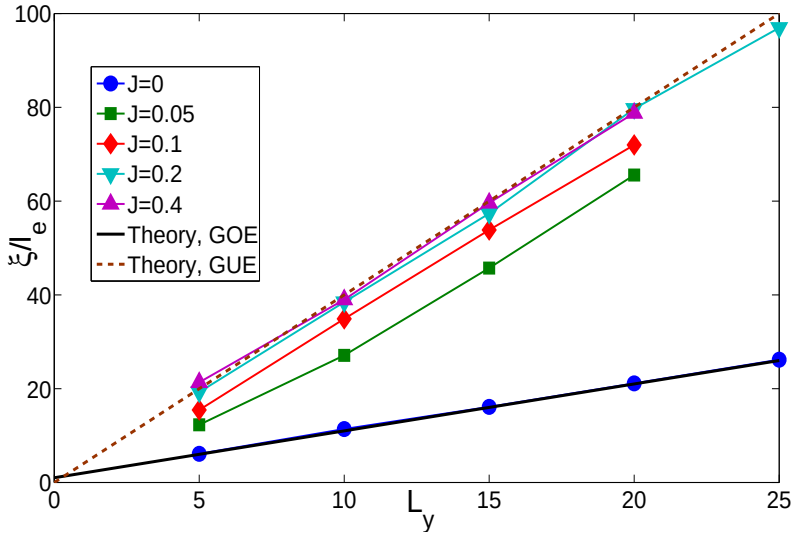

Figure 5.8: *Evolution of localization length as a function of transverse length. l_e is the mean free path of the diffusive sample. Different behavior of the localization length if $J = 0$ (GOE) or $J \neq 0$ (GUE).*

Notice that for intermediate values of the magnetic disorder (for instance consider the case $J = 0.05$ of figure 5.8) the behavior of the localization length with the transverse length of the system is incompatible with the linear universal law. This regime of intermediate magnetic disorder amplitudes is the relevant experimental case. Up to my knowledge, this non universal behavior is not yet understood analytically. This regime is presently under investigation: the determination of the localization length for smaller values of the transverse length L_y and for smaller values of magnetic disorder J allows to conclude that for small L_y and $J \approx 0$, ξ follows the $J = 0$ universal law, and that the slope of the linear behavior changes to the GUE case when L_y is increased. For moderate values of J (squares, diamonds), the law at large L_y seems to have the right slope but a different y-intercept. The accurate characterization of the localization length in both universal regimes opens the route for a study of the insulating regime on the one hand and of the metallic regime on the other hand. The next section deals with the study of universal properties in the localized regime.

5.2.2 Statistical distribution of conductance

A preliminary result

In the previous section we plotted the average conductance as a function of longitudinal size (see figure 5.2) to characterize the cross-over between the metallic and the insulating regimes. Consider now the whole statistical distribution of conductance to study the change of the shape of this distribution, while the length of the wire is increased. This is plotted in figure 5.9. From

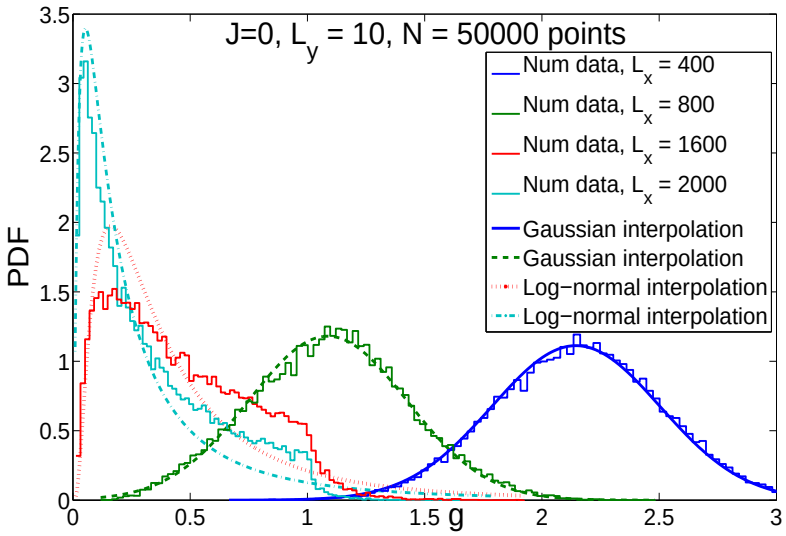

Figure 5.9: *Evolution of the statistical distribution of the conductance for different longitudinal sizes. $L_y = 10$ and $J = 0$. Plain lines are gaussian (if $g_{typ} > 1$) or log-normal (if $g_{typ} < 1$) interpolations of numerical data. PDF stands for Probability Density Function. $N = 50\,000$ is the number of configurations of disorder used to plot the statistical distributions.*

this curve one can make a preliminary conclusion: in the metallic regime the Probability Density Function (PDF) of the conductance is almost Gaussian as expected [128, 129], whereas it tends to a Log-normal distribution but only in the deep insulating regime ($L_x \gg \xi$). The Log-normal shape [129, 130] in the insulating regime has also been predicted. See [101] for a review. The convergence toward a Gaussian PDF is fast as soon as the system enters the metallic regime whereas the convergence is "slow" [3] to obtain a Log-normal distribution in the localized regime [129]. The other striking behavior illustrated on this curve is the appearance of a non-analytic point at $g = 1$ as soon as the system enters the localized regime, which is in agreement with [130, 131, 132, 133]. The next sub section studies this non analyticity.

Non-analyticity at $g = 1$ in the localized regime

To do so, we plot the PDF of conductance in the so called intermediate regime ($\langle g \rangle \lesssim 1$). The result is shown on figures 5.10 and 5.11. In the regime where $\langle g \rangle$ is very close to one, figure 5.11 shows that as soon as the system enters the metallic regime, the Gaussian shape for the PDF settles. For $\langle g \rangle = 0.995$ the PDF is no longer gaussian but the tail in the metallic regime ($g > 1$) is well approximated by a gaussian curve. This behavior shows that as soon as the system enters the localized regime, the statistical distribution of the conductance becomes non symmetric. If

[3] for a ratio $L_x/\xi \approx 2.5$, the difference between numerical data and a Log-normal interpolation is still perceptible

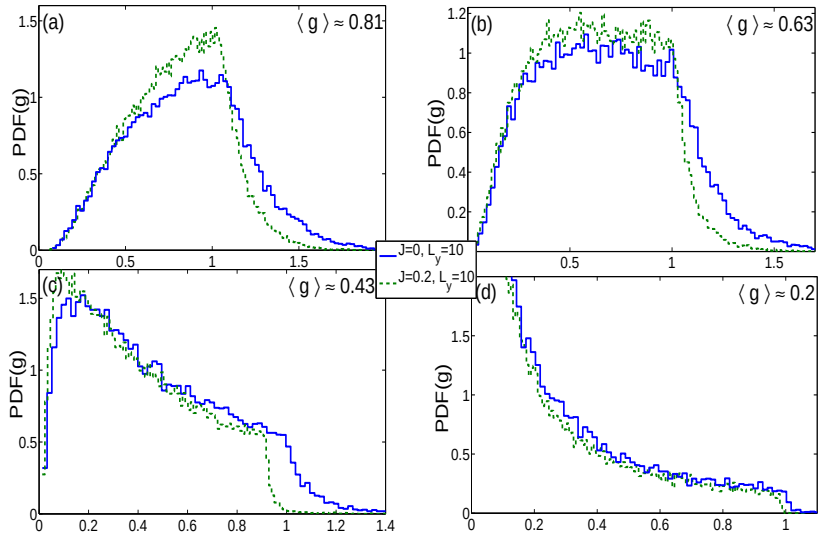

Figure 5.10: *Comparison of Probability density functions (PDF) of conductance for* $J = 0$ *(plain curves) and* $J = 0.2$ *(dashed curves). Plots are performed for different values of average conductance. (a):* $\langle g \rangle (J = 0) = 0.84$ *and* $\langle g \rangle (J = 0.2) = 0.79$. *(b):* $\langle g \rangle (J = 0) = 0.67$ *and* $\langle g \rangle (J = 0.2) = 0.62$. *(c):* $\langle g \rangle (J = 0) = 0.45$ *and* $\langle g \rangle (J = 0.2) = 0.42$. *(d):* $\langle g \rangle (J = 0) = 0.21$ *and* $\langle g \rangle (J = 0.2) = 0.18$.

the longitudinal length is increased figure 5.10 shows the appearance of a clear non analyticity that seems to develop around $g = 1$, that is to say at the entrance of the localized regime. One still open question is the way (sudden or smooth) this non analyticity appears when the system reaches the localized regime (*i.e* when its longitudinal length becomes greater than ξ). To try to answer this question, one possible way is to use the Cumulative Distribution Function (CDF) as plotted in figure 5.12, to fit it with polynomial functions on each side of the non analyticity and to derive each fit, to have access to the slope of the derivative of the PDF. Figure 5.12 is a preliminary result and further analysis is required to have a quantitative understanding of the phenomenon.

A second study consists in analyzing the influence of the symmetries and of the value of $\langle g \rangle$ on the non-analyticity. For similar values of $\langle g \rangle$ we compare the PDF of conductance in GUE ($J \neq 0$) and in GOE ($J = 0$). The results are plotted in figure 5.10. The shapes of these distributions are highly similar if $\langle g \rangle \ll 1$, showing that distributions for $J = 0$ and $J \neq 0$ tend to become Log-normal with the same cumulants. In the intermediate regime ($\langle g \rangle \approx 1$), shapes are symmetry dependent. Moreover the non-analyticity appears for different values of conductance (close to 1) and the rate of the exponential decay [130] in the metallic regime seems to differ from one ensemble to the other (see for instance curves (a) or (b)). One can then state that in the deep insulating regime statistical distributions for the same geometry but for vanishing or not magnetic disorder seem to collapse in one single curve, giving rise to super-universality, as described in [134], as opposed to the metallic regime.

After having concentrated on statistical distributions, we continue with the study of second and third cumulants of the logarithm of conductance to study the convergence of the conductance distribution towards a Log-normal. We also extract a remarkable scaling called the one parameter scaling: all cumulants of the distribution of $\log g$ are proportional to one single parameter [120, 135]. Strong evidence [136, 129] have been found to show that in the thermodynamic limit

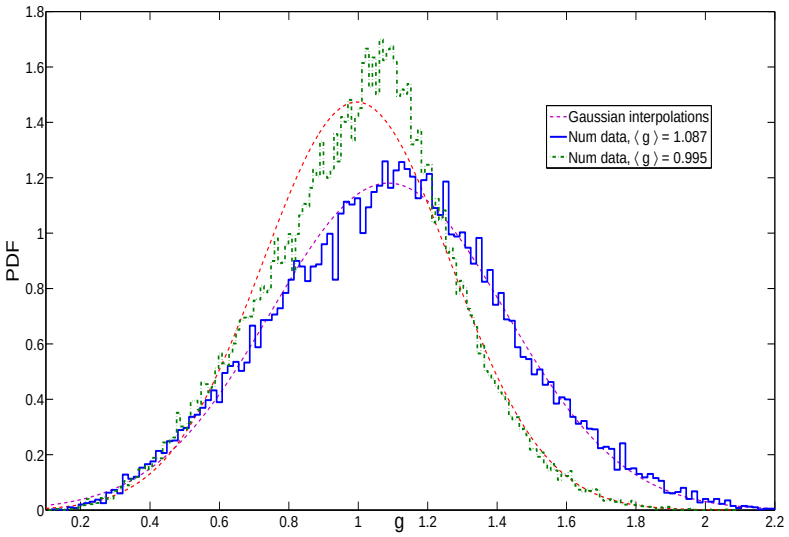

Figure 5.11: *PDF of conductance for* $\langle g \rangle < 1 (J = 0.2)$ *and* $\langle g \rangle > 1 (J = 0)$ *and Gaussian interpolations.* $L_y = 10$.

$(L_x \to \infty)$, the distribution of $\log g$ has a Gaussian shape. However, for a finite value of L_x, non-universal and non Gaussian tails are found.

The study of cumulants

As we have already plotted the evolution of the average logarithm of the conductance as a function of L_x (see for instance figure 5.5), we will now plot higher order cumulants as a function of the first one. On figure 5.13 or 5.14 we show the evolution of the second cumulant of $\log g$ versus $\langle \log g \rangle$. On figure 5.13, the plots for two different values of magnetic disorder ($J = 0$ and $J = 0.2$) and $L_y = 10$ show the same linear behavior of the variance of $\log g$ as a function of the average. One of the key points of this curve is the one parameter scaling that is verified for this cumulant in the deep insulating regime, as the second cumulant is proportional to the first one.

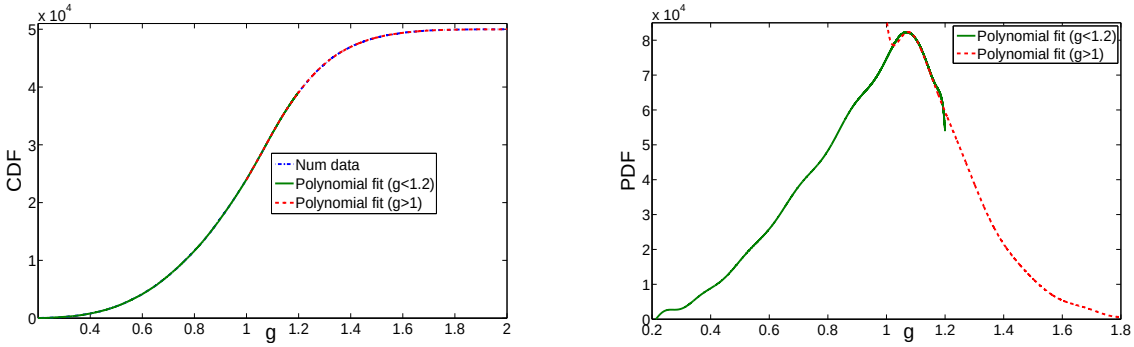

Figure 5.12: *Right: PDF of conductance for* $\langle g \rangle < 1 (J = 0.2)$ *and* $L_y = 10$. *Left: Cumulative Distribution Function (CDF) of the numerical results (50000 configurations of disorder were used for this study).*

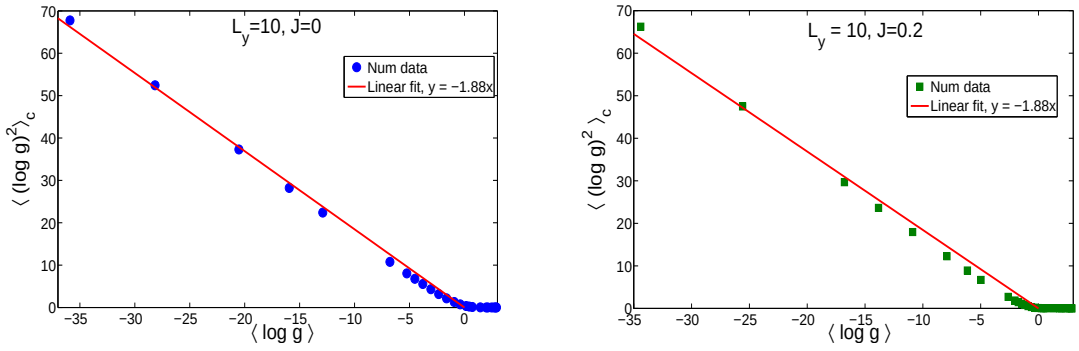

Figure 5.13: *Plot of the variance of* $\log g$ *as a function of the mean for* $J = 0$ *(left curve) and* $J = 0.2$ *(right curve). The slope of the linear fit is equal to* -1.88 *in both cases.*

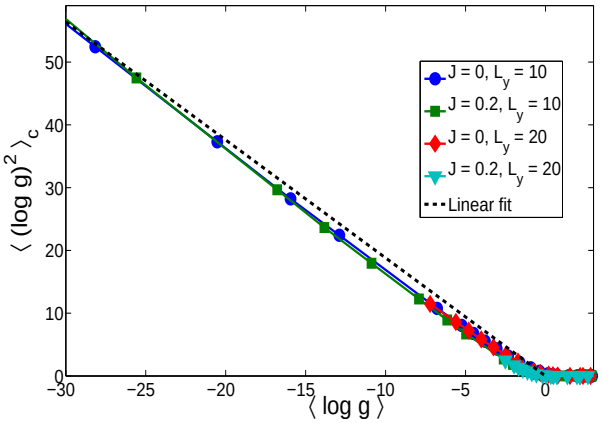

Figure 5.14: *Plot of the variance of* $\log g$ *as a function of the mean for the orthogonal and unitary case. The slope of the linear fit is equal to* -1.88*. This plot shows also super-universality as the behavior of the second cumulant does not depend neither on geometry of the wire nor on the universality class.*

The coefficient of proportionality is found via a fit of the linear part of the curve and gives a value that is very close to -1.88. Analytically, the second cumulant is expected to follow[137, 127]:

$$\langle (\log g - \langle \log g \rangle)^2 \rangle = \langle (\log g)^2 \rangle_c = -2 \langle \log g \rangle. \tag{5.11}$$

On these curves, the fit was a pure linear function (*i.e* of the form $x \to \alpha x$, with α a free parameter). Our numerical result shows a small discrepancy with that theoretical study (based on RMT). Notice that a fit of the linear parts of the curves of figure 5.13, with a function of the form $x \to \alpha x + \beta$, with α and β free, gives a result for α that is very close to 2, but with a non vanishing β, which is not in agreement with [127].

Another crucial result shown in these plots and more accurately in figure 5.14 is the confirmation of the super-universal behavior, as the second cumulant for both universality classes ($J = 0$ and $J \neq 0$) behaves in the same manner in the deep insulating regime.

Finally in figure 5.15, we show the third cumulant of $\log g$ as a function of the first one. The linear behavior for each value of magnetic disorder in the deep insulating regime ($\langle \log g \rangle < -5$) is in agreement with the single parameter scaling. We find that contrary to the second cumulant the coefficient of proportionality between the skewness and the average depends on the symmetry

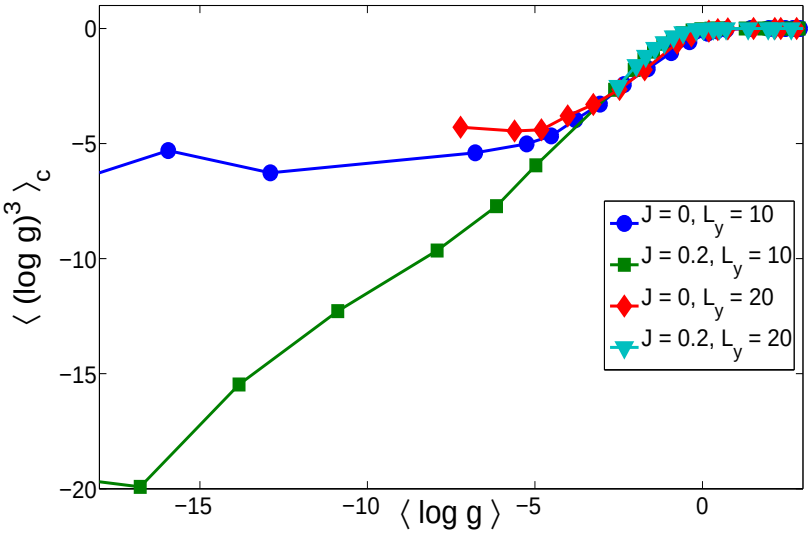

Figure 5.15: *Plot of the skewness of* $\log g$ *as a function of the mean for the orthogonal and unitary case.*

of disorder, which denotes a lack of super-universality concerning this cumulant. For instance dots and diamonds (which correspond to the case $J = 0$) have the same behavior, but it is not the case compared to squares or triangles ($J = 0.2$). We remark the strange behavior of the third cumulant for $J = 0.2$ and $L_y = 10$, which seems to be in contradiction with a Log-normal statistical distribution. To clear up this point a further analysis, that is currently performed, is needed. For instance, more statistics are needed to study the third cumulant in detail (see also the discussion on the third cumulant in the metallic regime).

The study of cumulants of the distribution of $\log g$ confirm the single parameter scaling of the distribution, with a slight discrepancy concerning the value of the coefficient of proportionality between second and first cumulant. Moreover, super-universality has been highlighted concerning the second cumulant but is not confirmed by the study of the third cumulant. Nevertheless, the curve (d) of figure 5.10 indicates that the total distribution possesses this super-universality as the influence of the third cumulant on the curve is moderate (it tends to zero in the deep insulating regime as the distribution becomes Log-normal).

5.3 The Universal metallic regime

We now focus on the universal metallic regime described by weak localization. By definition weak localization corresponds to metallic diffusion, expected for lengths of wire $l_e \ll L_x \ll \xi$. For this regime to be reached, we thus need to increase the number of transverse modes L_y and thus ξ for all other parameters fixed (see (5.10)). Moreover, for a fixed geometry, this regime will be easier to reach in the GUE class than in the GOE. The preceding study describes with precision the entrance in the localized regime. As we saw it in section 4, Fig. 5.10, the shape of the PDF of conductance is almost gaussian. In the following we will study the different cumulants of the conductance.

5.3.1 Universal Conductance Fluctuations (UCF): obtaining L_m

At first the study of the second cumulant (the variance) of the distribution of conductance is performed as it has a purely quantum origin: at the classical level, the conductance does not show any fluctuation (se Appendix A, section A.1). It allows a determination of the magnetic dephasing length L_m. Moreover we exhibit a universal regime where the fluctuations do not depend on geometry any more.

Fluctuations of conductance: analytical reminder

In the metallic regime, it is possible to find an expression for the fluctuations of conductance in the presence of magnetic impurities as a function of the longitudinal length, see [86, 138] and section 3.2.3. The expression is recalled hereafter:

$$\begin{aligned}\langle \delta g^2 \rangle = \langle g^2 \rangle_c &= \frac{1}{4} F_2(0) + \frac{3}{4} F_2\left(x\sqrt{\frac{4}{3}}\right) \\ &+ \frac{1}{4} F_2\left(x\sqrt{2}\right) + \frac{1}{4} F_2\left(x\sqrt{\frac{2}{3}}\right),\end{aligned}$$

where $x = L_x/L_m$ and the scaling function $F_2(x)$ is given by [86, 139] and equation (3.25). See section 3.2.3 for a few details on the calculation of these fluctuations, and the expression of this function and figure 3.14 for a plot. We conclude that $\langle g^2 \rangle_c \to \frac{1}{4} F_2(0) = \frac{1}{15}$ when $x \to \infty$. In this regime the fluctuations of conductance are constant. A similar study in the case of non-magnetic impurities (GOE) exhibits also a universal regime with $\langle g^2 \rangle_c = \frac{2}{15}$. Due to our convention (the spin degeneracy s is included in the definition of the quantum of conductance), it corresponds to $\langle G^2 \rangle_c = \frac{8}{15}\left(\frac{e^2}{h}\right)^2$. These values, known as the Universal Conductance Fluctuations (UCF) are in full agreement with equation (3.15).

The Universal regimes

In figure 5.2, we have calibrated the direct correspondence between the average conductance and the longitudinal length. As in the localized regime, we will then plot the cumulants of g as a function of the first one, as shown in figure 5.16 for the variance. This plot shows that for a suitable value of transverse length L_y, the system reaches a plateau in conductance fluctuations whose value depends on the symmetry of the system, in agreement with previous analytical results. Notice that the presence of the plateau depends strongly on the value of the transverse length L_y: for instance refer to the $J = 0$ curves (plain dots, squares and diamonds) of figure 5.16. It is easily understood as the localization length is a growing function of L_y: if L_y is too small, the inequality $l_e \ll L_x \ll \xi$ is never satisfied and the system enters the localized regime before reaching the Universal regime. In the same way, equation (5.10) and figure 5.8 show that for a given value of transverse length L_y, the localization length is greater for GUE than for GOE, which explains why the universal regime is more easily reached in presence of magnetic impurities. Figures 5.17 and 5.18 show that specific point more clearly. In these plots we show conductance fluctuations as a function of longitudinal size L_x for $J = 0$ and $J = 0.2$ and for two values of transverse length L_y. On the first plot, for both values of magnetic disorder the universal plateau arises, whereas it does not appear for non magnetic impurities ($J = 0$) if $L_y = 40$. In our study, values of UCF are reached with a maximal error of 1% for GOE and 3% for GUE with respect to the analytical value of the UCF in the regime independent of $\langle g \rangle$ (*i.e* with much higher precision than *e.g* [131] or [140]). In the first article the authors using the transfer matrix

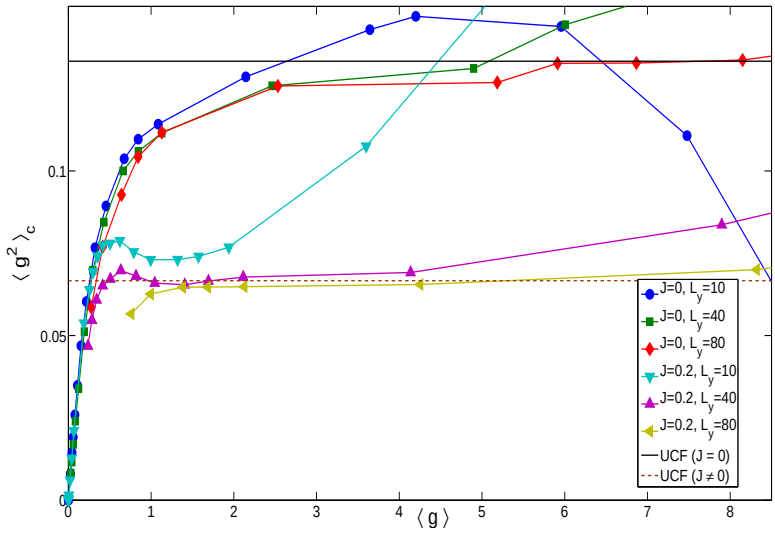

Figure 5.16: *Plot of the variance of g as a function of the mean for the orthogonal and unitary cases, for different width of the wire and different values of magnetic disorder. The Universal Value of the fluctuations of conductance is plotted for GOE (plain line) and for GUE (dotted line).*

and RMT found that their value of Universal Conductance Fluctuations in a Spin Glass is given with an error of almost 20% compared to the analytical value. Notice that this numerical study is done in two dimension and not in quasi one dimensional wires. In the second article, using a two-dimensional binding system coupled to a three dimensional Edwards-Anderson Ising spin glass, UCF in GOE are found with an error of approximately 10% with the quasi 1d scheduled value. In all cases the error is calculated exactly in the same way, and is just the relative distance between the obtained and the analytical values of UCF. To our knowledge it consists in the most accurate numerical determination of the UCF. In many studies, plots showing two or three points around the analytical plateau are called UCF. In the previous paragraphs we prove that it is not so easy to reach them, because of ξ.

Our numerical study accounts well for the universal regimes where fluctuations of conductance are independent of the length L_x of the wire. According to the section 5.1.3, the experimental regime of interest is the one for which the length of the wire is of order of the magnetic length. In this non-universal regime, the fluctuations of conductance will necessary depend on the length of the wire as $\langle g^2 \rangle_c = 2/15$ if $L_x \ll L_m$ and $\langle g^2 \rangle_c = 1/15$ if $L_x \gg L_m$. The question that immediately arises is the following: are we able to characterize numerically this non universal dependence? At this point we remind the reader that the answer to this question in the localized regime concerning the non universal dependence of the localization length with the width of the wire was negative.

Fit of the fluctuations of conductance

In figure 5.19, the fluctuations of conductance are plotted as a function of longitudinal length. The numerical data are fitted with equation (3.24), as the only free parameter is the magnetic length. From each fit, one extracts $L_m(J)$. One also notices from equation (3.24) the scaling form of the fluctuations of conductance. It then appears natural to plot the variance of conductance as

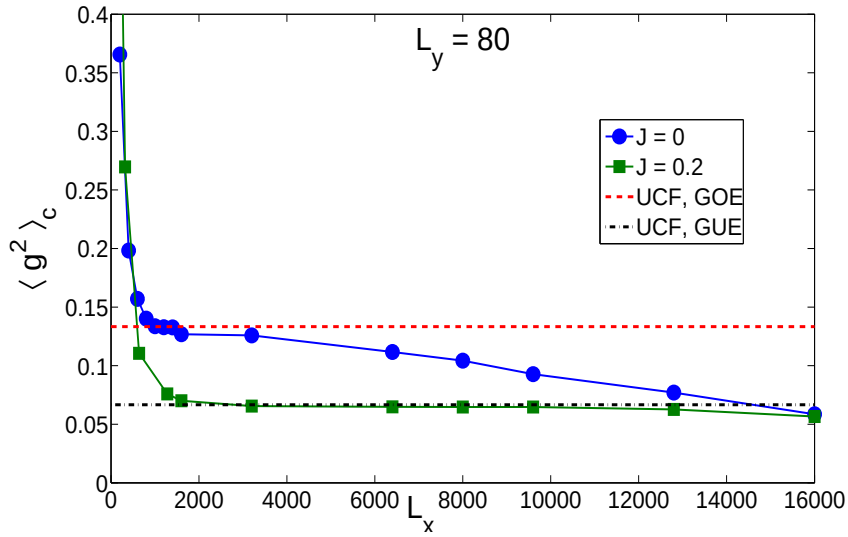

Figure 5.17: *Second cumulant of g as a function of longitudinal length. Dots represent data for $J = 0$ and squares for $J = 0.2$. The value of UCF is shown in each symmetry class (with or without magnetic disorder). UCF regime is reached in both cases.*

a function of $L_x/L_m(J)$, as shown in figure 5.20. The agreement between theory and numerical calculations is good. The difference between theory and numerics for small longitudinal lengths in figures 5.19 and 5.20 lies in the fact that the analytical formulae are valid in the limit of quasi one dimensional systems, which may not be reached for $L_x \approx 400$ and $L_y = 40$.

This study of the variance of the conductance in the metallic regime allows to determine accurately the universal regime (for which the fluctuations are constant) and the non universal one dimensional diffusive regime, which is the regime of experimental interest. This regime will be used in the next chapter to study correlations of conductance. Before that, there remains some uncertainty concerning the magnetic length L_m: how can we compare it to theoretical expression? To answer this question, we go on to the study of the other cumulants of the conductance and first we focus on the mean value.

5.3.2 The average conductance: determination of $L_m(J)$

Coming back to chapter 3, the probability of diffusion from $\vec{r}_1$ to $\vec{r}_2$ during time t has a classical and a quantum term, which leads to a quantum and a classical part for the average conductance. Up to now, we have performed extensive studies of the quantum contribution to the variance. We have shown in particular that its behavior is based on the new diffusion length: L_m. For a quasi one dimensional wire, it is possible to derive the quantum corrections for the conductance, see [86, 141] and Appendix A, section A.3:

$$\delta g_{WL} = \sum_{n=1}^{\infty} \left(\frac{-1/\pi^2}{n^2 + 2\left(\frac{L_x}{L_m}\right)^2} - \frac{3/\pi^2}{n^2 + \frac{2}{3}\left(\frac{L_x}{L_m}\right)^2} \right). \tag{5.12}$$

We now study the classical part of the conductance, defined as:

$$g_{\text{class}} = \langle g \rangle - \delta g_{\text{WL}}. \tag{5.13}$$

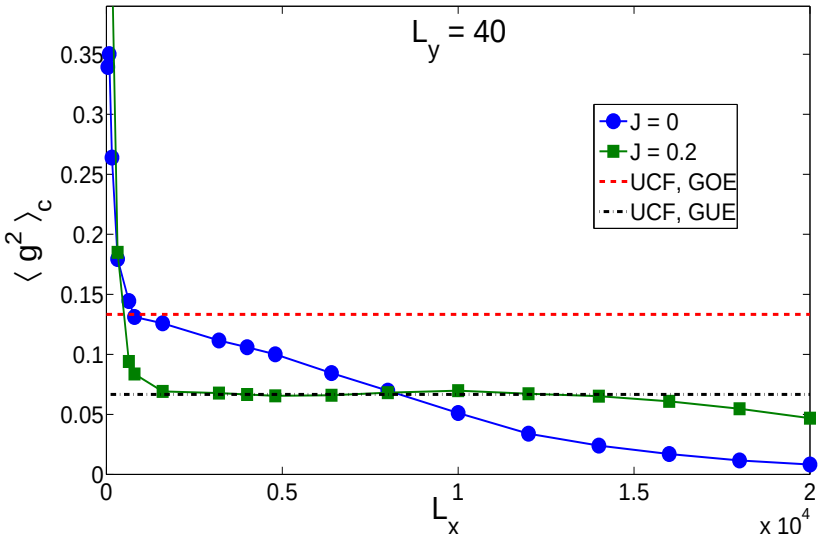

Figure 5.18: *Second cumulant of g as a function of longitudinal length. Dots represent data for $J = 0$ and squares for $J = 0.2$. The value of UCF is shown in each symmetry class (with or without magnetic disorder. UCF regime is reached in the case of magnetic impurities but not for scalar impurities.*

This classical conductance depends on J and L_x and not on L_m as this length is related to quantum transport (the weak localization term δg_{WL}).

The classical conductance, function of the longitudinal length

Classically, the evolution of conductance with the longitudinal length for a one dimensional system is of the form:

$$g(L) = \frac{\sigma}{L}, \tag{5.14}$$

where σ is called the conductivity. On figure 5.21 we plot the classical conductance as a function of L_x and from a single parameter fit using equation (5.14) one can determine the conductivity for each value of magnetic disorder. One easily sees that the agreement between theory and numerical calculations is not very good.

The development of mesoscopic physics and of conductance measurements raised this previous problem: the measurement of a ballistic resistance with two leads does not vanish. Every physicist has already measured the resistance of an electronic compound. To do so, the current that goes through the corresponding device is measured by plugging an ammeter[4] inside the circuit. The potential difference is measured by using a voltmeter in parallel. This suggests that a good measure of resistance requires four terminals. In the present study of coherent transport in a spin glass, only two terminals are considered. One then needs to add a contact resistance [142]. This new resistance comes from the use of only two terminals to measure both the current and the voltage. Adding this contact resistance[5] has the following effect on the relation between the conductance and the conductivity:

$$g_{class}(J, L_x) = \frac{1}{\frac{1}{L_y} + \frac{L_x}{L_y \sigma_0(J)}}. \tag{5.15}$$

[4] or a galvanometer.
[5] also called the Sharvin resistance.

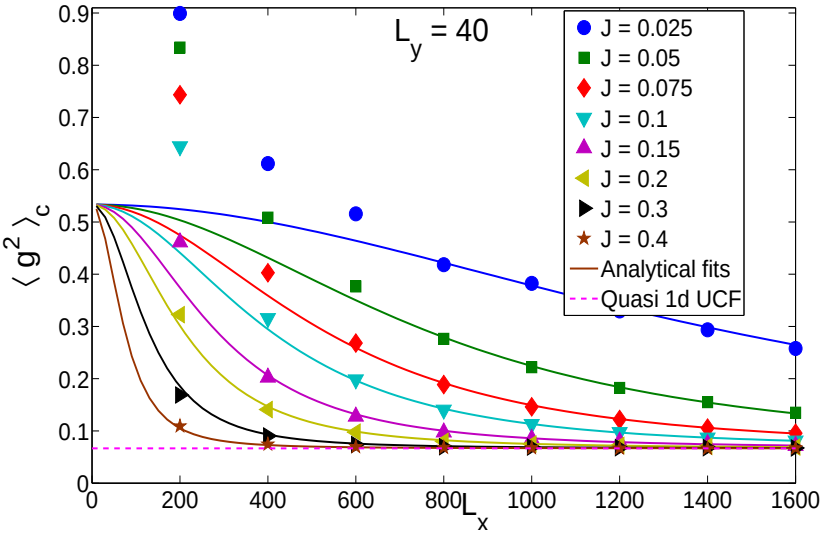

Figure 5.19: *Plot of the variance of the conductance as a function of longitudinal length for $L_y = 40$ and different values of magnetic disorder. Plain lines are analytical fits from equation (3.24). The value of L_m for each value of J is then extracted. The dotted line represents the universal value of fluctuations of conductance in GUE.*

Using this new expression for the conductance it is possible to fit again the numerical data. The results are shown in figure 5.22. The agreement is now very good, and the conductivity can be extracted with no difficulty.

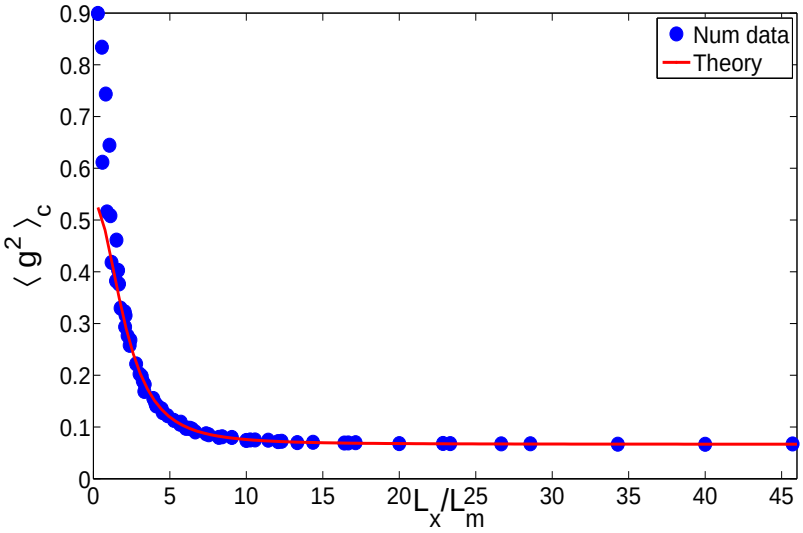

Figure 5.20: *Plot of the variance of the conductance as a function of the scaling variable $x = L_x/L_m$ for $L_y = 40$ and different values of magnetic disorder. All numerical points of figure 5.19 collapse on one scaling curve given by equation (3.24).*

Important:
it is essential to understand that the two terminal behavior lies in the equation we used to link the transmission probabilities $T_{m\leftarrow n}$ and the conductance. We found (see section 4.2)

$$g = \sum_{m,n} T_{m\leftarrow n}. \tag{5.16}$$

Consider the case of a perfect metal (with no impurity). We envisage that the conductance diverges as the occurrence of a non vanishing resistance is due to impurities. Without impurities, each transmission probability goes to 1, but the corresponding conductance, equation (5.16) does not diverge in that limit. In a four terminal setup, the link between the transmission probabilities and the conductance is given by:

$$g = \frac{\sum_{m,n} T_{m\leftarrow n}}{\sum_{m,n}(R_{m\leftarrow n})}, \tag{5.17}$$

where $R_{m\leftarrow n}$ are reflection amplitudes. For each value of n, we have: $\sum_m T_{m\leftarrow n} = 1 - \sum_m R_{m\leftarrow n}$. The resulting conductance diverges when all transmission probabilities $\sum_m T_{m\leftarrow n}$ are equal to one (or all reflection coefficients $\sum_m R_{m\leftarrow n}$ vanish), and the conductance reads:

$$g = \frac{\sum_{m,n} T_{m\leftarrow n}}{N_y - \sum_{m,n}(T_{m\leftarrow n})}, \tag{5.18}$$

The difference between both definitions of the conductance is the contact conductance (it is the inverse of the contact resistance).

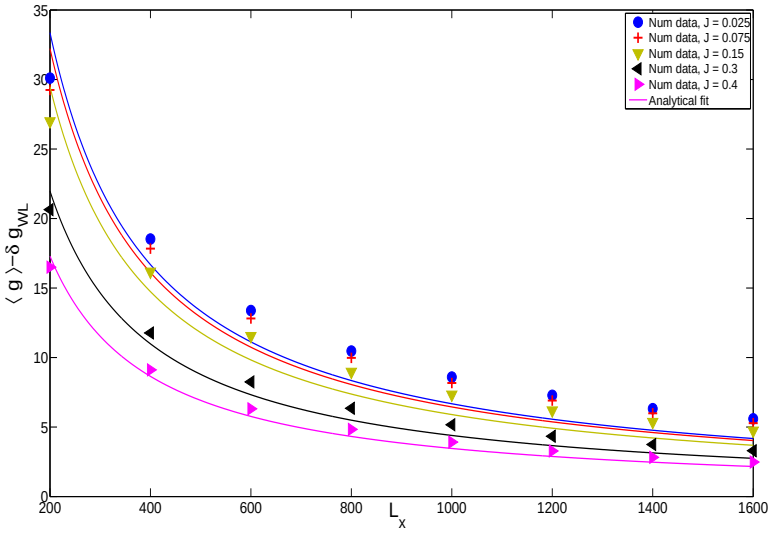

Figure 5.21: *Plot of the classical part of the conductance (dots, squares,...) and analytical fits using the result in one dimension: $g(L_x) = \sigma/L_x$. The agreement between numerical data and theory is not good.*

The classical conductivity

For each value of magnetic disorder, the classical conductivity is extracted. One can then try to plot that conductivity as a function of magnetic disorder and compare it to theoretical predictions. The Einstein relation links the conductivity to the diffusion coefficient D and the density of state at the Fermi level $\rho_0(\varepsilon_F)$:

$$\sigma_0 = se^2\rho_0(\varepsilon_F)D. \tag{5.19}$$

s is the spin degeneracy. By definition, in the case of non magnetic impurities, the diffusion coefficient reads:

$$D = v_F^2\tau_e, \tag{5.20}$$

with v_F the Fermi velocity and τ_e the elastic scattering time. It is related to the scalar disorder by:

$$\tau_e = \frac{1}{2\pi\rho_0 n_i v_0^2}, \tag{5.21}$$

where n_i is the impurity density and $v_0^2 = W^2/12$ is the variance of the distribution of scalar disorder. In the presence of magnetic impurities, another diffusive process is to be taken into account: the spin diffusion characterized by a length L_m and a time $\tau_m = L_m^2/D$. The Matthiesen rule explains how the scattering time τ_e must be modified for two diffusive processes:

$$\frac{1}{\tau_e} \to \frac{1}{\tau_e} + \frac{1}{\tau_m}. \tag{5.22}$$

More accurately the scattering time τ_m is directly related to the magnetic disorder, at the second order in J, see [102]:

$$\tau_m = \frac{1}{2\pi\rho_0 n_i J^2\langle S^2\rangle}. \tag{5.23}$$

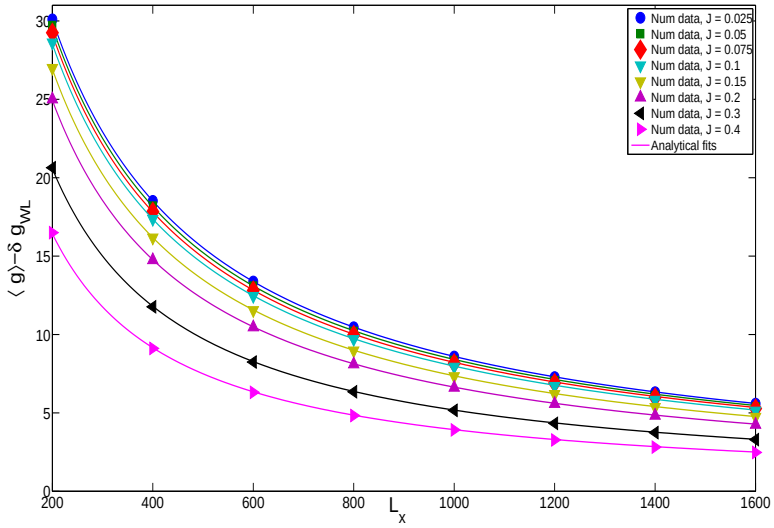

Figure 5.22: *Plot of the classical part of the conductance (dots, squares,...) and analytical fits using the contact resistance. The agreement between numerical data and theory is now good.*

Collecting all these results, one can deduce the magnetic disorder behavior of the classical conductivity:

$$\sigma_0(J) = \frac{\sigma_0(J=0)}{1+\frac{3}{W^2}J^2}. \tag{5.24}$$

In figure 5.23 we compare this previous equation with numerical evaluation of the conductivity (there are no free parameter here). The relatively good agreement between both curves ensures a good understanding of the physics of the transport in materials with magnetic impurities.

Fit of $L_m(J)$

This allows one to give an expression to second order in J for the magnetic dephasing length:

$$L_m(J) = \sqrt{D(J)\tau_m(J)} \propto \frac{1}{J\sqrt{\frac{W^2}{12}+\frac{J^2}{4}}}. \tag{5.25}$$

On figure 5.24 we plot numerical evaluation of the magnetic length as a function of magnetic disorder and we fit these values with the preceding function. The agreement is good. In that figure, error bars on the magnetic length are present but are contained in the width of dots. These error bars were found by using formula (3.24) on a plot of conductance fluctuations for a given J. Beginning with small values, L_m is increased until the fit is relatively good. This gives $L_m^{\text{low}}(J)$. In a similar way, beginning with a large value, L_m is decreased to reach a suitable fit, we determine $L_m^{\text{up}}(J)$. These two values are defined as the lower and upper bound of error bars on L_m respectively. This algorithm is applied for all values of magnetic disorder. In figure 5.24, the coefficient of proportionality is the only fitting parameter and equal to 6.07 for numerical data extracted from the study of conductance fluctuations, and is equal to 5.61 for numerical data extracted from conductance correlations for two different spin configurations. See section 6.3.2 for a more accurate description of the second determination of L_m.

The agreement between the numerical data and the expression for $L_m(J)$ is good, it ends the complete characterization of the quantum corrections to the conductance. The last point

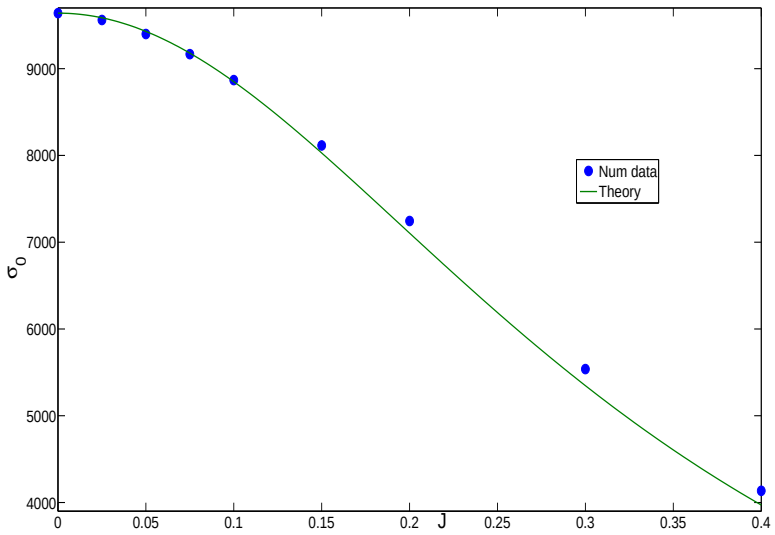

Figure 5.23: *Evolution of conductivity with magnetic disorder. Dots are numerical data. Plain line is the theory given by Einstein relation and Matthiesen rule for the conductivity. Agreement is good especially at low magnetic disorder.*

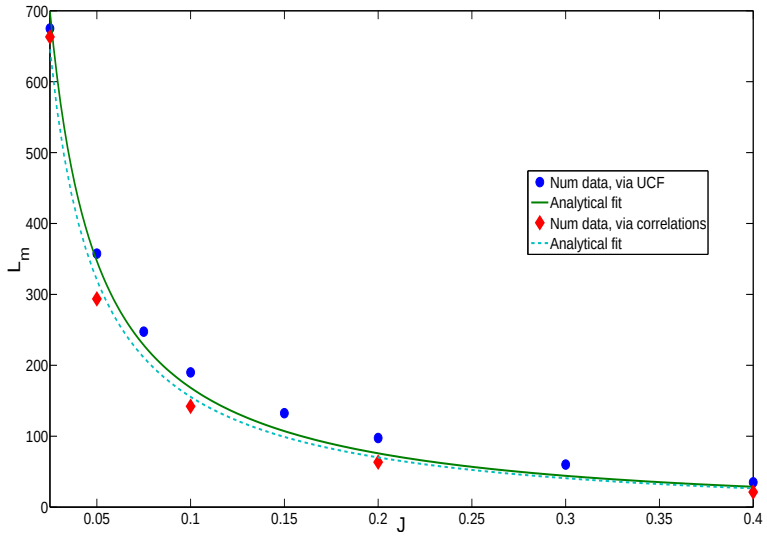

Figure 5.24: *Evolution of magnetic dephasing length with magnetic disorder. Dots are numerical data extracted from the study of UCF and diamonds are numerical data extracted from the study of conductance correlations for two different spin configurations. Plain and dotted lines are analytical fits from perturbation theory at second order in J. Error bars are smaller than dots and diamonds sizes.*

that has still not been debated is the Gaussian shape of the distribution of conductance that we expect. To study it, we focus on the third cumulant of the distribution.

5.3.3 The third cumulant: Gaussian distributions?

According to the analytical study of [132], this cumulant decays to zero in a universal way as $\langle g \rangle$ increases. Here in figure 5.26 we find a dependance of this decrease on the symmetry class: for GOE $\langle g^3 \rangle_c$ goes to zero in a monotonous way whereas it decreases, changes its sign and then goes to zero in GUE case. For $\langle g \rangle > 4$ numerical errors are dominant, then this part of the curve is irrelevant. Moreover, for GUE this decrease seems to be universal whereas it depends on the transverse length for GOE. On figure 5.25, is represented the convergence of the skewness

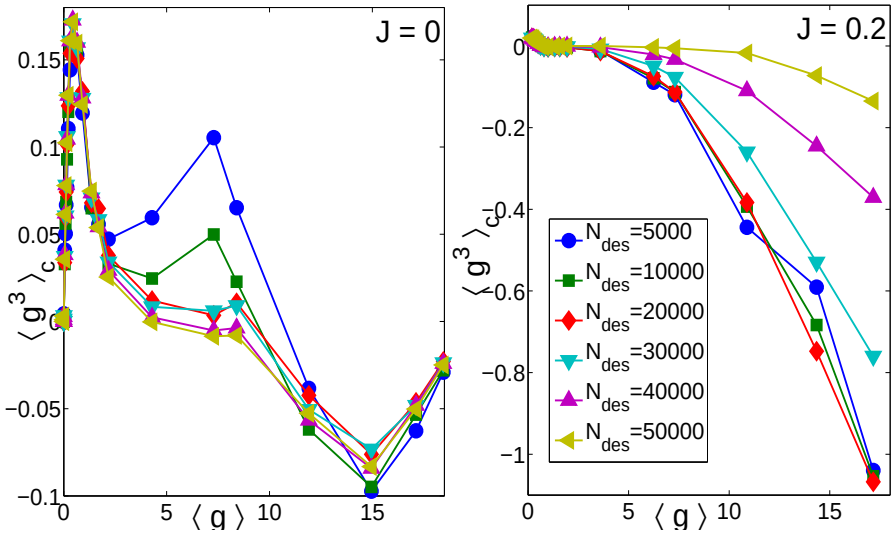

Figure 5.25: *Plot of $\langle g^3 \rangle_c$ as a function of $\langle g \rangle$ in the metallic regime, averages are performed with an increasing number of configurations N_{des}. Convergence curves are shown for $L_y = 10$ and $J = 0$ or $J = 0.2$.*

when increasing the number of configurations used to perform averages N_{des} for both GOE and GUE. Plots show a good enough convergence of averages to conclude that the third cumulant of conductance is not zero for all values of $\langle g \rangle$. Notice that the maximal number of averages is 50 000. Moreover this fast vanishing of the third cumulant confirms the faster convergence of the whole distribution towards the gaussian, compared to what happens in the insulating regime. Based on our numerical results, we cannot confirm nor refute the expected law $\langle g^3 \rangle_c \propto 1/\langle g \rangle^n$, with $n = 2$ in GOE and $n = 3$ in GUE [98, 143].

5.3.4 The ergodic hypothesis

In this section we study the statistical distribution of conductance with respect to the scalar disorder. In chapter 2 and 3, we have seen that experimental measurements of conductance are performed by applying a magnetic field (magneto resistances or conductances are measured). To compare theoretical and experimental results, we invoked the ergodic hypothesis. The goal of this section is to study numerically the validity of this ergodic hypothesis (see sections 3.2.1 and 6.1.3).

We consider the conductance as a function of two variables: the disorder configuration V and the magnetic flux[6] ϕ through the sample. ϕ is expressed in units of the quantum flux $\phi_0 = h/e$.

[6] the magnetic flux is defined by $\phi = B/\Sigma$, where Σ is the surface of the sample.

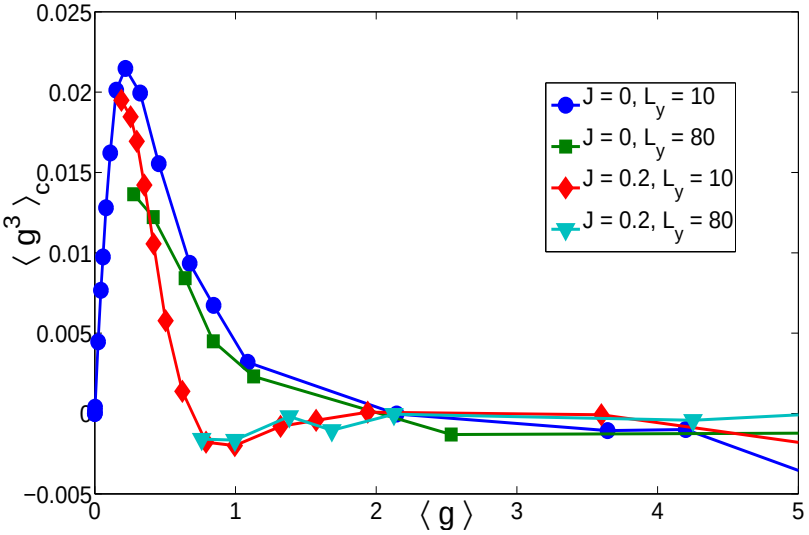

Figure 5.26: *Plot of $\langle g^3 \rangle_c$ as a function of $\langle g \rangle$ in the metallic regime.*

The conductance fluctuates in terms of both the scalar disorder and the magnetic flux [91], we will then compare statistical distributions of conductance sampled either over disorder or magnetic field and compare them.

Notations

We remind the reader that averages over the total number of scalar disorder configurations is denoted by $\langle \cdot \rangle$. Disorder averages over a smaller number of configurations (denoted $V_{\max}$) is defined by:

$$\langle g \rangle^{V_{\max}}(\phi) = \frac{1}{V_{\max}} \sum_{V=1}^{V_{\max}} g(V, \phi). \tag{5.26}$$

Averages over the total number of magnetic fluxes are denoted with strait brackets $[\cdot]$ as follows:

$$[g](V) = \frac{1}{N_\phi} \sum_{\phi=1}^{N_\phi} g(V, \phi), \tag{5.27}$$

where ϕ is the flux of the magnetic field. Averages over partial numbers of magnetic fluxes are denoted by $[g]_{\phi_{\max}}$ as in equation (5.26). In practice we sample the conductance of a system of size 1600×40 for $J = 0.4$ with 1600 disorder configurations and 1250 values of the magnetic flux ($\phi = 1 \rightarrow 1250$, in units of the quantum flux). Values of magnetic disorder and geometry are chosen so that the system is in the UCF regime. As a statistical distribution is entirely determined by its cumulants (irreducible moments) [144], we will study the average (first cumulant), the variance (second cumulant) and the skewness (third cumulant) separately. Higher cumulants are denoted in a similar way: for instance the variance of the conductance over scalar disorder for $V_{\max}$ configurations is written as:

$$\langle g^2 \rangle_c^{V_{\max}}. \tag{5.28}$$

We remark that this cumulant still depends on ϕ, as the conductance is now a function of two variables.

Cumulants over disorder

We first focus on cumulants with averages over disorder. We plot each partial cumulant $\langle g^n \rangle_c^{V_{\max}}$ as a function of $V_{\max}$, for different values of magnetic flux. We also plot on the same figure the crossed average:

$$[\langle g^n \rangle_c^{V_{\max}}] \quad \text{for} \quad n = 1 \to 3, \tag{5.29}$$

which is the mean value over magnetic field $[\cdot]$ of the cumulant of order n with respect to scalar disorder. We also define error bars as the following mean square root:

$$\text{error}_\phi(\langle g^n \rangle_c^{V_{\max}}) \equiv \pm \sqrt{2 \left[\left(\langle g^n \rangle_c^{V_{\max}} - [\langle\, g^n \rangle_c V_{\max}] \right)^2 \right]}. \tag{5.30}$$

Figure 5.27 shows the results we obtained. Note that concerning the second cumulant, we find

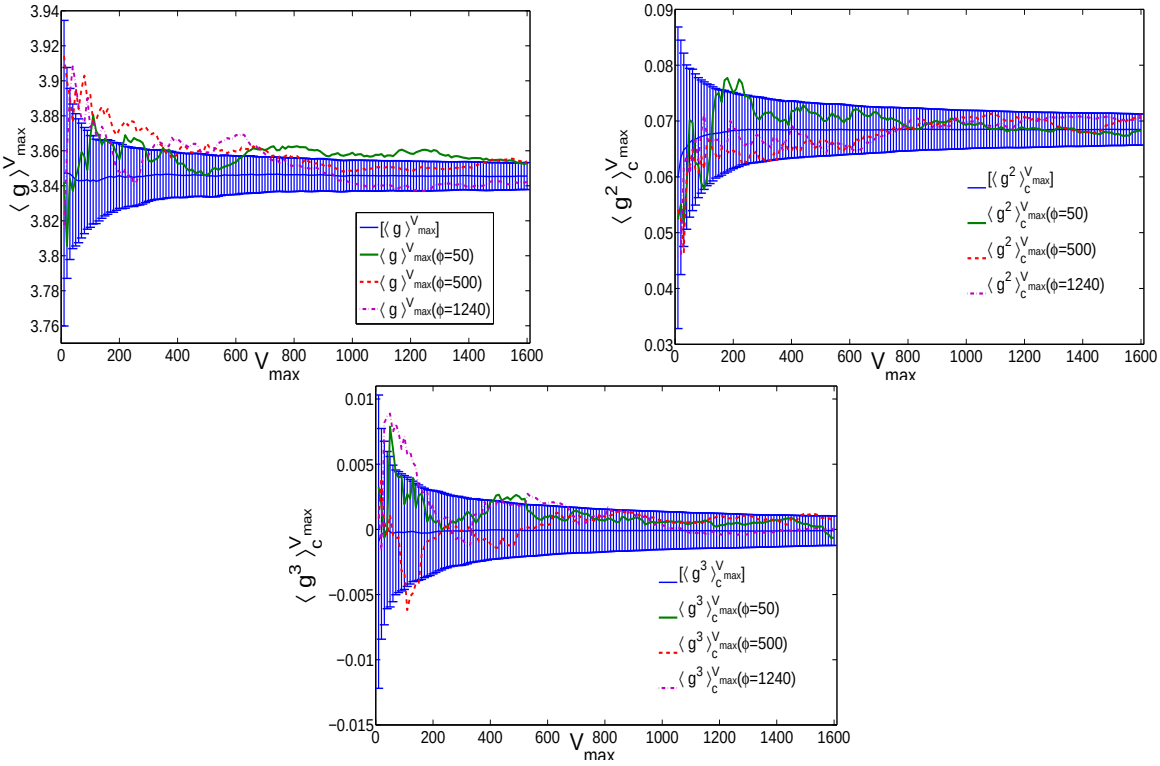

Figure 5.27: *Study of the fluctuations with magnetic flux of the first cumulants with respect to disorder. Error bars are defined in equation (5.30).*

the expected universal value of $1/15 \approx 0.067$.

Cumulants over magnetic flux

The study here is highly similar to the previous one provided that:

$$\begin{aligned} \langle \cdot \rangle &\leftrightarrow [\cdot] \\ V_{\max} &\leftrightarrow \phi_{\max} \end{aligned}$$

and we find the results of figure 5.28, which have essentially the same shape as figure 5.27.

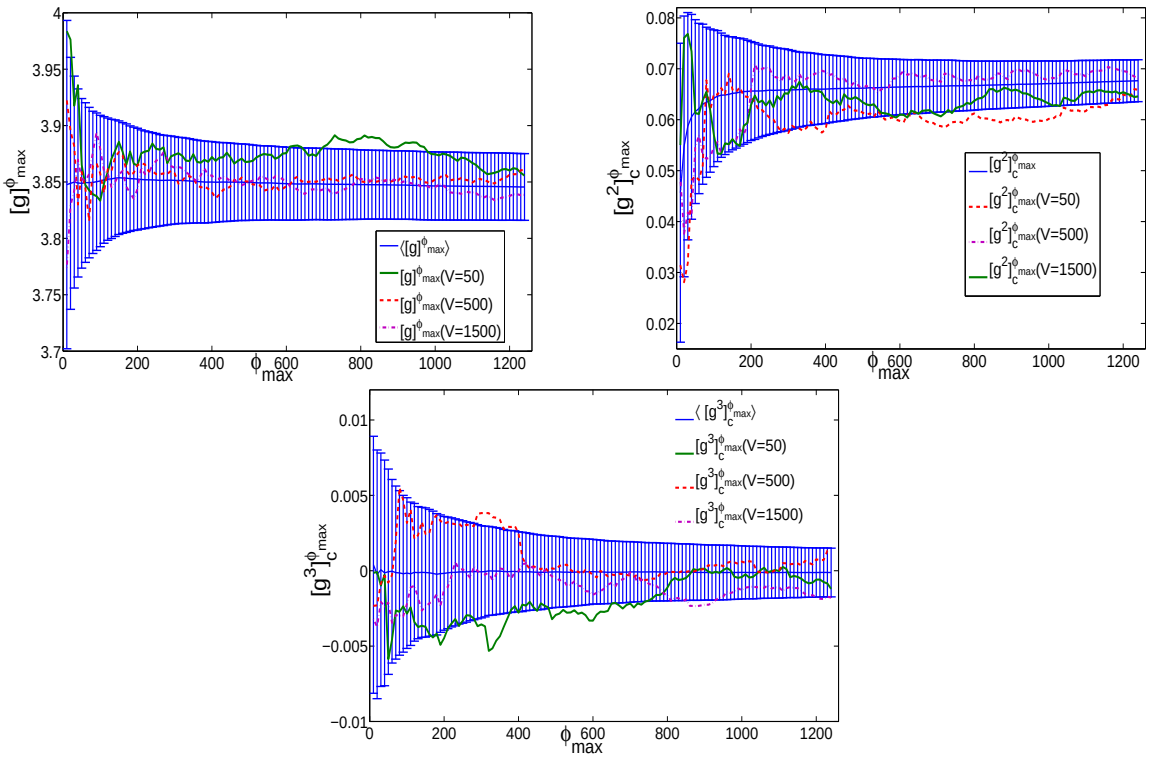

Figure 5.28: *Study of the fluctuations with disorder of the first cumulants with respect to magnetic flux. Error bars are defined similarly to equation (5.30).*

Comparison: the ergodicity issue

In this section, we compare residual fluctuations of the different cumulants. In the last section, we have shown that, for each cumulant, the quantities of interest are $\langle g^n \rangle_c^{V_{\max}}(\phi)$ on the one hand and $[g^n]_c^{\phi_{\max}}(V)$ on the other hand, where n goes from 1 to 3. Each of these objects have therefore a statistical distribution with respect to the magnetic flux ϕ and the scalar disorder respectively. For $n = 1$, we compare in figure 5.29, the mean value and the root mean square variation (see equation (5.30)) of $\langle g \rangle^{V_{\max}}(\phi)$ and $[g]^{\phi_{\max}}(V)$. It appears that these quantities have the same mean value but different second cumulant.

On the contrary, for $n = 2$ and $n = 3$, the statistical distributions of respectively $\langle g^n \rangle_c^{V_{\max}}(\phi)$ and $[g^n]_c^{\phi_{\max}}(V)$ are equal (figures 5.30 and 5.31). We note also that the expected UCF value is reached in figure 5.30, and that the evolution of figure 5.31 illustrates that conductance distributions are gaussians.

To conclude on the ergodicity hypothesis, the quantities $\langle g^n \rangle_c^{V_{\max}}(\phi)$ and $[g^n]_c^{\phi_{\max}}(V)$ are similar for $n = 2$ or 3, for these cumulants the ergodic hypothesis holds, which is not the case for the average value, in agreement with [145]. However, we showed that the quantities $\langle g \rangle(\phi)$ on the one side and $[g](V)$ on the other side have a Gaussian statistical distribution with respect to magnetic flux and scalar disorder respectively. These distributions have the same average value: $[\langle g \rangle] \equiv \langle [g] \rangle$, but a different variance: $\left[(\langle g \rangle - [\langle g \rangle])^2 \right] \neq \left\langle ([g] - \langle [g] \rangle)^2 \right\rangle$, which is an original result on the ergodicity issue in mesoscopic conductors. In the following, all our theoretical analysis of conductance correlations will be performed with averages over scalar disorder $V \equiv \{v_i\}_i$,

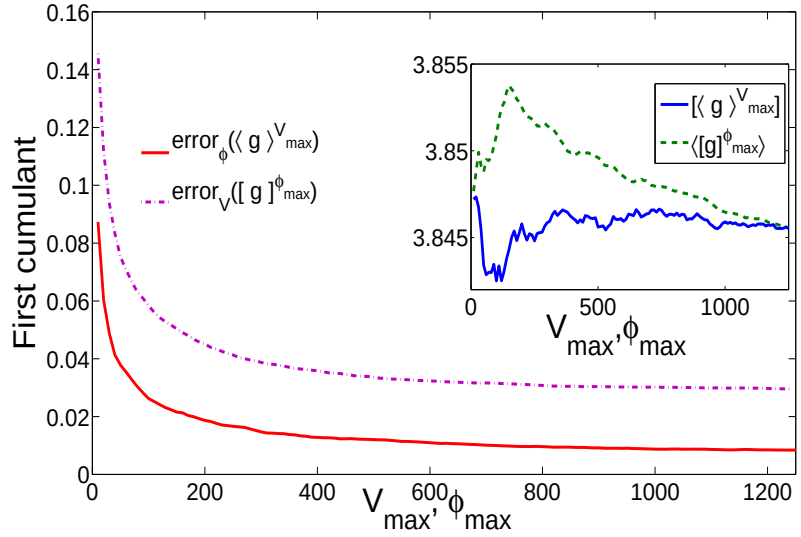

Figure 5.29: *Study of the statistical distributions of the mean value* $[g]^{\phi_{max}}(V)$ *and* $\langle g \rangle^{V_{max}}(\phi)$ *with respect to respectively* V *and* ϕ*. In inset is plotted the mean value of these distributions and the variances (the* error *functions as defined in equation* (5.30)*) are plotted in the main figure.*

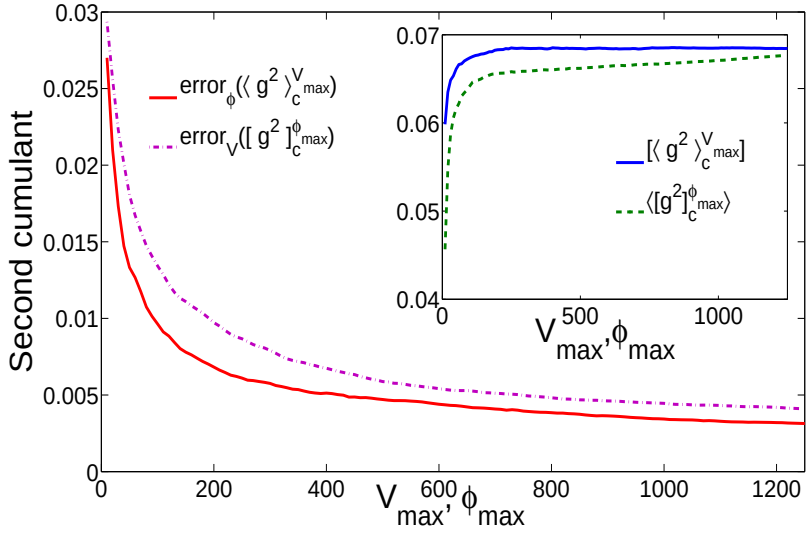

Figure 5.30: *Study of the statistical distributions of the variance* $[g^2]_c^{\phi_{max}}(V)$ *and* $\langle g^2 \rangle_c^{V_{max}}(\phi)$ *with respect to respectively* V *and* ϕ*. In inset is plotted the mean value of these distributions and the variances (the* error *functions as defined in equation* (5.30)*) are plotted in the main figure.*

no magnetic field will be applied any more.

Important: in chapter one we mentioned that, following the hierarchical vision of a spin glass, the system is trapped in an ergodic component of the phase space (one energy valley), and that the ergodicity is broken in the low temperature spin glass phase. This ergodicity deals with the ability for the system to reach all possible states in the energy landscape. It is broken in

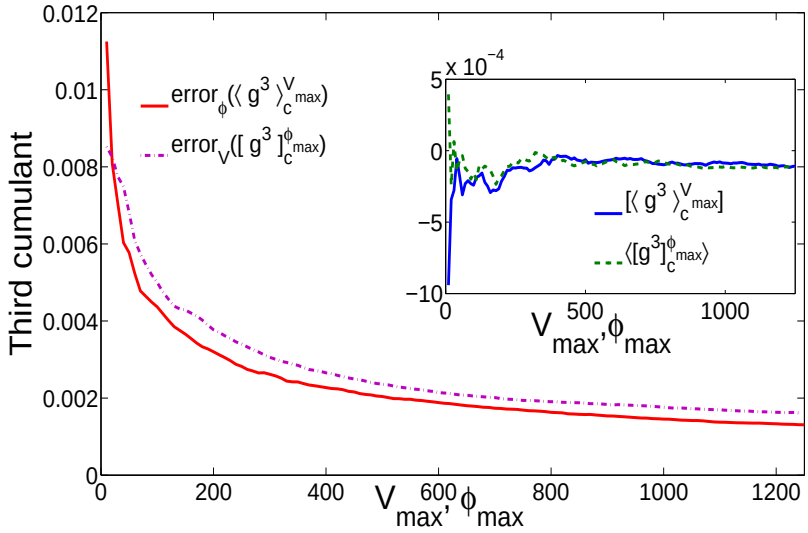

Figure 5.31: *Study of the statistical distributions of the skewness* $[g^3]_c^{\phi_{max}}(V)$ *and* $\langle g^3\rangle_c^{V_{max}}(\phi)$ *with respect to respectively* V *and* ϕ*. In inset is plotted the mean value of these distributions and the variances (the* error *functions as defined in equation* (5.30)*) are plotted in the main figure.*

a spin glass since the energy barriers are diverging at low temperature with no hope to escape them. In this chapter, the ergodic hypothesis can be applied to all conductors and not only to metallic spin glasses. It deals with the ability of the system to reach similar states in the energy landscape by changing the scalar disorder or the magnetic field of the system. These two types of ergodicity issues are different.

5.4 Conclusion

In this chapter, we have performed an extensive study of the universal properties of coherent transport in the presence of magnetic frozen impurities in both the metallic and the localized regimes. Comparing and extending previous analytical and numerical studies, we have identified the insulating and metallic regimes described by the universality classes GOE and GUE. We have paid special attention to the dependance on this symmetry of cumulants of the distribution of conductance in both metallic and insulating universal regimes. In particular, we have identified with high accuracy the domain of universal conductance fluctuations, and determined its extension in the present model. This study also allowed us to characterize with high precision the experimental regime of interest of non universal metallic diffusion, which will be useful for the study of conductance correlations in the next chapter.

Chapter 6
Conductance correlations as a probe of the spin glass state

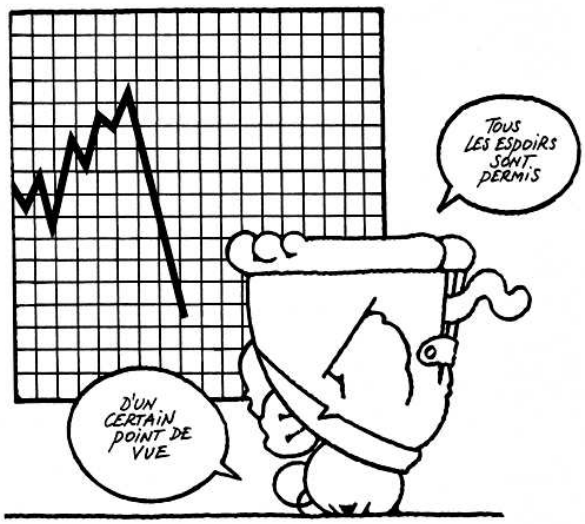

6.1 Introduction

6.1.1 Back to Spin Glass physics

One of the key conclusion on Spin Glass physics is that it is a very poorly understood state of matter (see chapter 1) as two competing theories claim to describe the ground and excited spin states of a spin glass. One crucial tool to study experimentally the internal spin state of a spin glass is the spin overlap (also called the spin configurations correlation), whose definition is generalized here for classical Heisenberg spins (see equation (1.17) section 1.4.1):

$$Q_{12} = \frac{1}{N_{imp}} \sum_{i=1}^{N_{imp}} \vec{S}_i^{(1)} \cdot \vec{S}_i^{(2)}, \tag{6.1}$$

where N_{imp} represents the number of impurities in the sample, and $\vec{S}_i^{(1,2)}$ are two different spin configurations. In this chapter, the spin overlap is denoted Q_{12} and not $Q^{\alpha\gamma}$ to enforce that we are dealing in this chapter with Heisenberg and not Ising spins. Notice again that the quantity $1 - Q_{12}$ defines a distance between spin configurations 1 and 2 (distance that is ultrametric [33] at the mean field level). In the simpler case of Ising spins, $1 - Q^{\alpha\gamma}$ simply counts the percentage of spin flips that occurred between spin configurations α and γ.

A more intuitive way to understand the usefulness of the overlap is to imagine the following experiments:

(i) **First experiment:** Consider a spin glass initially at high temperature ($T_i > T_{SG}$), in the paramagnetic phase. At time $t = 0$, the spin glass is quenched to a temperature $T_f < T_{SG}$, and imagine it is possible to take a "snapshot"[1] of the spin configuration. It is spin configuration number 0. Configuration number i consists in taking a snapshot of the spin state of the spin glass after waiting time $t_i = i \times t_W$.

(ii) **Second experiment:** Start again from a spin glass in the paramagnetic phase, and make successive quenching to temperature T_f and heating to temperature T_i. Snapshot of the spin configurations are taken after each quench of the system.

For each experiment, we end up with a set of spin configurations that are a priori different. As it is experimentally illusory to get a direct imaging of the spin configuration, it is highly challenging to be able to measure the spin overlap Q_{12}, as it encodes how different the configurations are. The knowledge of Q_{12} is crucial as it gives access to the evolution of the spins with time (*i.e* aging properties of the sample) in the first experiment. In the second one, successive quenches of the sample allow to sample the statistical distribution of overlaps, which is the order parameter of the spin glass transition. Up to now, this quantity has not been measured experimentally and we propose an original method to do it.

6.1.2 A qualitative approach

In the previous section, we imagined two experiments. In these experiments we also imagined to take a snapshot of the spin configuration. We propose to use conductance measurements (calculations) as a snapshot of the spin configuration, as we have already seen that in the coherent regime the conductance is a fingerprint of the disorder encountered. More precisely, comparison

[1] with snapshot we mean that we imagine a way to measure the spin configuration, and that measure takes a time t_{exp} negligible compared to the relaxation time of a spin glass (see section 1.3).

of the conductance in each spin state gives access indirectly to the spin overlap. This section is devoted to a qualitative analysis to show that conductance correlations, as defined below (equation (6.2)) depend on the spin overlap Q_{12}. We define the conductance correlation by:

$$\langle \delta g \left(V, \{\vec{S}_i^{(1)}\}\right) \delta g \left(V, \{\vec{S}_i^{(2)}\}\right) \rangle \equiv \langle g \left(V, \{\vec{S}_i^{(1)}\}\right) g \left(V, \{\vec{S}_i^{(2)}\}\right) \rangle_c, \tag{6.2}$$

where $\delta g \equiv g - \langle g \rangle$. As before, $\langle \cdot \rangle$ represents average over scalar disorder V.

We showed in section 3.1 that the calculation of the quantum corrections to the averaged conductance is based on the pairing of two electronic diffusion paths, which leads to two types of diagrams, the Diffuson and the Cooperon. As shown in equation (6.2), the correlation of conductance is a product of two conductances, each one calculated for the same scalar disorder configuration$V$ but for different spin configurations. The corresponding Diffuson and Cooperon terms take the form:

$$P_{d,c} \propto \sum_{\mathcal{C},\mathcal{C}'} \underbrace{\mathcal{A}_{\mathcal{C}}}_{\text{spin config 1}} \underbrace{\mathcal{A}^*_{\mathcal{C}'}}_{\text{spin config 2}} \quad . \tag{6.3}$$

Be aware that the terms

$$\begin{aligned} P_{d,c} &\propto \sum_{\mathcal{C},\mathcal{C}'} \underbrace{\mathcal{A}_{\mathcal{C}}}_{\text{spin config 1}} \underbrace{\mathcal{A}^*_{\mathcal{C}'}}_{\text{spin config 1}} \qquad \text{and} \\ P_{d,c} &\propto \sum_{\mathcal{C},\mathcal{C}'} \underbrace{\mathcal{A}_{\mathcal{C}}}_{\text{spin config 2}} \underbrace{\mathcal{A}^*_{\mathcal{C}'}}_{\text{spin config 2}} \end{aligned} \tag{6.4}$$

only contribute to $\langle g(V, \{\vec{S}_i^{(1,2)}\}_i)\rangle \langle g(V, \{\vec{S}_i^{(1,2)}\}_i)\rangle$, and not to the connected correlation (6.2).

These Diffuson and Cooperon terms have the same structure as in chapter 3 (but now each electronic path encounters a different spin configuration). Moreover each Diffuson or Cooperon term represents a pairing of spin 1/2, the natural basis to decompose the Diffuson and the Cooperon is still the singlet-triplet base as shown in the calculation of the conductance fluctuations in section 3.2.3. As previously said, the phase vanishes in the Diffuson term, it is not sensitive to random magnetic fields (or equivalently frozen magnetic impurities). In a singlet state the electrons have the same spin projection; this state is therefore not sensitive to a random magnetic field (and only this state). Consequently, only the Diffuson/singlet term is not sensitive to the frozen impurities if spin configurations are similar. The corresponding diffusion length[2] $L_m^{D,S}$ is diverging[3]. The other lengths (for the Diffuson/triplet, Cooperon/singlet and Cooperon/triplet) never diverge. If configurations of frozen impurities are different in each path, each electron of the Diffuson/singlet encounters a different spin landscape. These electrons will decorrelate from each other. If spin configurations are almost similar, the decorrelation will be moderate and then the value of the conductance correlations will be of the order of the conductance fluctuations (almost identical configurations). If configurations are far away from each other ($Q_{12} \approx 0$), the conductance will be maximally decorrelated.

To conclude on this qualitative part, we suggested that the correlations of conductance as defined in equation (6.2) are indeed function of the overlap. In the following we study numerically these correlations of conductance. Another useful remark is that the diffusion length $L_m^{D,S}$ plays a crucial role as it is the only length that diverges in the case of similar configurations. We use this fact in section 6.3.

[2] we associate a diffusion length to each of the four terms of equation (3.24): see below.

[3] This is the reason why we have a term $F_2(0)$ in equation (3.24) for the fluctuations of conductance.

6.1.3 An experimental proposal

To measure experimentally correlations of conductance, we propose [138] the protocol plotted in figure 6.1. At time $t = 0$, the system at temperature $T' > T_g \equiv T_{SG}$. It is frozen to reach

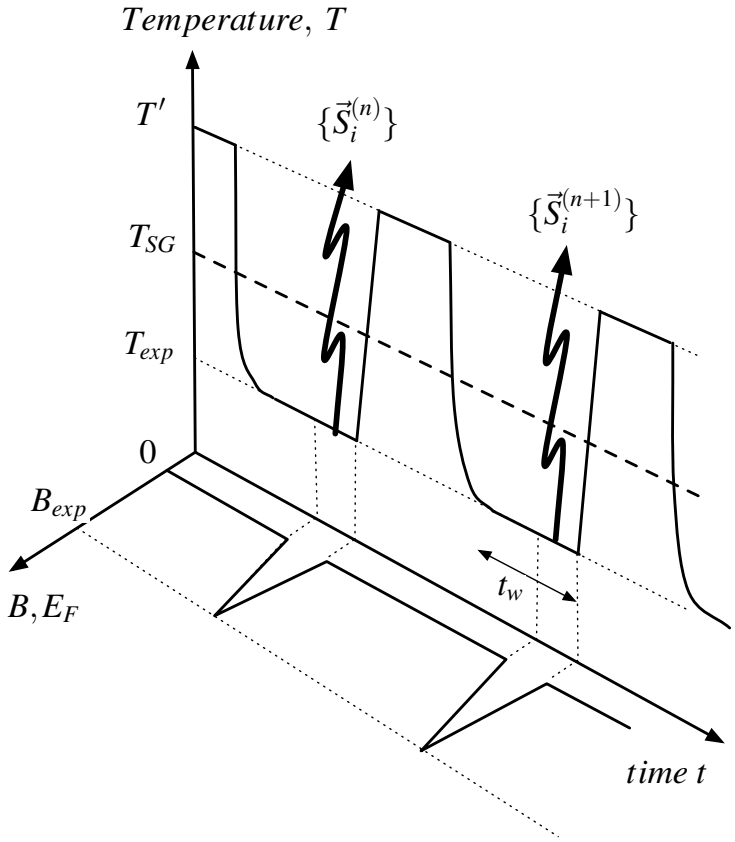

Figure 6.1: *Proposed experimental protocol to measure conductance correlations in a spin glass.*

$T_{\rm exp} < T_{SG}$. We let then the system relax for some time (to be determined experimentally), to obtain a "frozen" (at the experimental time scale) spin configuration $\{\vec{S}_i^{(n)}\}$. Afterwards, the measurement of the magnetoconductance is performed in the spin glass frozen in configuration $\{\vec{S}_i^{(n)}\}$. After the measurement, the temperature is increased again up to $T' > T_{SG}$. After a second waiting time at this temperature, the systems is frozen again to $T_{\rm exp}$. The spins freeze, after a waiting time, in a configuration $\{\vec{S}_i^{(n+1)}\}$, and the measurement of the magnetoconductance is performed. This protocol is very close to the experiment (ii) we imagined in section 6.1.1, with magneto conductance measurements as the "snapshot" of the spin configuration. Thanks to the ergodic hypothesis we described in section 3.2.1, the conductance measured with an increasing magnetic field has the same effect as sampling the conductance distribution by considering numerous configurations of scalar disorder. The correlations, as defined in equation (6.2) are then reachable experimentally. These experiments are performed at Institut Louis Néel in GRENOBLE by the Quantum Coherence group of L. Saminadayar and L. Lévy.

The study of the previous chapter is of great importance as we managed to characterize with high accuracy the experimental accessible regime of non universal metallic diffusion. We use this

extensive study to consider numerical systems that are in the experimentally relevant case in all that follows.

6.2 Conductance correlations and random configurations

In the following we first study directly the statistical distribution (still as scalar disorder is varied) of the difference of conductances, each one calculated with its own spin configuration and the same realization of disorder V. We show that this comparison leads to the study of the previous correlation. In a second time we come to the study of the correlation itself, as a function of the overlap. To begin, the algorithm of creation of random spin configurations but with a finite correlation (*i.e* with a non vanishing overlap between them) is described.

6.2.1 Random spin configurations

In this section we present how random configurations with a non vanishing correlation are built. The constraint is to build up different spin configurations with random orientations but the correlation Q_{12} must not vanish. A first spin configuration is created by choosing random orientation for each impurity. These orientations are chosen independently from each other. Other configurations are created by rotating of a random angle the spins of the first configuration with a probability $p \ll 1$. This probability changes from one configuration to the other so that we end up with a set of 24 configurations with mutual overlaps Q_{12} between 10^{-3} and 1 (identical configurations). The highest value of overlap for two different spin configurations is[4] $Q_{12} = 0.9992$. Figure 6.2 represents schematically the initial spin configuration, another one created via the previous algorithm, and the overlap between them, in the simpler case of Ising spins. Black squares for the overlap represents the spin flips that occurred. This figure illustrates that both spin configurations are random. Moreover spin flips occur uniformly in the whole sample, which mimics a mean field-like spin excitation [33].

6.2.2 Probability distribution of $g_1 - g_2$

A first quantity to study is the probability density function of variation of conductance between two different spin configurations. This quantity will be denoted by $g_1(V) - g_2(V)$ in the following.

$$g_1(V) - g_2(V) \equiv g\left(V, \{\vec{S}_i^{(1)}\}_i\right) - g\left(V, \{\vec{S}_i^{(2)}\}_i\right). \tag{6.5}$$

The averages are still performed over the scalar disorder V. In figure 6.3 we show that this quantity can be well approximated by a gaussian which allows us to deal either with the brut numerical data or with gaussian interpolations. Note that the statistical distributions of $g_1 - g_2$ are centered around zero: $\left\langle g\left(V, \{\vec{S}_i^{(j)}\}_i\right)\right\rangle = \left\langle g\left(V, \{\vec{S}_i^{(k)}\}_i\right)\right\rangle \forall (j,k)$. In detail, the variance $\langle (g_1(V) - g_2(V))^2\rangle_c \equiv \langle ((g_1(V) - g_2(V)) - \langle g_1 - g_2\rangle)^2\rangle_c$ is equal to:

$$\langle (g_1(V) - g_2(V))^2\rangle_c = 2\left(\langle g_{1,2}^2(V)\rangle_c - \langle g_1(V) g_2(V)\rangle_c\right), \tag{6.6}$$

Hence it encodes the correlations between the two conductances as defined in equation (6.2). The study of the variance of this distribution is then crucial to study how a change in Q_{12} affects the conductance correlation. We plot the statistical distributions of $g_1(V) - g_2(V)$ for different couples of spin configurations leading to different values of spin correlations Q_{12}. The results are shown in figure 6.4. This curve shows that we are able to discriminate different spin correlations

[4] it corresponds, in the case of Ising spins to about 26 spin flips between both configurations, each containing 64 000 spins.

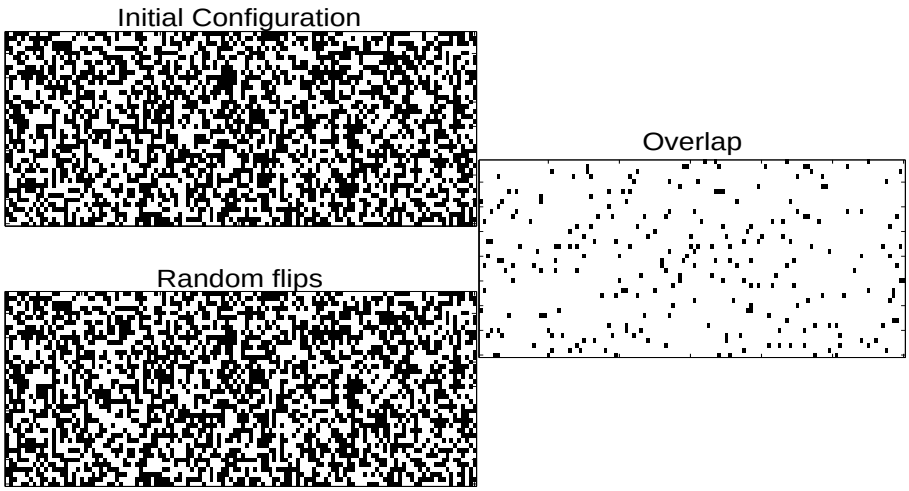

Figure 6.2: *Schematic view of two random configurations, and of the corresponding overlap. In the two plots on the left, black (respectively white) squares represent a positive (resp. negative) projection of the spin along the z−axis (axis perpendicular to the sample), and on the right black (resp. white) squares represent a positive (resp. negative) result to the scalar product* $\vec{S}_i^{(1)} \cdot \vec{S}_i^{(2)}$.

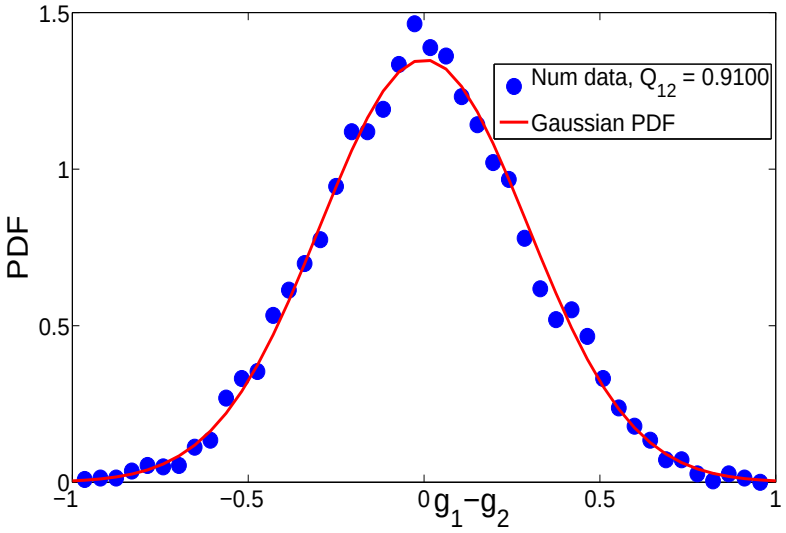

Figure 6.3: *Probability density function of the difference of conductances, each calculated for one spin configuration.* $Q_{12} = 0.9100$, $J = 0.1$, $L_x = 1600$ *and* $L_y = 40$. *Averages performed over* $N = 5000$ *realizations of scalar disorder.*

between two configurations with the help of conductance correlations. The statistical distribution of $g_1 - g_2$ is sensitive to changes in Q_{12}. One immediately remarks that the sensitivity is very high when Q_{12} is close to 1.

Note that the probability $P(g_1 - g_2 \simeq 0)$ is found on figure 6.4 to be highly sensitive on small departures from $Q_{12} = 1$. This is easily understood by using a Gaussian approximation

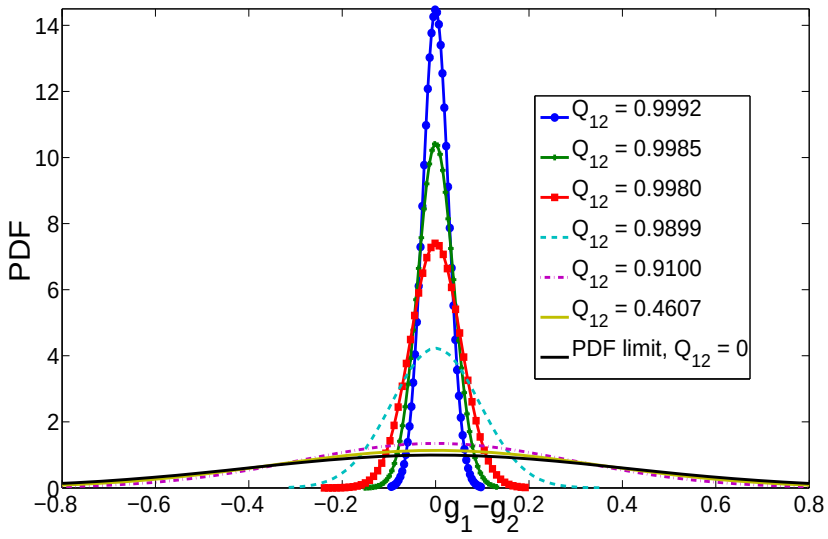

Figure 6.4: *Probability Density Function of $g_1 - g_2$ where g_k is the dimensionless conductance calculated for spin configuration k. Plain curves are Gaussian interpolation of numerical data.*

of $P(g_1 - g_2 \simeq 0)$. The probability of similar conductances then reads $P(0) = 1/\sqrt{2\pi\sigma}$ with $\sigma = 2(\langle(\delta g)^2\rangle_V - \langle\delta g_1 \delta g_2\rangle_V)$.

The last question concerning the distribution of $g_1 - g_2$ is the following: does the conductance correlation depend only on Q_{12} or does it also depend on each spin configuration? To answer this question we propose to plot the distribution of $g_1 - g_2$ for different configurations but with the constraint that the spin correlation is similar for each couple of configurations. The result is plotted on figure 6.5. This figure shows clearly that a same value of $Q_{12} \approx 0.91$ (dots, squares, diamonds and down triangles) leads to a same value of conductance correlation, and if we have a different spin correlation (up triangles), the distribution is different.

6.2.3 Conductance correlations, function of overlap

Theory

To deduce analytically the conductance correlations as a function of the spin overlap, the method is the same as what is described for the fluctuations of conductance at section 3.2.3. The difference lies in the fact that the spin rotation operators R_t are now different as each electron encounters its own spin configuration. Equation (3.20) is modified as:

$$Q_m(t) = \sum_{s_f=\pm} \langle s_f|R_{-t}^{(1)}|s_0\rangle^* \langle s_f|R_t^{(2)}|s_0\rangle = \sum_{s_f=\pm} \langle s_0|(R_{-t}^{(1)})^\dagger|s_f\rangle\langle s_f|R_t^{(2)}|s_0\rangle, \tag{6.7}$$

where $R_t^{(i)}$ is the rotation matrix with respect to the spin configuration number i. We end up with the following expression for the correlations [138]:

$$\langle\delta g_1(V)\delta g_2(V)\rangle = \frac{1}{4}F_2\left(\frac{L_x}{L_m^{D,S}}\right) + \frac{3}{4}F_2\left(\frac{L_x}{L_m^{D,T}}\right) + \frac{1}{4}F_2\left(\frac{L_x}{L_m^{C,S}}\right) + \frac{3}{4}F_2\left(\frac{L_x}{L_m^{C,T}}\right), \tag{6.8}$$

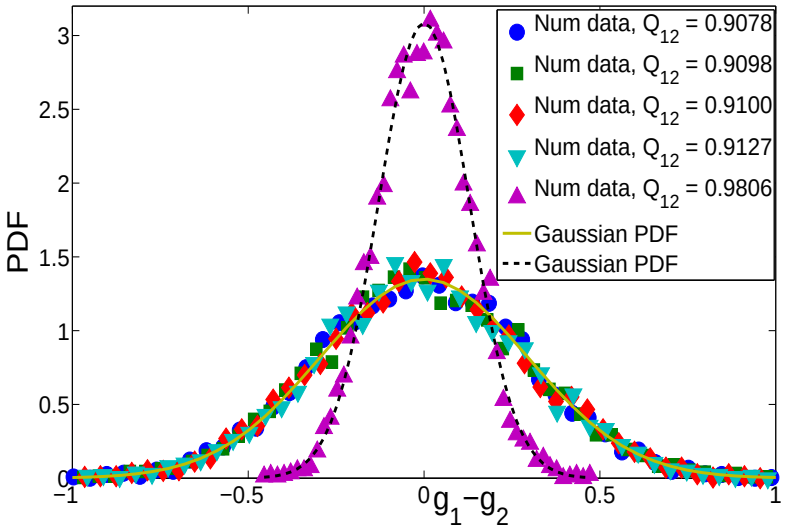

Figure 6.5: *Probability Density Function of $g_1 - g_2$ for comparable overlap $Q_{12} \approx 0.91$ (dots, squares, diamonds and down-pointing triangles). The up-pointing triangles represent two spin configurations with a different overlap: $Q_{12} \approx 0.98$. Plain and dotted lines are the gaussian interpolations for the respective value of Q_{12}.*

where $\delta g_i(V)$ and $g_i(V)$ are defined in the previous section. In the case of random excitations, explicit expressions for the diffusion lengths are derived:

$$\begin{aligned} L_m^{D,S} &= \frac{L_m}{\sqrt{1-Q_{12}}} \\ L_m^{D,T} &= \frac{L_m}{\sqrt{1+Q_{12}/3}} \\ L_m^{C,S} &= \frac{L_m}{\sqrt{1+Q_{12}}} \\ L_m^{C,T} &= \frac{L_m}{\sqrt{1-Q_{12}/3}} \end{aligned} \tag{6.9}$$

The function F_2 is defined in section 3.2.3.

Numerical results

The conductance correlation is plotted (figure 6.6) for each pair of spin configurations as a function of the spin correlation Q_{12}, and for different values of magnetic disorder J. The number of different spin configurations used for this study is 24. On these plots the correlation between spin configurations decreases from the left part to the right part (*i.e* from $Q_{12} = 1$ to 0) as we anticipated in section 6.1.2: the decorrelation between the conductances is larger if Q_{12} tends to zero (very different spin configurations). We also notice that the longer the sample, the larger the decorrelation of conductance: if the sample is longer, electrons diffuse on more impurities, the resulting dephasing is larger, and the corresponding correlation of conductance is smaller. The results presented in that figure consist in some of the **key results** of this study. For all values of magnetic disorder J there is a unique value of overlap that corresponds to a given value

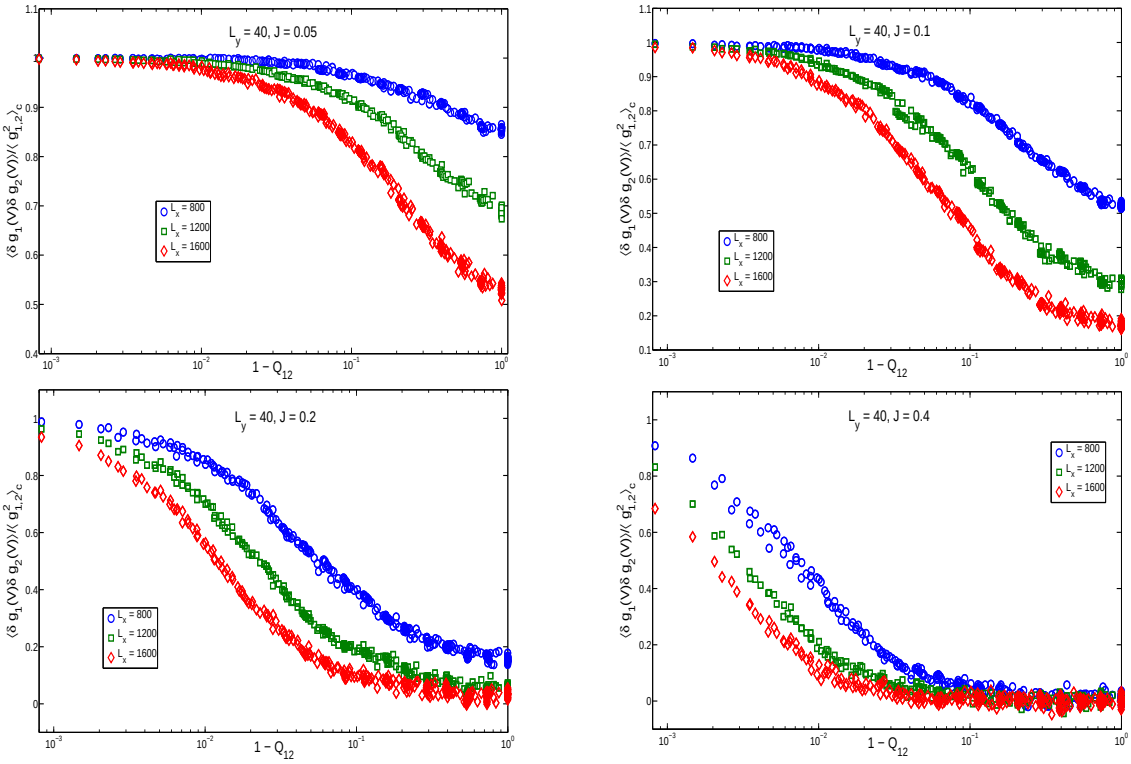

Figure 6.6: *Evolution of the conductance correlations, equation (6.2) as a function of overlap, in a semi-logarithmic scale. Different curves in the same plot correspond to different values of the longitudinal length L_x. Different figures correspond to different values of magnetic disorder J. The correlations of conductance are normalized by their value at $Q_{12} = 1$.*

of conductance correlation, and these plots *validate* the use of conductance correlations to have indirect access to the spin overlap of a spin glass.

The comparison of numerical calculations with the theoretical expression of equation (6.8) is given in figure 6.7. It appears that theory and numerical data are in good agreement. Note that theory is plotted with **no free parameter** as the magnetic length L_m has been determined with the study of the fluctuations of conductance, function of longitudinal length (section 5.3.1).

6.3 Spatially correlated spin excitations

In the previous study, we built spin configurations with random orientations between them as shown on figure 6.2. In this section we push our analysis further with the introduction of spatial correlations in the spin rotations.

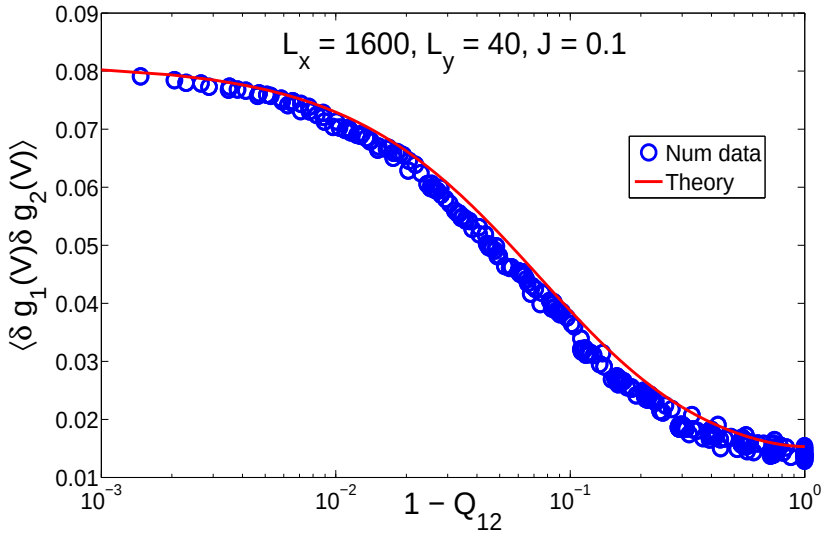

Figure 6.7: *Evolution of the conductance correlations, equation (6.2) as a function of overlap, in a semi-logarithmic scale, for a* 1600×40 *sample and* $J = 0.1$*. Numerical results are compared with theory.*

6.3.1 Creating spatially correlated spin configurations

Bounded box reversal

In the droplet theory [28], two different spin configurations differ by the reversal of all spins inside a bounded area of the sample (a droplet). To mimic this behavior[5] (as opposed to the previous mean field like excitations), we use the following algorithm to create new configurations. First we choose an initial random configuration and a value of overlap ($Q_{12} = 0.9$ in practice). The value of overlap imposes the number of spin flips occurring in the sample, denoted by N_{flips}. We then consider a box in the sample containing N_{flips} spins and we reverse almost all of them to create a first excited configuration. A second one is created by considering a box twice bigger and reversing half the spins in it, and so on until the box reaches the size of the sample[6]. Figure 6.8 shows both configurations and the overlap between them in the simpler case of Ising spins. As in the mean field case both configurations are random, but now spin flips occur preferentially in a bounded area of the sample. We allowed some spin flips outside the box, diminishing the number of flips inside the box (the total number of spin flips being fixed by the overlap) for a more realistic description of the excitation.

Spin Wave excitation

Another possible type of excitations in a Heisenberg spin glass consists in applying a spin wave to the sample. This corresponds to even stronger spatial correlations of the excitations. We first consider the same initial configuration as before, and we choose a value of overlap. The excited configuration is created by rotating all spins with the angle $\delta\phi = x\delta\phi_0$ along the z-axis, which is perpendicular to the sample. x is an integer that goes from 1 for the first row of the system to L_x for the last one. The value of $\delta\phi_0$ is determined by the overlap chosen, and is closely related

[5] we do not claim that we model real spin excitations that occur according to the droplet theory.

[6] the width w_{box} of all boxes is equal to L_y, the width of the sample. The length of each box is varied to produce the adequate excitation.

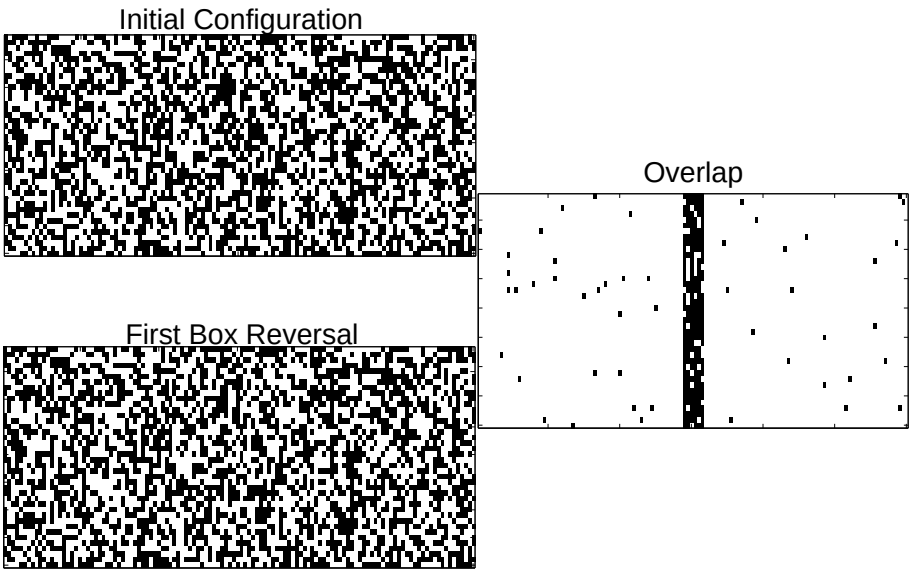

Figure 6.8: *Schematic view of two random configurations, and of the overlap in the case of bounded excitations. For the overlap, black squares represent spin flips between both configurations.*

to the spatial period of the Spin Wave. In figure 6.9 we plot the value of the overlap as a function of the period of the Spin Wave, to calibrate the Spin Wave.

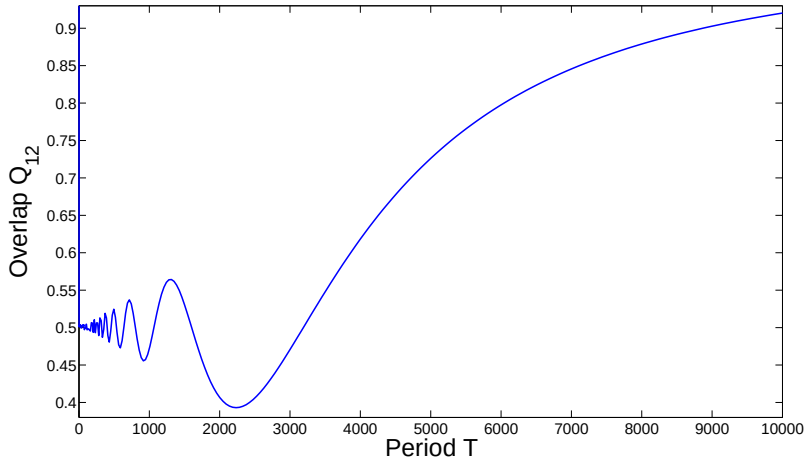

Figure 6.9: *Evolution of the overlap as a function of the period of the Spin Wave in units of lattice spacing. The sample has* $L_x = 1600$ *and* $L_y = 40$.

6.3.2 Random versus spatially correlated spin configurations

The study of the influence of the spatial correlations is performed at constant overlap, it is then impossible to draw curves of the type of 6.6. Moreover, no analytical expression such as equation (6.9) for the diffusion lengths is available for non mean field excitations. Hence we study the influence of spatial correlations through the behavior of these diffusion lengths as a function of the magnetic length L_m, for different values of magnetic disorder J.

Reduction of the number of parameters

In section 6.1.2, we have qualitatively shown that $L_m^{D,S}$ is the only diffusion length that diverges for $Q_{12} = 1$ and that is finite for $Q_{12} \neq 1$. Hence near $Q_{12} = 1$, this length dominates the behavior of the correlations. To show this, we define the difference:

$$\Delta\text{corr}(J, Q_{12}) = \langle g_{1,2}^2(V)\rangle_c - \langle \delta g_1(V)\delta g_2(V)\rangle. \tag{6.10}$$

This equation quantifies the variation of conductance correlations from $Q_{12} = 1$ to $Q_{12} < 1$. In figure 6.10, we plot this function for mean field like excitations (*i.e* using formulae (6.8) and (6.9)) in two cases: if all diffusion lengths are taken into account, or if only the Diffuson/singlet term is considered. Near the value $Q_{12} = 1$, this shows that it is justified to reduce the number of

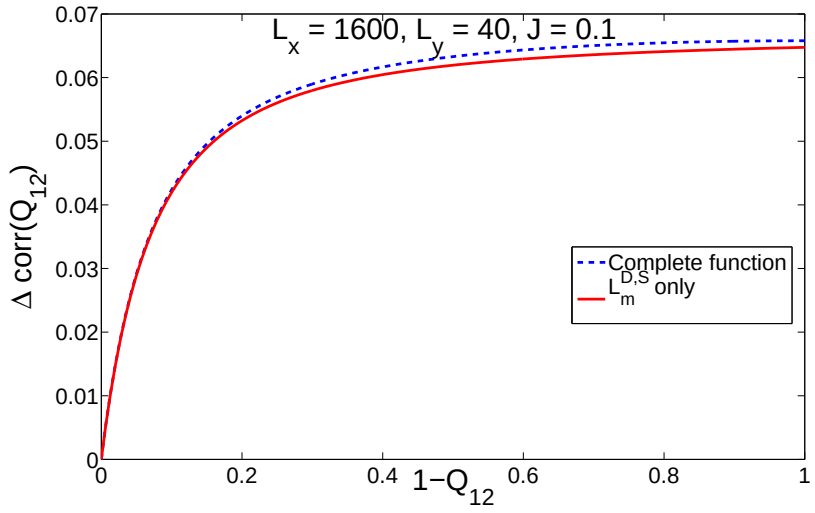

Figure 6.10: *Evolution of the function* Δcorr *(equation (6.10)) as a function of* Q_{12}*. The dashed line is plotted by considering the four terms of equation (6.8) and the plain line is plotted by taking into account only the Diffuson/singlet term.*

parameters and to consider only the Diffuson/singlet term. See also [146] for a non-linear sigma model study.

Numerical results

The function defined in equation (6.10) depends on Q_{12} but also on the longitudinal length of the system. It is then possible, as we did before for the UCF, to plot Δcorr as a function of longitudinal length and to fit the numerical data with theory (equation (6.8)). The fit parameter gives access directly to $L_m^{D,S}$; see figure 6.11 for the random configurations case. It allows a

determination of $L_m^{D,S}$ for the bounded as well as the Spin Wave excitations for different values of the magnetic disorder (*i.e* for different values of the magnetic length L_m).

Back to the magnetic length.
In section 5.3.2 we plotted the evolution of the magnetic length as a function of J (figure 5.21). On this curve we mentioned two different determinations of the magnetic length. The first one was a direct fit of the UCF curve as explained above. The second determination comes from the determination of $L_m^{D,S}$ and the application of the relation $L_m^{D,S} = L_m/\sqrt{1-Q_{12}}$. These two methods give comparable results.

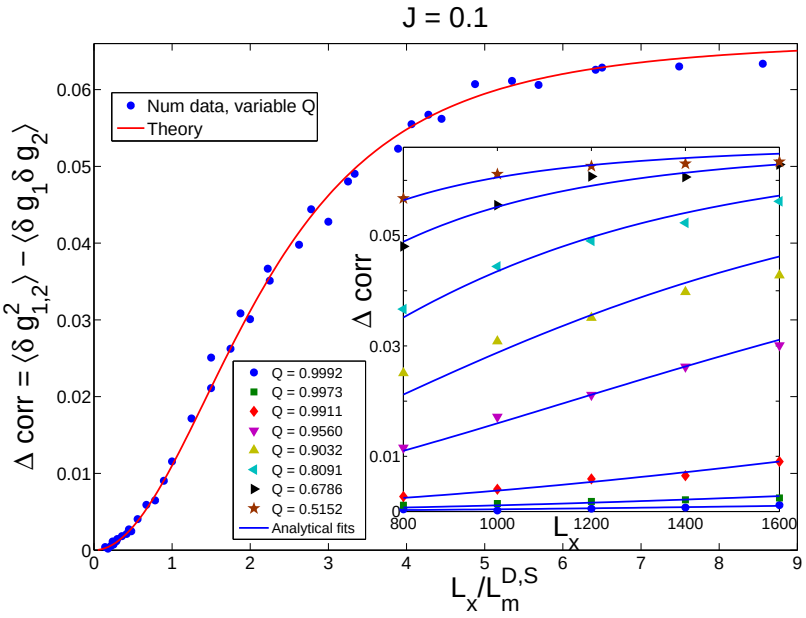

Figure 6.11: *Scaling evolution of the function* Δcorr *(equation (6.10)) as a function of* $L_x/L_m^{D,S}$ *for different values of overlap. In inset the fits of* Δcorr *as a function of* L_x *are shown. Different curves correspond to different values of overlap. The magnetic disorder is set to* 0.1.

The left curve of figure 6.12 gives the evolution of the dephasing rate for the Diffuson/singlet $(1/L_m^{D,S})^2$ as a function of the dephasing rate for electrons $(1/L_m)^2$ for random, bounded and Spin Wave excitations. $1/L_m^2$ is also a growing function of magnetic disorder J (see section 5.3.2). This plot shows that the Diffuson/singlet dephasing rate is proportional to the electron one as expected (blue dots), in the case of uniform configurations (mean field like). For spatially correlated configurations, the behavior is completely different, the Diffuson/singlet rate is a non-linear function of $(1/L_m)^2$. The more correlated the configurations, the stronger the effect, as $(1/L_m^{D,S})^2$ is almost constant in the case of Spin Wave excitations.

The right curve of figure 6.12 shows the evolution of the same quantities, for a different value of overlap and only for random and Spin Wave excitations for two different values of spatial period leading to the same value of overlap (see figure 6.9). The same conclusion applies.

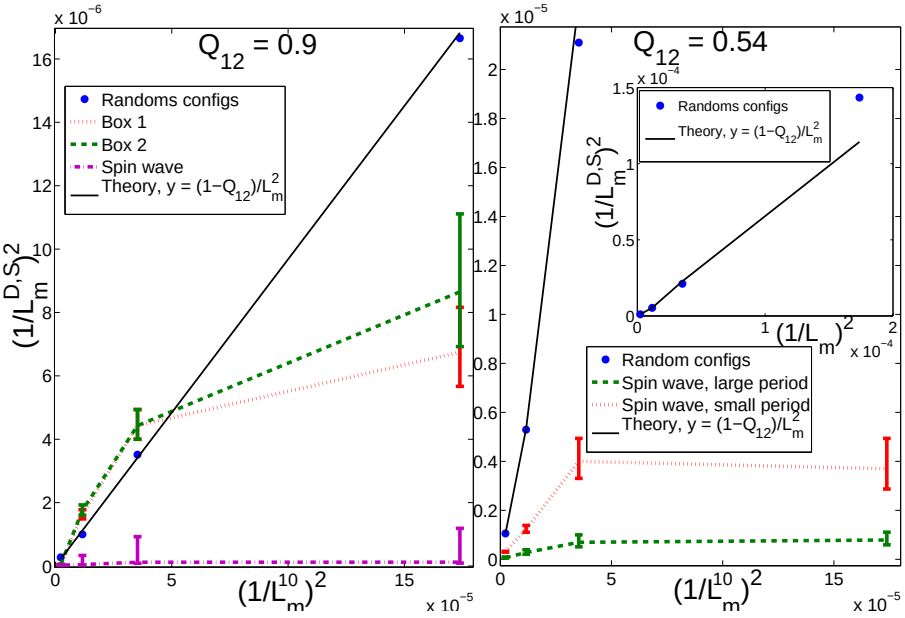

Figure 6.12: *Left figure : evolution of the Diffuson/singlet dephasing rate* $(1/L_m^{D,S})^2$ *as a function of the electronic dephasing rate* $(1/L_m)^2$ *for mean-field like, spin wave (dash dot), and boxed excitations. The overlap is 0.9 for all of them. The linear dependance corresponds to the analytical expression* $(1/L_m^{D,S})^2 = (1 - Q_{12})/(L_m^2)$*, valid in the absence of spatial correlations between the spin states. These results show a clear deviation from this behavior for strong spatial correlations, and the absence of any effective overlap. Right figure : same evolution for random configurations and for spin wave with two different spatial periods corresponding to the same overlap* ($Q_{12} = 0.54$)*. The stronger correlation (longer period) corresponds to the larger deviation from the linear law.*

Conclusion

In this part we validate the use of coherent transport as a probe of the spin state of a spin glass, as we managed to show that the difference between conductance distributions for each spin configurations is characteristic of the corresponding value of the overlap between the configurations. the route towards the experimental measurement of the overlap is open. Moreover we highlight at the end of this study a useful tool that discriminates between spatially correlated and spatially non correlated spin configurations. We now discuss the experimental studies in relation with these theoretical results and we show preliminary experimental results on measurements of conductance correlations.

6.4 Link with experiments

The experimental measurements of the conductance correlations in a Spin Glass nanowire are performed at the **Institut Louis Néel** in Grenoble (FRANCE) in the *Quantum Coherence* group lead by L. Saminadayar and L. Lévy. In figure 6.13 is a figure of one the experimental setup they use in that purpose. The experimental protocol followed is the one we presented in section 6.1.3.

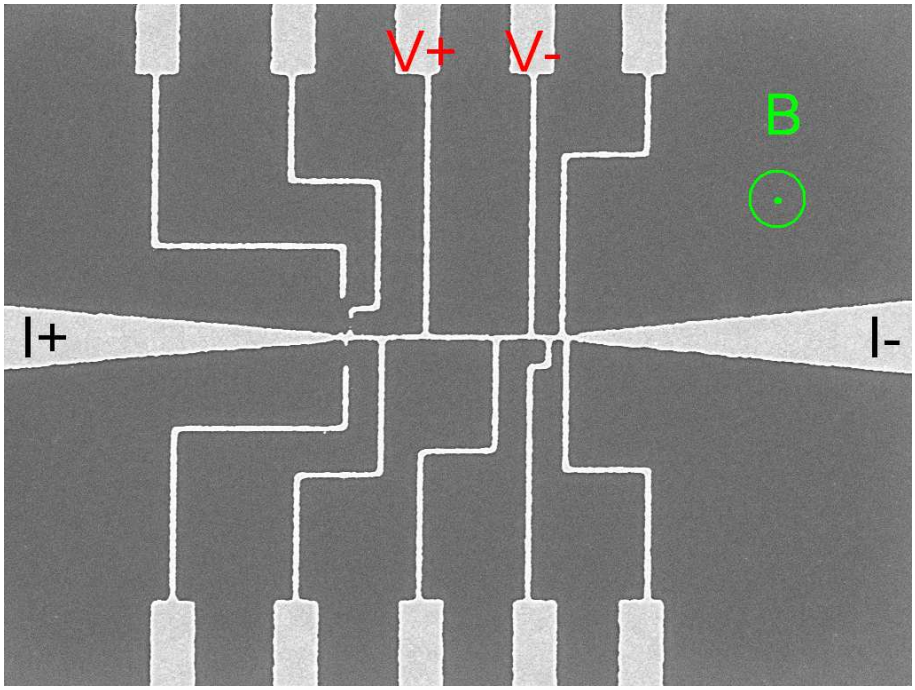

Figure 6.13: *View of an experimental Spin Glass nanowire, between the reservoirs denoted with $+I$ and $-I$. The total length of the wire is approximately $1\mu m$ ($\sim L_\phi$). The width of the wire is $w = 50nm$ and the thickness is $t = 40nm$. The presence of electrodes along the wire allows to measure the conductance for different longitudinal lengths.*

In figure 6.14, we present preliminary results of this work. The left curves of this figure are magnetoresistance measurements on the wire presented in figure 6.13, which is constituted of pure Ag. A first magneto fingerprint is made at low temperature T_0 (in practice, $T_0 \approx 500mK$), then the system is heated up to $T_1 = 15K$ during $15h$. After waiting at high temperature, the wire is cooled down again at temperature T_0, and a second magneto fingerprint is made. The correlation between both traces is almost 1.

If the wire considered is not pure Ag but a Spin Glass Ag:Mn, with 400 ppm of Mn, the results are different: the system, initially at temperature T_0' below the spin glass temperature T_g is heated up at temperature $T_1' = 20T_g$ during $15min$, and is then cooled down to T_0'. As previously, magneto conductance traces are measured at temperature T_0', before and after the heating. At that time, the correlation between both traces decreases to almost 20%. Notice that on the right part of the figure, both traces are vertically shifted for clarity. The conclusion of this preliminary study is that it is possible to decorrelate traces only by introducing magnetic impurities (the only difference between the results presented in the left and in the right part of figure 6.14 is the presence of magnetic impurities on the right).

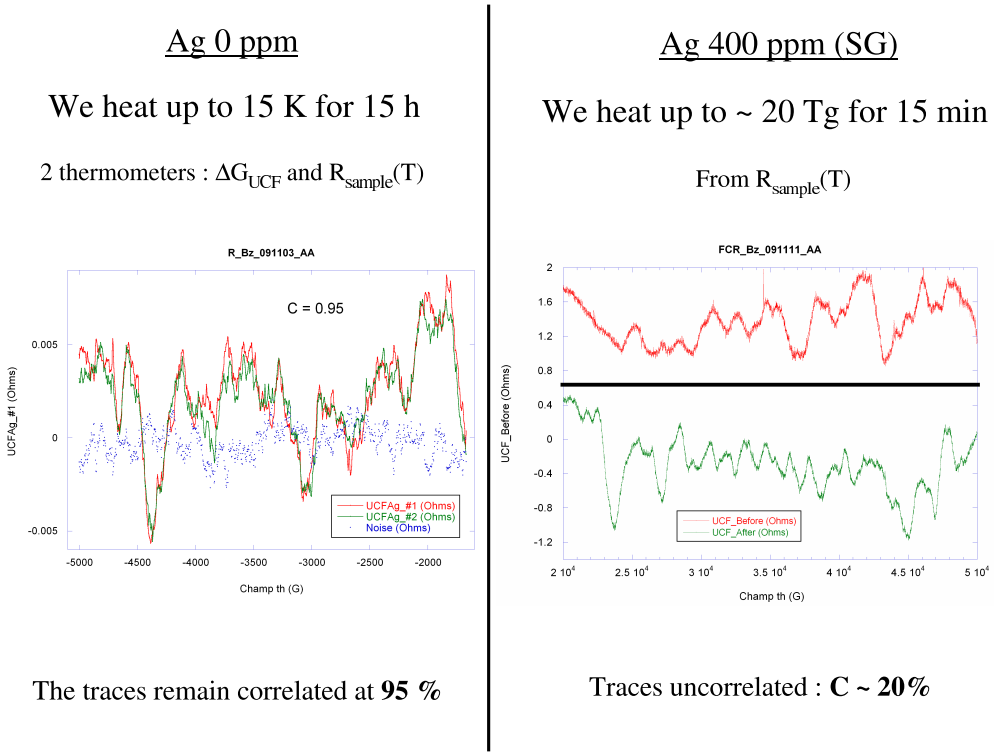

Figure 6.14: *Experimental results of magnetoresistance measurements, for a wire of pure Ag (left curves) and Ag:Mn (right curves) with Mn at a concentration of 400 ppm (parts per million).*

To conclude on this chapter, we proved numerically that it is possible to use electronic transport in the coherent regime to deduce crucial information on the spin overlap Q_{12}. We first showed that the statistical distribution of the difference of conductances calculated for the same value of scalar disorder (same realization of disorder V), but for two different realizations of magnetic disorder (different orientations of the frozen spins of each impurity) depend only on this spin overlap. Moreover, we quantized the decrease of the correlation when configurations are more and more uncorrelated (*i.e* $Q_{12} \to 0$). We also addressed the issue of the type of excitations, showing that one diffusion length ($L_m^{D,S}$) is sensitive to it, which opens the possibility to imagine a probe of the spatial correlations between two spin configurations. This theoretical study is related to experimental measurements of magnetoconductance through the ergodic hypothesis, whose validity was studied in the previous chapter, and preliminary results show that it is indeed possible to decorrelate conductance traces only by adding magnetic impurities.

Part III

The quantum Ising spin glass: a mean field viewpoint

L'ordre est le plaisir de la raison, mais le désordre est le délice de l'imagination.

Paul Claudel, Le Soulier de satin

Je crois pouvoir dire sans risque de me tromper que personne ne comprend la mécanique quantique...

Richard Feynman

Chapter 7
A quantum spin glass?

7.1 Introduction: the quantum SK model

7.1.1 The quantum SK model

In chapter 1, we introduced the classical SK model, whose goal is to model the low temperature spin glass phase at the mean field level for Ising spins, and the breaking of the freezing of the spins due to thermal fluctuations (see equation (1.14)). One way to take the quantum nature of the Ising spins into account consists in considering a quantum generalization of the random p-spin spherical model following [147, 148, 149].

Another way to take the quantum tunneling of spins into account is to consider the SK model in a transverse magnetic field. The advantage of this method lies in the fact that the intensity of the quantum effects is tunable via the intensity of the transverse magnetic field. In the next chapter, we use this method to deduce semi-classical solutions of the quantum SK model in the limit of a weak transverse magnetic field. The strength of quantum tunneling is denoted Γ in the following. At zero temperature, we envisage a quantum phase transition when the Γ of the quantum effects is varied: from a magnetically frozen state (a spin glass state) if $\Gamma < \Gamma_c$ to a paramagnetic phase if $\Gamma > \Gamma_c$. See [150] for a detailed study of quantum phase transitions and section 7.2.2 for a brief introduction. If things are clear on the lines $(T = 0, \Gamma)$ and $(T, \Gamma = 0)$, the goal of this part is to study the competition between thermal and quantum effects.

7.1.2 The replica theory

Reminder of chapter 1

As introduced in section 1.4.1, the replica theory is useful in the study of spin glasses in particular. Consider the more general case of a disordered system with a Hamiltonian that depends on a random parameter J. Recall that in the case of the SK model, J represents the random (in amplitude and in sign) coupling between the spins of impurities constituting the spin glass (see equation (1.14)) due to RKKY or dipolar interactions for instance. To find the ground state of such a system, the usual method consists in finding the minima of energy (or more precisely in free energy as the temperature is fixed and finite[1].). The physical quantity experimentally is the free energy of the system, and more accurately its disorder average $\overline{F[J]}$, as it is self-averaging. Disorder averages are defined as follows:

$$\overline{F[J]} = \int \mathcal{D}J \mathcal{P}[J] F[J], \tag{7.1}$$

where $\mathcal{P}[J]$ is the statistical distribution of the random parameter J. From now on, disorder averages are denoted with an over line as in the previous equation, and not with $\langle \cdot \rangle$ any more. Usual statistical mechanics [12] tells us that the free energy is related to the Hamiltonian of the system via its partition function $Z[J]$:

$$\overline{F[J]} = -k_B T \overline{\log Z[J]}, \tag{7.2}$$

where k_B is the Boltzmann constant and T is the temperature of the system. In section 1.4.1, we showed that the logarithm can be written as the limit:

$$\overline{\log Z[J]} = \lim_{n \to 0} \frac{\overline{Z^n[J]} - 1}{n}. \tag{7.3}$$

[1] we consider the canonic statistical ensemble.

The so called *replica trick* consists in considering n as an integer and in interpreting $Z^n[J]$ as the product of the partition function of n (non interacting) replicas of the system, all evaluated for the same value of disorder parameter J:

$$Z^n[J] = Z_1[J] \times Z_2[J] \times \cdots \times Z_n[J], \tag{7.4}$$

where $Z_\alpha[J]$ is the partition function of replica α. To derive the "true" partition function, it is necessary to take the limit $n \to 0$.

Important:
one interpretation of the replica trick is the following: the partition function of the system $Z[J]$ is a random quantity that depends on the random J's. It then has a given statistical distribution $\mathscr{P}[Z]$. The calculation of the terms $Z^n[J]$ for integer n replaces the study of the whole statistical distribution $\mathscr{P}[Z]$ by the study of all the moments of the distribution.

To compare the different replicas of the system, we have introduced the spin overlap $Q^{\alpha\gamma}$ in chapter 1, equation (1.17) (which is called Q_{12} in chapter 6, in the case of Heisenberg spins). We discuss this quantity in the case of a non standard full RSB[2] *Ansatz* [151, 152], as described below. In this part, we define β as:

$$\beta = \frac{1}{k_B T}, \tag{7.5}$$

where k_B is the Boltzmann constant.

Full RSB

Due to frustration, the ergodicity[3] of the phase space is broken [153], that is, the case where there are very many stable (or metastable) states. We have seen in chapter 1, for temperatures below T_g, a multi-valley picture for the free energy (see figure 1.14). This implies that the system is trapped in one region of phase space with no hope to traverse the complete phase space. A mean-field picture of spin glasses states the existence of a lot of these ergodic components called metastable states with diverging energy barriers (the barriers between energy valleys are diverging). Starting with two different replicas in the paramagnetic phase (*i.e* these replicas are two different points in phase space), they can be found in two different metastable states when lowering the temperature (in an ergodic system, they would be found at least in the same state, at low temperature). From this simplistic view, we illustrate the origin of the breaking of the symmetry of replicas (under permutation) as illustrated in figure 7.1.

Why do we use a non standard RSB scheme?
The *Ansatz* we describe here is non standard and is described in [151, 152]. This scheme of RSB allows to deduce from the Hamiltonian the identical free energy functional that has been calculated from dynamical arguments by Sompolinsky [154]. We use this algorithm by analogy with the classical case to deduce to deduce the low temperature solution of the SK model according to [155]. Moreover, this scheme breaks the symmetry of the replica matrix in both diagonal and off-diagonal blocks. The parameters r_i (see below) are representatives of this breaking scheme. These parameters were also introduced by Goldschmidt and Lai [156] for a one step RSB for

[2]Replica Symmetry Breaking.
[3]we remind the reader that in this part, the ergodicity describes the ability (or not) for the system to reach all states in the phase space.

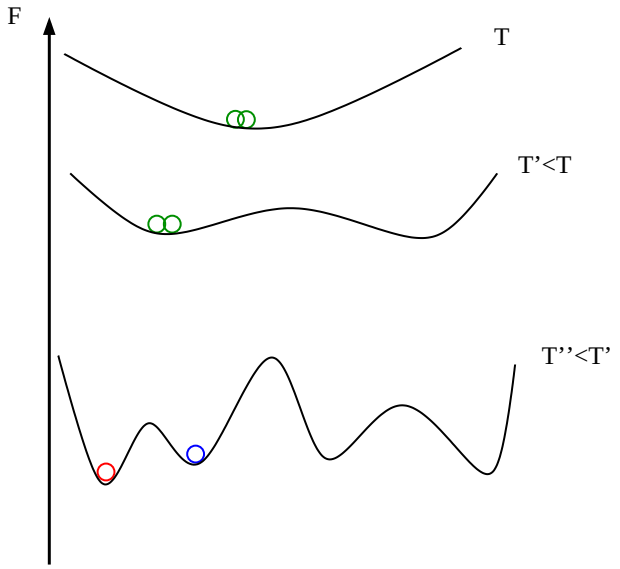

Figure 7.1: *Illustration of ergodicity breaking as in figure 1.14, and of the ansatz of replica symmetry breaking. Two replicas are schematically represented by circles. $T > T_g$ and $T' < T_g$.*

an Ising spin glass in a transverse magnetic field. To compare our solutions with theirs, it was obvious to use the De Dominici's RSB scheme.

$Q^{\alpha\gamma}$ is a $n \times n$ matrix. In the symmetric case, all the coefficients, except on the diagonal, are equal to q_{EA}. The algorithm to break the symmetry of replicas is recursive: consider **step 0** of symmetry breaking. The replicas are regrouped in different groups of same size p_0. The membership in a group is characterized by an overlap between the constituting replicas equal to q_0. The overlap between replicas of different groups is equal to r_0. By regrouping the replicas in the overlap matrix, we end up with the following block matrix:

$$Q^{\alpha\gamma} = \left(\begin{array}{c|c|c} q_0 & r_0 & r_0 \\ \hline r_0 & q_0 & r_0 \\ \hline r_0 & r_0 & q_0 \end{array}\right).$$

Here we have $(n/p_0)^2$ groups of replicas, each constituted of p_0 replicas.

The **first step** of RSB consists in considering the q_0 matrices of size $p_0 \times p_0$ and to apply the same algorithm as before. Each q_0 matrix reads then:

$$(q_0)_{p_0} = \left(\begin{array}{c|c|c} q_1 & q_0 & q_0 \\ \hline q_0 & q_1 & q_0 \\ \hline q_0 & q_0 & q_1 \end{array}\right).$$

In this matrix all blocks are of size $p_1 \times p_1$ ($p_1 < p_0$), and $q_1 > q_0$. We apply the same sequence to the r_0 matrices (they are of size $p_0 \times p_0$ too):

$$(r_0)_{p_0} = \left(\begin{array}{c|c|c} r_1 & r_0 & r_0 \\ \hline r_0 & r_1 & r_0 \\ \hline r_0 & r_0 & r_1 \end{array}\right).$$

This procedure is iterated K times on diagonal blocks $(q_i)_{p_i}$ and $(r_i)_{p_i}$ of size[4] p_i for a K-step RSB Ansatz. The successive sizes of matrices will be: $p_0 > p_1 > \cdots > p_K$. At that time, the limit $p_0 \gg p_1 \gg \cdots \gg p_K \to \infty$ will be considered, and the number of steps of RSB will be sent to infinity: $K \to \infty$. Consider a given step, denoted by i ($i \in [1, K]$). If we consider a full RSB, the variable i/K becomes continuous, is taken between 0 and 1 and is labeled with x. The evolution from step i to step $i+1$, becomes infinitely small and is labeled by δx. The quantity $q_i - q_{i-1}$ will be equal to $\mathrm{d}q/\mathrm{d}x\delta x$ at first order in δx. In the next chapter we will study the influence of this procedure on the thermodynamic quantities of the quantum Ising spin glass. The next section deals with the presentation of the model and the motivations of this work.

At this stage, notice that the use of a hierarchical algorithm is evident as the structure of the free energy is also hierarchical, and that the variable $x = i/K$ that has just been defined, is a measure of the energy scale under consideration: the step number i characterizes the number of different groups of replicas we consider, which corresponds roughly to the number of energy valleys existing in the energy landscape: if we look at figure 7.1, the first free energy is at temperature $T > T_g$, replicas are symmetric which corresponds to one single minimum in the free energy landscape. If the temperature is decreased such as $T' \lesssim T_g$, the free energy landscape presents two minima, which can be associated to two different groups of replicas (one step of RSB). If the temperature is further decreased, the appearance of more energy valleys is related to higher steps of RSB.

7.2 Quantum fluctuations

7.2.1 A two-level model

To explain hallmarks of disordered materials in general as the anomalous temperature behavior[5] in the specific heat C_v, Anderson et al [157] and Philips [158] proposed a two level system (TLS) approach. In its standard form, we assume the presence in the amorphous solid of degrees of freedom (atoms, defects, ...) that possess two states of local quasi-equilibrium (*i.e* local minima in the energy landscape). In the case of spin glasses, these two states are related with the vision of a hierarchical free energy landscape of figure 1.14. We moreover suppose that the temperature is low enough to avoid thermal activation between the two states: the height of energy barriers is big enough compared to thermal energy. As thermally activated processes are highly improbable, one is left with the idea of tunneling between two states. Tunneling can occur if the height V and the width d of the barrier are small enough. In the same way, the energy difference Δ between both states must be not too large. See figure 7.2 for the notations. As concerns disordered systems in general, the precise nature of these tunneling objects is still controversial. We note $\Delta = E_2 - E_1$, and Δ^0 the tunneling amplitude which is given by:

$$\Delta^0 = \hbar\omega e^{-d/\xi}, \tag{7.6}$$

where $\hbar\omega$ is approximately the zero point enregy $(E_1 + E_2)/2$ and ξ is the penetration length in the energy barrier

$$\xi = \sqrt{\frac{\hbar}{2mV}}. \tag{7.7}$$

The Hamiltonian of such a system is then:

$$\mathcal{H}_{TLS} = \frac{\Delta}{2}\sigma^z + \frac{\Delta^0}{2}\sigma^x, \tag{7.8}$$

[4] the off diagonal blocks $(q_{i-1})_{p_i}$ and $(r_{i-1})_{p_i}$ are remained untouched.

[5] *i.e* the linear dependence of the heat capacity in temperature in amorphous materials for temperatures below $1K$.

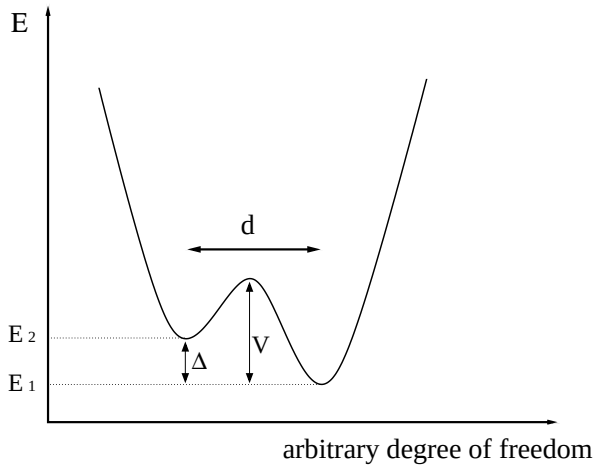

Figure 7.2: *Double well potential with an energy barrier of height V and width d. The energy difference between the two states is Δ. The x-axis is an arbitrary degree of freedom. It is the orientation of the spin in the case of an Ising spin glass.*

where σ^z and σ^x are Pauli matrices. In the case of Ising spin glasses, the local TLS represents the equilibrium orientations of the Ising spin (aligned or anti aligned with the z-axis), and the tunneling between both states accounts for the quantum fluctuations of the spins. Hence this Hamiltonian (7.8) models the quantum fluctuations of an Ising spin. Thermal fluctuations of the spins are modeled by the first term in the SK Hamiltonian, which alone accounts for the description of the spin glass phase in the case of classical Ising spins.

7.2.2 A transverse magnetic field as source of quantum fluctuations

In the previous section, we have seen that the quantum fluctuations of an Ising spin are taken into account with a term that has the form:

$$\Gamma\sigma^x, \tag{7.9}$$

where Γ is the tunneling amplitude. This term can be written as:

$$\Gamma\sigma^x = \vec{\Gamma}\cdot\vec{\sigma}, \tag{7.10}$$

with $\vec{\Gamma}$ pointing in the x direction. Then both terms in the TLS Hamiltonian can be written as:

$$\mathcal{H}_{TLS} = (\vec{h}+\vec{\Gamma})\cdot\vec{\sigma}, \tag{7.11}$$

where $\vec{h}$ is a longitudinal magnetic field and $\vec{\Gamma}$ is the previous transverse magnetic field.

This model is a particular case of a more general model, called the rotor spins model [159, 160] and defined as:

$$H_{Rd} = \frac{g}{2}\sum_i \mathbf{L}_i^2 - \frac{1}{2}\sum_{(i,j)} J_{ij}\vec{n}_i\cdot\vec{n_j}, \tag{7.12}$$

where $n_{i\mu}$ are the M components of a unit-length rotor $\vec{n}_i$ at site i ($i \in [1,N]$). The $L_{i\mu\nu}$ ($\mu<\nu$, $\mu,\nu=1,\ldots,M$) are the $M(M-1)/2$ components of the angular-momentum generator $\vec{L}_i$ in the rotor space, and J_{ij} are mutually uncorrelated exchange constants. At zero temperature,

this system presents a quantum phase transition. The corresponding Ising model is found by imposing that the rotor spins only have two components ($M = 2$). See [150] for a complete review.

7.2.3 Mean field level

The mean field model we will consider in the following is the Sherrington-Kirkpatrick model in a transverse magnetic field, which is equivalent to the previous rotor model with $M = 2$, and a longitudinal magnetic field term:

$$\mathcal{H}_{QSK} = -\sum_{(i,j)} J_{ij}\sigma_i^z\sigma_j^z - \Gamma\sum_i \sigma_i^x - h\sum_i \sigma_i^z. \tag{7.13}$$

In this model, (i, j) represents distinct pairs of spins, and each pair is counted once. We consider a set of N spins. $\sigma_{i,j}^{z,x}$ are Pauli matrices as explained in the previous section. The couplings J_{ij} are distributed with a gaussian statistics as written in equation (1.9):

$$\mathcal{P}[J_{ij}] = \prod_{i<j}\sqrt{\frac{N}{2\pi J}}\exp\left(-\frac{NJ_{ij}^2}{2J^2}\right).$$

This distribution has zero mean and a variance which is equal to J^2/N. The factor $1/N$ has been explicitly written in this equation to obtain finite thermodynamic quantities when $N \to \infty$.

The phase diagram of the quantum SK model is presented schematically in figure 7.3. As studied in the previous section, a quantum phase transition appears at zero temperature. Moreover, a "classical" phase transition occurs for $\Gamma = 0$ is shown in chapter 1: without any transverse magnetic field, the quantum tunneling amplitude for the Ising spins vanishes. From these two extremal points, we extrapolate the phase diagram. At the end of the derivation of the free energy, we will consider the limit of a weak transverse magnetic field[6], to derive the equations of motions. The study will also be performed at low temperature, as shown on figure 7.3. See also [161].

7.3 Experimental realization of a quantum spin glass

In this section we present results showing the experimental interest of studying theoretically the quantum SK model.

7.3.1 The proton glass

First, an extension of the SK model has been proposed to describe the proton glass. Experimentally, the compound used is $Rb_{1-x}(NH_4)_xH_2PO_4$ [162]. This is a hydrogen-bonded solid solution of ferroelectric (RbH_2PO_4) and antiferroelectric ($NH_4H_2PO_4$) isostructural[7] crystals, commonly abbreviated as RADP. By analogy with spin glasses, the frozen state is believed to be due to quenched random interactions between the pseudospin degrees of freedom which represent the equilibrium positions of the hydrogen bonds [163, 164], as schematically plotted in figure 7.4. Each hydrogen atom is linked with a covalent bond (plain line) to an oxygen atom and with a so called hydrogen bond (dashed line) with another oxygen atom. The "up" state of the pseudospin represents the configuration where the hydrogen is covalently bounded to oxygen 1, the "down"

[6] *i.e* we consider a semi-classical development of the solutions.

[7] in the high-temperature disordered paramagnetic phase.

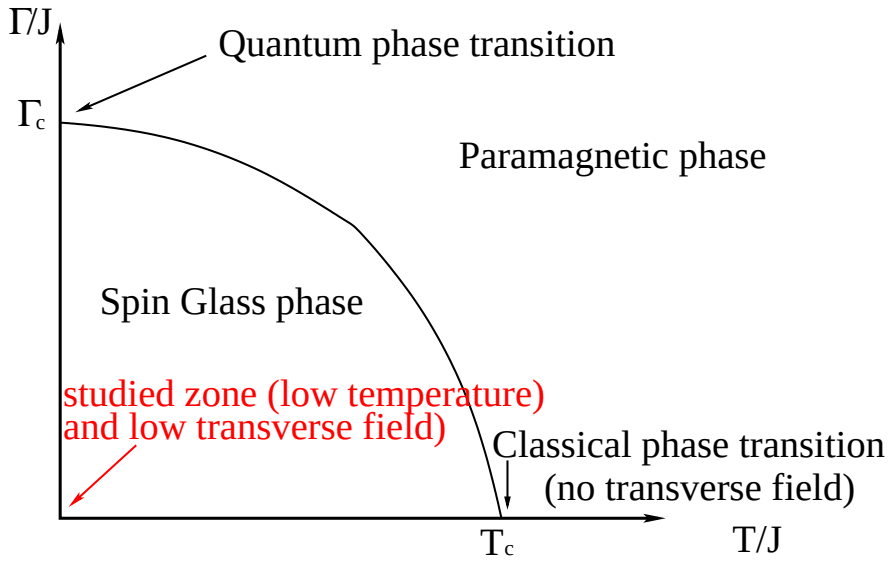

Figure 7.3: *Schematical representation of the phase diagram of the quantum SK model.* Γ *is the tunneling amplitude of the Ising spins and* T *is the temperature.*

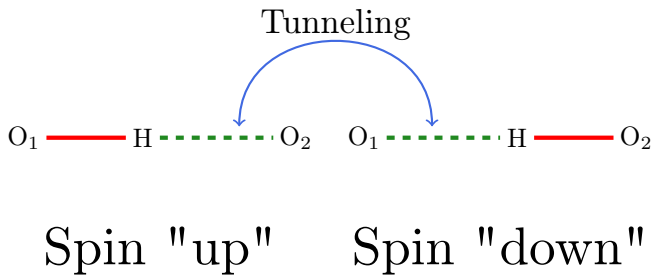

Figure 7.4: *Representation of the pseudospin degree of freedom. Solid line represent a covalent bond, the dashed line represent a hydrogen bond.*

state of the pseudospin represents the configuration when the hydrogen is covalently bound to oxygen 2. The tunneling of the proton from one state to the other, gives the direct relation between this compound and the quantum SK model. It appears nevertheless that the proton glass is not just an analogue of the quantum spin glass as the presence of an intrinsic random field adds new features to the proton glass. This presence of the intrinsic random field is due to the nonsymmetrical position of the NH_4 groups with respect to the surrounding cations (Rubidium ions), that tilts randomly the proton double well potential.

7.3.2 Lithium-Holmium compounds

Another example of an experimental realization of a quantum Ising spin glass is $LiHo_xY_{1-x}F_4$. Generic compounds $LiRF_4$ where R is a rare earth ion are body centered tetragonal lattices [165]. The Ho^{3+} ion is magnetic whereas the Y^{3+} ion is non magnetic. The single-ion anisotropy is Ising with the moments ($\mu_{eff} = 7\mu_B$) derived from the ground state doublet of Ho^{3+} lying

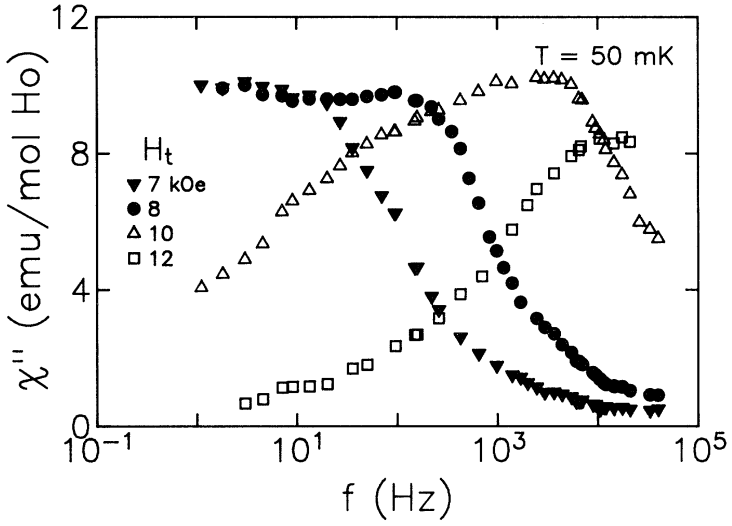

Figure 7.5: *Imaginary part of the susceptibility over many decades in frequency f for $T < T_g$. The flat response at low f for small transverse fields H_t is a signature of spin glasses. With increasing H_t, the spectral response becomes paramagnetic.*

parallel to the c axis. The dominant interactions between the magnetic ions are dipolar, and the pure compound ($x = 1$) is a ferromagnet with an essentially perfect mean field transition at $T_c = 1.53$K. When this compound is diluted (by replacing Ho^{3+} ions by Y^{3+} ions), the long range order can be broken (due to the competition between ferro- and antiferromagnetic interactions in a dipolar-coupled system), and disorder leads to a spin glass at $x = 0.167$, with a transition temperature T_g of order 0.1K.

The first excited crystal-field level in $LiHo_xY_{1-x}F_4$ is 9.4K above the ground state doublet. At the low temperatures of the experiments of [166, 167, 168] ($0.025K \leq T \leq 0.25K$), only the Ising doublet is appreciably populated. The application of an external magnetic field perpendicularly to the crystallographic direction of the spins of this Ising spin glass, gives an experimental realization of a quantum spin glass with tunable quantum fluctuations. In figure 7.5 is presented one result on the imaginary part of the susceptibility for different values of the transverse field. It shows that if the system is in the spin glass phase for $\Gamma = 0$ (it is called H_t in that figure), it enters the paramagnetic phase if the transverse field is increased.

Recent numerical studies [169] using the Monte Carlo method have renewed interest on the subject, establishing the occurrence of a transition for the classical system, but questioning the issue of the transition at finite temperature and transverse magnetic field, idea also supported experimentally in [170]. In this last article, the authors also claim the occurrence of the quantum phase transition at zero temperature. Their analysis of experimental results under the picture of the droplet theory (see section 1.4.2) supports the validity of this picture. Nevertheless, both articles question the description of this compound in terms of a transverse field Ising spin glass.

In the next chapter, we present the derivation of the Quantum SK model as well as its results at low temperature and low magnetic field.

Chapter 8
Mean field treatment of the quantum Ising spin glass

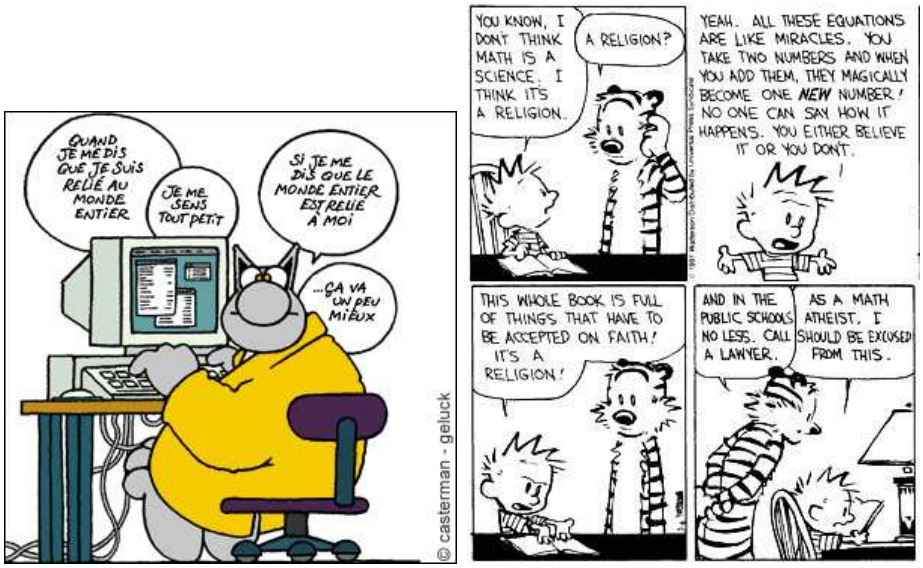

8.1 The free energy and replica theory

8.1.1 The Interaction Representation

The model

As we have seen in chapter 7, we consider in the following the Hamiltonian $\mathcal{H}_{QSK}$ of equation (7.13). The couplings J_{ij} are random and their statistical distribution $P[J_{ij}]$ is given by (7.14). σ^x and σ^z are the usual Pauli matrices:

$$\sigma^z = \begin{pmatrix} 1 & 0 \\ 0 & -1 \end{pmatrix} \quad \text{and} \quad \sigma^x = \begin{pmatrix} 0 & 1 \\ 1 & 0 \end{pmatrix}$$

Application of the replica theory

As explained in section 7.1.2, it is possible to replace the study of the statistical distribution of partition functions $\mathscr{P}[Z]$ by the study of the moments $\overline{Z^n[J]}$ of that distribution (n is supposed integer and large). This replicated partition function is given by:

$$Z^n[J] = \operatorname*{Tr}_{\{S_i^\alpha\}} \exp(-\beta \mathcal{H}_{\text{rep}}), \tag{8.1}$$

where $\mathcal{H}_{\text{rep}}$ is the replicated Hamiltonian

$$\mathcal{H}_{\text{rep}} = -\sum_{(i,j)} J_{ij} \sum_{\alpha=1}^{n} \sigma_i^{z,\alpha}\sigma_j^{z,\alpha} - \Gamma \sum_{i=1}^{N}\sum_{\alpha=1}^{n} \sigma_i^{x,\alpha} - h\sum_{i=1}^{N}\sum_{\alpha=1}^{n} \sigma_i^{z,\alpha}, \tag{8.2}$$

and $\{S_i^\alpha\}$ is a basis of the Hilbert space of the replicated Hamiltonian. Remember that $\beta = 1/(k_B T)$. As σ^x and σ^z do not commute, we need to find a new way to calculate the partition function, by comparison to the classical case. Numerous work has been done on the quantum Ising spin glass [161, 171] using, at this point, the so called Suzuki-Trotter formula [172, 173]. This formula replaces a d dimensional quantum system by a $(d+1)$ dimensional Ising system. The extra dimension is a time dimension. Using this technique, much work has been done either at zero temperature [171], or using only the replica symmetric ansatz [161] or one step of RSB [156].

We will not apply this strategy, as the results from this method do not give directly comparable results with the classical case. We choose to use the Interaction Representation to extend the classical case, and the derivation initiated by Parisi, which implies a full (*i.e* infinite number of steps) RSB, following [151, 152].

The Interaction Representation

We choose the free part H_0 of the Interaction Representation to be the transverse field part of the replicated Hamiltonian. The reason of this choice is that the σ^x term is the only one that is purely linear in spin operator (as we have one linear and one quadratic term in σ^z in equation (7.13)). This implies that the only time dependent operator is σ^z as we will see below (equation (8.9)). See reference [174] for a pedagogical introduction to this representation:

$$H_0 = -\Gamma \sum_{i=1}^{N}\sum_{\alpha=1}^{n} \sigma_i^{x,\alpha}. \tag{8.3}$$

In this interaction representation, we write the operator $\exp -\beta\mathcal{H}_{\text{rep}}$ as

$$e^{-\beta\mathcal{H}_{\text{rep}}} = U(\tau=\beta), \quad \text{with} \quad U(\tau) = e^{-\tau\mathcal{H}_{\text{rep}}} = e^{-\tau H_0}U_I(\tau). \tag{8.4}$$

The determination of the operator $U_I(\tau)$ goes as follows: we differentiate U with respect to τ, and we deduce a differential equation for U_I:

$$\frac{\mathrm{d}U(\tau)}{\mathrm{d}\tau} = -\mathcal{H}_{\text{rep}} \underbrace{U(\tau)}_{e^{-\tau H_0}U_I(\tau)} = -H_0 e^{-\tau H_0}U_I(\tau) + e^{-\tau H_0}\frac{\mathrm{d}U_I(\tau)}{\mathrm{d}\tau} \tag{8.5}$$

$$\Rightarrow \frac{\mathrm{d}U_I(\tau)}{\mathrm{d}\tau} = -e^{\tau H_0}(\mathcal{H}_{\text{rep}} - H_0)e - \tau H_0 U_I(\tau) = -(\mathcal{H}_{\text{rep}} - H_0)U_I(\tau) \tag{8.6}$$

$$\Rightarrow U_I(\tau) = \mathcal{T}e^{-\int_0^\tau \mathrm{d}\tau'(\mathcal{H}_{\text{rep}}-H_0)(\tau')}, \tag{8.7}$$

where the $\mathcal{T}$ operator is the time ordering operator and is defined as (A and B are two operators which do not commute):

$$\mathcal{T}A(\tau)B(\tau') = \theta(\tau-\tau')A(\tau)B(\tau') + \theta(\tau'-\tau)B(\tau')A(\tau). \tag{8.8}$$

The function θ is the Heaviside step function.

Note that in this representation, it is possible to express explicitly the time[1] dependent component of the Hamiltonian. We now focus on the two spin components σ^x and σ^z. It is obvious to see that the first one commute with $\exp(-\tau H_0)$, so σ^x is independent of τ. Therefore, the other component σ^z becomes time dependent and its dependence is given by:

$$\sigma_i^{z,\alpha}(\tau) = e^{\tau H_0}\sigma_i^{z,\alpha}e^{-\tau H_0} = e^{\tau\Gamma\sigma_i^{x,\alpha}}\sigma_i^{z,\alpha}e^{-\tau\Gamma\sigma_i^{x,\alpha}} \text{ as } [\sigma_i^{x,\alpha},\sigma_j^{z,\gamma}] = 0 \text{ if } i\neq j \text{ or } \alpha\neq\gamma. \tag{8.9}$$

This time dependent spin component can be written in the following way:

$$\sigma_i^{z,\alpha}(\tau) = \cosh(2\tau\Gamma)\sigma^z - \sinh(2\tau\Gamma)\imath\sigma^y, \tag{8.10}$$

where σ^z is the matrix defined above and σ^y is the third Pauli matrix, which verifies:

$$[\sigma^x,\sigma^z] = -2\imath\sigma^y. \tag{8.11}$$

To lowest order in Γ (semi-classical limit), equation (8.10) reads:

$$\sigma_i^{z,\alpha}(\tau) = \sigma^z - 2\imath\tau\Gamma\sigma^y + \mathscr{O}(\Gamma^2). \tag{8.12}$$

8.1.2 The free energy under the static hypothesis

Derivation of the averaged free energy

Collecting the previous results on the Interaction representation, it is possible to write the time dependent replicated partition function as [175, 176]:

$$Z^n[J] = \operatorname*{Tr}_{\{S_i^\alpha\}}\left(e^{\beta\Gamma\sum_i\sum_\alpha\sigma_i^{x,\alpha}}\mathcal{T}e^{-\int_0^\beta\mathrm{d}\tau'\left(\sum_{(i,j)}J_{ij}\sum_\alpha\sigma_i^{z,\alpha}(\tau')\sigma_j^{z,\alpha}(\tau')+h\sum_i\sum_\alpha\sigma_i^{z,\alpha}(\tau')\right)}\right). \tag{8.13}$$

Using the gaussian distribution for the couplings of equation (7.14), it is possible to perform the disorder average following:

$$\overline{Z^n[J]} = \int \mathcal{D}J\mathcal{P}[J]Z^n[J]. \tag{8.14}$$

[1] τ is called the imaginary Matsubara time [174].

Refer to Appendix B (section B.1) for the complete integration. We find:

$$\begin{aligned}\overline{Z^n} = Tr\exp\Big[\beta\Gamma\sum_i\sum_{\alpha=1}^{n}\sigma_i^{x,\alpha}\Big] \\ \times\mathcal{T}\exp\Big[\frac{1}{4N}\Big(\sum_{\alpha\neq\gamma}\int_0^\beta \mathrm{d}\tau\int_0^\beta \mathrm{d}\tau'(\sum_i\sigma_i^{z,\alpha}(\tau)\sigma_i^{z,\gamma}(\tau'))^2 \\ +\sum_\alpha\int_0^\beta \mathrm{d}\tau\int_0^\beta \mathrm{d}\tau'(\sum_i\sigma_i^{z,\alpha}(\tau)\sigma_i^{z,\alpha}(\tau'))^2\Big) + h\sum_i\sum_\alpha\int_0^\beta \mathrm{d}\tau\sigma_i^{z,\alpha}(\tau)\Big].\end{aligned} \tag{8.15}$$

Using a **Hubbard-Stratonovitch** transform [177, 178]

$$e^{\frac{1}{2}\lambda a^2} = \sqrt{\frac{\lambda}{2\pi}}\int \mathrm{d}x e^{-\frac{1}{2}\lambda x^2+\lambda a x} \tag{8.16}$$

we decouple the quadratic terms, and we find for the averaged free energy ($\beta\overline{\mathscr{F}} = \lim_{n\to 0}\frac{1}{n}\left(\overline{Z^n}-1\right)$ using the replica trick):

$$\beta\overline{\mathscr{F}} = -\lim_{n\to 0}\frac{1}{n}\Big\{\int\prod_{\alpha\neq\gamma}\sqrt{\frac{N\beta^2}{4\pi}}\mathcal{D}y^{\alpha\gamma}(\tau,\tau')\prod_\alpha\sqrt{\frac{N\beta^2}{4\pi}}\mathcal{D}w^{\alpha\alpha}(\tau,\tau')\exp\big(-Nf_n(y^{\alpha\gamma},w^{\alpha\alpha})\big)-1\Big\}, \tag{8.17}$$

where

$$\begin{aligned}f_n(y^{\alpha\gamma},w^{\alpha\alpha}) = \\ \frac{1}{4}\int_0^\beta \mathrm{d}\tau\int_0^\beta \mathrm{d}\tau'\left(\sum_{\alpha\neq\gamma}(y^{\alpha\gamma}(\tau,\tau'))^2+\sum_\alpha(w^{\alpha\alpha}(\tau,\tau'))^2\right) \\ -\ln\Big[Tr\exp\Big\{\beta\Gamma\sum_\alpha\sigma_\alpha^x\Big\} \\ \mathcal{T}\exp\Big\{\frac{1}{2}\int_0^\beta \mathrm{d}\tau\int_0^\beta \mathrm{d}\tau'\Big(\sum_{\alpha\neq\gamma}\sigma_\alpha^z(\tau)\sigma_\gamma^z(\tau')y^{\alpha\gamma}(\tau,\tau') \\ +\sum_\alpha\sigma_\alpha^z(\tau)\sigma_\alpha^z(\tau')w^{\alpha\alpha}(\tau,\tau')\Big)+h\int_0^\beta \mathrm{d}\tau\sum_\alpha\sigma_\alpha^z(\tau)\Big\}\Big]\end{aligned} \tag{8.18}$$

is the free energy per spin. From now on, we note $\sigma_{\alpha/\gamma}^{x/z}\equiv\sigma^{x/z,\alpha/\gamma}$. Looking at equation (8.17), it is on the form to apply the saddle point expansion of the f_n function inside the exponential, thanks to the N factor multiplying the f_n function. See Appendix B (section B.2) for the detail of the saddle point expansion. We get, for the variables $y^{\alpha\gamma}$ and $w^{\alpha\alpha}$:

$$y^{\alpha\gamma}(\tau,\tau')|_{\text{saddle point}} = Q^{\alpha\gamma}(\tau,\tau') = \langle\mathcal{T}\sigma_\alpha^z(\tau)\sigma_\gamma^z(\tau')\rangle_T, \qquad \alpha\neq\gamma \tag{8.19}$$

$$w^{\alpha\alpha}(\tau,\tau')|_{\text{saddle point}} = R(\tau,\tau') = \langle\mathcal{T}\sigma_\alpha^z(\tau)\sigma_\alpha^z(\tau')\rangle_T, \tag{8.20}$$

and the free energy (8.17) reads (where we have noted $\overline{\mathscr{F}}|_{\text{saddle point}} = f$)

$$-\beta f = \lim_{n\to 0}\frac{1}{n}\Bigg\{ -\frac{1}{4}\int_0^\beta \mathrm{d}\tau \int_0^\beta \mathrm{d}\tau' \left(\sum_{\alpha\neq\gamma}(Q^{\alpha\gamma}(\tau,\tau'))^2 + \sum_\alpha (R(\tau,\tau'))^2\right) + \ln\Bigg[Tr\exp\Big\{\beta\Gamma\sum_\alpha \sigma_\alpha^x\Big\} \times \mathcal{T}\exp\Big\{\frac{1}{2}\int_0^\beta \mathrm{d}\tau\int_0^\beta \mathrm{d}\tau'\Big(\sum_{\alpha\neq\gamma}\sigma_\alpha^z(\tau)\sigma_\gamma^z(\tau')Q^{\alpha\gamma}(\tau,\tau') + \sum_\alpha \sigma_\alpha^z(\tau)\sigma_\alpha^z(\tau')R(\tau,\tau')\Big) + h\int_0^\beta \mathrm{d}\tau\sum_\alpha\sigma_\alpha^z(\tau)\Big\}\Bigg]\Bigg\}. \tag{8.21}$$

$\langle\cdots\rangle_T$ represents thermal average. The function $Q^{\alpha\gamma}$ that has just been defined (equation (8.19)) is equivalent to the definition we proposed for the spin overlap in chapter 1 in equation (1.17):

$$Q^{\alpha\gamma} = \frac{1}{N}\sum_i \sigma_i^{z,\alpha}\sigma_i^{z,\gamma}.$$

The static hypothesis

To simplify the calculations, we suppose that the order parameters $Q^{\alpha\gamma}(\tau,\tau')$ are static. For $\alpha \neq \gamma$, this quantity describes the coupling between distinct replicas and, as a consequence of invariance with respect to the translation of time, $Q^{\alpha\gamma}(\tau,\tau')$ cannot depend on time labels. Moreover, the work of Miller and Huse [171] is in favor of the static hypothesis at least in the semi-classical limit of "small" transverse field, which is confirmed by the work of Rozenberg and Grempel [179]. Furthermore, we approximate[2] $R(\tau,\tau') = r$, and we write:

$$Q^{\alpha\gamma}(\tau,\tau') = q^{\alpha\gamma}, \tag{8.22}$$
$$R(\tau,\tau') = r. \tag{8.23}$$

Using this hypothesis, the free energy reads:

$$-\beta f = \lim_{n\to 0}\frac{1}{n}\Bigg\{ -\frac{\beta^2}{4}\left(\sum_{\alpha\neq\beta}(q^{\alpha\beta})^2 + \sum_\alpha r^2\right) + \ln\Bigg[Tr\exp\Big\{\beta\Gamma\sum_\alpha\sigma_\alpha^x\Big\} \exp\Big\{\frac{\beta^2}{2}\Big(\sum_{\alpha\neq\beta}\sigma_\alpha^z\sigma_\beta^z q^{\alpha\beta} + \sum_\alpha \sigma_\alpha^z\sigma_\alpha^z r\Big) + \beta h\sum_\alpha\sigma_\alpha^z\Big\}\Bigg]\Bigg\}. \tag{8.24}$$

8.2 The equations of motion

8.2.1 Reparametrization and full RSB

To continue the calculation of the replicated free energy, we apply the full RSB procedure described in the previous chapter. It allows to find the structure of the $q^{\alpha\gamma}$ matrix for any step of RSB. The details of the transformation of the sums on replicas of the previous equation are

[2] it appears morre obvious that this function does not depend on time: all replicas have a similar behavior.

presented in appendix C (sections C.1 and C.2). The hierarchical structure of the RSB scheme leads to a hierarchical structure in the free energy. It is then possible to define an iterative function Ψ_{l-1}, where l is the step of RSB under consideration. This procedure is similar to the approach of [151, 152]. The form of the function Ψ_{l-1} is given by:

$$\begin{aligned}\big(\exp p_{l-1}\Psi_{l-1}(h,\Gamma)\big) &= \int \frac{\mathrm{d}z_l}{\sqrt{2\pi}} \exp -\frac{z_l^2}{2} \\ &\times \left(\int \frac{\mathrm{d}y_l}{\sqrt{2\pi}} \exp p_l\Big[-\frac{y_l^2}{2} + \Psi_l\big(h+\sqrt{q_l-q_{l-1}}z_l + \sqrt{-\Delta_l'}y_l,\Gamma\big)\Big]\right)^{p_{l-1}/p_l}. \\ l = 0..K \qquad & p_{-1}\equiv n \qquad q_{-1}\equiv 0 \end{aligned} \tag{8.25}$$

For the different notations, see appendix C. $\Delta(x)$ is defined by Sompolinsky in [154], and represents (in a dynamic view) the slow response due to overturning of large clusters, and therefore is a decreasing function of x with its maximum value $\Delta(0)$. This function is sometimes called the "response anomaly" [180].

Looking carefully at this equation, we remark that a saddle point method can be applied with respect to the variables y_l (see appendix B, section B.2). To justify this method, it is necessary that the size p_l tends to the infinity. This is well satisfied as we have seen that the full RSB procedure is characterized by $p_0 \gg p_1 \gg \cdots \gg p_K \to \infty$. It leads to:

$$\begin{aligned}&\exp p_{l-1}\Psi_{l-1}(h,\Gamma) = \\ &\quad \int \frac{\mathrm{d}z_l}{\sqrt{2\pi}} e^{-\frac{z_l^2}{2}} \exp p_{l-1}\left(-\frac{y_c^2}{2} + \Psi_l(h+\sqrt{q_l-q_{l-1}}z_l + \sqrt{-\Delta_l'}y_c,\Gamma)\right) \\ &\quad \text{and} \qquad y_c = \frac{\partial\Psi_l}{\partial y_c}(h+\sqrt{q_l-q_{l-1}}z_l + \sqrt{-\Delta_l'}y_c,\Gamma). \end{aligned} \tag{8.26}$$

This equation is the starting point to reach the full RSB limit (*i.e* with an infinite number of RSB steps). We consider the following limits: $K\to\infty$, $l/K \to x$, $\{\Psi_l(h,\Gamma)\}_l \to \Psi(x,h,\Gamma)$ and, to the order δx, $q_l - q_{l-1} \to \dot{q}(x)\delta x$, as this was defined[3] in section 7.1.2. In this vision, we end up with an infinite number of order parameters: a function $q(x)$ of the interval $[0,1]$ [34].

$$\Psi_l\left(h+\sqrt{q_l-q_{l-1}}z_l + \sqrt{-\Delta_l'}y_c,\Gamma\right) \to \Psi(x,h+\sqrt{\dot{q}(x)\delta x}z + \sqrt{-\dot{\Delta}(x)\delta x}y_c), \tag{8.27}$$

$$\text{and} \qquad y_c \to \frac{\partial\Psi(x,h,\Gamma)}{\partial h} \times \sqrt{-\dot{\Delta}(x)\delta x}. \tag{8.28}$$

Equation (8.28) is obtained directly with a change of variables in equation (8.26). From (8.27), we deduce a development of Ψ to first order in δx:

$$\begin{aligned}\Psi(x,h+\sqrt{\dot{q}(x)\delta x}z + \sqrt{-\dot{\Delta}(x)\delta x}y_c) &\to \Psi(x,h,\Gamma) + z\sqrt{\dot{q}(x)\delta x}\frac{\partial\Psi}{\partial h} \\ &- \left(J^2\dot{\Delta}(x)\left(\frac{\partial\Psi}{\partial h}\right)^2 - \frac{1}{2}z^2\dot{q}(x)\frac{\partial^2\Psi}{\partial h^2}\right)\delta x + \mathcal{O}(\delta x^{3/2}). \end{aligned} \tag{8.29}$$

We then develop equation (8.26) in powers of p_{l-1}, and the continuous limit of the resulting equation at first order in p_{l-1} is considered:

$$\begin{aligned}&\frac{\partial\Psi}{\partial x}(x,h,\Gamma) = -\frac{1}{2}\left(-\dot{\Delta}(x)\left(\frac{\partial\Psi}{\partial h}(x,h,\Gamma)\right)^2 + \dot{q}(x)\frac{\partial^2\Psi}{\partial h^2}(x,h,\Gamma)\right) \\ &\text{and} \qquad \Psi(1,h,\Gamma) = \ln\left(2\cosh(\beta\sqrt{h^2+\Gamma^2})\right). \end{aligned} \tag{8.30}$$

[3] in the following, derivatives with respect to x are denoted with a dot.

We simplify this expression by using the so-called "Parisi gauge" which is defined as [181, 182]:

$$\dot{\Delta}(x) = x\dot{q}(x). \tag{8.31}$$

The name of this gauge lies in the fact that imposing it to equation (8.27) allows to find back the so-called Parisi equation [154, 183]:

$$\frac{\partial \Psi}{\partial x}(x,h,\Gamma) = -\frac{\dot{q}(x)}{2}\left(x\left(\frac{\partial \Psi}{\partial h}(x,h,\Gamma)\right)^2 + \frac{\partial^2 \Psi}{\partial h^2}(x,h,\Gamma)\right). \tag{8.32}$$

Similarly, the function Ψ_{-1} can be expresed in a different way if we come back to equation (8.26):

$$\exp n\Psi_{-1}(h,\Gamma) = \int \frac{\mathrm{d}z_0}{\sqrt{2\pi}} e^{-\frac{z_0^2}{2}} \exp n\left(-\frac{y_c^2}{2} + \Psi_0(h+\sqrt{q_0}z_0 + \sqrt{-\Delta_0'}y_c)\right). \tag{8.33}$$

Using the continuous limit, we get:

$$\begin{aligned} \Psi_{-1}(h,\Gamma) &= \int \frac{\mathrm{d}z}{\sqrt{2\pi}} e^{-\frac{z^2}{2}} \left(-\frac{1}{2}\left(\frac{\partial \Psi}{\partial y_c}\right)^2 + \Psi(0, h+\sqrt{q(0)}z + \sqrt{-\dot{\Delta}(0)}\frac{\partial \Psi}{\partial y_c}, \Gamma)\right) \\ \text{and} \qquad y_c &= \frac{\partial \Psi}{\partial y_c}(0, h+\sqrt{q(0)}z + \sqrt{-\dot{\Delta}(0)}y_c, \Gamma). \end{aligned} \tag{8.34}$$

In Parisi gauge, $\dot{\Delta}(0) = 0$. The above equation becomes then:

$$\begin{aligned} \Psi_{-1}(h,\Gamma) &= \int \frac{\mathrm{d}z}{\sqrt{2\pi}} e^{-\frac{z^2}{2}} \left(-\frac{1}{2}\left(\frac{\partial \Psi}{\partial y_c}\right)^2 + \Psi(0, h+\sqrt{q(0)}z, \Gamma)\right) \\ \text{and} \qquad y_c &= 0. \end{aligned} \tag{8.35}$$

Ψ does not depend explicitly on y_c from equations (8.34) and (8.35).
As a consequence, the free energy in this gauge is:

$$-\beta f = \frac{\beta^2}{4}\left((1-q(1))^2 - (1-r)^2 + 2\int_0^1 \mathrm{d}x x q(x)\dot{q}(x)\right) + \int \frac{\mathrm{d}y}{\sqrt{2\pi q(0)}} e^{-\frac{(y-h)^2}{2q(0)}} \Psi(0,y), \tag{8.36}$$

where we introduced the variable y which is defined as: $y = h + \sqrt{q(0)}z$. Do not forget the constraints on the Ψ function:

$$\frac{\partial \Psi}{\partial x}(x,h,\Gamma) = -\frac{\dot{q}(x)}{2}\left(x\left(\frac{\partial \Psi}{\partial h}(x,h,\Gamma)\right)^2 + \frac{\partial^2 \Psi}{\partial h^2}(x,h,\Gamma)\right), \tag{8.37a}$$

$$\text{and} \qquad \Psi(1,h,\Gamma) = \ln\left(2\cosh(\beta\sqrt{h^2+\Gamma^2})\right). \tag{8.37b}$$

8.2.2 The variational method

We can directly take into account the previous constraints (equations (8.37a) and (8.37b)) into the free energy of equation (8.36) by introducing two Lagrange multipliers $P(x,y)$ and $P(1,y)$. We also introduce a new function $\phi(x,y)$ as

$$\beta\phi(x,y,\Gamma) = \Psi(x,y,\Gamma) \tag{8.38}$$

to enforce Ψ to be a free energy. With these new notations, we find:

$$\begin{aligned} - \quad & f = \frac{\beta}{4}\left((1-2q(1)) - (1-r)^2 + \int_0^1 \mathrm{d}x q^2(x)\right) + \int \frac{\mathrm{d}y}{\sqrt{2\pi q(0)}} e^{-\frac{(y-h)^2}{2q(0)}} \phi(0,y,\Gamma) \\ - \quad & \int_0^1 \mathrm{d}x \int \mathrm{d}y P(x,y)\left(\dot{\phi}(x,y,\Gamma) + \frac{\dot{q}(x)}{2}\left(\phi''(x,y,\Gamma) + \beta x \phi'^2(x,y,\Gamma)\right)\right) \\ + \quad & \int \mathrm{d}y P(1,y)\left(\phi(1,y,\Gamma) - T\ln\left(2\cosh\left(\beta\sqrt{y^2+\Gamma^2}\right)\right)\right), \end{aligned} \tag{8.39}$$

where the dot represent the partial derivative with respect to x, and the prime the partial derivative with respect to y. This equation is the variational form of the Parisi equation [152, 181].

To solve this problem, we use a variational approach developed in the classical case by Sommers and Dupont [181]. It consists in imposing the stationnarity of the free energy with respect to the variations of $P(x,y)$, $P(1,y)$, $\phi(x,y,\Gamma)$, $\phi(0,y,\Gamma)$ and $q(x)$.

For each quantity, it gives:

- P(x,y): differential equation verified by $\phi(x,y,\Gamma)$

$$\dot{\phi}(x,y,\Gamma) = -\frac{\dot{q}(x)}{2}\left(\phi''(x,y,\Gamma) + \beta x \phi'^2(x,y,\Gamma)\right). \tag{8.40}$$

- P(1,y): boundary condition verified by $\phi(1,y,\Gamma)$:

$$\phi(1,y,\Gamma) = T\ln\left(2\cosh\left(\beta\sqrt{y^2+\Gamma^2}\right)\right). \tag{8.41}$$

- $\phi(x,y,\Gamma)$: we obtain, after an integration by parts of the term P$(x,y)\times\dot{\phi}(x,y,\Gamma)$, the equation verified by $P(x,y)$

$$\dot{P}(x,y) = \frac{\dot{q}(x)}{2}\left(P''(x,y) - 2\beta x\left(\phi'(x,y)P(x,y)\right)'\right). \tag{8.42}$$

- $\phi(0,y,\Gamma)$: we deduce the form for $P(0,y)$:

$$P(0,y) = \exp\left(-\frac{(y-h)^2}{2q(0)}\right)/(2\pi q(0))^{-1/2}. \tag{8.43}$$

Without any longitudinal magnetic field h, the boundary condition for $P(0,y)$ becomes:

$$P(0,y) = \delta(y). \tag{8.44}$$

The previous expression for the function $P(x,y)$ can be explained using the dynamical interpretation of Sompolinsky [154]: $q(x)$ represents the proportion of spin-spin correlations that did not have decayed at the time scale τ_x. In that vision, $q(x)$ is defined as [154]:

$$q(x) = \overline{\langle S_i(0)S_i(\tau_x)\rangle}. \tag{8.45}$$

Thus, $q(x)$ is a monotonous increasing function with a maximum value $q(1) = q_{EA}$, which the frozen correlations measured in finite time. τ_0 is the longest time scale (this is purely static limit). We thus understand easily why $q(0) = 0$, which also explains why $P(0,y)$ is a delta function in the absence of a longitudinal magnetic field.

- $q(x)$:

$$q(x) = \int \mathrm{d}y P(x,y)\phi'^2(x,y) \tag{8.46}$$

Again, this equation is obtained by integration by parts of the stationnarity equation of f with respect to $q(x)$.

We modify the previous equation (8.46) and we show, with an integration by parts on variable y that it is equivalent to equation

$$1 = \int \mathrm{d}y P(x,y) \left(\phi''(x,y)\right)^2 . \tag{8.47}$$

We can indeed derive equation (8.46) with respect to x

$$\dot{q} = \int \mathrm{d}y \dot{P}\phi'^2 + \int \mathrm{d}y P(\dot{\phi'^2}) = \frac{\dot{q}}{2}\left(\int \mathrm{d}y P''\phi'^2 - 2\int \mathrm{d}y P\phi'\phi''\right),$$

and then integrate this result by parts with respect to y.

Most of these equations depend on the first derivative of the function $\phi(x,y,\Gamma)$ with respect to y, we introduce the following quantity:

$$m(x,y,\Gamma) = \phi'(x,y,\Gamma). \tag{8.48}$$

The introduction of this new parameter has two main consequences:

(i) First, both partial differential equations for m and P becomes highly similar, they will be solved in the same way. The equation for m is given by derivating equation (8.40) with respect to y:

$$\dot{m} = -\frac{\dot{q}}{2}\left(m'' + 2\beta x m m'\right). \tag{8.49}$$

The boundary condition verified by this new function is:

$$m(1,y,\Gamma) = \frac{y}{\sqrt{y^2+\Gamma^2}} \tanh\left(\beta\sqrt{y^2+\Gamma^2}\right). \tag{8.50}$$

(ii) The second consequence of the introduction of m lies in the interpretation of the set of functions m, P and q. As previously seen, a time scale τ_x can be associated to the order parameter $q(x)$, in the way that for times of order τ_x, states with an overlap greater than $q(x)$ can be reached by the system as explained by Crisanti and Rizzo [184]. In this picture, P is interpreted as the statistical distribution of local frozen fields y and m is the local magnetization in a local field y, at time scale fixed by the value of x. We have indeed:

$$q(x) = \int \mathrm{d}y P(x,y) m^2(x,y,\Gamma). \tag{8.51}$$

This expression is very similar to the definition of the overlap as a correlation function of magnetization: see equation (1.17). Moreover, $P(x,y)$ has a probabilistic interpretation: it verifies a continuity equation (8.42), its normalization is conserved:

$$\int \mathrm{d}y P(x,y) = 1 \qquad\qquad P(x,y) \geq 0. \tag{8.52}$$

And, for $x \to 0$, it approaches a gaussian thanks to equation (8.43).

Finally, the issue of the nature of the spin glass phase at low temperature and low transverse field has been found equivalent to the resolution of the following system of partial differential equations for the functions $m(x, y, \Gamma)$, $P(x, y, \Gamma)$ and $q(x)$.

$$q(x) = \int \mathrm{d}y P(x, y) m^2(x, y, \Gamma) \tag{8.53a}$$

$$\dot{m}(x, y, \Gamma) = -\frac{\dot{q}(x)}{2} \left[m''(x, y, \Gamma) + 2\beta x m(x, y, \Gamma) m'(x, y, \Gamma) \right] \tag{8.53b}$$

$$\dot{P}(x, y) = \frac{\dot{q}(x)}{2} \left[P''(x, y) - 2\beta x \left(m(x, y, \Gamma) P(x, y) \right)' \right] \tag{8.53c}$$

with the boundary conditions (without any longitudinal magnetic field)

$$m(1, y, \Gamma) = \frac{y}{\sqrt{y^2 + \Gamma^2}} \tanh\left(\beta \sqrt{y^2 + \Gamma^2} \right) \tag{8.54a}$$

$$P(0, y) = \delta(y) \tag{8.54b}$$

These equations (8.53) are highly similar to the ones that have been found in the classical case by Sommers and Dupont [181]. The only difference lies in the presence of a Γ term in the boundary condition for the local magnetization (8.54a). It turns out that the influence of the transverse field is to modify the local field in the system.

8.3 Numerical solutions

These equations (8.53) will be solved numerically using a pseudo spectral method, which is very efficient for this type of differential equations[4] [184, 185]. This work was done in collaboration with E. Lévêque, at the École Normale Supérieure of Lyon. This pseudo spectral method has the advantage to be efficient in terms of calculation time and in memory allocation.

8.3.1 The order parameter

The first study consists in solving the equations to deduce the order parameter $q(x)$ for different temperatures and transverse fields. In the classical case ($\Gamma = 0$), considering the definition of the function $q(x)$ and the definition of the Edwards-Anderson order parameter, it is clear that $q(x) = q_{EA}$, for x close to 1. In the paramagnetic phase, the Edwards-Anderson order parameter is equal to zero and is non vanishing in the spin glass. In figure 8.1, is represented the evolution of the order parameter $q(x)$ numerically calculated, for different temperatures ($\beta = T_c/T$, where T_c is the critical temperature. On this curve, it is clear that in the paramagnetic phase, the order parameter is equal to zero, whereas it possesses a non trivial behavior at low temperature. A plateau ($q(x) = q_{EA}$) appears near $x = 1$ when the temperature decreases. The length of that plateau decreases with the temperature. We notice that in the presence of a transverse magnetic field, the transition does not occur at T_c any more, as expected classically (see the phase diagram of the previous chapter: figure 7.3). At given temperature, the evolution of the order parameter is given by figure 8.2. These curves of the order parameter also give information about the very low temperature behavior of the spins: if $T \to 0$, $q_{EA} \to 1$, which implies that the overlap between the different replicas is almost 1 at very low temperatures. The function

[4] at the origin, this method was used in hydrodynamics to solve the Navier-Stokes equation. It is used here as the equations we have obtained are close to this hydrodynamic equation of motion.

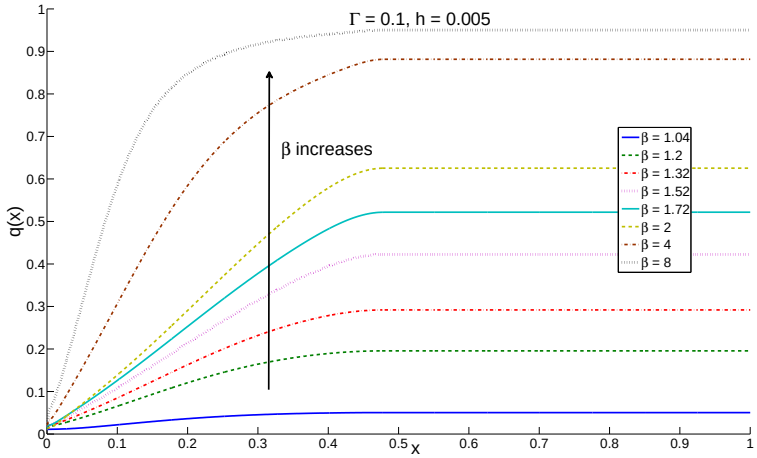

Figure 8.1: *Evolution of the order parameter $q(x)$ for different temperatures ($\beta = T_c/T$, where T_c is the spin glass transition temperature). At high temperatures, the $q(x)$ is almost constant and equal to zero, whereas a plateau appears near $x = 1$ if the temperature decreases. $\Gamma = 0.1$, $h = 0.005$.*

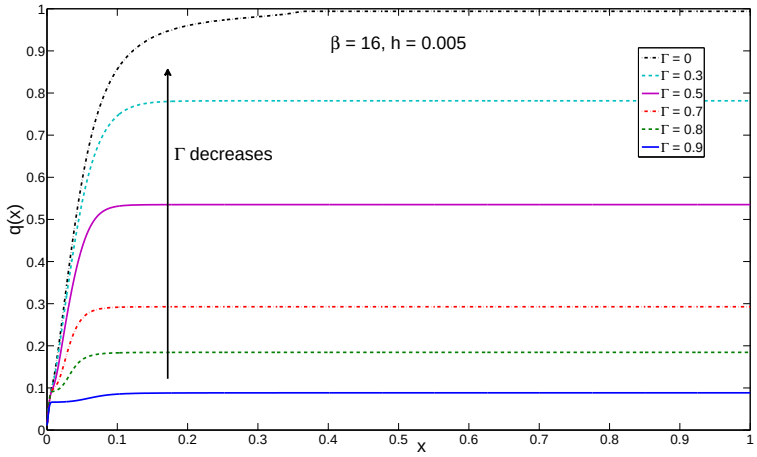

Figure 8.2: *Evolution of the order parameter $q(x)$ for different transverse magnetic fields at given temperature (lower than T_c). $\beta = 16$, $h = 0.005$.*

$q(x)$ is interpreted in terms of a probability distribution for the overlap $Q^{\alpha\gamma}$, defined in the previous chapter as a distance between two different spin states. Parisi [35] gave an equilibrium interpretation of his Ansatz, showing that $P(Q^{\alpha\gamma}) = (\mathrm{d}x/\mathrm{d}q)_{q(x)=Q^{\alpha\gamma}}$ describes the probability of two configurations α and γ of the system, sampled with a Boltzmann weight, to have mutual overlap $Q^{\alpha\gamma}$. This interpretation has recently been generalized beyond the mean-field case [186].

An alternative to this static interpretation is the dynamic one by Sompolinsky [154]. He assumes the existence of a hierarchical set of time scales τ_x as explained in section 8.2. The dynamic overlap defined in this formalism: $q(x) = \overline{\langle s_i(\tau_x) s_i(0) \rangle}$ appears to be identical to Parisi's one [45, 187].

The parameterization of the previous section allows also to determine numerically some other local properties of a spin glass as the probability distribution of local fields $P(x, y)$, which is investigated hereafter.

8.3.2 The distribution of local fields

We also determine by integration of the equations of motion (8.53), the evolution of the distribution of local fields $P(1, y)$ for different temperatures, and/or different transverse fields. In the paramagnetic phase, this distribution is gaussian, centered at $y = h$, as in the paramagnetic phase the local field felt by the spins is the external field. In the spin glass phase in the classical case, a pseudo gap opens in this distribution at $y = 0$ due to the freezing of all spins. This also happens in in the mean field theory of the three-dimensional Coulomb glass [180]. As concerns the quantum spin glass, we plot $P(1, y)$ as a function of y for different temperatures and a non vanishing transverse magnetic field in figure 8.3. In fact, y depends on x and the value $y(x = 1)$

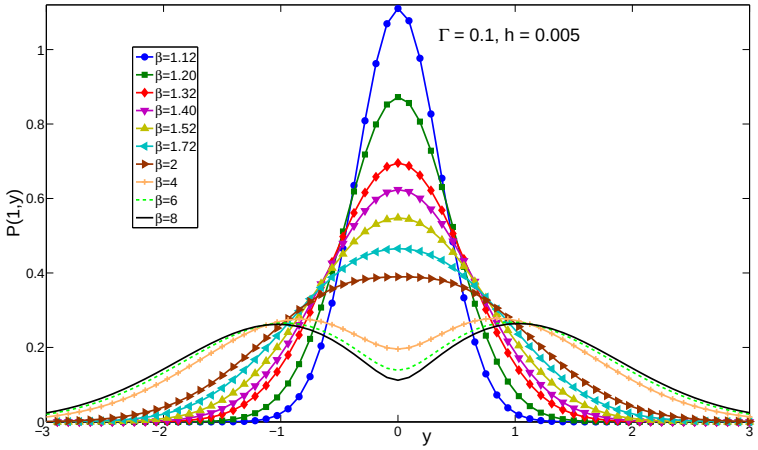

Figure 8.3: *Evolution of the distribution of local fields y for $x = 1$ ($y(x = 1)$ represents the physical total field). A pseudo gap opens at $y = 0$ in the spin glass phase due to ergodicity breaking.* $\Gamma = 0.1$, $h = 0.005$.

represents the total local field. $y(x)$ represents the part of the total local field $y(1)$ that is not affected by averaging on a time scale τ_x (see section 8.2.2 and [181]). The shape of the distribution changes well from a gaussian at high temperature to a double peak distribution at low temperature, but the transition does not occur at $T = T_c$. The transverse field modifies the transition temperature. This can also be seen on figure 8.4. It is clear that the classical system is in the paramagnetic phase (a gaussian distribution), whereas it is in the spin glass phase for the largest values of Γ.

8.3.3 Conclusion

In this chapter we have presented a generalization of the non standard full RSB procedure of de Dominicis et al [34, 33, 183, 152, 181] in the case of the Infinite Range Quantum Ising spin glass (SK model in transverse magnetic field). The equations of motion that have been derived are highly similar to the one derived in the classical case [155], the only difference coming from the boundary condition in the local magnetization. Quantum effects were taken into account by considering the Interaction representation, which implied that the spin operators in the z direction (the axis of quantification) were time[5] dependent. The static hypothesis allowed us to simplify the equations and the quantum nature of the remaining operators (*i.e* σ^x and σ^z do not commute) lead to a modification of the boundary condition for the local magnetization (8.54a).

[5] more precisely, this is the Matsubara imaginary time [174].

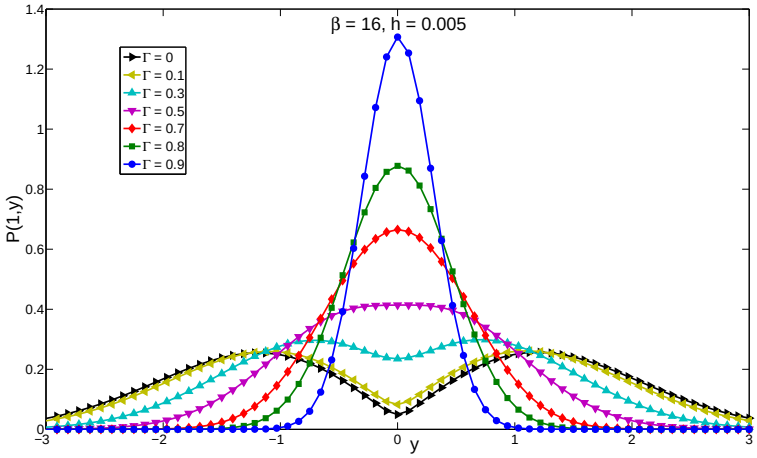

Figure 8.4: *Evolution of the distribution of local fields y for $x = 1$ for different values of the transverse field Γ. $T/T_c = 0.06$, $h = 0.005$.*

We moreover managed to solve numerically these equations using a pseudo spectral method with the help of Emmanuel Lévèque at the ENS of Lyon. We found that the influence of the transverse field is to break the short range order of the spins and to enter the paramagnetic phase at lower temperatures. We also find that the distribution of local fields is modified. Further study on the low temperature behavior of the pseudo gap is at the time performed.

To go further on this project, we will in the future try to find a similar scaling behavior at low temperature of the equations of motion as in the classical case following [155]. We hope that this scaling would give information on the behavior of the pseudo gap in the distribution of local fields, as it is the case in the classical SK model.

Conclusion

Il n'existe que deux choses infinies, l'univers et la bêtise humaine... mais pour l'univers, je n'ai pas de certitude absolue.

Albert Einstein

The main goal of this Thesis was to prove and extend the validity of an original theoretical proposal to study spin glasses using coherent transport, this in close relation with experimental constraints (this numerical work is a part of an ANR financial support: ANR MESOGLASS, in collaboration with the Quantum Coherence group at Institut Louis Néel in Grenoble). The goal was also to clarify the different regimes of conduction of a spin glass nanowire and to study in detail the relevant differences with what happens in purely metallic nanowires. The second goal of this work was to generalize the mean field model (SK model) of a generic classical Ising spin glass to a quantum Ising spin glass, only by adding a transverse magnetic field.

In a first part, we have studied in detail the Anderson localized regime, which is characterized by a vanishingly small conductance. We have been able to extract with accuracy the localization length which represents the length of the wire beyond which the system is called localized. The universal variation of that length with the width of the sample has allowed us to compare it in the case of a metallic and a spin glass nanowire. We have shown that it is larger in the case of a spin glass, since Anderson localization is an interference effect and impurities break the interference pattern. Moreover, the universal behavior of this length with the transverse dimension of the wire has allowed us to discriminate universal from non-universal regimes. In particular, experimentally relevant samples appear to be non-universal as their magnetic disorder is moderate (in comparison with the amplitude of the scalar disorder W). In the localized regime, we confirm that the statistical distribution of conductance is Log-Normal at the limit of infinite length, and we highlight the presence of a non-analyticity at $g = 1$ in both universal classes, and we also confirm the occurrence of a one parameter scaling of the distribution. We show that the second cumulant of the distribution of $\log g$ becomes super-universal in the sense that it does not depend on universality class, in the deep insulating regime.

For wires, whose length is smaller than the localization length but larger than the elastic mean free path, the *metallic diffusive* regime is reached. This regime is characterized by a universally fluctuating conductance: the fluctuations of the conductance only depend on the symmetries of the system. We have also shown that the experimentally relevant case of moderate magnetic disorders is non-universal but is well described by weak localization calculations. We managed to reach numerically the universal regime with an accuracy that has never been reached, to our knowledge. Moreover, contrary to what was well-spread in the literature, it is not that simple to reach the metallic diffusive regime as the localization length plays a crucial role. We confirm that in the metallic regime, the statistical distribution of conductance is almost gaussian. This extensive study of the conductance distribution in the metallic regime was the preliminary to enter the main part of the Thesis: the study of conductance correlations to have access to the spin overlap in a spin glass nanowire. We have first studied the statistical distribution (with respect to scalar disorder) of the difference $g_1 - g_2$, where g_k is the conductance calculated for one given realization of scalar disorder and spin configuration number k. We have shown that this distribution is centered around 0 (the average conductance does not depend on the spin configuration) and that it only depends on the spin overlap Q_{12}. Therefore we have gone on the study of the correlations of conductance, which appear to be a unique function of the spin overlap, which obviously opens the route for an experimental determination of that intrinsic property of spin glasses. Very recent preliminary experimental results show that it is indeed possible to decorrelate the conductance only by introducing magnetic impurities and applying temperature steps.

A second part of the Thesis was the study of a mean field model for Ising spin glasses: the Sherrington-Kirkpatrick model in a transverse magnetic field. Using the Replica theory and

the Interaction representation, we managed to derive equations of motions in the full-Replica Symmetry Breaking Ansatz. We found very similar equations in comparison with the classical case (*i.e* with no transverse magnetic field). We solved numerically these equations using a standard pseud-spectral method and we found a solution for the continuous order parameter $q(x)$ and the distribution of local fields $P(1, y)$.

Appendix A
Coherent transport and conductivity

A.1 The Drude model for the conductivity

Classical (incoherent) electrons contribute to the conductivity. To find an expression for this conductivity, we apply the Drude model [84]: the elastic scattering time τ_e is interpreted as the inverse of a damping coefficient. The corresponding damping force acts on the electrons to stop them. If an electric field $\vec{\mathscr{E}}$ is also applied[1], we find, by application of the second law of Newton on one electron:

$$m_e \frac{\mathrm{d}\vec{v}}{\mathrm{d}t} = \frac{1}{\tau_e}\vec{v} - e\vec{\mathscr{E}}. \tag{A.1}$$

If we use complex notations for the velocity $\vec{v}(t) = \vec{v_0}e^{\imath\omega t}$, we find for the conductivity:

$$\underline{\sigma}(\omega) = \frac{ne^2/m_e}{\frac{1}{\tau_e} - \imath\omega}, \tag{A.2}$$

where n_e is the number of electrons per unit volume.

A.2 The Kubo formalism of coherent transport

This formalism has been built to calculate the conductivity of a disordered metal, with the help of Green's functions.

A.2.1 The Kubo formula and disorder averaging

For a quasi-one dimensional system as the one that is considered in this manuscript, the longitudinal conductivity is expressed as:

$$\sigma_{xx}(\omega) = \frac{s\hbar}{2\pi V}\mathrm{ReTr}\left(\hat{j}_x\hat{G}^R(E_F)\hat{j}_x\hat{G}^A(E_F-\hbar\omega)\right). \tag{A.3}$$

To derive this expression, the hypothesis of linear response to an electric field has been assumed, and this formula is valid for a degenerate gas of electrons, where $\hat{j}_x$ is the current operator in the x direction. It is defined as: $\hat{j}_x = \imath\hbar\frac{e}{m}\partial_x$. Terms as G^RG^R and G^AG^A are not taken into account here, as they lead to negligible contributions to the conductivity.

We then obtain for the disorder averaged conductivity:

$$\sigma(\omega) = \langle\sigma_{xx}(\omega)\rangle \propto \int \mathrm{d}\vec{r}_1\mathrm{d}\vec{r}_2\mathrm{Re}\left\langle\partial_{x_1}G^R(E_F,\vec{r}_1,\vec{r}_2)\partial_{x_2}G^A(E_F-\hbar\omega,\vec{r}_2,\vec{r}_1)\right\rangle, \tag{A.4}$$

or, in the momentum space:

$$\sigma(\vec{q},\omega) \propto \sum_{\vec{k}_1,\vec{k}_2} k_{1,x}k_{2,x}\mathrm{Re}\left\langle G^R(\vec{k}_1+\vec{q}/2,\vec{k}_2+\vec{q}/2,E_F)G^A(\vec{k}_1-\vec{q}/2,\vec{k}_2-\vec{q}/2,E_F-\hbar\omega)\right\rangle. \tag{A.5}$$

In chapter 3, we have seen that the probability of diffusion of an electron from one point of the sample to another in time t is the sum of one incoherent term, plus two coherent terms: the Diffuson and the Cooperon. With similar arguments we will study, in the next section, the different terms contributing to the conductivity.

[1] more accurately, a potential difference is applied to the diffusive sample.

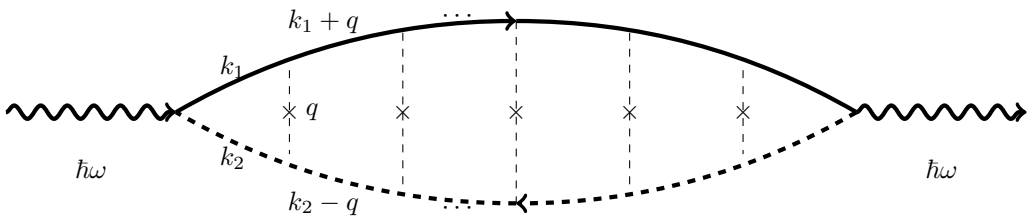

Figure A.1: *The Diffuson of figure 3.3 as a Feynman diagram. Crosses are impurities, which are encountered with the same sequence for both electronic paths (up and down arcs). Dashed lines are interactions with these impurities. q is the momentum transfered by each impurity.*

A.2.2 Incoherent diffusion

This approximation, which is the simplest thing we can imagine consists in taking in equation (A.5):

$$\langle G^R G^A \rangle \approx \langle G^R \rangle \langle G^A \rangle, \tag{A.6}$$

which means that both averaged Green's functions are independent with respect to each other. In optics this is equivalent to consider that the intensity at a point enlightened by two sources is the sum of intensities of each source. Interferences are not taken into account: it is an "incoherent" term. One can show that this term gives the Drude conductivity as in the first section of this appendix.

Using perturbation theory for interacting systems[2], it is possible to develop the product of Green's functions under the following formal equation [60]:

$$\langle G^R G^A \rangle \approx \langle G^R \rangle \langle G^A \rangle + \langle G^R \rangle \langle G^A \rangle \Gamma_\omega \langle G^R \rangle \langle G^A \rangle, \tag{A.7}$$

where Γ_ω is a form factor that depends on interactions.

A.2.3 The Diffuson

Concerning the Diffuson term, we find for the conductivity:

$$\begin{aligned} \sigma_d(\vec{q},\omega) \quad &\propto \quad \sum_{\vec{k}_1,\vec{k}_2} k_{1,x} k_{2,x} \mathrm{Re}\Big(\langle G^R(\vec{k}_1 + \vec{q}/2) \rangle \langle G^A(\vec{k}_1 - \vec{q}/2) \rangle \Gamma_\omega(\vec{k}_1 - \vec{k}_2) \langle G^R(\vec{k}_2 + \vec{q}/2) \rangle \\ &\times \quad \langle G^A(\vec{k}_2 - \vec{q}/2) \rangle \Big), \end{aligned} \tag{A.8}$$

where the form factor is calculated self-consistently, using figure A.2 and a Dyson equation [60]:

$$\Gamma_\omega(\vec{k}_1 - \vec{k}_2) = \gamma_e + \frac{\gamma_e}{V} \sum_{\vec{q}_1} \Gamma_\omega(\vec{k}_1 - \vec{k}_2) \langle G^R(\vec{k}_2 + \vec{q}_1) \rangle \langle G^A(\vec{k}_2 + \vec{q}_1) \rangle, \tag{A.9}$$

where γ is the quantity defined by $\gamma_e = 1/(2\pi\rho_0\tau_e) = n_i v_0^2$ (see section 5.3.2 for the notations). τ_e is the elastic time of flight of electrons in the sample.

[2]Interaction between the electrons mediated by impurities.

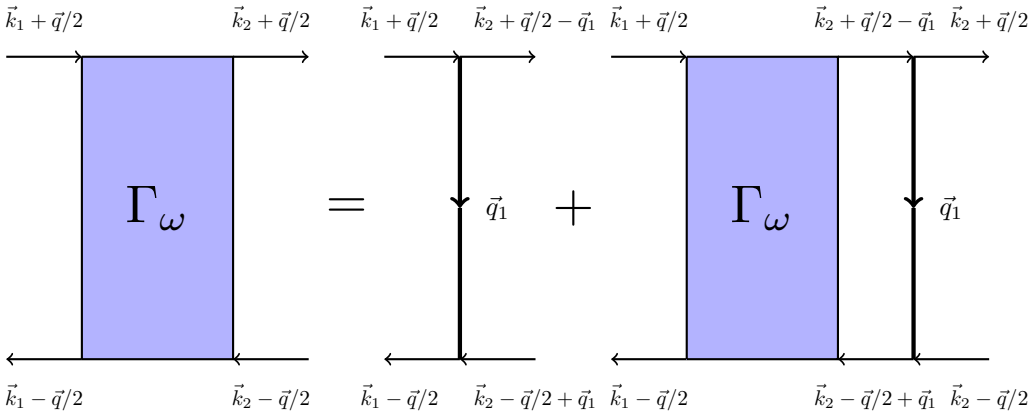

Figure A.2: *Illustration of the recursive calculation of the Diffuson term Γ_ω. The analytical expression is given in equation (A.9).*

Back to the probability of diffusion.
Notice that this term Γ_ω enters in the calculation of the probability of diffusion from point $\vec{r}_1$ to $\vec{r}_2$ during time t: in momentum space, this probability is proportionnal to:

$$P_d(\vec{k}_1,\vec{k_2},\omega) \propto \sum_{\vec{k}_1,\vec{k}_2} \mathrm{Re}\Big(\langle G^R(\vec{k}_1+\vec{q}/2)\rangle\langle G^A(\vec{k}_1-\vec{q}/2)\rangle\Gamma_\omega(\vec{k}_1-\vec{k}_2)\langle G^R(\vec{k}_2+\vec{q}/2)\rangle \times \langle G^A(\vec{k}_2-\vec{q}/2)\rangle\Big). \quad \text{(A.10)}$$

This equation is highly similar to equation (A.8). This term is of high importance as it is possible to show that only the sum of the probability of both the inoherent part and the Diffuson part is normalized to one.

Due to the presence of the product $k_{1,x}k_{2,x}$, the contribution of the Diffuson term to the conductvity is zero, in the case of **isotropic**[3] collisions. It is now time to discuss the Cooperon contribution to the conductivity.

A.2.4 The Cooperon

The diagram of a Cooperon, as already said in section 3.1.3, is the same as a Diffuson diagram with one electronic path reversed. In figure A.1, we reverse the dashed line, and we end up with a so-called maximally crossed diagram (figure A.3). The conductivity is then given by a formula, that is very close to equation (A.8):

$$\sigma_c(\vec{q},\omega) \propto \sum_{\vec{k}_1,\vec{k}_2} k_{1,x}k_{2,x}\mathrm{Re}\Big(\langle G^R(\vec{k}_1+\vec{q}/2)\rangle\langle G^A(\vec{k}_1-\vec{q}/2)\rangle\Gamma'_\omega(\vec{k}_1+\vec{k}_2)\langle G^R(\vec{k}_2+\vec{q}/2)\rangle \times \langle G^A(\vec{k}_2-\vec{q}/2)\rangle\Big), \quad \text{(A.11)}$$

[3] which we assume to be the case in all this manuscript.

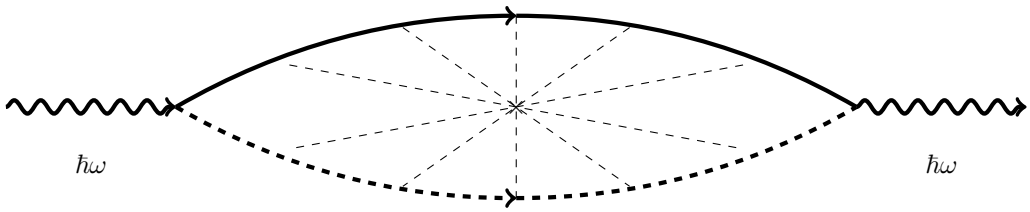

Figure A.3: *The Cooperon of figure 3.5 as a Feynman diagram. Crosses are impurities, which are encountered with the same sequence but in reversed order, in comparison with the Diffuson term. Dashed lines are interactions with these impurities.*

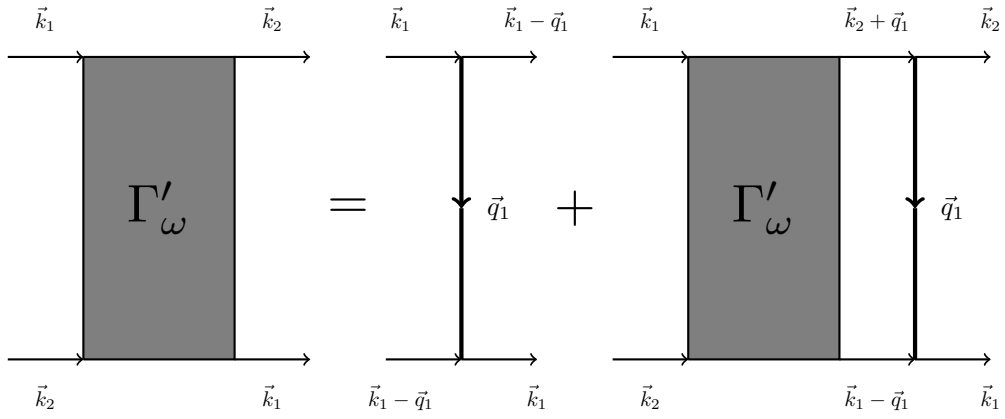

Figure A.4: *Illustration of the recursive calculation of the Cooperon term Γ'_ω. The analytical expression is given in equation (A.12).*

where the form factor is also calculated recursively via the summation of an infinite number of diagrams [188], as geometrically shown in figure A.4:

$$\Gamma'_\omega(\vec{k}_1 + \vec{k}_2) = \gamma + \frac{\gamma}{V} \sum_{\vec{q}_1} \Gamma'_\omega(\vec{k}_1 + \vec{k}_2) \langle G^R(\vec{k}_2 + \vec{q}_1) \rangle \langle G^A(\vec{k}_1 - \vec{q}_1) \rangle, \tag{A.12}$$

Consider the diffusive limit as in section 3.1.3 ($Ql_e \gg 1$), where $\vec{Q} = \vec{k}_1 + \vec{k}_2$. In this limit, the previous equation can be inverted, and we find:

$$\Gamma'_\omega(\vec{Q}) = \frac{\gamma}{\tau_e(-\imath\omega + DQ^2)}, \tag{A.13}$$

where D is the diffusion coefficient, and $\tau_e = l_e/v_F$. This is the kernel of a diffusion equation. This shows that, in the diffusive limit, the Cooperon term is solution of a diffusion equation. Therefore, the quantum corrections to the classical conductivity (which is only the Cooperon contribution), is:

$$\Delta\sigma(\omega) \propto -\sum_{\vec{Q}} \frac{1}{-\imath\omega + DQ^2}. \tag{A.14}$$

A.3 Weak localization correction

More generally, it is possible to show [89, 88] that the presence of a magnetic field and/or of magnetic impurities are taken into account in the conductivity in the form (see [86] for a complete review):

$$\Delta\sigma(\omega) \propto -\sum_{\vec{Q}} \left(\underbrace{\frac{1/2}{-\imath\omega + E_n(\vec{Q}) + \frac{2}{\tau_m}}}_{\text{Singlet term}} + \underbrace{\frac{3/2}{-\imath\omega + E_n(\vec{Q}) + \frac{2}{3\tau_m}}}_{\text{Triplet term}} \right). \tag{A.15}$$

The Singlet/Triplet decomposition comes from the presence of magnetic impurities: see section 3.2.2 and [88, 138], and is due to pairing of two spins 1/2 (two electronic paths). Usual quantum mechanics states indeed that a system with two spins 1/2 is properly described in the Singlet/Triplet basis [103]. In this equation, $E_n = DQ^2$ if the magnetic field is zero and is equal to $(n+1/2)4eDB/\hbar$ in a uniform magnetic field B. τ_m is the magnetic scattering time, this the characteristic scattering time of the magnetic impurities. It is also possible to define a related magnetic scattering length, with the help of the relation: $L_m = \sqrt{D\tau_m}$. See section 3.2.5 for more details on this length.

In a two dimensional system, $Q = n\pi/L_y$, where L_y is the transverse length of the sample. We find [72], in the absence of magnetic impurities for the corrections to the conductance g:

$$\Delta g = g(B) - g(0) \propto \frac{1}{B^{1/2}}, \tag{A.16}$$

for perfectly coherent wires ($L_\phi > L_x$). This expression allows to fit the average conductance of figure 3.8A. In the presence of magnetic impurities and no magnetic field, this expression is modified to obtain the equation (3.26) of section 3.2.3 for quantum corrections to the average conductance. In this equation, only the Cooperon term is present as the contribution of the Diffuson to the average conductance vanishes.

More generally, Lee et al [89] showed that for any diffusive process with diffusion time τ, the corrections to conductivity (or conductance) are calculated by replacing the diffusion pole DQ^2 by $DQ^2 + \tau^{-1}$. If the process is spin dependent, we must use the Singlet/Triplet basis [103].

Appendix B
Derivation of the disorder averaged partition function

B.1 Disorder averaging

The starting point of disorder averaging is equation (8.13) of section 8.1.1. We introduce the statistical distribution of couplings J_{ij} as defined in equation (7.14) and we find:

$$\begin{aligned}\overline{Z^n} = Tr\exp\Big[\beta\Gamma\sum_i\sum_{\alpha=1}^n\sigma_i^{x,\alpha}\Big] \\ \times\mathcal{T}\int\mathcal{D}J_{ij}\exp\Big[\int_0^\beta d\tau\Big\{\sum_{i<j}\sum_{\alpha=1}^n J_{ij}\sigma_i^{z,\alpha}(\tau)\sigma_j^{z,\alpha}(\tau) \\ -\sum_{i<j}\frac{N}{2J^2}J_{ij}^2+h\sum_i\sum_{\alpha=1}^n\sigma_i^{z,\alpha}(\tau)\Big\}\Big].\end{aligned} \tag{B.1}$$

We collect both the quadratic and the linear terms in J_{ij}

$$\begin{aligned}\int_0^\beta d\tau\sum_{ij}\sum_{\alpha=1}^n J_{ij}\sigma_i^{z,\alpha}(\tau)\sigma_j^{z,\alpha}(\tau)-\sum_{i<j}\frac{N}{2J^2}J_{ij}^2 \\ =-\sum_{i<j}\left(\frac{N}{2J^2}J_{ij}-\sqrt{\frac{J^2}{2N}}\int_0^\beta d\tau\sum_\alpha\sigma_{i\alpha}^z(\tau)\sigma_{j\alpha}^z(\tau)\right)^2 \\ +\frac{J^2}{2N}\left(\int_0^\beta d\tau\sum_\alpha\sigma_i^{z,\alpha}\sigma_j^{z,\alpha}\right)^2.\end{aligned} \tag{B.2}$$

to find a generalized gaussian integral for the J_{ij} dependence. It is integrated over $\mathbb{R}$, which gives a constant number that will be "forgotten" in the following as it is of no use from a physical point of view. Considering the next step:

$$\begin{aligned}&\frac{1}{2}\sum_{i\neq j}\left(\int_0^\beta d\tau\sum_\alpha\sigma_i^{z,\alpha}(\tau)\sigma_j^{z,\alpha}(\tau)\right)^2 \\ &= \frac{1}{2}\sum_{i,j}\sum_{\alpha,\gamma}\left(\int_0^\beta d\tau\int_0^\beta d\tau'\sigma_i^{z,\alpha}(\tau)\sigma_j^{z,\alpha}(\tau)\sigma_i^{z,\gamma}(\tau')\sigma_j^{z,\gamma}(\tau')\right)^2-cst \\ &= \frac{1}{2}\sum_{\alpha\gamma}\int_0^\beta d\tau\int_0^\beta d\tau'\left(\sum_i\sigma_i^{z,\alpha}(\tau)\sigma_i^{z,\gamma}(\tau')\right)^2-cst,\end{aligned} \tag{B.3}$$

where the constant term cst is of the form:

$$cst=\sum_i\sum_{\alpha,\gamma}\int_0^\beta d\tau\int_0^\beta d\tau'\left(\sigma_i^{z,\alpha}(\tau)\right)^2\left(\sigma_i^{z,\gamma}(\tau')\right)^2. \tag{B.4}$$

As a quadratic term in the spin operators, it does not depend on the spin any more, it is useless in the derivation. We end up with the following disorder averaged partition function as written

in section 8.1.1, equation (8.15):

$$\overline{Z^n} = Tr \exp\Big[\beta\Gamma \sum_i \sum_{\alpha=1}^{n} \sigma_i^{x,\alpha}\Big] \times \mathcal{T} \exp\Big[\frac{1}{4N}\Big(\sum_{\alpha\neq\gamma} \int_0^\beta \mathrm{d}\tau \int_0^\beta \mathrm{d}\tau' (\sum_i \sigma_i^{z,\alpha}(\tau)\sigma_i^{z,\gamma}(\tau'))^2 + \sum_\alpha \int_0^\beta \mathrm{d}\tau \int_0^\beta \mathrm{d}\tau' (\sum_i \sigma_i^{z,\alpha}(\tau)\sigma_i^{z,\alpha}(\tau'))^2\Big) + h \sum_i \sum_\alpha \int_0^\beta \mathrm{d}\tau \sigma_i^{z,\alpha}(\tau)\Big].$$

The first step of this integration is justified because the Trace operator runs over the whole set of spin configurations $\{S_i^\alpha\}$.

B.2 The saddle point method

This method [189] allows to evaluate the following type of integrals:

$$\int \mathrm{d}y e^{-NG(y)}, \tag{B.5}$$

where the function G is at least a twice differentiable function. N is a large number. Assume that G has a unique global minimum at y_0. If we multiply this function by a large number N, the gap between $NG(y_0)$ and $NG(y)$ will be large. Then, significant contributions to the integral will only come from points y very close to y_0. We assume that y_0 is not an endpoint of the interval of integration (which can be infinite), that the values of $G(y)$ cannot be close to $G(y_0)$ unless y is close to y_0 and that the second derivative of G at point y_0 is positive: $G''(y_0) > 0$.

Using Taylor's theorem, we expand G around y_0:

$$G(y) = G(y_0) + G'(y_0)(y - y_0) + \frac{1}{2}G''(y_0)(y - y_0)^2 + o((y - y_0)^3). \tag{B.6}$$

Since y_0 is a minimum for the function G, the expansion reads:

$$G(y) \approx G(y_0) + \frac{1}{2}G''(y_0)(y - y_0)^2, \tag{B.7}$$

which gives:

$$\int \mathrm{d}y e^{-NG(y)} \approx e^{-NG(y_0)} \int \mathrm{d}y e^{-\frac{N}{2}G''(y_0)(y-y_0)^2}. \tag{B.8}$$

Appendix C
Equation verified by the function Ψ_l

The starting point of this derivation is the equation (8.24) for the disorder averaged free energy under the static hypothesis, and it is recalled here:

$$-\beta f = \lim_{n\to 0}\frac{1}{n}\Bigg\{ -\frac{\beta^2}{4}\left(\sum_{\alpha\neq\gamma}(q^{\alpha\gamma})^2 + \sum_{\alpha} r^2\right) + \ln\Bigg[Tr\exp\Big\{\beta\Gamma\sum_{\alpha}\sigma_\alpha^x\Big\} \exp\Big\{\frac{\beta^2}{2}\Big(\sum_{\alpha\neq\gamma}\sigma_\alpha^z\sigma_\gamma^z q^{\alpha\gamma} + \sum_{\alpha}\sigma_\alpha^z\sigma_\alpha^z r\Big) + \beta h\sum_{\alpha}\sigma_\alpha^z\Big\}\Bigg]\Bigg\}.$$

To continue the calculation, we will break an arbitrary number (K) of times the symmetry of replicas, and then explicitly calculate the sums that appear in the previous. The scheme of replica symmetry breaking is the same as the classical one, which has been presented in the previous chapter, and it gives the shape of the $q^{\alpha\gamma}$.

C.1 Calculation of the sum of the $(q^{\alpha\gamma})^2$

In a first part, we will calculate the quadratic term in $q^{\alpha\gamma}$, that does not depend on the spin configurations σ:

$$\sum_{\alpha\neq\gamma}(q^{\alpha\gamma})^2, \tag{C.1}$$

This sum is calculated recursively using [154, 152], and is based on the determination of the number of spins in each block and the corresponding size of the block:

$$\sum_{\alpha\neq\beta}(q^{\alpha\beta})^2 = q_K^2\frac{n}{p_K}(p_K^2 - p_K) + r_0^2(n^2 - \frac{n}{p_0}p_0^2) + \sum_{i=0}^{K-1} q_i^2\frac{n}{p_i}(p_i^2 - \frac{p_i}{p_{i+1}}p_{i+1}^2) + \sum_{i=0}^{K-1}(r_{i+1}^2 - r_i^2)\frac{p_i}{p_{i+1}}p_{i+1}^2((\frac{n}{p_i})^2 - \frac{n}{p_i}). \tag{C.2}$$

Note that the notations are the same as in the previous chapter: p_i is the size of blocks in the $q^{\alpha\gamma}$ matrix at step i, and q_i is the corresponding value of overlap. Re-arrangements of the different terms leads to:

$$\lim_{n\to 0}\frac{1}{n}\sum_{\alpha\neq\beta}(q^{\alpha\beta})^2 = q_K^2(p_K - 1) - r_0^2 p_0 + \sum_{i=0}^{K-1} q_i^2 p_i - \sum_{i=0}^{K-1} q_i^2 p_{i+1} - \sum_{i=1}^{K}(r_i^2 - r_{i-1}^2)p_i. \tag{C.3}$$

We introduce a new quantity Δ_i' in order to obtain, in the limit of $p_i \to \infty$:

$$-2\Delta_i' q_i = 2\sum_i p_i q_i\left((q_i - r_i) - (q_{i-1} - r_{i-1}\right) \underset{p_i\to\infty}{\approx} p_i\left(\left(q_i^2 - r_i^2\right) - \left(q_{i-1}^2 - r_{i-1}^2\right)\right). \tag{C.4}$$

Consequently, we get for the term in front of the logarithm in equation (8.24):

$$\frac{\beta^2 J^2}{4}\left(q_K^2 - r^2 + 2\sum_{i=0}^{K}\Delta_i' q_i\right). \tag{C.5}$$

It is now time to go to the calculation of the linear term in $q^{\alpha\beta}$.

C.2 Calculation of the linear term in $q^{\alpha\gamma}$

As this term is harder to calculate, we will only present the method for the first two RSB, but it is possible to find an equation for the case of K RSB. The term to calculate is the following

$$\sum_{\alpha\neq\beta} q^{\alpha\beta}\sigma_\alpha\sigma_\beta. \tag{C.6}$$

It is harder to calculate because of the presence of the spins. We consider here the first two steps of symmetry breaking. We introduce, as seen in the previous chapter, the quantities q_0, r_0, q_1 and r_1. The $q^{\alpha\gamma}$ matrix will have a set of blocks, of size p_0 after step 1, and of size p_1 after step 2 ($p_1 < p_0$). The number of blocks is respectively n/p_0 and n/p_1. We also introduce new indices j_0 and j_1. They run respectively from 1 to n/p_0 and from 1 to n/p_1. Moreover, we introduce an index α that runs from 1 to p_1. With a combination of these three indices, the whole matrix is covered. Consider first that the matrix is only constituted of r_0 terms. At this stage, the linear term reads:

$$r_0(\sum_{j_0 j_1 \alpha} \sigma_{j_0 j_1 \alpha})^2. \tag{C.7}$$

However, the first of RSB consists in replacing the r_0 with q_0 on diagonal blocks of size p_0. We then add to the previous term the following one:

$$(q_0 - r_0)\sum_{j_0}(\sum_{j_1\alpha} \sigma_{j_0 j_1 \alpha})^2. \tag{C.8}$$

The second step consists in replacing r_0 terms by r_1 ones in diagonal blocks of size p_1 (in the remaining blocks of size p_0 with r_0 terms) on the one hand and similarly q_0 terms by q_1 ones in blocks of size p_0 with only q_0 terms. The replacement of r_0 by r_1 leads to a supplementary term of the form:

$$(r_1 - r_0)\left(\sum_{j_1}(\sum_{j_0\alpha} \sigma_{j_0 j_1 \alpha})^2 - \sum_{j_0 j_1}(\sum_{\alpha} \sigma_{j_0 j_1 \alpha})^2\right) \tag{C.9}$$

and the replacement of q_0 by q_1 leads to the following expression:

$$(q_1 - q_0)\sum_{j_0 j_1}(\sum_{\alpha} \sigma_{j_0 j_1 \alpha})^2 - nq_1. \tag{C.10}$$

One can continue the RSB sheme to reach K steps in a similar way.

All the terms (equations (C.7), (C.8), (C.9) and (C.10)) are quadratic in spin operators σ except the last one: nq_1. It is proportional to n, it can then be extracted from the exponential and even from the $\lim_{n\to 0}$ operation. As a consequence, the quadratic term in $q^{\alpha\gamma}$ and this terms read:

$$\frac{\beta^2}{4}\left(q_K^2 - r^2 - 2q_K + 2r + 2\sum_{i=0}^{K}\Delta'_i q_i\right) \tag{C.11}$$

$$= \frac{\beta^2}{4}\left((1-q_K)^2 - (1-r)^2 + 2\sum_{i=0}^{K}\Delta'_i q_i\right) \tag{C.12}$$

From what, we get

$$-\beta f = \frac{\beta^2}{4}\left((1-q_K)^2 - (1-r)^2 + 2\sum_{i=0}^{K}\Delta'_i q_i\right) + \lim_{\substack{n\to 0 \\ p_0 \gg p_1 \gg \ldots \gg p_K \to \infty}} \Psi_{-1}(\Gamma, h)^1. \tag{C.13}$$

[1] the denomination of this function as Ψ_{-1} will become clearer in section C.3

All the terms which appear in $\Psi_{-1}(\Gamma, h)$ are quadratic in spin operators. We will linearize them by using a **Hubbard-Stratonovitch** transform as in section 8.1.2.

C.3 From discrete to continuous sums

Following [152], it is possible to change the sums in the logarithm into a succession of hierarchical integrals. In the simpler case of two steps of RSB, we obtain for the term of (C.7) an integral under the form:

$$\exp r_0(\sum_{j_0 j_1 \alpha} \sigma_{j_0 j_1 \alpha})^2 \to \int \frac{\mathrm{d}z_0}{\sqrt{2\Pi}} \exp\left(-\frac{z_0^2}{2} + z_0\sqrt{r_0}\beta \sum_\alpha \sigma_\alpha^z\right). \tag{C.14}$$

In the same way, the term of equation (C.8) can be written as:

$$\exp(q_0 - r_0) \sum_{j_0} (\sum_{j_1 \alpha} \sigma_{j_0 j_1 \alpha})^2 \to \prod_{j_0} \int \frac{\mathrm{d}y_{j_0}}{2\Pi} \exp\left(-\frac{y_{j_0}^2}{2} + y_{j_0}\sqrt{q_0 - r_0}\beta \sum_\alpha \sigma_\alpha^z\right). \tag{C.15}$$

The expressions (C.9) and (C.10) concerning the second step of RSB read

$$\exp(r_1 - r_0) \left(\sum_{j_1} (\sum_{j_0 \alpha} \sigma_{j_0 j_1 \alpha})^2\right) \to \prod_{j_1} \int \frac{\mathrm{d}z_{j_1}}{2\Pi} \exp\left(-\frac{z_{j_1}^2}{2} + z_{j_1}\sqrt{r_1 - r_0}\beta \sum_\alpha \sigma_\alpha^z\right), \tag{C.16}$$

and

$$\exp\left((q_1 - q_0) - (r_1 - r_0)\right) \left(\sum_{j_0 j_1} (\sum_\alpha \sigma_{j_0 j_1 \alpha})^2\right) \to$$

$$\prod_{j_0} \prod_{j_1} \int \frac{\mathrm{d}y_{j_0 j_1}}{2\Pi} \exp\left(-\frac{y_{j_0 j_1}^2}{2} + y_{j_0 j_1}\sqrt{(q_1 - q_0) - (r_1 - r_0)}\beta \sum_\alpha \sigma_\alpha^z\right). \tag{C.17}$$

By extension to a number $K \gg 1$ of steps of RSB, we get the formula for the function $\exp n\Psi_{-1}(\Gamma, h)$

$$\begin{aligned}
&\exp n\Psi_{-1}(\Gamma, h) \\
&\quad = \int \frac{\mathrm{d}z_0}{\sqrt{2\pi}} \exp -\frac{z_0^2}{2} \prod_{j_1} \frac{dz_{j_1}}{2\pi} \exp -\frac{z_{j_1}^2}{2} ... \prod_{j_K} \frac{dz_{j_K}}{\sqrt{2\pi}} \exp -\frac{z_{j_K}^2}{2} \\
&\quad \times \prod_{j_0=1}^{n/p_0} \Big(\int \frac{\mathrm{d}y_{j_0}}{\sqrt{2\pi}} \exp -p_0 \frac{y_{j_0}^2}{2} \prod_{j_1=1}^{p_0/p_1} \Big[\int \frac{\mathrm{d}y_{j_0 j_1}}{\sqrt{2\pi}} \exp -p_1 \frac{y_{j_0 j_1}^2}{2} \\
&\quad \times \prod_{j_2=1}^{p_1/p_2} \Big(... \prod_{j_K=1}^{p_{K-1}/p_K} \Big[\int \frac{\mathrm{d}y_{j_0 ... j_K}}{\sqrt{2\pi}} \exp -p_K \frac{y_{j_0 ... j_K}^2}{2} \\
&\quad \times \underset{(p_K)}{Tr} \exp \beta \sum_\alpha^{p_K} (\sigma_\alpha^z H_z + \sigma_\alpha^x \Gamma) \Big] ... \Big) \Big] \Big),
\end{aligned} \tag{C.18}$$

where we have the notation:

$$H_z = h + \sqrt{q_0} z_0 + ... + \sqrt{q_K - q_{K-1}} z_{j_K} + \sqrt{-\Delta_0'} y_{j_0} + ... + \sqrt{-\Delta_K'} y_{j_0 ... j_K}. \tag{C.19}$$

The operator σ^x can be reintroduced inside the exponential that does only depend on σ^z in equation (8.24). This is allowed thanks to the presence of the Trace operator: if one considers two operators that do not commute, we all the same have the following equality:

$$Tr\left(e^A e^B\right) = Tr\left(e^{A+B}\right). \tag{C.20}$$

The trace operation on the following operator

$$\sigma_\alpha^z H_z + \sigma_\alpha^x \Gamma, \tag{C.21}$$

is calculated by diagonalizing this 2×2 matrix, which leads to the eigenvalues:

$$\pm\sqrt{H_z^2 + \Gamma^2}. \tag{C.22}$$

The calculation of the trace gives

$$\begin{aligned}
&\exp n\Psi_{-1}(h,\Gamma) \\
&\quad = \int \frac{\mathrm{d}z_0}{\sqrt{2\pi}} \exp\left(-\frac{z_0^2}{2}\right) \prod_{j_1} \frac{dz_{j_1}}{2\pi} \exp\left(-\frac{z_{j_1}^2}{2}\right) ... \prod_{j_K} \frac{dz_{j_K}}{\sqrt{2\pi}} \exp\left(-\frac{z_{j_K}^2}{2}\right) \\
&\quad \times \prod_{j_0=1}^{n/p_0} \Big(\int \frac{\mathrm{d}y_{j_0}}{\sqrt{2\pi}} \exp\left(-p_0 \frac{y_{j_0}^2}{2}\right) \prod_{j_1=1}^{p_0/p_1} \Big[\int \frac{\mathrm{d}y_{j_0 j_1}}{\sqrt{2\pi}} \exp\left(-p_1 \frac{y_{j_0 j_1}^2}{2}\right) \\
&\quad \times \prod_{j_2=1}^{p_1/p_2} \Big(... \prod_{j_K=1}^{p_{K-1}/p_K} \Big[\int \frac{\mathrm{d}y_{j_0 ... j_K}}{\sqrt{2\pi}} \exp\left(-p_K \frac{y_{j_0 ... j_K}^2}{2}\right) \\
&\quad \times \ln p_K \exp(2\cosh\sqrt{H_z^2 + \Gamma^2}) \Big] ... \Big) \Big] \Big).
\end{aligned} \tag{C.23}$$

From this expression, we define iteratively the set of functions $(\Psi_l)_{l \geq -1}$ (equation (8.26)). Their structure is given in the following equation and it is suggested by the hierarchical form of $\exp n\Psi_{-1}(h,\Gamma)$.

$$\begin{aligned}
\exp p_{l-1}\Psi_{l-1}(h,\Gamma) &= \int \frac{\mathrm{d}z_l}{\sqrt{2\pi}} \exp -\frac{z_l^2}{2} \\
&\times \left(\int \frac{\mathrm{d}y_l}{\sqrt{2\pi}} \exp p_l \Big[-\frac{y_l^2}{2} + \Psi_l\big(h + \sqrt{q_l - q_{l-1}} z_l + \sqrt{-\Delta_l'} y_l, \Gamma\big) \Big] \right)^{p_{l-1}/p_l}. \\
l = 0..K \qquad & p_{-1} \equiv n \qquad\qquad q_{-1} \equiv 0
\end{aligned}$$

More precisely, this form has been proposed *a priori* but it allows to get $\Psi_{-1}(h,\Gamma)$ back, provided that we impose:

$$\begin{aligned}
&\exp p_l \Psi_l(h + \sqrt{q_l - q_{l-1}} z_l + \sqrt{-\Delta_l'} y_l, \Gamma) \\
&\quad = \underset{(p_l)}{Tr} \exp \times \Big\{ \sum_{\alpha=1}^{p_l} \Big[\sum_{i=0}^{l} \Big(\beta\sqrt{q_i - q_{i-1}} z_i + \beta\sqrt{-\Delta_i'} y_i \Big) + \beta h \Big] \sigma_\alpha^z + \Gamma \sigma_\alpha^x \\
&\quad + \frac{\beta^2}{2} \sum_{\alpha \neq \beta}^{p_l} (Q^{\alpha\beta} - q_l) \sigma^\alpha \sigma^\beta \Big\}.
\end{aligned} \tag{C.24}$$

C.4 Justifications

Form of Ψ_l

In equation (C.24), we have chosen an iterative form for the function Ψ_l. In this section, we are interested in the justification of that particular form.

Consider step l of the RSB procedure ($1 \leq l \leq K$). At this step, we have already performed all the Hubbard-Stratonovitch transforms described in the previous section on blocks of size greater than p_l, which is indicated by the presence of the indices z_i and y_i in sums for i running from 1 to l. Then the next RSB step begins: the terms q_l are replaced by generic terms $q^{\alpha\gamma}$, which leads to the appearance of the term $\sum_{\alpha\neq\gamma}^{p_l}(q^{\alpha\gamma} - q_l)\sigma_\alpha\sigma_\gamma$. The block structure of [151] is found by writing this term as:

$$\sum_{\alpha\neq\beta}^{p_l}(r_{\alpha\beta} - r_l)\sigma_\alpha\sigma_\beta + \sum_{\alpha\neq\beta}^{p_l}[(q_{\alpha\beta} - q_l) - (r_{\alpha\beta} - r_l)]\sigma_\alpha\sigma_\beta. \tag{C.25}$$

Boundary conditions

As seen in section C.3, the continuous version of RSB is performed by assuming that the total number of steps of RSB $K \to \infty$, $l/K \to x$, where l is the step number. To find the boundary condition on $\Psi(x = 1, h, \Gamma)$, we only have to put $l \equiv K$ in equation (C.24). At that point, as we are performing the last RSB step, the last sum is equal to zero ($q^{\alpha\gamma} = q_K$). We immediately deduce that the remaining terms can be written in the form (equation (8.27)):

$$\Psi(1, h, \Gamma) = \ln\left(2\cosh\left(\beta\sqrt{h^2 + \Gamma^2}\right)\right).$$

Bibliography

[1] D. Sherrington. Physics and Complexity. *Phil. Trans. R. Soc. A*, 368:1175–1189, 2010.

[2] Ill Condensed Matter. In R. Balian, editor, *Les Houches Summer School*. North Holland, Amsterdam, 1978.

[3] M.A. Ruderman and C. Kittel. Indirect exchange coupling of nuclear magnetic moments by conduction electrons. *Phys. Rev.*, 96:99, 1954.

[4] T. Kasuya. A theory of metallic ferro- and antiferromagnetism on zener's model. *Prog. Theor. Phys.*, 16:45, 1956.

[5] K. Yosida. Magnetic properties of cu-mn alloys. *Phys. Rev.*, 106:893, 1957.

[6] M.J. Harris, S.T. Bramwell, D.F. McMorrow, T. Zeiske, and K.W. Godfrey. Geometrical frustration in the ferromagnetic pyrochlore $Ho_2Ti_2O_7$. *Phys. Rev. Lett.*, 79:2554, 1997.

[7] S.T. Bramwell and M.J. Gingras. Spin ice state in frustrated magnetic pyrochlore materials. *Science*, 294:1495, 2001.

[8] K. H. Fischer and J.A. Hertz. *Spin Glasses*. Cambridge University Press, 1991.

[9] J.A. Mydosh. *Spin Glasses, An Experimental Introduction*. Taylor and Francis, London, 1993.

[10] K. Binder and W. Kob. *Glassy materials and disordered solids: an introduction to their statistical mechanics*. Hackensack, NJSingapore: World Scientific, 2005.

[11] C.AM. Mulder, A.J. van Duyneveldt, and J.A. Mydosh. Susceptibility of the cu:mn spin-glass: Frequency and field dependences. *Phys. Rev. B*, 23:1384, 1981.

[12] B. Diu, C. Guthmann, D. Lederer, and B. Roulet. *Physique Statistique*. Hermann, 2001.

[13] L.E. Wenger and P.H. Keesom. Calorimetric investigation of a spin glass alloy: Cu:mn. *Phys. Rev. B*, 13:4053, 1976.

[14] R. Omari, J.J. Prejean, and J. Souletie. Critical measurements in the spin glass cu:mn. *J. Phys*, 44:1069, 1983.

[15] J. Chalupa. Scaling at the critical temperature of a spin glass. *Solid State Commun.*, 24:429, 1977.

[16] P. Monod and H. Bouchiat. Equilibrium magnetization of a spin glass: is mean-field theory valid? *J Phys Lett*, 43:L–45, 1982.

[17] D. Hüser, L.E. Wenger, A.J. van Duyneveldt, and J.A. Mydosh. Dynamical behavior of the susceptibility around the freezing temperature in (Eu,Sr)S. *Phys. Rev. B*, 27:3100, 1983.

[18] S. Nagata, P.H. Keesom, and H.R. Harrison. Low-dc-field susceptibility of cu:mn spin glass. *Phys. Rev. B*, 19:1633, 1979.

[19] L.E. Wenger. In J.L. van Hemmen and I. Morgenstern, editors, *Poceedings of the Heidelberg Colloquium on Spin Glasses, Lecture Notes in Physics*, volume 192, page 60. Springer (Berlin), 1983.

[20] E. Vincent, J. Hammann, M. Ocio, J-P. Bouchaud, and L.F. Cugliandolo. Slow dynamics and aging in spin glasses. In *Complex behavior of glassy systems. Proceedings*, volume 476, page 184. Springer (Berlin), 1997.

[21] L. Lundgren, P. Svedlindh, P. Nordblad, and O. Beckman. Dynamics of the relaxation-time spectrum in a cu:mn spin glass. *Phys. Rev. Lett.*, 51:911, 1983.

[22] P.Nordblad and P.Svelindh. *Spin Glasses and Random Fields*, volume 12 of *Directions in Condensed Matter Physics*, pages 1–27. World Scientific, Singapore, 1998.

[23] K. Jonason, E. Vincent, J. Hammann, J-P. Bouchaud, and P. Nordblad. Memory and chaos effects in spin glasses. *Phys. Rev. Lett.*, 81:3243, 1998.

[24] D. X. Viet and H. Kawamura. Monte Carlo studies of chiral and spin ordering of the three-dimensional Heisenberg spin glass. *Phys. Rev. B*, 80:064418, 2009.

[25] A. Sharma and A.P. Young. The de Almeida-Thouless line in vector spin glasses. *ArXiv:1003.5599*, 2010.

[26] S.F. Edwards and P.W. Anderson. Theory of spin glasses. *J. Phys. F*, 5(5):965, 1975.

[27] S.F. Edwards and P.W. Anderson. Theory of spin glasses: II. *J. Phys. F*, 6(10):1927, 1976.

[28] D.S. Fisher and D.A. Huse. Ordered phase of short-range Ising spin-glasses. *Phys. Rev. Lett.*, 56:1601, 1986.

[29] D. Sherrington and S. Kirkpatrick. Solvable model of a spin glass. *Phys. Rev. Lett.*, 35:1792, 1975.

[30] M. Mézard, G. Parisi, and M. Virasoro. *Spin Glass Theory and Beyond*. World Scientific, 1987.

[31] V. Dotsenko. *Introduction to the Replica theory of disordered statistical systems*. Cambridge University Press, 2001.

[32] J.R.L. de Almeida and D.J. Thouless. Stability of the sherrington-kirkpatrick solution of a spin glass model. *J. Phys. A*, 11:983, 1978.

[33] G. Parisi. The order parameter for spin glasses: a function on the interval 0-1. *J. Phys. A*, 13:1101, 1980.

[34] G. Parisi. Infinite number of order parameters for spin glasses. *Phys. Rev. Lett.*, 43:1754, 1979.

[35] G. Parisi. Order parameter for spin glasses. *Phys. Rev. Lett.*, 50:1946, 1983.

[36] A.P. Young. Phase transitions in spin glasses. *JMMM*, 310:1482, 2007.

[37] A.J. Bray and M.A. Moore. Critical behavior of the three-dimensional ising spin glass. *Phys. Rev. B*, 31:631, 1985.

[38] W.L. MacMillan. Monte carlo simulation of the two-dimensional random (+/- j) ising model. *Phys. Rev. B*, 28:5216, 1983.

[39] W.L. MacMillan. Domain-wall renormalization-group study of th three-dimensional random ising model at finite temperature. *Phys. Rev. B*, 31:340, 1985.

[40] Y. Imry and S-K. Ma. Random-field instability of the ordered state of continuous symmetry. *Phys. Rev. Lett.*, 35:1399, 1975.

[41] L. Cugliandolo. Dynamics of glassy systems. In *Lecture notes, Les Houches Session LXXVII*, 2002.

[42] J.-P. Bouchaud. Weak ergodicity breaking and aging in disordered systems. *J. Phys. I*, 2:1705, 1992.

[43] B. Derrida. Random Energy Model: an exactly solvable model of disordered systems. *Phys. Rev. B*, 24:2613, 1981.

[44] J-P. Bouchaud and D.S. Dean. Aging on Parisi's Tree. *J. Phys. I*, 5:265, 1995.

[45] L. Cugliandolo and J. Kurchan. Analytical solution of the off-equilibrium dynamics of a long-range spin-glass model. *Phys. Rev. Lett.*, 71:173, 1993.

[46] L. Cugliandolo, D.S. Dean, and J. Kurchan. Fluctuation-Dissipation Theorem and entropy production in relaxational systems. *Phys. Rev. Lett.*, 79:2168, 1997.

[47] E. Vincent, J. Hamman, and M. Ocio. Real spin glasses relax slowly in the shade of hierarchical trees. In Journal of Statistical Physics, editor, *Wandering with Curiosity in Complex Landscapes*, volume to appear, 2009.

[48] L. Cugliandolo, J. Kurchan, and L. Peliti. Energy flow, partial equilibration, and effective temperatures in systems with slow dynamics. *Phys. Rev. E*, 55:3898, 1997.

[49] D. Hérisson and M. Ocio. Off-equilibrium fluctuation-dissipation relation in a spin glass. *Eur. Phys. J. B*, 40:283, 2004.

[50] T.R. Kirkpatrick and D. Thirumalai. Dynamics of the structural glass transition and the p-spin-interaction spin glass model. *Phys. Rev. Lett.*, 58:2091, 1987.

[51] T.R. Kirkpatrick and P.G. Wolynes. Stable and metastablestates in mean-field Potts and structural glasses. *Phys. Rev. B*, 36:8552, 1987.

[52] F. Krzakala. *Aspects géométriques et paysage d'énergie des verres de spins.* PhD thesis, Université Paris 6, 2002.

[53] P.R. Clayton. *Fundamentals of electric circuit analysis.* John Wiley & sons, 2001.

[54] P. Drude. Zur elektronentheorie der metalle. *Annalen der Physik*, 306:566, 1900.

[55] P. Drude. Zur elektronentheorie der metalle; *ii*. galvanomagnetische und thermomagnetische effecte. *Annalen der Physik*, 308:369, 1900.

[56] E. Hecht. *Optics.* Addison-Wesley, 2002.

[57] Y. Imry. *Introduction to mesoscopic physics.* Oxford University Press, 2002.

[58] P. Debye. Zur theorie der spezifischen waerme. *Annalen der Physik*, 39:789, 1912.

[59] D.J. Thouless. Maximum metallic resistance in thin wires. *Phys. Rev. Lett.*, 39:1167, 1977.

[60] S. Chakravarty and A. Schmid. Weak localization: the quasiclassical theory of electrons in a random potential. *Phys. Rep.*, 140:193, 1986.

[61] B.L. Al'tshuler. *Soviet Scientific reviews. Section A: physics reviews*. Harwood Academic, New York, 1987.

[62] B.L. Al'tshuler, A.G. Aronov, and P.A. Lee. Interaction effects in disordered fermi systems in two dimensions. *Phys. Rev. Lett.*, 44:1288, 1980.

[63] B.L. Al'tshuler, A.G. Aronov, and D.E. Khmelnitskii. Effects on electron-electron collisions with small energy transfers on quantum localization. *J. Phys. C*, 15:7367, 1982.

[64] B.L. Al'tshuler and A.G. Aronov. Electron-electron interaction in disordered conductors. In *Electron-electron interaction in disordered systems*, page 1. Elsevier, 1985.

[65] D. Pines and P. Nozières. *The theory of quantum liquids*, volume 1. Addison-Wesley, 1989.

[66] E. Abrahams, P.W. Anderson, P.A. Lee, and T.V. Ramakrishnan. Quasiparticle lifetime in disordered two dimensional systems. *Phys. Rev. B*, 24:6783, 1981.

[67] W. Eiler. Electron-electron interaction and weak localization. *J. Low Temp. Phys.*, 56:481, 1984.

[68] W.J. de Haas and G.J. van den Berg. *Physica*, 3:440, 1936.

[69] J. Kondo. Resistance minimum in dilute magnetic alloys. *Prog. Theor. Phys.*, 32:37, 1964.

[70] P. Nozières. A "Fermi-liquid" description of the Kondo problem at low temperatures. *J. Low Temp. Phys.*, 17:31, 1974.

[71] G.D. Mahan. *Many-particle physics*. Plenum press, 1981.

[72] B.L. Al'tshuler and A.G. Aronov. Magnetoresistance of thin films and of wires in a longitudinal magnetic field. *JETP Lett.*, 33:499, 1981.

[73] J.C. Licini, G.J. Dolan, and D.J. Bishop. Weakly localized behavior in quasi-one-dimensional li films. *Phys. Rev. Lett.*, 54:1585, 1985.

[74] P.M. Echternach, M.E. Gershenson, H.M. Bozler, A.L. Bogdanov, and B. Nilsson. Nyquist phase relaxation in one-dimensional metal films. *Phys. Rev. B*, 48:11516, 1993.

[75] F. Pierre, A.B. Gougam, A. Anthore, H. Pothier, D. Esteve, and N. Birge. Dephasing of electrons in mesoscopic metal wires. *Phys. Rev. B*, 68:85413, 2003.

[76] C. Bäuerle, F. Mallet, F. Schopfer, D. Mailly, G. Eska, and L. Saminadayar. Experimental test of the numerical renormalization group theory for inelastic scattering from magnetic impurities. *Phys. Rev. Lett.*, 95:266805, 2005.

[77] P. Mohanty, E.M.Q. Jariwala, and R.A. Webb. Intrinsic decoherence in mesoscopic systems. *Phys. Rev. Lett.*, 78:3366, 1997.

[78] P. Mohanty and R.A. Webb. High-field measurements of electron decoherence time in metallic nanowires: switching off magnetic impurity spins. *Phys. Rev. Lett.*, 91:066604, 2003.

[79] D.S. Golubev and A.D. Zaikin. Quantum decoherence in disordered mesoscopic systems. *Phys. Rev. Lett.*, 81:1074, 1998.

[80] L. Saminadayar, P. Mohanty, R.A. Webb, P. Degiovanni, and C. Bäuerle. Electron coherence at low temperatures: the role of magnetic impurities. *Physica E*, 40:12–24, 2007.

[81] Y. Niimi, Y. Baines, T. Capron, D. Mailly, F-Y. Lo, A.D. Wieck, T. Meunier, L. Saminadayar, and C. Bäuerle. Quantum coherence at low temperatures in mesoscopic systems: effect of disorder. *ArXiv:0911.3201*, 2009.

[82] F. Schopfer, C. Bäuerle, W. Rabaud, and L. Saminadayar. Anomalous temperature dependence of the dephasing time in mesoscopic Kondo wires. *Phys. Rev. Lett.*, 90:056801, 2003.

[83] P.G.N. de Vegvar, L.P. Lévy, and T.A. Fulton. Conductance fluctuations of mesoscopic spin glasses. *Phys. Rev. Lett.*, 66:2380, 1991.

[84] N. W. Ashcroft and N. D. Mermin. *Solid state physics*. MacGraw Hill, 1976.

[85] S. Hikami, A. Larkin, and Y. Nagaoka. Spin-orbt interaction and magnetoresistance in the two dimensional random system. *Prog. Theor. Phys.*, 63:707, 1980.

[86] E. Akkermans and G. Montambaux. *Mesoscopic Physics of electrons and photons*. Cambridge University Press, 2007.

[87] D. Vollhardt and P. Wölfle. Diagrammatic, self-consistent treatment of the Anderson localization problem in d‘2 dimensions. *Phys. Rev. B*, 22:4666, 1980.

[88] B.L. Al'tshuler and B.Z. Spivak. Variation of the random potential and the conductivity of samples of small dimensions. *JETP Lett.*, 42:447, 1985.

[89] P.A. Lee, D. Stone, and H. Fukuyama. Universal conductance fluctuations in metals: Effects of finite temperature, interactions, and magnetic field. *Phys. Rev. B*, 35:1039, 1987.

[90] D. Mailly and M. Sanquer. Sensitivity of quantum conductance fluctuations and of $1/f$ noise to time reversal symmetry. *J. Phys. I, France*, 2:357, 1992.

[91] B.L. Al'tshuler. Fluctuations in the extrinsic conductivity of disordered conductors. *JETP Lett.*, 41:648, 1985.

[92] B.L. Al'tshuler and B. Shklovskii. Repulsion of energy levels and conductivity of small metal samples. *Sov. Phys. JETP Lett*, 64:127, 1986.

[93] P. A. Lee and A. D. Stone. Universal conductance fluctuations in metals. *Phys. Rev. Lett.*, 55(15):1622, 1985.

[94] Y. Imry. Active transmission channels and Universal Conductance Fluctuations. *Europhys. Lett.*, 1:249, 1986.

[95] K. A. Muttalib, J-L. Pichard, and A.D. Stone. Random-Matrix Theory and universal statistics for disordered quantum conductors. *Phys. Rev. Lett.*, 59:2475, 1987.

[96] P.A. Mello. Macroscopic approach to Universal Conductance Fluctuations in disordered metals. *Phys. Rev. Lett.*, 60:1089, 1988.

[97] P.A. Mello and A.D. Stone. Maximum-entropy model for quantum-mechanical interference effects in metallic conductors. *Phys. Rev. B*, 44:3559, 1991.

[98] A. M. S. Macêdo. Random-matrix approach to the quantum-transport theory of disordered conductors. *Phys. Rev. B*, 49:1858, 1994.

[99] E. P. Wigner. *Proc. Canadian Mathematical Congress*, page p174. Univ. of Toronto Press, Toronto, 1957.

[100] F. J. Dyson. The threefold way. algebraic structure of symmetry groups and ensembles in quantum mechanics. *J. Math. Phys.*, 3:1199, 1962.

[101] C. W. J. Beenakker. Random-matrix theory of quantum transport. *Rev. Mod. Phys.*, 69:731, 1997.

[102] A.A. Golubentsev. Direct calculation of the conductivity of films with magnetic impurities. *JETP Lett.*, 41:642, 1985.

[103] V. Chandrasekhar, P. Santhanam, and D.E. Prober. Effect of spin-orbit and spin-flip scattering on conductance fluctuations. *Phys. Rev. B*, 42:6823, 1990.

[104] M. Pascaud and G. Montambaux. Interference effects in mesoscopic disordered rings and wires. *Physics - Uspekhi*, 41:182, 1998.

[105] N.E. Israeloff, M.B. Weissman, G.J. Nieuwenhuys, and J. Kosiorowska. Electrical noise from spins fluctuations in cumn. *Phys. Rev. Lett.*, 63:794, 1989.

[106] M.B. Weissman. 1/f noise and other slow, nonexponential kinetics in condensed matter. *Rev. Mod. Phys.*, 60:537, 1988.

[107] J. Jaroszynski, J. Wrobel, G. Karczewski, T. Wojtowicz, and T. Dietl. Magnetoconductance noise and irreversibilities in submicron wires of spin-glass n+-cdmnte. *Phys. Rev. Lett.*, 80:5635, 1998.

[108] T. Dietl. *Handbook on semiconductors*, volume 3b, page 1251. North-Holland, Amsterdam, 1994.

[109] S. Feng, A. Bray, P. Lee, and M. Moore. Universal conductance fluctuations as a probe of chaotic behavior in mesoscopic metallic spin glasses. *Phys. Rev. B*, 36:5624, 1987.

[110] G. Neuttiens, C. Strunk, C. Van Haesendonck, and Y. Bruynseraede. Universal conductance fluctuations and low-temperature 1/f noise in mesoscopic aufe spin glasses. *Phys. Rev. B*, 62:3905, 2000.

[111] P.W. Anderson. Absence of diffusion in certain random lattice. *Phys. Rev.*, 109:1492, 1958.

[112] S. Datta. *Electronic transport in mesoscopic systems*. Cambridge University Press, 1997.

[113] R. Landauer. Spatial variation of currents and fields due to localized scatterers in metallic conduction. *IBM J. Res. Dev.*, 1:223, 1957.

[114] J-L. Basdevant and J.Dalibard. *Mécanique quantique*. Ellipses, editions de l'ecole polytechnique edition, 2002.

[115] M. Buttiker, Y. Imry, R. Landauer, and S. Pinhas. Generalized many-channel conductance formula with application to small rings. *Phys. Rev. B*, 31:6207 – 6215, 1985.

[116] L. I. Deych, M. V. Erementchouk, and A. A. Lisyansky. Scaling in the one-dimensional anderson localization problem in the region of fluctuation states. *Phys. Rev. Lett.*, 90:126601, 2003.

[117] D. S. Fisher and P.A. Lee. Relation between conductivity and transmission matrix. *Phys. Rev. B*, 23:6851–6854, 1981.

[118] S. Doniach and E.H. Sondheimer. *Green's functions for solid state physicists*. W.A Benjamin, 1974.

[119] A. Croy, R. A. Roemer, and M. Schreiber. Localization of electronic states in amorphous materials: recursive green's function method and the metal-insulator transition at e<>0. In K. Hoffman and A. Meyer, editors, *Lecture notes in Computational Science and Engineering*, volume Lecture notes in Computational Science and Engineering. Springer (Berlin), 2006.

[120] E. Abrahams, P.W. Anderson, D.C. Licciardello, and T.V. Ramakrishnan. Scaling theory of localization: Absence of quantum diffusion in two dimensions. *Phys. Rev. Lett.*, 42:673, 1979.

[121] Juliette Billy, Vincent Josse, Zhanchun Zuo, Alain Bernard, Ben Hambrecht, Pierre Lugan, David Clément, Laurent Sanchez-Palencia, Philippe Bouyer, and Alain Aspect. Direct observation of anderson localization of matter waves in a controlled disorder. *Nature*, 453:891–894, 2008.

[122] Giacomo Roati, Chiara D'Errico, Leonardo Fallani, Marco Fattori, Chiara Fort, Matteo Zaccanti, Giovanni Modugno, Michele Modugno, and Massimo Inguscio. Anderson localization of a non-interacting bose–einstein condensate. *Nature*, 453:895–898, 2008.

[123] B. Derrida, K. Mecheri, and J-L. Pichard. Lyapunov exponents of products of random matrices: weak disorder expansion. Application to localization. *J. Phys. France*, 48:733, 1987.

[124] P. Markos. Weak disorder expansion of lyapunov exponents of products of random matrices: A degenerate theory. *Journal of Statistical Physics*, 70(3/4):899, 1993.

[125] J-L. Pichard. Random matrix theory of scattering in chaotic and disordered media. In P. Sebbah, editor, *Waves and Imaging through Complex Media*. Kluwer Academin Publishers, 2001.

[126] P.W. Anderson, D.J. Thouless, E. Abrahams, and D.S. Fisher. New method for a scaling of localization. *Phys. Rev. B*, 22:3519, 1980.

[127] J-L. Pichard. In NATO ASI SERIES B254 B. KRAMER, editor, *Quantum Coherence in Mesoscopic systems*, page 369. PLENUM, NEW YORK, 1991.

[128] B.L. Al'tshuler, V.E. Kravtsov, and I.V. Lerner. *Sov. Phys. JETP*, 64:1352, 1986.

[129] B. Shapiro. Conductance distribution at the mobility edge. *Phys. Rev. Lett.*, 65:1510, 1990.

[130] K. A. Muttalib and P. Wölfle. "one-sided" log-normal distribution of conductances for a disordered quantum wire. *Phys. Rev. Lett.*, 83(15):3013, 1999.

[131] P. Markos. Dimension dependance of the conductance distribution in the nonmetallic regime. *Phys. Rev. B*, 65:104207, 2002.

[132] L.S. Froufe-Pérez, P. Garcia-Mochales, P.A. Serena, P.A. Mello, and J.J. Saenz. Conductance distributions in quasi-one-dimensional disordered wires. *Phys. Rev. Lett.*, 89(24):246403, 2002.

[133] K. A. Muttalib, P. Wölfle, A. García-Martín, and V. A. Gopar. Nonanalyticity in the distribution of conductances in quasi-one-dimensional wires. *Europhys. Lett.*, 61:95, 2003.

[134] Z. Qiao, Y. Xing, and J. Wang. New universal conductance fluctuation of mesoscopic systems in the crossover regime from metal to insulator. *ArXiv:0910.3475v1*, 2009.

[135] A. MacKinnon and B. Kramer. One-parameter scaling of localization length and conductance in disordered systems. *Phys. Rev. Lett.*, 47(21):1546, 1981.

[136] A. Cohen, Y. Roth, and B. Shapiro. Universal distributions and scaling in disordered systems. *Phys. Rev. B*, 38:12125, 1988.

[137] C. W. J. Beenakker and H. van Houten. Quantum transport in semiconductor nanostructures. *Solid State Physics*, 44:1, 1991.

[138] D. Carpentier and E. Orignac. Measuring overlaps in mesoscopic spin glasses via conductance fluctuations. *Phys. Rev. Lett.*, 100:057207, 2008.

[139] G. Paulin and D. Carpentier. Probing correlations between random spin configurations through conductance fluctuations : a numerical landauer study. preprint, 2009.

[140] M. Cieplak, B.R. Bulka, and T. Dietl. Universal conductance fluctuations in spin glasses. *Phys. Rev. B*, 44:12337, 1991.

[141] B.L. Al'tshuler, A.G. Aronov, and A.Y. Zyusin. *JETP*, 59:415, 1984.

[142] H. L. Engquist and P.W. Anderson. Definition and measurement of the electrical and thermal resistances. *Phys. Rev. B*, 24:1151, 1981.

[143] M.C.W. van Rossum, Igor V. Lerner, Boris L. Altshuler, and Th. M. Nieuwenhuizen. Deviations from the gaussian distribution of mesoscopic conductance fluctuations. *Phys. Rev. B*, 55:4710, 1997.

[144] M. G. Kendall and A. Stuart. *Advanced Theory of Statistics*. 6th ed. Griffin, London, 1976.

[145] O. Tsyplyatyev, I.L. Aleiner, V.I. Fal'ko, and I.V. Lerner. Applicability of the ergodic hypothesis to mesoscopic fluctations. *Phys. Rev. B*, 68:121301, 2009.

[146] A. A. Fedorenko and D. Carpentier. Magnetic dephasing in a mesoscopic spin glass. ArXiv:0904.1011v1, 2009.

[147] Y.Y. Goldschmidt. Solvable model of the quantum spin glass in a transverse field. *Phys. Rev. B*, 41:4858, 1990.

[148] L.F. Cugliandolo, D.R. Grempel, and C.A. da Silva Santos. From second to first order transitions in a disordered quantum magnet. *Phys. Rev. Lett.*, 85:2589, 2000.

[149] G. Biroli and L.F. Cugliandolo. Quantum Thouless-Anderson-Palmer equations for glassy systems. *Phys. Rev. B*, 64:014206, 2001.

[150] S. Sachdev. *Quantum Phase Transition*. Cambridge University Press, 1999.

[151] C. de Dominicis, M. Gabay, and H. Orland. Replica derivation of sompolinsky free energy functional for mean field spin glasses. *J Phys Lett*, 42:L523, 1981.

[152] C. de Dominicis, M. Gabay, and B. Duplantier. A parisi equation for sompolinsky's solution of the SK model. *J. Phys. A*, 15:L47–L49, 1982.

[153] R.G. Palmer. *Adv. Phys.*, 31:669, 1982.

[154] H. Sompolinsky. Time-dependent order parameters in spin-glasses. *Phys. Rev. Lett.*, 47:935, 1981.

[155] S. Pankov. Low-Temperature solution of the Sherrington-Kirkpatrick model. *Phys. Rev. Lett.*, 96:197204, 2006.

[156] Y.Y. Goldschmidt and P-Y. Lai. Ising spin glass in a transverse field: Replica-symmetry-breaking. *Phys. Rev. Lett.*, 64:2467, 1990.

[157] P.W. Anderson, B.I. Halperin, and C.M. Varma. *Philos. Mag.*, 25:1–9, 1972.

[158] W.A. Philips. Tuneling states in amorphous solids. *Journ. of low Temp. Phys.*, 7:351–360, 1972.

[159] J. Ye, S. Sachdev, and N. Read. Solvable spin glass of quantum rotors. *Phys. Rev. Lett.*, 70:4011, 1993.

[160] N. Read, S. Sachdev, and J. Ye. Landau theory of quantum spin glasses of rotors and Ising spins. *Phys. Rev. B*, 52:384, 1995.

[161] D. Thirumalai, Q. Li, and T.R. Kirkpatrick. Inifinite-range Ising spin glass in a transverse field. *J. Phys. A*, 22:3339–3349, 1989.

[162] E. Courtens. Competing structural orderings and transitions to glass in mixed crystals of $Rb_{1-x}(NH_4)_xH_2PO_4$. *J Phys Lett*, 43:L199–L204, 1982.

[163] R. Blinc, D. C. Ailion, B. Günther, and S. Zumer. Nuclear Magnetic Resonance in random fields: cluster formation and local dynamics of a Deuteron glass. *Phys. Rev. Lett.*, 57:2826, 1986.

[164] R. Pirc, B. Tadic, and R. Blinc. Random-field smering of the proton-glass transition. *Phys. Rev. B*, 36:8607, 1987.

[165] C. Keller and H. Schmutz. Die reaktion von lithiumfluorid mit den trifluoriden der lanthaniden und einiger actiniden. *J. Inorg. Nucl. Chem.*, 27:900, 1965.

[166] W. Wu, B. Ellmann, T.F. Rosenbaum, G. Aeppli, and D.H. Reich. From classical to quantum glass. *Phys. Rev. Lett.*, 67:2076, 1991.

[167] W. Wu, D. Bitko, and T.F. Rosenbaum. Quenching of the nonlinear susceptibility at a $T = 0$ spin glass transition. *Phys. Rev. Lett.*, 71:1919, 1993.

[168] J. Brooke, W. Wu, T.F. Rosenbaum, and G. Aeppli. Quantum annealing of a disordered magnet. *Science*, 284:779, 1999.

[169] K-M. Tam and M.J.P. Gingras. Spin glass transition at nonzero temperature in a disordered dipolar system: the case of $LiHo_xY_{1-x}F_4$. *ArXiv:0810.0854v2*, 2009.

[170] M. Schechter and N. Laflorencie. Quantum spin glass and the dipolar interaction. *Phys. Rev. Lett.*, 97:137204, 2006.

[171] J. Miller and D.A. Huse. Zero-temperature critical behavior of the infinite-range quantum Ising spin glass. *Phys. Rev. Lett.*, 70:3147, 1993.

[172] H.F. Trotter. On the product of semi-groups of operators. *Proc. Am. Math. Soc.*, 10:545, 1959.

[173] M. Suzuki. Relationship between d-dimensional qauantal spin systems and $(d + 1)$-dimensional Ising systems. *Prog. Theor. Phys.*, 56:1454, 1976.

[174] H. Bruus and K. Flensberg. *Many-Body Quantum Theory in Condensed Matter Physics.* Oxford Graduate Texts, 2004.

[175] A.J. Bray and M.A. Moore. Replica theory of quantm spin glasses. *J. Phys. C: Solid State Phys.*, 13:L655, 1980.

[176] D-H. Kim and J-J. Kim. Infinite-range Ising spin glass with a transverse field under the static approximation. *Phys. Rev. B*, 66:054432, 2002.

[177] R.L. Stratonovich. On a method of calculating Quantum Distribution functions. *Soviet Physics Doklady*, 2:416, 1958.

[178] J. Hubbard. Calculation of partition functions. *Phys. Rev. Lett.*, 3:77, 1959.

[179] M.J. Rozenberg and D.R. Grempel. Dynamics of the infinite-range Ising spin glass model in a transverse field. *Phys. Rev. Lett.*, 81:2550, 1998.

[180] M.Müller and S. Pankov. Mean-field theory for the three-dimensional Coulomb glass. *Phys. Rev. B*, 75:144201, 2007.

[181] H-J. Sommers and W. Dupont. Distribution of frozen fields in the mean field theory of spin glasses. *J. Phys. A*, 17:5785, 1984.

[182] A.V. Goltsev. *J. Phys. A*, 17:237, 1984.

[183] G. Parisi. A sequence of approximated solutions to the SK model for spin glasses. *J. Phys. A*, 13:L115, 1980.

[184] A. Crisanti and T. Rizzo. Analysis of the ∞-replica symmetry breaking solution of the Sherrington Kirkpatrick model. *Phys. Rev. E*, 65:046137, 2002.

[185] S.A. Orszag. Numerical simulation of imcompressible flows within simple boundaries. 1 Galerkin (spectral) representations. *Studies in applied mathematics*, 1:293, 1971.

[186] S. Franz, M. Mézard, G. Parisi, and L. Peliti. The response of glassy systems to random perturbations: a bridge between equilibrium and off-equilibrium. *J. Stat. Phys.*, 97:459, 1999.

[187] L. Cugliandolo and J. Kurchan. On the out-of-equilibrium relaxation of the Sherrington-Kirkpatrick model. *J. Phys. A*, 27:5749, 1994.

[188] J.L. Langer and T. Neal. Breakdown of the concentration expansion for the impurity resistivity of metals. *Phys. Rev. Lett.*, 16:984, 1966.

[189] A. Erdelyi. *Asymptotic expansions.* Dover, 1956.